Gold Metallogeny of the Southern Swayze Area, Abitibi Greenstone Belt

by

Evan Carman George Hastie

A thesis submitted in partial fulfillment
of the requirements for the degree of
Doctor of Philosophy (PhD) in Mineral Deposits and Precambrian Geology

The Faculty of Graduate Studies
Laurentian University
Sudbury, Ontario, Canada

THESIS DEFENCE COMMITTEE/COMITÉ DE SOUTENANCE DE THÈSE
Laurentian Université/Université Laurentienne
Faculty of Graduate Studies/Faculté des études supérieures

Title of Thesis Titre de la thèse	Gold Metallogeny of the Southern Swayze Area, Abitibi Greenstone Belt
Name of Candidate Nom du candidat	Hastie, Evan
Degree Diplôme	Doctor of Philosophy
Department/Program Département/Programme	Mineral Deposits and Precambrian Geology
Date of Defence Date de la soutenance	April 29, 2021

APPROVED/APPROUVÉ

Thesis Examiners/Examinateurs de thèse:

Dr. Daniel Kontak
(Co-Supervisor/Co-directeur(trice) de thèse)

Dr. Bruno Lafrance
(Co-Supervisor/Co-directeur(trice) de thèse)

Dr. Doug Tinkham
(Committee member/Membre du comité)

Approved for the Faculty of Graduate Studies
Approuvé pour la Faculté des études supérieures
Dr. Lace Marie Brogden
Madame Lace Marie Brogden
Acting Dean, Faculty of Graduate Studies
Doyenne intérimaire, Faculté des études supérieures

Dr. Andy Tomkins
(External Examiner/Examinateur externe)

Dr. John Ayer
(Internal Examiner/Examinateur interne)

ACCESSIBILITY CLAUSE AND PERMISSION TO USE

Abstract

Understanding ore forming processes and their control on mineralization is essential for the proper classification of Archean, and also younger, Au deposits and mineral exploration success. This study evaluates Archean Au-forming processes using examples across the Superior Province (Canada), with an emphasis on the Swayze area in the Abitibi greenstone belt. It combines detailed field mapping with various discriminants (e.g., in-situ stable isotopes, whole-rock and trace-element geochemistry, LA-ICP-MS elemental mapping and chemistry of native gold) to differentiate between orogenic and intrusion-related Au deposits. Based on previous work and newly generated data on 44 deposits, the dataset suggests that Ag, Te and Hg are the only metals consistently associated with Au across different deposit types. Although these metals represent universal elemental vectors for Au exploration, other criteria such as rock and mineral textures, timing of Au mineralization, stable isotope data, and bulk geochemistry must be used to differentiate between Au-deposit types. An important finding is the recognition of a distinct subset of intrusion-related Archean deposits related to sanukitoid-type magmatism. These deposits, generally younger than 2690 Ma, predate shearing and are characterized by Te and Hg elemental associations, relatively high fO_2, and $\delta^{34}S \leq -5‰$. They differ from other intrusion-related deposits in terms of their timing and geochemistry and, thus, require a different exploration strategy.

Of importance to both academia and industry is the origin of late-stage high-grade Au zones in many deposits. This study suggests such zones result from coupled dissolution-reprecipitation of Au-bearing sulfides and generation of polymetallic Au melts and/or Au nanoparticles, which

aggregate as coarse native gold. Both of the processes can elegantly explain ultra high-grade gold zones and are widely applicable to many Au deposits formed throughout Earth's history.

Keywords

Gold, Au, Archean, Swayze area, Abitibi greenstone belt, Superior Province, Au-forming processes, economic geology, geochemistry, Jerome, Kenty, Rundle, Namex, 4K, Au remobilization, dissolution-reprecipitation, gold nanoparticle, S isotopes, O isotopes, LA-ICP-MS, TEM, SEM-EDS, TIMS, SIMS.

Co-Authorship Statement

This thesis consists of three manuscripts (Chapters 2, 3 and 4) that are formatted for separate journal requirements. Chapter 2 is co-authored by E.C.G. Hastie, D.J. Kontak, B. Lafrance, J.A. Petrus, R. Sharpe and M. Fayek (to be submitted to Economic Geology). Chapter 3 is co-authored by E.C.G. Hastie, D.J. Kontak and B. Lafrance (published in Economic Geology, v. 115, p. 241-277). Chapter 4 is co-authored by E.C.G. Hastie, M. Schindler, D.J. Kontak and B. Lafrance (accepted and soon to be published in Communications Earth & Environment). Field mapping, sample collection, sample preparation and sample characterization by petrographic and scanning electron microscopy was completed by E.C.G. Hastie. E.C.G. Hastie is also responsible for all interpretations presented in the manuscripts and thesis. Manuscript preparation benefited from suggestions and revisions by co-authors.

Acknowledgments

The most profound thanks to my supervisors, Dr. Bruno Lafrance and Dr. Dan Kontak, for their mentorship during this incredible project. I would like to acknowledge the generous support offered by the Ontario Geological Survey (OGS), the Mineral Exploration Research Centre (MERC) and the Goodman School of Mines at Laurentian University. This work was supported through the Ontario Geological Survey-Laurentian University Graduate Mapping School Agreement. Special thanks are offered to Charlie Mortimer, Larry Salo, Rundle-Swayze Mines Inc. and IAMGOLD Corp. for their help during field work. In addition, special thanks to the Royal Ontario Museum (ROM), specifically Katherine Dunnell and Dr. Kim Tait, for providing access to the historic gold samples examined. Thank you to faculty, staff and fellow graduate students for discussions during my time at the Harquail School of Earth Sciences. Thank you to individuals that assisted with analytical methods: LA-ICP-MS (Joe Petrus), SEM-EDS and EMPA (Sandra Clarke and Dave Crabtree), SIMS (Ryan Sharpe and Dr. Mostafa Fayek), TEM (Dr. Michael Schindler). Finally, thank you to my wife Heather Hastie and our son Hunter for all of their support during this journey.

Table of Contents

List of Tables

List of Figures

List of Appendices

Chapter 1

1 General Introduction

Archean Au deposits are globally significant resources, with many of the largest and highest grade known examples sourced in Archean terranes (Goldfarb et al., 2005; Goldfarb and Groves, 2015). Many precious-metal deposit types (i.e., VMS-, epithermal-, and porphyry-type) have achieved a broad consensus in terms of their genetic origins, however, many aspects of orogenic Au deposits continue to be debated: deposit type classification, geochemical discrimination, sources for Au, mechanisms of Au transport, and formation of high-grade ore zones (e.g., Kerrich, 1993; Groves et al., 2003; Goldfarb et al., 2005; Goldfarb and Groves, 2015). These debates are further complicated in Archean deposits by their complex metamorphic, deformation and overprinting histories that render much of the evidence for Au-forming processes equivocal (e.g., Marshall and Gilligan, 1987, 1993; Groves et al., 2003; Hastie et al., 2020).

Over the past 30 years, Au deposit classification and terminology have changed with most studies now using the term “orogenic” versus lode gold, mesothermal, shear zone-related quartz-carbonate and gold-only (Kerrich, 1993; Phillips and Powell, 1993; Groves et al., 1998; McCuaig and Kerrich, 1998, Hagemann and Cassidy, 2000; Poulsen et al., 2000; Goldfarb et al., 2005; Dubé and Gosselin, 2007; Goldfarb and Groves, 2015). The term “orogenic” (Groves et al., 1998) is currently favored for epigenetic Au deposits that share common formational processes during collisional orogeny, but distinguishing Archean intrusion-hosted orogenic deposits (Goldfarb et al., 2005) from intrusion-related deposits (Goldfarb et al., 2005; Robert et al., 2005; Katz et al., 2017, McDivitt et al., 2018) can be fraught with problems because orogenic

Au deposits can be spatially associated with intrusions and intrusion-related deposits may be emplaced during orogenic events.

Since the 1970s, multi-discipline investigations that include bulk geochemical analysis have been used as tools for studying Archean Au deposits. While the results and related interpretations of these data have significantly advanced our understanding of Au-forming processes and related genetic models (e.g., Kerrich and Wyman, 1990; Kerrich, 1993; McCuaig and Kerrich, 1998; Hagemann and Cassidy, 2000; Goldfarb et al., 2005; Goldfarb and Groves, 2015), most findings remain equivocal. For exploration companies targeting Archean Au deposits, this means that these findings have limited application (Kerrich, 1993; McCuaig and Hronsky, 2014; Laflamme et al., 2018). Furthermore, the misclassification of orogenic-type versus intrusion-related-type deposits can negatively affect the search for those deposits, as they require different exploration strategies. Thus, the relevant question follows: can geochemistry help discriminate between orogenic and intrusion-related deposits and their formational processes? If this is possible, what discriminants can be used for this purpose?

The formation of high-grade zones in Archean Au deposits is also a critical question to both academia and industry. These deposits are often the result of multiple enrichment events (Groves et al., 2003; Goldfarb et al., 2005; Velásquez et al., 2014; Hastie et al., 2020), but the evidence presented in favor of Au remobilization versus a second distinct epigenetic Au event is often equivocal. Another problem is that traditional fluid transport mechanisms cannot account for the high-grade gold found in these zones because of the low solubility of gold in hydrothermal fluids (Hastie et al., 2020; Voisey et al., 2020). How high-grade zones and ore shoots form in Au deposits is critical to understanding deposit evolution and important for exploration because they allow companies to predict more reliably the location of these zones.

The Archean Abitibi greenstone belt (AGB) in the Superior Province, Canada (Fig. 1.1A, B), is a globally significant gold setting with over 300 Moz of Au from past production and current reserves and resources (Mercier-Langevin et al., 2020; Dubé and Mercier-Langevin, 2021). This includes Au from volcanogenic massive sulfide (VMS), orogenic and intrusion-related deposits and makes the Abitibi an ideal area to conduct research on Archean Au-forming processes. The Swayze area (Fig. 1.1C) of northern Ontario (also discussed as Swayze greenstone belt; Heather, 2001) represents the southwestern extension of the Au-rich AGB (van Breemen et al., 2006; Thurston et al., 2008; Ayer et al., 2010; Monecke et al., 2017). The 2010 discovery of the Côté Gold deposit (>8 Moz Au), an Archean, intrusion-related porphyry-type deposit (Kontak et al., 2013; Katz et al., 2017; Katz et al., 2020), has stimulated exploration activity in the Swayze area, which historically has only produced approximately 0.1 Moz gold (van Hees et al., 2019). Although the increase in exploration activity in the belt led to the sponsoring of this research by the Ontario Geological Survey, the Swayze area also represents an ideal location to study Au-forming processes due to its simple mineralization history and lack of multiple overprinting events that obscure evidence of formational processes elsewhere in the Abitibi.

The main goal of this thesis is to understand the Au metallogeny of the southern Swayze area and use this new knowledge to evaluate Archean Au-forming processes and answer questions fundamental to Au deposit formation. More specifically, the objectives of the thesis are to evaluate different Archean Au deposit types, their discrimination and how late-stage high-grade Au zones form. Accomplishing these objectives included: 1) performing reconnaissance on all prospective Au occurrences in the Swayze area (>170) and selecting from these representatives of the different Au-deposit types and mineralization styles; (2) performing

detailed geological mapping and sampling of selected representative deposits (n =5); and (3) characterizing the latter in terms of mineralogy, geochemistry, geochronology and structural geology. Field work and mapping was complemented by an array of bulk and in-situ geochemical techniques in a comprehensive approach. Techniques included: (1) bulk whole-rock, trace-element and trace-metal geochemistry; (2) in-situ mineral analysis by SEM-EDS and EMPA microscopy; (3) in-situ LA-ICP-MS elemental mapping of sulfides; (4) in-situ stable isotope (O and S) geochemistry by SIMS; (5) nano-scale mineral observations by TEM; and (6) U-Pb geochronology by TIMS and LA-ICP-MS.

1.1 Thesis format

This thesis consists of three journal manuscripts. Chapter 1 is a general introduction to the thesis. It provides a general background for the thesis and presents the goals of the thesis. This is followed by three manuscripts: Chapter 2 evaluates bulk and in-situ geochemical data in an effort to better understand Au-forming processes and the utility of geochemical discriminants in Archean Au deposits (intended for Economic Geology). Chapter 3 presents insights into Au remobilization and how this process leads to the formation of high-grade ore zones in Au deposits. It is published in Economic Geology (https://doi.org/10.5382/econgeo.4709). Chapter 4 reports results on Au nanoparticle processes and how gold coarsens during the evolution of an Archean orogenic Au deposit. The manuscript has been accepted and is soon to be published in Communications Earth & Environment (new online journal of Nature Research). Chapter 5 is a concluding chapter that summarizes the main findings of the thesis and their global significance. Preliminary summary of field work articles for the Ontario Geological Survey (Hastie, 2014; Hastie et al., 2015; Hastie et al., 2016; MacDonald et al., 2017) and a field trip guidebook

(Hastie, 2017) have also been published and a miscellaneous release of all geochemical data gathered throughout this project will be released by the Ontario Geological Survey following completion of the thesis.

1.2 References

Ayer, J.A., Goutier, J., Thurston, P.C., Dubé, B., and Kamber, B.S., 2010, Tectonic and metallogenic evolution of the Abitibi and Wawa subprovinces: in Summary of Field Work and Other Activities, 2010, Ontario Geological Survey, Open File Report 6260, p. 3-1 to 3-6.

Dubé, B., and Gosselin, P., 2007, Greenstone-hosted quartz-carbonate vein deposits: *in* Goodfellow, W.D., ed., Mineral deposits of Canada: A synthesis of major deposit-types, district metallogeny, the evolution of geological provinces, and exploration methods: Geological Association of Canada, Mineral Deposits Division, Special Publication no. 5, p. 49-73.

Dubé, B., and Mercier-Langevin, P., 2021, Gold deposits of the Archean Abitibi greenstone belt, Canada: Society of Economic Geologists, Special Publication no. 23, p. 669-708.

Goldfarb, R.J., Baker, T., Dubé, B., Groves, D.I., Hart, C.J.R., and Gosselin, P., 2005, Distribution, character, and genesis of gold deposits in metamorphic terranes: Economic Geology 100th Anniversary Volume, p. 407-450.

Goldfarb, R.J. and Groves, D.I., 2015, Orogenic gold: Common or evolving fluid and metal sources through time: Lithos, v. 233, p. 2-26.

Groves, D.I., Goldfarb, R.J., Gebre-Mariam, M., Hagemann, S.G., and Robert, F., 1998, Orogenic gold deposits: A proposed classification in the context of their crustal distribution and relationship to other gold deposit types: Ore Geology Reviews, v. 13, p. 7-27.

Groves, D.I., Goldfarb, R.J., Robert, F., and Hart, C.J.R., 2003, Gold deposits in metamorphic belts: Overview of current understanding, outstanding problems, future research, and exploration significance: Economic Geology, v.98, p.1-29

Hagemann, S.G. and Cassidy, K.F., 2000, Archean Orogenic lode gold deposits: Reviews in Economic Geology, v. 13, p. 9-68.

Hastie, E.C.G., 2014, Gold metallogeny of the southern Swayze greenstone belt; *in* Summary of Field Work and Other Activities 2014, Ontario Geological Survey, Open File Report 6300, p. 7-1 to 7-8.

Hastie, E.C.G., 2017, Gold metallogeny of the southern Swayze area, Abitibi greenstone belt: a field trip guidebook: Ontario Geological Survey, Open File Report 6334, 19 p.

Hastie, E.C.G., Kontak, D.J., and Lafrance, B., 2016, Update on activities related to a gold metallogenic study of the southern Swayze greenstone belt: *in* Summary of Field Work and Other Activities 2016, Ontario Geological Survey, Open File Report 6323, p. 8-1 to 8-11.

Hastie, E.C.G., Kontak, D.J. and Lafrance, B. 2020. Gold remobilization: Insights from gold deposits in the Archean Swayze greenstone belt, Abitibi Subprovince, Canada; Economic Geology, v. 115, p. 241-277.

Hastie, E.C.G., Lafrance, B., and Kontak, D.J., 2015, Observations on the Kenty and Rundle deposits, Swayze greenstone belt: *in* Summary of Field Work and Other Activities, 2015, Ontario Geological Survey, Open File Report 6313, p. 9-1 to 9-9.

Heather, K.B., 2001, The geological evolution of the Archean Swayze greenstone belt, Superior Province, Canada: unpublished PhD thesis, Keele University, Keele, England, 370 p.

Katz, L.R., Kontak, D.J., Dubé, B., and McNicoll, V., 2017, The geology, petrology, and geochronology of the Archean Côté Gold large-tonnage, low-grade intrusion-related Au(-Cu) deposit, Swayze greenstone belt, Ontario, Canada: Canadian Journal of Earth Sciences, v. 54, p. 173-202.

Katz, L.R., Kontak, D.J., Dubé, B., McNicoll, V., Creaser, R., and Petrus, J.A., 2020, An Archean porphyry-type gold deposit: The Côté Gold Au(-Cu) deposit, Swayze greenstone belt, Superior Province, Ontario, Canada: Economic Geology (2020), https://doi.org/10.5382/econgeo.4785.

Kerrich, R. and Wyman, D., 1990, Geodynamic setting of mesothermal gold deposits: An association with accretionary tectonic regimes: Geology, v. 18, p. 882-885.

Kerrich, R., 1993, Perspectives on genetic models for lode gold deposits: Mineralium Deposita, v. 28, p. 362-365.

Kontak, D.J., Creaser, R.A., and Hamilton, M.A., 2013, Section 2: Geological and geochemical studies of the Côté Lake Au(-Cu) deposit area, Chester Township, Northern Ontario; report *in* Results from the Shining Tree, Chester Township and Matachewan Gold Projects and the

Northern Cobalt Embayment Polymetallic Vein Project, Ontario Geological Survey, Miscellaneous Release-Data 294.

Laflamme, C., Sugiono, D., Thébaud, N., Caruso, S., Fiorentini, M., Selvaraja, V., Jeon, H., Voute, F. and Martin, L., 2018, Multiple sulfur isotopes monitor fluid evolution of an Archean orogenic gold deposit: Geochimica et Cosmochimica Acta, v. 222, p. 436-446.

MacDonald, P.J., Hastie, E.C.G., and Davis, D.W., 2017, Preliminary geology of Osway and Huffman Townships and parts of Eric, Fingal and Arbutus Townships, southern Swayze area, Abitibi greenstone belt: *in* Summary of Field Work and Other Activities 2017, Ontario Geological Survey, Open File Report 6333, p. 7-1 to 7-13.

Marshall, B., and Gilligan, L.B., 1987, An introduction to remobilization: information from ore-body geometry and experimental considerations: Ore Geology Reviews, v. 2, p. 87-131.

Marshall, B., and Gilligan, L.B., 1993, Remobilization, syn-tectonic processes and massive sulphide deposit: Ore Geology Reviews, v. 8, p. 39-64.

Mercier-Langevin, P., Lawley, C.J.M., Castonguay, S., Dubé, B., Bleeker, W., Pinet, N., Bécu, V., Pilote, J –L., Jackson, S. E., Wodicka, N., Honsberger, I.W., Davis, W.J., Petts, D.C., Yang, Z., Jautzy, J., and Lauzière, K., 2020, Targeted Geoscience Initiative 5, Gold Project: a summary of contributions to the understanding of Canadian gold systems, *in* Mercier-Langevin, P., Lawley, C.J.M., Castonguay, S. eds., Targeted Geoscience Initiative 5: contributions to the understanding of Canadian gold systems: Geological Survey of Canada, Open File 8712, p. 1-30.

McCuaig, T.C. and Hronsky, J.M.A., 2014, The mineral systems concept: the key to exploration targeting: Society of Economic Geologists Special Publication 18, p. 153-175.

McCuaig, T.C. and Kerrich, R., 1998, P-T-t-deformation-fluid characteristics of lode gold deposits: evidence from alteration systematics: Ore Geology Reviews, v. 12, p. 381-453.

McDivitt, J.A., Kontak, D.J., Lafrance, B., and Robichaud, L., 2018, Contrasting fluid chemistries, alteration characteristics, and metamorphic timing relationships recorded in hybridized orebodies of the Missanabie-Renabie gold district, Archean Wawa Subprovince, Ontario, Canada: Economic Geology, v. 113, p. 397-420.

Monecke, T., Mercier-Langevin, P., Dubé, B., and Frieman, B.M., 2017, Geology of the Abitibi greenstone belt: Reviews in Economic Geology, v. 19, p. 7-49.

Ontario Geological Survey, 2011, 1:250 000 scale bedrock geology of Ontario: Ontario Geological Survey, Miscellaneous Release—Data 126–Revision 1.

Phillips, G.N., and Powell, R., 1993, Link between Gold Provinces: Economic Geology, v. 88, p. 1084-1098.

Poulsen, K.H., Robert, F., and Dubé, B., 2000, Geological classification of Canadian gold deposits: Geological Survey of Canada Bulletin 540, 106 p.

Robert, F., Poulsen, K.H., Cassidy, K.F., and Hodgson, C.J., 2005, Gold metallogeny of the Yilgarn and Superior cratons: Economic Geology 100th Anniversary Volume, p. 1001-1033.

Thurston, P.C., Ayer, J.A., Goutier, J., and Hamilton, M.A., 2008, Depositional gaps in Abitibi greenstone belt stratigraphy: A key to exploration for syngenetic mineralization: Economic Geology, v. 103, p. 1097-1134.

van Breemen, O., Heather, K.B., and Ayer, J.A., 2006, U-Pb geochronology of the Neoarchean Swayze sector of the southern Abitibi greenstone belt: Geological Survey of Canada, Current Research 2006-F1, 32 p.

van Hees, E.H., Bousquet, P., Suma-Momoh, J., Daniels, C.M., Hinz, S.L.K., Boucher, C., Sword, P., Wang, L., Fudge, S.P., Millette, A., and Patterson, C., 2020, Report of Activities 2019, Resident Geologist Program, Timmins Regional Resident Geologist Report: Timmins and Sault Ste. Marie Districts: Ontario Geological Survey, Open File Report 6366, 160p

Velásquez, G., Béziat, D., Salvi, S., Siebenaller, L., Borisova, A.Y., Pokrovski, G.S., and de Parseval, P., 2014, Formation and deformation of pyrite and implications for gold mineralization in the El Callao District, Venezuela: Economic Geology, v. 109, p.457-486.

Voisey, C.R., Willis, D., Tomkins, A.G., Wilson, C.J.L., Micklethwaite, S., Salvemini, F., Bougoure, J., and Rickard, W.D.A., 2020, Aseismic refinement of orogenic gold systems: Economic Geology, v. 115, p. 33-50.

1.3 Figures

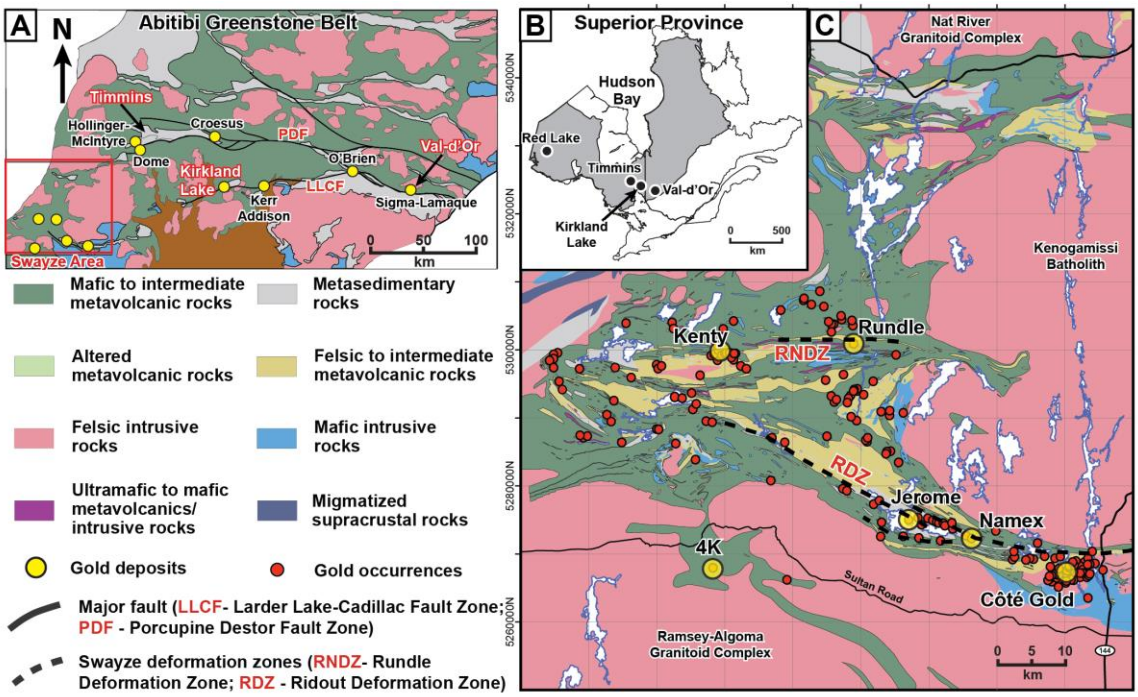

Figure 1.1. Geologic map of the Swayze area, southwest Abitibi greenstone belt, Superior Province, Canada. A) Simplified geologic map of the Abitibi greenstone belt (modified after Dubé and Gosselin, 2007) with the Swayze area bounded by a red rectangle. B) Location of the study area within the Superior Province. C) Simplified geologic map of the Swayze area with Au deposits studied shown by yellow circles and gold occurrences by red circles. Location information provided as Universal Transverse Mercator (UTM) co-ordinates using North American Datum 1983 (NAD83) in Zone 17 (modified after Ontario Geological Survey, 2011; 2019; MacDonald et al., 2017 and Hastie et al., 2020).

Chapter 2

2 Evaluating the utility of geochemical discriminants in Archean Au deposits: A Superior Province perspective with emphasis on the Abitibi greenstone belt

Evan C.G. Hastie[1, 2], Daniel J. Kontak[1], Bruno Lafrance[1], J.A. Petrus[1], R. Sharpe[3] and M. Fayek[3]

[1]Harquail School of Earth Sciences, Laurentian University, Sudbury, Ontario P3E 2C6;
[2]Earth Resources and Geoscience Mapping Section, Ontario Geological Survey, Sudbury, Ontario P3E 6B5
[3]Department of Geological Sciences, University of Manitoba, Winnipeg, Manitoba R3T 2N2

To be submitted to Economic Geology

2.1 Abstract

Discriminating among Archean Au deposit types and related ore-forming processes is challenging, but it is paramount for increasing Au exploration success. This study tests the validity of using geochemical data generated using traditional bulk versus more modern in-situ methods as discriminants for classifying Au deposits in the Archean Swayze greenstone belt (SGB) with further comparison to other deposits in the contiguous Abitibi greenstone belt and Red Lake area (Superior Province, Canada). The study used five well characterized Au settings based on our new mapping as a basis for generating in-situ ($\delta^{18}O_{quartz}$, $\delta^{33,34}S_{sulfide}$, LA-ICP-MS sulfides, native gold) and whole-rock geochemical datasets to resolve if intrusion-related can be discriminated from orogenic-type Au deposits. Results show that in-situ methods provide insight into processes responsible for Au mineralization, both primary and subsequent remobilization and upgrading, and define elemental and isotopic correlations not possible using bulk methods. For example, results show that only Ag, Te, and Hg show a consistent correlation with Au across deposit types. Furthermore, the whole-rock datasets combined with in-situ isotopic analysis

further suggest the Archean sanukitoid-associated Au deposits represent a distinct group of intrusion-related deposits with mineralization characterized by low $\delta^{34}S_{pyrite}$ (<-5 to -25‰), inferred high fO_2, a Hg-Te signature, and hosted in intrusions <2690 Ma that predate shearing. The protocol presented herein provides a template that we suggest should be widely utilized in future studies of all Au-deposit types.

2.2 Introduction

Discriminating among Au deposit types in the Archean and their formational processes is critical to understanding one of the most significant Au resources on Earth. Classification and nomenclature of these deposits have evolved over the past 30 years to include: lode gold, mesothermal, orogenic, shear zone-related quartz-carbonate and gold-only deposits, with many authors now favoring the term orogenic (Kerrich, 1993; Phillips and Powell, 1993; Groves et al., 1998; McCuaig and Kerrich, 1998, Hagemann and Cassidy, 2000 Poulsen et al., 2000; Goldfarb et al., 2005; Dubé and Gosselin, 2007; Goldfarb and Groves, 2015). While it may be appropriate to use the terms orogenic or shear zone-related quartz-carbonate for epigenetic shear zone-hosted deposits that formed during a collisional orogenic event (Groves et al., 1998; Dubé and Gosselin, 2007), intrusion-related deposits form a distinct group of Archean deposits that either predated or formed early during the same collisional event and are typically hosted by intrusions (Robert, 2001; Dubé and Mercier-Langevin, 2021). Some of the best examples of intrusion-related Au deposits are in the Abitibi greenstone belt (AGB) of the Superior Province, Canada, where they are hosted by early tonalite-trondhjemite-granodiorite (TTG) intrusions (e.g., circa 2740 Ma Côté gold deposit; Katz et al., 2017; 2021) and late, syn-Timiskaming, ca. 2680 to 2670 Ma, “syenitic" intrusions (Robert, 2001; but see Dubé and Mercier-Langevin, 2021 for terminology).

Other pre-orogenic Au-rich deposits include the volcanogenic massive sulfide (VMS) Horne, Quemont, Bousquet, and LaRonde Penna deposits, which are associated with syn-volcanic intrusions (Robert, 2001, Galley, 2003; Mercier-Langevin et al., 2011; Galley and Lafrance, 2014).

For exploration companies targeting Au deposits in Archean terranes, such as the AGB, the distinction between orogenic and intrusion-related deposits is important, as this dictates the strategy used to explore for these different deposit types. Thus, the question addressed herein is whether geochemistry can be used to discriminate between orogenic and intrusion-related deposits and processes related to their formation and, if so, what geochemical discriminants are best suited for this.

The application of bulk geochemical data to potentially discriminate processes has been applied to Archean Au deposits since the 1970s (summaries in McCuaig and Kerrich, 1998; Hagemann and Cassidy, 2000; Beaudoin, 2011). While significantly advancing the understanding of Au-forming processes, and hence genetic models (e.g., Kerrich and Wyman, 1990; Kerrich, 1993; McCuaig and Kerrich, 1998 Goldfarb et al., 2005), many of the findings remain equivocal, and therefore of limited application to mineral exploration (Kerrich, 1993; McCuaig and Hronsky, 2014; Laflamme et al., 2018). In contrast, recent advances of in situ methods have provided spatial resolution (i.e., micrometer- to nanometer-scales) and detection limits that can resolve subtleties bulk methods cannot. For example, cathodoluminescence (CL) or high-contrast back-scattered electron (BSE) images combined with laser ablation inductively-coupled mass spectrometry (LA-ICP-MS) and/or secondary ion mass spectrometry (SIMS) allow the imaging and analysis of individual mineral generations and zones in minerals that would be

homogenized by bulk methods (e.g., Neyedley et al., 2017; Kerr at al. 2018; Hastie et al., 2020a; McDivitt et al., 2020).

To address the aforementioned issues, this study uses well-constrained Archean Au deposits from the SGB supplemented by examples from well-known Au districts across the AGB and Superior Province, Canada. Detailed characterization of these samples provides the basis to evaluate the potential utility of geochemical discriminants, such as bulk whole-rock geochemistry, in-situ isotopes (O and S) and trace-metal geochemistry, for assessing ore-forming processes in orogenic and intrusion-related gold deposits. The study also aims to advance the understanding of fluid reservoirs and Au associations critical to exploration for new deposits.

2.3 Regional Geology

The AGB (Fig. 2.1) hosts numerous globally significant Au deposits and has a total Au endowment (production, reserves and measured and indicated resources) of over 300 Moz of Au from orogenic, intrusion-related and volcanogenic massive sulfide (VMS) deposits, which accounts for a significant portion of the Au endowment of the Superior Province (Mercier-Langevin et al., 2020; Dubé and Mercier-Langevin, 2021). The AGB was constructed during six volcanic episodes (2750-2735 Ma Pacaud; 2734-2724 Ma Deloro; 2723-2720 Ma Stoughton-Roquemaure; 2720-2710 Ma Kidd-Munro; 2710-2704 Tisdale; 2704-2695 Blake River; Ayer et al., 2002; Monecke et al., 2017) followed by the deposition of two sedimentary successions (2690-2685 Ma Porcupine; 2680-2669 Ma Timiskaming). At least one deformation event occurred prior to Timiskaming sedimentation, which was followed by further shortening, strike-slip movement and shear zone development (Robert 2001; Dubé and Gosselin 2007; Bateman et al., 2008; Thurston et al., 2008; Monecke et al. 2017). Some of these shear zones coincide with

earlier crustal-scale breaks, such as the prominent Porcupine-Destor and Larder-Lake-Cadillac fault zones, which, along with second and third-order splays, host many of the Au deposits in the AGB (Dubé and Gosselin 2007; Monecke et al. 2017). The western AGB attained maximum metamorphic pressures of ≈3 kbars and temperatures of 350°C to 450°C after the deposition of the Timiskaming sedimentary rocks (Thompson, 2005).

The Swayze area (Fig. 2.1) in northern Ontario (also referred to as Swayze greenstone belt; Heather, 2001) represents the southwestern extension of the Au-rich AGB (Ayer et al., 2002; van Breemen et al., 2006; Thurston et al., 2008; Ayer et al., 2010; Monecke et al., 2017). While it is considered to be part of the AGB, herein it is referred to as the Swayze greenstone belt (SGB) to facilitate geographical location. Although the discovery of the ≈10 Moz intrusion-related Côté Gold deposit (Fig. 2.1C; Katz et al., 2017, 2021) has renewed exploration interest in the SGB, its historical production was ≈0.1 Moz Au over the last century (van Hees et al., 2019). Its geology is dominated by intrusive and extrusive rocks of ultramafic to felsic composition with lesser chemical and clastic metasedimentary rocks. These rocks were deposited and emplaced semi-continuously from 2750 Ma to 2670 Ma as volcanic episodes (Pacaud, Deloro, Kidd-Munro, Tisdale, Blake River) and sedimentary successions (Timiskaming) that are identical to those in the AGB (Heather, 2001; Ayer et al., 2002; van Breemen et al., 2006; Gemmell and MacDonald, 2016; OGS, 2019). The southern SGB also has two regional deformation zones, known as the Rundle and Ridout deformation zones, which have a spatial association with Au occurrences and deposits (Fig. 2.1C). In addition to the ca. 2740 Ma intrusion-related Côté Gold deposit (Katz et al., 2017), Au deposits in the southern SGB are similar in mineralization styles to those in the AGB, including greenstone-hosted orogenic, BIF-hosted orogenic and syn-Timiskaming intrusion-hosted Au deposits (Hastie et al., 2017; MacDonald et al., 2017; Ontario

Geological Survey, 2019; Hastie et al., 2020a). The SGB experienced regional greenschist facies metamorphism and localized amphibolite facies metamorphism near large granitoid complexes along its northern, southern and eastern margins (Heather, 2001). The ‘meta’ prefix is omitted from rock names for the sake of brevity.

2.4 Sampling and Analytical Techniques

2.4.1 Deposit and Sample Selection

Over 170 Au occurrences from the SGB were considered for this study through detailed field examination. Of these, five deposits that have different and representative Au mineralization types (Rundle, Namex, Jerome, Kenty and 4K) were selected based on the availability of field exposures and samples. Also relevant, is that the selected study areas escaped overprinting events that typify many of the world-class deposits of the AGB, and thus they provide an excellent opportunity to examine relevant processes in rocks equivalent to the Au-endowed AGB (Hastie et al., 2020a).

A total of 378 samples were collected for a comprehensive geochemical study that included whole-rock analysis (i.e., major and trace-elements) stable isotopes (O and S) and LA ICP-MS pyrite chemistry. These were collected over three field seasons (2014 to 2016) from the Kenty (n=97), Rundle (n=95), Jerome (n=62), Namex (n=48) deposits and 4K prospect (n=76). The distinct styles of Au mineralization represented at these localities were mapped at both regional- and deposit scales with mineralized and non-mineralized samples collected from both outcrop and drill core.

To provide a more regional context, an additional 219 samples from 39 well-known Au deposits across the AGB and the Red Lake district (over 29 Moz produced; Peterson et al., 2020) were selected from archived suites at the Royal Ontario Museum (ROM). These deposits included both conventional (orogenic and intrusion-related) and non-conventional (VMS) Au deposits for comparison. From these samples, a subset of 41 were selected for stable isotopic (O, S) analysis

2.4.2 Petrography and SEM-EDS

Transmitted and reflected light petrography was done on all samples using conventional optical microscopy and scanning electron microscopy, the latter with a Zeiss EVO 50 SEM housed at the Geoscience Laboratories, Sudbury, Ontario. This work was done to determine mineral assemblages and rock types in addition to select locations for SIMS and LA-ICP-MS analyses. The SEM is equipped with an Oxford X-Max 50 mm2 energy dispersive spectrometer (EDS) that uses Oxford's Aztec© software package. Operating conditions were 20 kV and 750 pA at working distance of 8.5 mm with counting times ranging per spot analysis (20 to 40 seconds).

2.4.3 SIMS O and S isotopic analyses

A subset 291 quartz and 158 sulfide (i.e., pyrite, chalcopyrite, pyrrhotite, arsenopyrite,) grains were selected from samples from the study area and ROM Superior Province samples (see details below) for in situ SIMS analysis at the Manitoba Isotope Research Facility, Winnipeg, Manitoba. All minerals were mounted in epoxy pucks except for one thin section containing chemically zoned pyrite. SIMS analysis was done using a CAMECA 7f ion microprobe coupled with an ETP 133H electron multiplier and an ion-counting system to detect ions. Instrumental mass fractionation was corrected by calibrating on mineral standards having a composition similar to the target mineral (see details in Sheehan et al., 2016). Minerals of interest and standards were

measured in the same analytical session. To assess intragrain variability, a “duplicate” analysis was performed on every third grain, at a minimum, but in a different location.

The arsenopyrite standard used in this study is from the Beaver Dam deposit, Nova Scotia (Kontak and Smith, 1989) and has not previously been characterized by SIMS. It was chosen based on its previous characterization and reproducibility of data. It has a $\delta^{34}S$ value of 10‰, which compares to an average of 10.6‰ (±0.6‰, 1σ) based on 11 arsenopyrite separates analysed from this deposit, as determined using conventional bulk thermal ionization mass spectrometry (TIMS) measurements. SIMS analysis of this arsenopyrite has a spot-to-spot reproducibility of 0.5‰ (Table 2.2). A full list of operating conditions and parameters, including a list of standards and their spot-to-spot reproducibility, is given in Table 2.2.

2.4.4 Whole-rock and trace-element chemistry

After cleaning and removal of weathered material, whole-rock and trace-element geochemistry was obtained for both representative least altered and mineralized samples from the studied deposits (Rundle, n=102; Kenty, n=81; Namex n=44; Jerome n=58; 4K, n=63; App. Table A1). Analyses were performed at Geoscience Laboratories at the Ontario Geological Survey, Sudbury, Ontario. Method codes for each step are italicized in parentheses and refer to fee schedules from Geoscience Laboratories 2014 to 2016 inclusive.

Samples were pulverized using an agate mill to minimize contamination (i.e., Cr, Fe, Al). Major element analysis (i.e., Al_2O_3, BaO, CaO, Cr_2O3, Fe_2O_3, K_2O, MgO, MnO, Na_2O, P_2O_5, SiO_2, TiO_2) was done by X-ray Fluorescence (XRF-M01) with loss on ignition determined at 105°C under a nitrogen atmosphere and 1000°C under an oxygen atmosphere. Following this, the calcined samples were fused with a borate flux to produce glass beads for analysis. Ferrous

iron (FEO-ION) was determined by dissolving samples in a non-oxidizing acid mix and quantifying by potentiometric titration with a standardized permanganate solution. Total carbon and sulfur (IRC-100) were determined by combusting samples in an oxygen-rich environment and measuring them by infrared absorption. Trace element analysis (i.e., Ba, Be, Bi, Cd, Ce, Cs, Cr, Co, Cu, Dy, Er, Eu, Gd, Ga, Hf, Ho, In, La, Pb, Li, Lu, Mo, Nd, Ni, Nb, Pr, Rb, Sb, Sm, Sc, Sr, Ta, Tb, Tl, Th, Tm, Sn, Ti, W, U, V, Yb, Y, Zn, Zr) was performed by ICP-MS (IMC-100) with samples prepared using a closed vessel multi-acid digest (SOL-CAIO). For increased elemental working ranges and to determine other important metal abundances, metal concentrations (i.e., As, Ag, Au, Bi, Cd, Cr, Co, Cu, Hg, Mo, Ni, Pb, Pt, Sb, Se, Sn, Te, Tl, Zn) were determined by ICP-MS (IML-100) after an open-vessel aqua regia digestion (SOL-ARD). Au concentrations by this method were confirmed using fire assay with a gravimetric finish (GFA-PBG). Quality assurance for precision and accuracy of the methods comprised duplicate analyses, blanks and both in-house (not listed) and inter-laboratory standard reference materials: BHVO-2, GSP-2, SY-4, UB-N (XRF-M01); AGV-2, BHVO-2, GSP-2 (IMC-100); BIR-1, FER-1, FER-2, FER-3, MRG-1, PM-S, SY-3, SY-4 (FEO-ION); FER-4, JDo-1, KC-1A, MP-1a, NIST-8607, PR-1, STSD-1, STSD-2, TLS-1 (IRC-100); CH-4, MA-1b, STSD-1, STSD-3, LKSD-2, LKSD-3, LKSD-4 (IML-100); SQ47 (GFA-PBG). In addition, Geoscience Laboratories is certified under ISO 9001:2008 and the XRF-M01, IMC-100, IML-100 and GFA-PBG methods are ISO/IEC 17025:2005 accredited. Detection limits for all analyses as well as quality assurance and quality control (QA/QC) data can be found in Appendix Table A1.

2.4.5 LA-ICP-MS analysis of pyrite

Pyrites from the SGB deposits were mapped for their trace elements by LA-ICP-MS in the Chemical Fingerprinting Laboratory of Laurentian University. A single representative, Au-bearing example from Kenty, Jerome, Rundle and Namex were used for comparison. The analyses were done using a Thermo X-Series II quadrupole ICP-MS coupled with a Resonetics, RESOlution M-50 193nm, 20 ns pulse width, ArF excimer LA system and a Laurin Technic two-volume cell. Laser spot sizes for the different maps generated via line traverses ranged from 10 to 20 μm depending on expected resolution and sulfide grain size. Reference materials included NIST 610, Po725, GSD-1G and GSE-1G with each analyzed twice every 15 lines. Prior to each line traverse, background acquisition times of 30 seconds were completed both on unknowns and reference materials. The trace element reduction scheme in Iolite 3 (Paton et al., 2011) was used to quantify the raw data using Fe as the internal standard. Most elements were calibrated using GSD-1G (three maps) and GSE-1G (one map) except for Au, Fe and S, which were calibrated on Po725. Because Te does not occur in GSD-1G, GSE-1G, or Po725, it was calibrated on NIST610 and should be considered as an informational value. For Namex and Rundle pyrite specifically, As and Se had to be calibrated on NIST610 also because of low counts close to background and variability in GSD-1G. Detailed quality control protocol and assessment of calibration standards can be found in Hastie et al. (2020a).

Data derived from LA-ICP-MS line traverses were also reduced to singular points for plotting. This follows the protocol proposed by Gourcerol et al. (2018) where the data is converted into 0.35 second increments, the time for a complete analysis, and is referred to as a time-slice dataset (TSD). This data represents a qualitative to semi-quantitative assessment of

elemental concentrations and is useful in displaying elemental trends and detecting micro-inclusions, both within and outside pyrite.

2.5 Results

2.5.1 Geology of Au deposits

Features observed in Au deposits of the SGB are summarized in Table 2.1 and presented below.

2.5.1.1 Rundle Au deposit:

The deposit is located in the central portion of the SGB (Fig. 2.1C) along the northern margin of a complex of ultramafic to felsic rocks that intrude ultramafic to mafic volcanic rocks and sedimentary rocks (Fig. 2.2). Several Au-rich zones define the deposit and two were studied in detail: the A-South and the Main/Shaft zones (Fig. 2.2).

The Main/Shaft zone consists of heavily altered (carbonate, chlorite, albite), Fe-oxide-rich gabbroic rocks cut by altered, pink monzonitic intrusions (Fig. 2.3A-C). The Au mineralization, from 40 to 100 ppm Au in the gabbroic rocks and 1 to 5 ppm Au in pink to altered pink monzonite, is associated with early fracture-controlled pyrite (Fig. 2.3A, B, D, E, F; App. Table A1).

The A-South zone contains ultramafic and mafic volcanic rocks and minor sedimentary rocks that were intruded by porphyritic intrusive rocks prior to shearing. These include phlogopite-lamprophyre, monzodiorite, least altered grey monzonite of 2688±2 Ma, and altered and mineralized monzonite of 2680±5 Ma (Fig. 2.2B; MacDonald et al., 2017; Ontario Geological Survey, 2019). The Au mineralization (up to 45 ppm) is associated with early

fracture-controlled pyrite (Love and Roberts 1991), which is typically subhedral, inclusion-rich and porous (Fig. 2.3E, F). These pyrite-bearing fractures are boudinaged and folded around the noses of Z-shaped dextral drag folds (Fig. 2.3G, H), suggesting that mineralization predates shearing.

2.5.1.2 Namex Au-Ag deposit:

This deposit is located within the Ridout deformation zone (Fig. 2.1C) roughly 30 km southeast of the Rundle Au deposit, where it is exposed on two stripped outcrops: Namex East (Fig. 2. 4A) and Namex West. The host rocks consist of polymictic conglomerate cut by a monzogranitic intrusion (Fig. 2.4A, B). The conglomerate contains flattened clasts of mafic to felsic volcanic rocks, iron formation, gabbro, breccia and feldspar-porphyry (Fig. 2.4C) in a matrix of quartz-feldspar-ankerite-muscovite to chlorite-feldspar-quartz-muscovite. The monzogranite consists of 15 modal % K-feldspar phenocrysts (0.5 to 2 cm) within a medium- to fine-grained matrix of quartz, K-feldspar, muscovite, albitic plagioclase, and ankerite (Fig. 2.4D, E). A U-Pb zircon age of 2680±4 Ma (see location in Fig. 2.4A) provides the time of emplacement of the intrusion and overlaps the U-Pb age for the youngest detrital zircons in the conglomerate; this suggests the conglomerate and intrusion are synchronous within error (MacDonald et al., 2017).

Monzogranite is the main host for Au mineralization. Early, low-grade mineralization (0.1–1 ppm Au; App. Table A1) is associated with disseminated pyrite throughout the intrusion, and later higher-grade mineralization (1.5–11 ppm Au; App. Table A1) is associated with Ag-bearing tetrahedrite, galena, and Au-Ag-tellurides in quartz veins mainly centred on the intrusion (Fig. 2.4F). The latter have S- and Z-shaped folds oriented anticlockwise and clockwise, respectively, to a strong foliation overprinting the intrusion which suggests the veins predate deformation (Fig. 2.4G).

2.5.1.3 Jerome Au deposit:

The deposit is located within the Ridout deformation zone 9 km west and along strike of the Namex deposit (Fig. 2.1C). It produced 56 878 oz of Au from 1941 to 1943 and has an inferred resource of 1 Moz Au (Burt et al., 2011). The host rocks consist of an altered and deformed felsic intrusion of syenite to monzonite composition, which intrudes polymictic conglomerate (Fig. 2.5A-D). The monzonite consists of 15 modal % subhedral to anhedral K-feldspar phenocrysts (1 to 5 mm) within a medium- to fine-grained matrix of K-feldspar, albitic plagioclase, muscovite, quartz, and ankerite (Fig. 2.5B, E). It has a U-Pb zircon age of 2684±3 Ma, which is similar to that at the Namex deposit (MacDonald et al., 2017), and interpreted as the time of emplacement. The syenite contains less matrix plagioclase than the monzonite, but is otherwise similar. The polymictic conglomerate contains moderately to strongly deformed, elongate clasts of mafic to felsic volcanic rocks, gabbro, iron formation, and feldspar porphyry (Fig 2.5C) in a felsic matrix of quartz, feldspar, ankerite and muscovite. Ore zones are expressed as hydrothermal breccias and stockworks of quartz-carbonate veins (Fig. 2.5D) with Au grades up to 130 ppm Au (App. Table A1). The wall rock to veins has up to 10% pyrite characterized by As-rich oscillatory and sector zoning that contains up to 0.5 wt. % Au. Native gold inclusions in the pyrite and free gold in the rock matrix result from local, small-scale remobilization of Au from the arsenian pyrite attributed to coupled dissolution-reprecipitation (CDR) processes (Hastie et al., 2020a).

2.5.1.4 Kenty Au deposit:

The deposit is located in the central part of the SGB (Fig. 2.1C) and is best exposed at three stripped outcrops: C1 Mortimer (Fig. 2.6A), Salo and Mortimer Camp. The C1 Mortimer outcrop exposes pillowed basalts intruded by a 2684.7±1.5 Ma (U-Pb zircon age; Hastie et al., 2021) granodioritic intrusion (Fig. 2.6A). The basalts are fine-grained, aphyric, with up to 1 m-size pillows. The granodiorite is characterized by quartz and plagioclase phenocrysts (1 to 5 mm) within a medium- to fine-grained matrix composed of albitic plagioclase, quartz, muscovite, K-feldspar and ankerite (Fig. 2.6B-D). Quartz-feldspar veins, which cut all rock types, are up to 10 cm thick and are surrounded by ankerite-albite-sericite-pyrite ± chlorite alteration halos up to 5 m wide (Fig. 2.6A, B, E). The veins dip shallowly to subvertical, are typically northwest-striking, and are transected by thinner conjugate quartz-feldspar veins (1 to 3 cm width) striking 210° and 310° (Hastie et al., 2020a). One prominent, shallowly-dipping quartz vein is located along the contact between the intrusion and pillowed basalt and has been gently folded (Fig. 2.6A, E).

The Au mineralization is concentrated within the ankerite alteration adjacent to the quartz-feldspar veins and in the veins themselves (Fig. 2.6E, F) with whole-rock samples of the altered wall rock and veins ranging between 1 to 85 ppm Au (App. Table A1). Pyrite within the alteration halo contains up to 1500 ppm Au as both micro-inclusions and invisible gold (Hastie et al., 2020a; 2021). Native gold remobilized via CDR reactions from this pyrite (Fig. 2.6F) is associated with Au-Ag tellurides in conjugate fractures cutting the quartz-feldspar veins (Hastie et al., 2020a).

2.5.1.5 4K Au prospect:

This prospect is associated with strongly folded banded iron formation (BIF) that is traceable for over 8 km along the southern margin of the SGB (Heather, 2001; Ontario Geological Survey, 2020). The prospect consists of three stripped outcrops with the westernmost one (4K West) having the most elevated Au values and is therefore described here (Fig. 2.7A). This outcrop exposes magnetite-chert BIF and associated sedimentary rocks. The magnetite beds are <1 to 3 cm thick and are interlayered with light-grey chert of 1 to 5 cm thickness (Fig. 2.7B). Some thicker siliceous units, which superficially resemble the chert, appear to be quartz veins in-folded with the BIF. Graphitic siltstone units (Fig. 2.7A), 2 to 10 cm thick and spaced from 1 m to 3 m, contain garnet and amphibole porphyroblasts within a graphite-rich matrix (Fig. 2.7C). Deformed basalt and a biotite-rich siltstone (schist; 1 to 2 m thick) occur along the northern and southern margins of the outcrop without clear contact relationships with the BIF due to intrafolial isoclinal folding (Fig. 2.7A). The BIF is transected by a medium-grained dioritic dike that yielded a U-Pb zircon age of 2682±2 Ma, which is considered the time of dike emplacement (Ontario Geological Survey, 2019).

All rock units, with the exception of the diorite, are isoclinally folded and have a strong bedding-parallel foliation (Fig. 2.7A). These structures are refolded by open to tight late folds with an axial planar, chlorite- and magnetite-rich cleavage best expressed in the hinge of the folds (Fig. 2.7D). A mineral stretching lineation lies along the foliation and is similar in orientation to the late fold axes (Fig. 2.7A).

The graphitic siltstone and BIF units yielded low Au grades (0.1 to 1 ppm; App. Table A1) where cut by fractures lined by pyrite (Fig. 2.7E, F), pyrrhotite and arsenopyrite. Garnet

porphyroblasts contain inclusions of pyrite (Fig. 2.7F), suggesting a pre- to syn-metamorphic timing for mineralization.

2.5.2 Oxygen isotopes

Oxygen isotope values for in situ SIMS analysis of quartz from the SGB deposits and across the Superior Province are presented in Figure 2.8 along with different fluid reservoir subdivisions after Sheppard (1986) represented as quartz equivalent values ($\delta^{18}O_{VSMOW}$ quartz) at the bottom of Figure 2.8B for 250°C and 400°C. From the SGB a comprehensive analysis of 185 quartz grains was done from the studied deposits which included: Jerome: 6 samples, 18 grains; Namex: 14 samples, 42 grains; Rundle: 14 samples, 42 grains; Kenty, 23 samples, 69 grains; 4K: 14 samples, 14 grains. In addition, 3 quartz grains were analysed for each of the other major gold deposits in the Superior Province sampled from the ROM suites.

For the SGB deposits, $\delta^{18}O_{quartz}$ values for the intrusion-hosted Jerome (mean 12.6‰), Namex (mean 12.2‰) and Rundle (mean 12.4‰) deposits are lower than those for the BIF-hosted 4K deposit (mean 15.3‰) and the greenstone-hosted Kenty deposit (mean 13.8‰). On a larger scale across the Superior Province, the $\delta^{18}O_{quartz}$ values are generally lower for the intrusion-hosted Au deposits sampled, such as the Powell (mean 9.1‰) in the Noranda camp, Macassa, Teck-Hughes, Lake Shore and Tough-Oakes (Toburn) in the Kirkland Lake camp (10-14‰), Preston and Dome (11-15‰) in the Timmins camp, and McKenzie (mean = 12.6‰) in the Red Lake camp, compared to those of the greenstone-hosted Au deposits, such as Hollinger, McIntyre, Broulan, Vipond, Dixon Claims, Paymaster and Vedron (11-16‰) in the Timmins

camp and Madsen, Campbell Red Lake, Cochenour Willans, Red Lake and Dickenson (14-23‰) in the Red Lake camp.

Quartz from the Campbell-Red Lake, Red Lake and Dickenson deposits have $\delta^{18}O_{quartz}$ values that plot in the metamorphic fluid reservoir even at the lowest likely temperature (250°C) of formation. If 250°C and 400°C are used as end-members of possible temperatures (Fig. 2.8B), then it is possible for all other deposits across the Superior Province to plot within the magmatic fluid reservoir with the exception of the Powell deposit, which has $\delta^{18}O_{quartz}$ values in the metamorphic/meteoric field.

To test for intragrain variation due to changes in extensive (i.e., the $\delta^{18}O_{H2O}$ values) and/or intensive (i.e., temperature) parameters versus analytical variability, multiple analyses were done on the same quartz grains. In 11 of 109 quartz grains, the $\delta^{18}O$ values vary from 2.5 to 4‰, which is more than the 2σ precision of repeat analyses on the SIMS standard suggesting a natural cause for these variations (Fig. 2.9). The other 98 quartz grains had $\delta^{18}O$ values within error indicating their variation could be natural or analytical.

2.5.3 Sulfur Isotopes

The $\delta^{34}S$, $\delta^{33}S$ and $\Delta^{33}S$ values for sulfide grains for SGB and AGB samples are presented in Figures 2.10 and 2.11. The number of analyzed samples and sulfide grains are: Jerome: 5 samples, 23 pyrite grains; Namex: 6 samples, 19 pyrite grains; Rundle: 6 samples, 28 pyrite grains; Kenty: 8 samples, 39 pyrite grains; and 4K: 5 samples, 5 pyrite, 15 pyrrhotite and 4 arsenopyrite grains. Three sulfide grains each (pyrite and/or chalcopyrite) from five deposits of the ROM's Abitibi collection (Dome, Broulan, Paymaster, Preston, Quemont) were also analyzed.

Intrusion-hosted deposits of the SGB (Jerome, Rundle, Namex) have the most depleted $\delta^{34}S_{pyrite}$ and $\delta^{33}S_{pyrite}$ values (Fig. 2.10A). The Jerome pyrite has an average $\delta^{34}S$ value of -16.0‰ and an average $\delta^{33}S$ value of -7.6‰. This pyrite shows the widest range of results for all the studied samples with $\delta^{34}S_{pyrite}$ = -9.0 to -25.0‰ and $\delta^{33}S_{pyrite}$ = -3.0 to -12.0‰. The Rundle deposit has two distinct pyrite generations, here denoted as Py_1 and Py_2. The early Au-bearing, euhedral to subhedral Py_1 pyrite (n= 21; Fig. 2.10B-D) has an average $\delta^{34}S$ value of -8.6‰ and an average $\delta^{33}S$ value of -3.9‰. In contrast, Au-barren, anhedral porous and inclusion-rich Py_2 (n=18), which replaces Py_1 (Fig. 2.10B, E, F), has an average $\delta^{34}S$ value of 2.1‰ and average $\delta^{33}S$ value of 1.3‰, but both, in particular $\delta_{34}S$, have large ranges. The Namex deposit has the least depleted average $\delta^{34}S$ and $\delta^{33}S$ values for early pyrite in intrusion-hosted deposit settings at -4.1‰ and -2.0‰, respectively. The remaining SGB deposits, Kenty and 4K, along with the AGB deposits (i.e., Dome, Preston, Paymaster, Broulan and Quemont), have similar average $\delta^{34}S_{sulfide}$ and $\delta^{33}S_{sulfide}$ values between 0‰ and 2.5‰, but we note in particular the large overall range for the Kenty pyrite where $\delta^{34}S$ ranges from -5.4 to 7.3‰.

A binary plot of $\delta^{34}S$ versus $\Delta^{33}S$ values for all the deposits (Fig. 2.11) shows that most of the $\Delta^{33}S$ values fall within 2σ error (i.e., 1.5 to 2.2‰) of zero. Encircled samples that plot outside this 2σ error have duplicate analyses that fall within the 2σ error, which suggests that the encircled sample values are caused by analytical error.

Multiple analyzes were done on each of three zoned pyrite grains from the Jerome deposit. As at Rundle, two textural varieties of pyrite are noted. Early pyrite (Py_1) is characterized by oscillatory and sector zoning, as defined by As- and Au-rich domains (≤4 wt. % As; <0.5 wt. % Au). This pyrite shows modification (Py_{1a}) in the form of porosity and micro-inclusions development due to CDR processes (Hastie et al., 2020a). In the least altered pyrite

grain dominated by Py_1, the $\delta^{34}S$ values are uniform between -17 and -18.2‰ (Fig. 2.12A). In contrast, the other two pyrites which record textures that indicate modification by CDR, the primary Py_1 areas have $\delta^{34}S$ values that range overall from 14.3 to -19‰ with a distinct trend of enrichment in ^{34}S from core-to-rim (i.e., from -14.3 to -19‰; Fig. 2.12B, C). We also note that there is no systematic variation between As-rich and As-poor domains (Fig. 2.12). This range is significantly more than the ±0.8 ‰ (2σ) variation attributed to repeat analysis of the standard.

The Au-bearing pyrites from the Kenty setting are noted to record a large range in $\delta^{34}S$ (Fig. 2.11A). This variation on the deposit scale was noted for a single large sample where $\delta^{34}S$ for multiple pyrites in vein and altered wall rock varied from -5.7 to 2.7, but no obvious spatial pattern is noted (Fig. 2.13).

2.5.4 Geochemistry of intrusion-hosted Au lithologies

Here the geochemistry of different intrusions hosting Au mineralization from different settings in the SGB are examined and also compared to similar intrusion-hosted settings from well-known localities in the AGB using data from Ispolatov et al. (2008; Kirkland Lake) and MacDonald and Piercey (2019; Timmins). In addition, the data are compared and contrasted with relevant compilations of Archean granitoid-type rocks after Laurent et al. (2014). For relevant plots, major oxides have been normalized to volatile-free.

In the total alkalis versus silica (TAS) plot (Figure 2.14A), samples from the Jerome, Rundle, Namex and Kirkland Lake intrusions plot in the alkaline field, whereas samples from the Kenty and Timmins intrusions (Preston, Paymaster and Dome) plot in the subalkaline field. On the Winchester and Floyd (1977) plot of immobile element ratios (Zr/TiO_2 versus Nb/Y; Fig. 2.14B), gabbroic rocks from Rundle plot in the basalt/andesite field, Kirkland Lake syenites

mainly plot in the andesite field, and all other intrusive samples from the SGB and AGB plot in the rhyodacite/dacite field.

In Harker-type diagrams of SiO_2 versus TiO_2, P_2O_5, MgO and Fe_2O_3 total (Figs. 2.14C-G), monzonitic to syenitic intrusions from Kirkland Lake, Rundle and Jerome have the lowest SiO_2 and highest TiO_2, P_2O_5, MgO and Fe_2O_{3total} values, whereas monzogranitic to granodioritic rocks from Timmins, Kenty and Namex, have the highest SiO_2 and lowest TiO_2, P_2O_5, MgO and Fe_2O_3 values. The monzonitic to syenitic intrusions from Kirkland Lake, Rundle and Jerome, also have higher Cr and Ni concentrations than the monzogranitic to granodioritic rocks from Timmins, Kenty and Namex (Fig. 2.14H).

In the ternary A/CNK - Na_2O/K_2O - FMSB diagram (Fig. 2.15), where FMSB = ($[FeO+MgO]_{wt.\%}$ * $[Sr + Ba]_{wt.\%}$), the Kenty granodiorite plots in the TTG field, Namex monzogranite plots in the two-mica granite field, and Kirkland Lake syenites plot in the sanukitoid field. The Jerome syenite and monzonite plot between the sanukitoid field and the two-mica granite field, whereas Rundle monzonite plots in linear fashion extending from the sanukitoid field to the TTG field.

In the binary Nb versus Y and Ta versus Yb plots used as tectonic discriminants for felsic igneous rocks (Pearce et al., 1984), syenite and monzonite from Kirkland Lake, Rundle, and Jerome, and monzogranite and granodiorite from Timmins, Kenty, and Namex, plot as two distinct groups that fall in the volcanic arc and syn-collisional granite fields (Fig. 2.16A, B). In contrast, the Rundle gabbroic samples are generally more enriched in Y and Yb and thus plot in the ocean ridge granite (ORG) field.

With the exception of the Rundle gabbroic samples, which have a flat, unfractionated, chondrite-normalized REE pattern (Fig. 2.16C), all other intrusions have fractionated LREE-enriched patterns with chondrite-normalized La/Yb_{CN} values varying from 15-50. The monzonitic to syenitic intrusions from Kirkland Lake, Rundle and Jerome also display REE patterns that are three times greater in total abundance than those of monzogranitic to granodioritic rocks from Timmins, Kenty and Namex. In all cases there are either no Eu anomalies, or if present small negative anomalies.

2.5.5 Au-Ag elemental associations: Whole-rock versus in-situ methods

Whole-rock Au/Ag ratios for mineralized samples from the SGB deposits (Fig. 2.17) vary from 0.1 to 10 for the Kenty, Rundle and Jerome deposits and from 0.01 to 0.1 for the Namex deposit (Fig. 2.17). In addition, the Kenty, Rundle and Jerome deposits have higher Au grades (up to 100 ppm) than those of the Namex deposit (generally 1-10 ppm). Also highlighted is the change in the Au/Ag values at increasing Au values (i.e., generally >5 ppm Au), which is most obvious for the Kenty and Rundle samples. These latter values converge on an Au/Ag value of 10 in Au-rich samples. Also of note are the lower Au/Ag ratios at the Namex deposit, which is consistent with the presence of Ag-bearing phases at this site (Table 2.1). In contrast to these settings, Au correlates poorly with Ag at the 4K prospect and also differs by lower overall Au grades (0.1 to 1.0 ppm), thus these data are not further discussed.

Figures 2.18 to 2.21 show binary plots of Au versus Ag concentrations for the Kenty, Jerome, Rundle and Namex deposits for both whole-rocks and also in-situ LA-ICP-MS analysis (LA henceforth) of pyrite. In these plots, trace-metal concentrations (e.g., Bi, Te, Hg, Sb, Pb, Mo, W, Ti, As, Se) are displayed as cold to hot colors with a 10% bin size increase in

concentration. In each these diagrams, the left plot corresponds to whole-rock data and the plot to the right represents the in-situ LA analysis.

2.5.5.1 Kenty Au deposit (Fig. 2.18):

Whole-rock and LA metal data show strong agreement for Au-Ag and element associations with a few exceptions. The Au-Ag associations with Bi, Te and Hg best correlate between the two methods (Fig. 2.18B-D), whereas Sb, Pb, Mo, and W correlate well between methods (Fig. 2.18E-H), but there are lower concentrations of these elements at the highest Au and Ag concentrations for the LA data. Titanium shows some agreement between methods, but whole-rock data shows less correlation between high Ag-Ag and Ti (Fig. 2.18I). Finally, As and Se have the poorest correlation between methods (Fig. 2.18J and K).

2.5.5.2 The Jerome Au deposit (Fig 2.19):

Whole-rock and LA metal data for Jerome only shows obvious agreement between methods in a few cases. The Au-Ag association with As and Hg agree best between methods (Fig. 2.19B, C), while Te Sb, Cu, and Pb are poorly correlated (Fig 2.19D-G). Both methods indicate higher Sb, Pb and Te are associated with higher Au values, but these elements also show high concentrations at mid- and low Au contents. Finally, Zn has the poorest correlation between methods (Fig. 2.19H).

2.5.5.3 The Rundle Au deposit (Fig. 2.20):

Whole-rock and LA metal data only shows good agreement between methods for a few elements. For Au-Ag associations, only Te strongly correlates between methods (Fig. 2.20B) while Bi and Pb show less agreement (Fig. 2.20C, D). The remaining elements that correlate in the whole-rock data (Co, Se, Sb, Ti, W) show little to no agreement with the LA data (Fig. 2.20 E-I).

2.5.5.4 The Namex Au deposit (Fig. 2.21):

Whole-rock and LA metal data only show strong agreement between methods for a few elements. The Au-Ag associations with Te and Hg show the best agreement between methods (Fig. 2.21B, C). There is some agreement for Bi, Cu and Pb (Fig. 2.21D-F) between methods, but the LA data is less obvious in its correlations. There is less agreement between methods for Sb, As and Zn (Fig. 2.21G-I) with the poorest agreement for Se (Fig. 2.21J).

2.6 Interpretation of Results

2.6.1 Deposit type classification based on field data

Based on mapping, field relationships, geochronology and petrography, the SGB Au deposits can be divided into intrusion-related, greenstone-hosted and BIF-hosted orogenic deposit types.

The Au mineralization at the Rundle deposit is hosted exclusively within altered coeval gabbroic and monzonitic intrusions with porphyritic textures and fine-grained matrices (e.g., Fig. 2.3C), hence consistent with the crystallization of the phenocrysts prior to the emplacement of the magma at upper crustal levels. Shear zones overprint the margins of these intrusions and Au-

bearing pyrite lining fractures within the shear zones are folded, thus they predate shearing (Fig. 2.3G, H). The 2680 ±5 Ma age for the mineralized monzonitic intrusion (Fig 2.2B; MacDonald et al., 2017) is consistent with the pre- to early emplacement of the intrusions during regional deformation. These lines of evidence collectively suggest that the Rundle deposit is intrusion-related.

Similarly, the porphyritic textures of the monzogranite intrusion at the Namex deposit suggests emplacement at a high crustal level (Fig. 2.4D, E). Early, disseminated Au mineralization is hosted throughout the monzogranite in both strongly and weakly deformed parts of the intrusion (App. Table A1). The 2680±4 Ma age of the intrusion is coeval with the intruded Timiskaming conglomerates that contain detrital zircons dated at 2680±3 Ma (MacDonald et al., 2017). The presence of localized high-grade Au mineralization in pre to syn-shearing extensional quartz veins (Fig. 2.4F, G) suggest remobilization from the early-disseminated pyrite. Collectively these data suggest that the Namex deposit is intrusion-related.

The Jerome deposit is hosted by porphyritic monzonitic to syenitic intrusions. It contains early, Au-rich arsenian pyrite that is chemically zoned and native gold. There are significant Hg concentrations within native gold, and elevated Hg-Sb-Mo concentrations within pyrite and associated minerals (Hastie et al., 2020a). The porphyritic textures of the intrusions, the Hg-Sb-Mo elemental association, and nature of the pyrite zoning, which is indicative of rapid crystallization of pyrite during cooling (Shore and Fowler, 1996; Fougerouse et al., 2016; Hastie et al., 2020a), are consistent with an epizonal-type mineralization (e.g., Goldfarb and Groves, 2015) and suggests high-level setting for the deposit. Importantly, this deposit is 10 km along strike from Namex, in the Ridout deformation zone, intrudes the same package of Timiskaming

conglomerates, and is associated with a 2684±3 Ma intrusion that is similar in age to that at Namex. Thus, the Jerome deposit is also interpreted as intrusion-related.

The Kenty deposit has many characteristics of shear-zone-related quartz-carbonate orogenic deposits with the Au mineralization in laminated quartz-carbonate veins cutting Fe-carbonate-altered basalt (Fig. 2.6E). A prominent vein occurs at the sheared contact between the altered basalt and a granodioritic intrusion (Fig. 2.6A). Gold is associated with pyrite disseminated within the alteration halo of the veins and occurs as native gold in fold hinges and conjugate fractures (Hastie et al., 2020a). These features suggest this deposit is a greenstone-hosted orogenic type.

Finally, Au mineralization at the 4K prospect is hosted in fault and fracture-controlled pyrite and arsenopyrite within BIF and garnet-bearing graphitic siltstone (Fig. 2.7A, E, F). This Au mineralization is late, is not associated with known intrusions, and is heterogeneously distributed, suggesting epigenetic rather than syngenetic or intrusion-related origins. Garnet porphyroblasts contain pyrite inclusions and are surrounded by pyrite tails, which suggest that gold and pyrite were deposited during the amphibolite-grade metamorphism of the area (Fig. 2.7F; Heather, 2001; Thompson, 2005). This data is consistent with a BIF-hosted orogenic classification.

On the basis of the classifications noted above, the validity of various geochemical discriminants are tested and further discussed below.

2.6.2 Oxygen Isotopes

Within the entire oxygen isotope dataset, some plot outside the overlap of values between intrusion- and non-intrusion-hosted deposits (Fig. 2.8). These include data from intrusion-hosted (Powell, Sigma, Namex, Rundle) and non-intrusion-hosted (Kenty, 4K, Cochenour Willans, Dickenson, Red Lake, Campbell Red Lake) settings.

The non-intrusion-hosted 4K and Red Lake deposits (Campbell Red Lake, Dickenson, Red Lake) very likely reflect a metamorphic fluid reservoir and perhaps also Kenty, Madsen, Cochenour Willans and many of the Timmins deposits, which have similarly higher $\delta^{18}O_{quartz}$ values (Fig. 2.8). The Red Lake deposits are distinct, however, in their extreme ^{18}O enrichment (14.3 to 23.0‰), which is highly anomalous for global compilations of orogenic gold settings (McCuaig and Kerrich, 1998; Hagemann and Cassidy, 2000; Beaudoin, 2011). The latter suggests, therefore, that it is highly unlikely for quartz to attain such enriched values in the absence of a local source enriched in ^{18}O. Thus, a more plausible explanation for these values is interaction with a low-temperature ^{18}O-enriched fluid, as suggested for similar noted enrichment in VMS deposit settings (e.g., Huston et al., 1995; King et al., 1997; Beaudoin et al., 2014) or interaction and exchange with carbonate-altered wall rock enriched in ^{18}O (e.g., Kontak et al., 2011). The isotopic variation within intrusion-hosted deposits is interpreted in more detail below.

2.6.2.1 Assessing oxygen isotope variation in intrusive-hosted deposits:

There is still debate over the processes responsible for the oxygen isotope signatures of intrusion-hosted deposits. There is consensus that fluid-host rock exchange at low fluid/rock ratios affects $\delta^{18}O_{quartz}$ values, but there is much disagreement on the type and number of fluids responsible (e.g., Beaudoin and Pitre, 2005; Olivo et al., 2006; Helt et al., 2014a; Beaudoin and Raskevicius,

2014; Helt et al., 2014b; Beaudoin and Chiaradia, 2016; Raskevicius et al., 2020). The large range in data for intrusion-hosted deposits from the SGB settings and other locations (i.e., Kirkland Lake) could be the result of temperature, fluid/rock exchange, Rayleigh fractionation, and fluid mixing, or some combination of these.

If quartz crystallized from a single fluid at temperatures varying from 250°C to 400°C, $\delta^{18}O_{quartz}$ values can vary by up to 5‰ (Matsuhisa et al., 1979). As shown in quartz veins of the Val-d'Or area (Beaudoin and Pitre, 2005, Beaudoin et al., 2006; Beaudoin and Chiaradia, 2016), temperature gradients of this nature are unlikely given that the distribution of $\delta^{18}O_{quartz}$ isopleths (proxies for temperature gradients) cut across geological contacts and structures and do not show any systematic spatial relationship with respect to intrusions in the area (Beaudoin and Pitre, 2005). The deposits from Kirkland Lake (Fig. 2.8) occur along a strike length of approximately 6 km and are commonly thought to define a single deposit (Goldfarb et al., 2005; Ispolatov et al., 2008). From west to east, the Macassa, Teck-Hughes, Lake Shore, and Tough-Oakes (Toburn) deposits occur at progressively shallower depths. Although Macassa has lower $\delta_{18}O_{quartz}$ values than Teck-Hughes and Tough-Oakes, the values from Lake Shore are lower than those for Macassa and thus argues against a systematic thermal gradient. This also cannot be explained solely by a decrease in temperature from west to east, which must be greater than 150°C as the $\delta^{18}O_{quartz}$ values vary by >5‰ (Fig. 2.8; 9.9 to 15.6‰). Similarly, for the SGB settings, the range in $\delta^{18}O_{quartz}$ values is >6‰, except for Jerome which has a range of 5‰. This variation in $\delta^{18}O_{quartz}$ values occurs within a radius area of <1 km at the Rundle and Namex deposits, which is even more difficult to explain by a temperature gradient alone.

Fluid-host rock exchange with relatively low fluid/rock ratios can affect $\delta^{18}O_{quartz}$ values (Fig 2.8B). At the intrusion-hosted Canadian Malartic deposit, Raskevicius et al., (2020) have

shown that it could have formed at fluid/rock ratios of 0.5 and a temperature as low as 300°C, however, these conditions only represent a 2‰ change from the modeled metamorphic $\delta^{18}O_{fluid}$ value. Intragrain variation (Fig. 2.9) for Rundle and Namex clearly show that a single quartz grain can account for up to 4‰ $\delta^{18}O_{quartz}$ variation, which is >60% of the total range for these deposits. Furthermore, many intrusion-hosted deposits show pervasive alteration associated with stockwork veining and relationships to shear zones that suggest higher fluid/rock ratios. These points collectively indicate that the role of fluid-host rock exchange is minor and unlikely to account for large variation in $\delta^{18}O_{quartz}$ values shown in Figure 2.8.

Rayleigh distillation models have also been proposed to explain variations in $\delta^{18}O$ values (Kontak et al., 2016; Neyedley et al., 2017). However, the few studies that combined detailed cathodoluminescence (CL) imagery with in-situ SIMS isotopic analyses (e.g., McDivitt et al., 2020), reported increases in $\delta^{18}O_{quartz}$ values from the core to rim of quartz veins, which cannot be explained by progressive Rayleigh distillation. More studies incorporating CL imagery and in-situ analyses are essential to understand how Rayleigh distillation may contribute to $\delta^{18}O_{quartz}$ variation, but it is difficult to assess completely with the present data.

In terms of fluid mixing, the range of $\delta^{18}O_{quartz}$ data from Kirkland Lake and the SGB intrusive-hosted deposits cannot be explained solely by quartz precipitation from magmatic fluids (Fig. 2.8). If a temperature of 250°C is assumed, most $\delta^{18}O_{quartz}$ values fall outside the magmatic fluid range (Fig. 2.8B) and therefore requires at least two fluids (i.e., metamorphic/magmatic and meteoric). However, if a temperature of 400°C is assumed, then magmatic fluids can explain the range of $\delta^{18}O_{quartz}$ values for all but a few of the intrusion-hosted deposits (i.e., Paquette, Lake Shore, Siscoe, Macassa, Dome, Preston, McKenzie). Otherwise, intrusion-hosted deposits have some $\delta^{18}O_{quartz}$ values that fall outside the magmatic fluid range

(Fig. 2.8B) and would require more than a single fluid (i.e., magmatic-metamorphic, magmatic-meteoric, magmatic-metamorphic-meteoric). It could be argued that a single metamorphic fluid alone could cover the range of values, but this would require a large temperature gradient (not likely) or fluid-host rock exchange (possible, but not alone). Thus, it is likely that fluid mixing is the dominant mechanism to explain the range in $\delta^{18}O_{quartz}$ values seen in our data.

2.6.3 Sulfur Isotopes

The $\delta^{34}S$ data for the SGB are subdivided into the two groups, these being orogenic and intrusion-hosted. In the first case, most of the $\delta^{34}S_{sulfide}$ values for 4K and Kenty range from -1 to 3‰ (1st to 3rd quartile) and compares thus to the values for other orogenic Au deposits analysed in this study (e.g., Broulan, Dome, Paymaster). Thus the results centre on the typical range of $\delta^{34}S_{sulfide}$ values for orogenic Au systems of Archean age from 0 to 5‰ (Fig. 2.10A; Lambert et al., 1984; Cameron and Hattori, 1987; McCuaig and Kerrich, 1998; Robert, 2001; Goldfarb et al., 2005; Beaudoin, 2011). Notably, the rare exception to these global values is where fluid oxidation related to wall-rock alteration has occurred (e.g., Lambert et al., 1984; Phillips et al., 1986; Evans et al., 2006). The latter is perhaps relevant in the context of the data for the Kenty where a few $\delta^{34}S_{pyrite}$ values fall to -5.4‰. The presence of hematite as part of the alteration here (Hastie et al., 2020a) suggests that at least some local increase in fO_2 occurred due to wall-rock related alteration (e.g., Evans et al., 2006). This would have increased the SO_4/H_2S ratio in the fluid and led to fractionation of the sulfur isotopes which can account for the rare cases of ^{34}S depletion in pyrite (Ohmoto and Rye 1979).

In contrast to the orogenic data, the $\delta^{34}S_{sulfide}$ values for the intrusion-hosted settings of the SGB fall at much lower values, the most extreme being -25‰. That such unusual depletion in ^{34}S is primary and retained in the sulfides is clearly evidenced from the textures in early arsenian

pyrite, in particular for the grain from the Jerome deposit where nine in situ analysis on zoned pyrite average -17.6 (± 0.5, 1σ; Fig. 2.12A). As noted above for the Kenty data, such low excursions in $\delta^{34}S$ are interpreted to reflect fluid oxidation with the fO_2 at or near the magnetite-pyrite buffer, but in this case the feature is considered primary, that is intrinsic to the magmatically-sourced hydrothermal fluid rather than an alteration mediated process. That other low $\delta^{34}S_{sulfide}$ values are reported for intrusion-related/hosted Au settings in the AGB (to -17.5‰; Cameron and Hattori 1987) and Archean St. Ives district of western Australia (to -8.5‰; Neumayr et al., 2008) also supports the contention that these are primary signature of oxidized Archean felsic magmas.

2.6.3.1 Assessing sulfur isotopic variation at the micro-scale:

The sulfur isotope data for the Rundle and Jerome deposits are further interpreted below due to the noted spatial variability of results provided from in situ analysis. For Rundle, the early Au-bearing euhedral pyrite (Fig. 2.10B, C, D) has relatively depleted values (averages of $\delta^{34}S$ = -8.6‰ and $\delta^{33}S$ = -3.9‰) compared to the later porous- and inclusion-rich barren pyrite (averages of $\delta^{34}S$ = 2.1‰ and $\delta^{33}S$ = 1.3‰; see Fig. 2.10B, E, F). Two factors may account for the noted ^{34}S enrichment of the later pyrite: (1) a drop in pH due to dissolution of Au-bearing pyrite (Py_1), hence shift to a lower SO_4/H_2S ratio for the fluid, with related relative enrichment of ^{34}S in the newly formed pyrite (Py_2; Ohmoto and Rye, 1979); and/or (2) an influx of a S-bearing reduced fluid enriched in ^{34}S and with lower inherent fO_2 that promotes pyrite formation via sulfidation of the rock and related high fluid:rock ratios. Given CDR-related textures in the late pyrite (Py_2), such as its porous- and inclusion-rich nature (Fig. 2.10B, E, F; Putnis, 2002; 2009), and that such reactions are considered to enhance Au mobilization from earlier pyrite (Py_1; Hastie et al.,

2020a), it is reasonable that changing fO_2 and pH both contributed to the noted ^{34}S enrichment of the paragenetically later pyrite (Py_2).

In the case of the sulfur isotope data for Jerome pyrite (Fig. 2.12), there are no systematic changes between the Au-As-rich and poor zones, but there is a change in $\delta^{34}S$ values from the core to rim of -4‰ (Fig. 2.12B, C). Processes that might be considered to generate such depleted values might include biogenic processing of sulfur (e.g., Caruso et al., 2018), but the temperature of ore formation, likely between 300° to 400°C, and its Archean age make this unlikely. Thus, the two variables more likely to account for these data, temperature and oxidation, are further considered below.

As discussed above, an increase in fluid fO_2 would increase its SO_4/H_2S ratio (Ohmoto and Rye, 1979). Thus, if pyrite formed during progressive oxidation of the fluid this could account for the observed core to rim lowering of $\delta^{34}S$ values (Fig. 2.12B, C), as was modeled for alteration haloes around veins in the Kalgoorlie deposit, Australia (Evans et al., 2006). Alternatively, if the pyrites formed during a temperature decrease of at least 50°C (see Fig. 10.9 from Ohmoto and Rye, 1979) then this could account for a depletion of $\delta^{34}S$ values of at least 5‰ (i.e., -14 to -19‰). A significant temperature drop would also cause rapid crystallization of pyrite, which has been suggested to account for As-rich zoning in pyrite due to chemical disequilibrium at the fluid-mineral interface (Shore and Fowler, 1996; Fougerouse et al., 2016; Hastie et al., 2020a). Thus, the range and depletion of $\delta^{34}S$ values, along with the presence of oscillatory and sector zoning in the pyrite, suggest their formation under oxidizing conditions and/or temperature drop. These data, along with previous examination of sector zoning in the pyrite (Hastie et al., 2020a), offers an alternative model to the pulsing of chemically distinct fluids for the formation of As-rich zoning within pyrite, as was suggested by Peterson and

Mavrogenes (2014) for Au-rich arsenian pyrite with depleted ^{34}S values at the Porgera porphyry deposit, Papa New Guinea.

2.6.4 $\Delta^{33}S$ and S reservoirs

To address the potential role of crustal cycling of sulfur and its importance in Au deposit formation, as suggested for some Archean and Paleoproterozoic gold deposit settings (e.g., Farquhar and Wing, 2003; Laflamme et al., 2018), the $\Delta^{33}S$ signature of pyrite was determined. Relevant in this regard is that the $\Delta^{33}S$ values for all the pyrites analyzed (Fig. 2.11) lack any significant deviation from zero when accounting for analytical precision (2σ = 1.5-2.2‰) excepting seven analyses from four deposits. Of these analyses, three have duplicate analysis within error of zero, which suggests that these analyses are outliers. Thus, none of the pyrites studied appear to record $\Delta^{33}S$ values consistent with mass independent fractionation, although sulfides with non-zero $\Delta^{33}S$ values are present in two deposit types in the AGB (VMS deposits: Sharman et al., 2015; komatiite-hosted Ni-Cu-PGE deposit: Hiebert et al., 2016). Instead, these near-zero $\Delta^{33}S$ values are consistent with sulfur sourced from juvenile magmas or assimilation of sulfur from another source (e.g., volcanic rocks) with a mantle signature (Farquhar and Wing, 2003), but other sources cannot be completely ruled out.

Based on the above, the low $\delta^{34}S_{pyrite}$ data for the intrusion-hosted deposits can be further evaluated. That the signatures for the early pyrite (Py_1) vary from about -5 to -25‰ can be attributed to variable oxidation of the fluid and related fractionation of the sulfur isotopes (i.e., ^{34}S, ^{32}S) into H_2SO_4 and H_2S species, respectively. Given that the $\Delta\delta^{34}S_{H2S}$-$\delta^{34}S_{fluid}$ can attain values of -25 to -15‰ at 250° to 350°C depending on fO_2 of the fluid (Ohmoto and Rye, 1979), this implies that the $\delta^{34}S_{\sum S}$ signature of the mineralizing fluid was near 0‰ and the variation of

the $\delta^{34}S_{pyrite}$ data for early pyrite is a function of variable fluid oxidation and is not necessarily due to different $\delta^{34}S$ signatures of the source reservoirs.

2.6.5 Late-Archean granitoid classification and formation of Au-bearing intrusive rocks

Very few geochemical plots exist for intrusive rocks relevant to Archean Au deposits. Here we use Figures 2.14 to 2.16 to highlight the diverse geochemistry of Au-bearing intrusive rocks and show they appear to plot in distinct groups on multiple diagrams. Typically, rocks are simply named based on petrographic (e.g., monzonite-syenite) or field-based (e.g., quartz-feldspar porphyry) classification, which, as can be seen, do little to highlight their geochemical diversity.

The TAS, chondrite-normalized REE, Harker-type and other binary plots (TiO_2 vs Fe_2O_3 total, Ni vs Cr, Nb vs Y, Ta vs Yb; Figs. 2.14, 2.16), which integrate other relevant datasets from intrusion-hosted Au deposits (Ispolatov et al., 2008; Laurent et al., 2014; MacDonald and Piercey, 2019), appear to differentiate among TTG, biotite-, two-mica granite, sanukitoid and hybrid granitoid types. Intrusions at the Rundle, Jerome and Kirkland Lake deposits have lower SiO_2 and higher Na_2O+K_2O, TiO_2, P_2O_5, MgO, Fe_2O_3, Ni and Cr concentrations than the intrusions at the Kenty, Namex and Timmins area deposits. When compared to empirically classified late-Archean granitoids (Laurent et al., 2014), the closest chemical affinity for the more alkaline Rundle, Jerome and Kirkland Lake intrusions is between the sanukitoid and hybrid intrusion types, while the Timmins, Kenty and Namex intrusions plot closer to TTG and biotite-, two-mica granite intrusion types.

Laurent et al. (2014) introduced a ternary diagram for the classification of late-Archean granitoids (Fig. 2.15); its three poles are: (1) Na_2O/K_2O, which is a proxy for the melting of metamorphosed, mafic igneous rocks that have low to moderate K_2O; (2) A/CNK (molar), which represents the melting of Al-rich and felsic rocks such as metasedimentary and TTG; and (3) FMSB, which stands for $(FeO_{total} + MgO)_{wt.\%} * (Sr + Ba)_{wt.\%}$, and reflects the interaction between incompatible element-rich components and peridotite. In this diagram, TTGs, biotite- and two-mica granites, and sanukitoids plot towards the Na_2O/K_2O, A/CNK and FMSB poles, respectively. This classification diagram uses a global geochemical dataset encompassing many Archean cratons (Laurent et al, 2014). Added fields and average compositions represent granitoids from the Superior craton and Limpopo belt in South Africa respectively.

Similar to the other whole-rock geochemistry plots mentioned above (Figs. 2.14, 2.16), the more alkaline intrusions from the Rundle, Jerome and Kirkland Lake deposit settings plot within or near the Superior Province sanukitoid field and close to average sanukitoid compositions (Fig. 2.15). Rundle monzonite and gabbro plot as two parallel arrays extending from the lower right to the top of the diagram showing more variability than Jerome and Kirkland Lake. The Namex intrusive rocks plot toward the biotite-, two-mica granite field and the Kenty intrusive rocks plot within the TTG field close to the average TTG composition. This ternary diagram shows therefore a reasonable discrimination among the intrusive rocks plotted, but it can also be used to further interpret their formation and/or alteration history.

The Jerome and Namex deposits, within 10 km of each other and of similar age (see above), are hosted by intrusions emplaced into a molassic, conglomeratic basin at <2680±3 Ma, thus Timiskaming age in the AGB (Ayer et al., 2002; Monecke et al., 2017), and are overprinted by the Ridout high-strain zone (Fig. 2.1C). The dated samples were also analyzed and they plot

towards the A/CNK and FMSB apices, respectively, in Figure 2.15. As seen, the Jerome intrusion is more akin to sanukitoids whereas the Namex intrusion is more aluminous. The latter could have assimilated sedimentary material during its emplacement or, alternatively, the two intrusions may have different magma sources (Fig. 2.15).

For the Rundle deposit, the monzonitic rocks cluster on geochemical plots (Figs. 2.14, 2.16), but overlap the sanukitoid and TTG fields in Figure 2.15. The LOI, Na_2O, CO_2, and S values for those rocks with ages determined suggest that the monzonite dated at 2688±2 Ma is less altered and plots within the sanukitoid field (LOI = 5.1%, Na_2O = 4.7%, CO_2 = 4.5%, S = 0.3%), whereas the other monzonite dated at 2680±5 Ma is more altered (LOI = 6.4%, Na_2O = 6.3%, CO_2 = 7.4%, S = 1.2%) and plots closer to the TTG field. This is generally consistent with other Rundle monzonite data plotted (Fig. 2.15; App. Table 1) and field observations (Fig. 2.2B). These ages are close enough to be considered part of the same intrusion and the data suggests that the monzonitic rocks experienced variable alteration (albite, carbonate, chlorite). Albitization in particular (Fig. 2.3; App. Table 1; Love and Roberts, 1991) would shift a sanukitoid composition to towards the TTG field in this plot. This interpretation is favored because the rocks that plot within the sanukitoid field are generally less altered that those outside this field (Fig. 2.15; App. Table 1) and all of these rocks plot together in tight clusters near the average sanukitoid/hybrid composition in the TAS, chondrite-normalized REE, Harker and binary plots (Figs. 2.14, 2.16).

2.6.6 Elemental mapping and combined whole-rock and LA-ICP-MS analysis

Elemental mapping has become an integral part of ore deposit research as it can not only provide a spatial assessment of elemental associations, but when used in conjunction with TSD plots (e.g., Figs. 2.18-2.21) can assess elemental coupling/decoupling and changes relative to ore tenor

(e.g., changes in Au fineness changes during remobilization; Hastie et al., 2020). Elemental maps for pyrite from Kenty, Rundle and Jerome and Namex (Figs, 2.18A, 2.19A, 2.20A, 2.21A) show commonly that Ag, Te, Hg, and Bi share associations with Au within and external to pyrite. This suggests that these elements remain coupled to Au during its liberation from pyrite via CDR processes and thus are likely to play a role in ore development (e.g., Au-LMCE melts; Hastie et al., 2020a).

Using both whole-rock and LA-ICP-MS data (Figs., 2.18-2.21), the following trace metals in bold show the strongest correlation with Au-Ag: Kenty (**Au-Ag-Bi-Te-Hg**-Sb-Pb-As-Mo-W; Fig. 2.18A-G), Jerome (**Au-Ag-As-Hg**; Fig. 2.19A, B), Rundle (**Au-Ag-Te**-Bi-Pb; Fig. 2.20A-C), Namex (**Au-Ag-Te-Hg**-Bi-Cu-Pb; Fig. 2.21A-E). Similar to spatial associations discussed above, Hg and Te are trace metals that are consistently associated with Au and Ag, as they are in most deposits across the Superior Craton (Ashley, Dome, Hemlo, Kirkland Lake (Macassa, Teck-Hughes, Lake Shore, Tough-Oakes-Toburn), Powell, Preston, Robb-Montbray; Sigma-Lamaque, Upper Canada, Vipond, Vedron; Poulsen at al., 2000; Hastie et al., 2020a) and in other Au deposit types of all ages worldwide (Boyle, 1979).

The plots of Au versus Ag show there is a shift in the Au/Ag ratio commensurate with increasing Au content for Kenty, Rundle, and Jerome where this ratio changes from <1 to 10, whereas for Namex it stays more uniform at about 0.1. Based on more detailed studies of pyrite geochemistry of these samples noted above, these data suggest there has been mobilization of Au and Ag on a scale larger than the samples, which are typically a few kg in size. This enrichment in Au is matched with elevated Ag, Te, Hg, ±Bi (Figs. 2.18-2.20) and suggests further that these metals are coupled in metal transport.

2.7 Discussion

The SGB deposits can be classified as intrusion-related (Rundle, Jerome, Namex) and BIF-hosted (4K) and greenstone-hosted (Kenty) orogenic based on field relationships. How geochemistry can be used to discriminate between intrusion-related and orogenic Archean Au deposits is discussed below.

2.7.1 Oxygen Isotopes

Oxygen isotopes have long been used as a tool for evaluating fluid sources in ore deposits (e.g., Taylor, 1974; Sheppard, 1986). However, this is not without issues for Archean Au systems. Notwithstanding that gold typically occupies fractures cutting quartz, thus introduced late during a hydrothermal events or subsequent remobilization, oxygen isotopes alone cannot discriminate between fluid sources because of the overlap of magmatic and metamorphic fluid reservoirs (Taylor, 1974; Sheppard, 1986). This latter point has been noted in relation to Archean Au systems (McCuaig and Kerrich, 1998).

Published bulk whole-rock oxygen isotope data from quartz in the Abitibi greenstone belt and elsewhere in the Superior Province generally ranges from 9.0 to 19.0‰ with most values between 10.0 to 15.0‰ (McCuaig and Kerrich, 1998; Goldfarb et al., 2005; Beaudoin, 2011). In-situ SIMS analyses from this study (Table 2.3) show that in-situ $\delta^{18}O_{quartz}$ values can have very different ranges than the bulk quartz analysis: thus they can be wider in some settings (Kirkland Lake; Siscoe; Kerr Addison (lower only)), completely disagree in others (Dome, Campbell Red Lake), or show reasonable agreement (Hollinger-McIntyre, Sigma, Powell). These are important observations because the wider the range of $\delta^{18}O_{quartz}$ values, the harder it is to explain

fractionation without a component of fluid mixing. This also collectively suggests that bulk $\delta^{18}O$ data are a poor comparative baseline for in-situ data and that a new baseline must be established for in-situ techniques before regional-scale comparisons can be properly assessed.

Further examination of the in-situ data shows that individual quartz grains can vary by up to 4‰ (Fig. 2.9), which may explain the discrepancy between bulk and in-situ techniques. Homogenizing oxygen isotope values, as done by bulk analysis, may therefore lead to erroneous interpretations of temperature fluctuation and/or the inference of multiple fluids being involved.

An obvious trend in the in-situ oxygen isotope data for the SGB and other Superior deposits (Fig. 2.8) is the lower $\delta^{18}O_{quartz}$ values for intrusion-hosted compared to non-intrusion-hosted deposits. While Figure 2.8B may appear at first to be encouraging as a potential geochemical discriminant, the overlap of intrusion- and non-intrusion-hosted deposits is unfortunately significant (9.7 to 16.5‰). This reinforces our earlier point that oxygen isotopes alone cannot discriminate Au-deposit types.

2.7.2 Sulfur Isotopes

Published bulk whole-rock $\delta^{34}S$ data for both orogenic and intrusion-hosted Archean Au deposits generally ranges from -18.0 to 10.0‰, with most between -5.0 to 5.0‰ (Lambert et al., 1984; McCuaig and Kerrich, 1998; Goldfarb et al., 2005; Beaudoin, 2011). The famous Hemlo deposit (northern Ontario) is an exception, as it has values from -17.5 to 6.3‰ (Cameron and Hattori, 1987; Thode et al., 1991), thus almost the entire range reported for Archean sulfides.

Of all the deposits analyzed herein by in-situ SIMS, only the Dome and Quemont deposits have published bulk $\delta^{34}S$ values (Moritz, 1998; Sharman et al., 2015). These vary from

0.5 to 4.0‰ for the Dome deposit and from -0.5 to 2.2‰ for the Quemont deposit. These are similar to our in-situ δ34S ranges (Dome = 0 to 2.8‰; Quemont = 0.2 to 1.4‰), but our work on the SGB deposit samples indicates that in fact in-situ analyses on multiple samples are necessary to determine their full range of $\delta^{34}S_{sulfides}$, given that it is apparent that bulk analyses tend to homogenize the natural variation of single grains.

A discriminatory trend can be seen in both the SGB and regional sulfide samples from the Superior Province (Fig. 2.10), with Au-bearing sulfides from Jerome, Rundle (Py_1) and Namex being depleted in ^{34}S compared to those from Kenty, 4K, Broulan, Dome, Paymaster, Preston and Quemont. While the bulk and in-situ $\delta^{34}S_{sulfide}$ values for most Au deposits may range between -5 to 5‰, negative values are atypical of orogenic deposits (Cameron and Hattori, 1987) excepting, as noted herein, where alteration may cause fluid oxidation and fractionation of sulfur isotopes (e.g., Kenty data in Fig. 2.10A). As for the depleted values typical of the intrusion-hosted settings in the SGB, this indicates more oxidized conditions which are commonly associated with alkaline intrusions (Fig, 2.10; Table 2.4; Robert, 2001). Thus, S isotopes are a possible discriminant between alkaline intrusion-related deposits and other deposit types, particularly when used in conjunction with other geochemical discriminants.

2.7.3 Comparing Intrusive Rock Geochemistry

The use of whole-rock major and trace-element geochemical data to classify Archean intrusions associated with Au deposits is challenging because of the altered nature of these rocks. This is made even more difficult by the multiple local and historic names given to these rocks (e.g., quartz-feldspar porphyry, feldspar porphyry, syenite, mafic syenite, albitite, quartz-monzonite, monzonite, sanukitoid, monzodiorite; granite; quartz-diorite, tonalite-trondhjemite-granodiorite:

e.g., Shirey and Hanson, 1984; Burrows et al., 1993; Robert, 2001; Ispolatov et al., 2008; Moyen and Martin, 2012; Laurent et al., 2014; Fayol and Jébrak, 2017; MacDonald and Piercey, 2019). Many classification schemes for intrusive rocks are based on modal mineralogy and, as such, many geochemical plots, which were originally devised for other rock types (e.g., volcanic), remain dubious in their effectiveness. For example, the TAS diagram featuring the plutonic subdivisions of Middlemost et al. (1994) is an obvious choice for classifying plutonic rocks and determining their magma series (subalkaline versus alkaline). However, it uses major elements that may be mobile during hydrothermal alteration and also cannot distinguish late-Archean granitoids, i.e. sanukitoids (sensu stricto: Shirey and Hanson, 1984; sensu lato: Laurent et al., 2014), from alkaline and subalkaline plutons. In contrast, the ternary A/CNK - Na_2O/K_2O - FMSB diagram (Fig. 2.15) of Laurent et al. (2014) offers promise for classifying Archean intrusive rocks because of its separate fields for common Archean plutonic rocks, such as TTG, two-mica granitoids, sanukitoids, and hybrid granitoids.

Although originally conceived for volcanic rocks, Winchester and Floyd's (1977) Nb/Y versus Zr/TiO_2 diagram is used to classify plutonic rocks as it minimizes the effect of element mobility, (e.g., Helt et al. 2014; Fayol and Jébrak, 2017; MacDonald and Piercey, 2019; Raskevicius et al., 2020). However, as seen in Figure 2.14B, the overlap in the average compositions of all late-Archean granitoids (Laurent et al., 2014), including the SGB, Kirkland Lake and Timmins intrusions, suggests it cannot be used to discriminate. In addition to high Zr and Nb values, sanukitoid intrusions are also characterized by high TiO_2 and Y values compared to other Archean granitoids which results in similar Nb/Y and Zr/TiO_2 ratios and position in the derived diagram (Fig. 2.14B). However, these suites can be distinguished using binary element

diagrams of TiO_2 versus Fe_2O_3 total and Ni versus Cr because of the greater abundance of such elements in sanukitoid intrusions.

The Y versus Nb and Yb versus Ta granite tectonic discrimination diagrams (Fig. 2.16A, B; Pearce et al., 1984) are largely irrelevant for Archean intrusive felsic rocks (i.e., granitoids) because most plot in the volcanic-arc field, although sanukitoid and hybrid granites trend towards the within-plate granite field and the Rundle gabbro plots towards the ocean-ridge granite field. While these diagrams are not particularly useful for distinguishing Archean tectonic settings, they may be more useful for differentiating different groups of intrusions, as demonstrated by the distinct clusters of the Timmins, Kenty and Namex intrusions and the more alkaline Rundle, Jerome and Kirkland Lake intrusions.

Chondrite-normalized rare-earth element (REE) plots (Sun and McDonough, 1989) are among the most commonly used trace-element diagrams and here are good discriminators for the different types of late-Archean granitoids associated with SGB and AGB Au deposits. Thus, the Rundle gabbroic rocks (Fig. 2.16C) has a distinct flat pattern whereas the more alkaline Rundle, Jerome, and Kirkland Lake intrusions are enriched in light REE and plot between the trace-element patterns of average sanukitoid and two-mica (biotite-) granite. The Timmins, Kenty and Namex are slightly less enriched in light REE and they have similar patterns and magnitude as average TTGs.

2.7.4 Whole-rock and LA-ICP-MS trace-metal data evaluated

Whole-rock trace-metal data: Now more than ever the simplicity and cost of whole-rock analyses make it a widely used option in the mineral exploration industry. The quality of commercial lab data has greatly improved over the last twenty years with companies routinely accumulating

large multi-element datasets (Halley, 2020). Whole-rock data are used to resolve the geochemical footprint of a deposit, thereby increasing the size of the exploration target. However, the lack of resolution of those analyses in terms of the spatial distribution and mineralogical host of gold and indicator trace-metals makes it a less than ideal tool for determining meaningful co-genetic correlations between Au and trace-metals. For example, Ti and W analysis for whole-rock samples from Rundle shows a correlation with Au and Ag (Fig. 2.19H, I), but LA-ICP-MS data do not. This difference based on methods is because Au-bearing samples commonly contain rutile, which is related to alteration, that is not directly associated with gold. However, at Kenty native gold is coeval with rutile (Figs. 2.3G, H; Hastie et al., 2020a) and thus results in a good correlation between Ti, W and Au, and Ag for both whole-rock and LA-ICP-MS trace-metal data (Fig. 2.19H, I). Thus, designing an exploration model that includes Ti and W based on whole-rock data alone may not yield exploration success without preliminary testing of the nature of those correlations using in-situ data.

Another example is the correlation between Pb, Se, Au, Ag at the Namex, Kenty, Rundle, and Jerome deposits. These elements are most commonly found in galena (e.g., Fig. 2.21F, J; Hastie et al., 2020a) and thus designing an exploration model that includes Pb and Se as priorities will help find galena and likely Ag (Hastie et al., 2018, 2020a), but not necessarily Au because galena is typically late in the paragenesis and not necessarily associated with gold.

2.7.4.1 In-situ LA-ICP-MS trace-metal data:

LA-ICP-MS analysis of sulfides has the potential to refine and prioritize Au associations critical to mineral exploration. The list of elements associated with Au is typically exhaustive and LA-ICP-MS trace-metal data provides information about the timing of Au and mineral deposition

that is critical for determining the trace-metals that are not only associated, but also coeval with Au (e.g., Gourcerol et al. 2018, 2020; Kerr et al., 2018; Hastie et al., 2020a). The drawback of the LA-ICP-MS method however, is that it is both cost and time intensive, the latter in part due to the needed petrographic study for sample selection.

2.7.4.2 Evaluating the utility of whole-rock Au/Ag ratios:

Previous research on Au-Ag values in pyrite from Au mineralized samples has shown early stage sulfides typically have a Au/Ag ratio close to 1, whereas gold formed from remobilization of this early refractory Au has a Au/Ag ratio close to 9 or 900 fineness (Velasquez et al., 2014; Hastie et al, 2020a). These results can therefore be used to predict the host phase or Au if remobilization has occurred. For example, Rundle and Namex have Au/Ag ratios near 9 and 0.1, respectively. Rundle has significant mineralization in the form of native gold and the textures of pyrite indicate significant CDR has occurred, which is consistent with remobilization of Au out of the early primary pyrite (Table 2.1, Fig., 2.3G, H). In contrast, at Namex most of the Au is still hosted by primary pyrite and Au-Ag tellurides (Table 2.1, Fig. 2.21A), which is consistent with its 0.1 Au/Ag ratio. Comparison of the LA data on the pyrite with the whole-rock data for the studied deposits (Figs. 2.18-2.21) show good correlation of the two data sets in regards to both Au/Ag and elemental associations. Thus the Au/Ag ratios based on whole-rock analysis can be used as a geochemical tool in early stages of an exploration program to define the host phase of Au, refine the deposit model, and provide critical information on the metallurgical recovery of Au for the deposit under exploration.

2.7.5 Chemistry of native gold

Figure 2.22 shows the Au, Ag and Cu chemistry of native gold grains for the Kenty and Superior Province deposits, which is summarized after Hastie et al. (2020a). Native gold varies in composition from 1 to 19 wt. % Ag and 300 to 1500 ppm Cu. On the Au-Ag-Cu ternary diagram using subdivisions from of Townley et al. (2003), all gold grains plot between the epithermal and gold-rich porphyry deposit fields without obvious preference for host rock (Fig. 2.22A), thus highlighting the non-discriminatory nature of these fields for Archean Au deposits.

In Figure 2.22B, gold grains from Timmins, Kirkland Lake and Val-d'Or camps are represented by different colors. Figure 2.22C is similar, but uses a greater scaling factor for Cu and lists the deposits included in each camp. Kirkland Lake gold grains differ in composition from those from Timmins and Val-d'Or by having a distinct composition with more Au and Cu and less Ag. Of these samples, Macassa and Teck-Hughes are the most Au-rich. Composition data for native gold grains from the Kenty deposit overlap with those from Timmins and Val-d'Or. Gold grains from other SGB deposits could not be extracted and reliably analyzed due to their small size.

Native gold in the Kirkland Lake camp having less Ag and more Cu than that in the Val-d'Or, Timmins and SGB (Kenty) camps suggests a regional metallogenic control on native gold chemistry and its fineness as suggested previously (Boyle, 1979). The obvious difference between these camps is the significant concentrations of Te in Kirkland Lake relative to the Val-d'Or and Timmins (Hastie et al., 2020a) with some mines in Kirkland Lake (i.e., Sylvanite) even named after tellurides. High Te abundances suggest that zone refining and gold remobilization could be controlled by polymetallic melts (Tomkins et al., 2004; Tomkins et al., 2007; Tooth et

al., 2011; Zhou et al., 2017; Hastie et al. 2020a), resulting in higher gold fineness (Velasquez et al., 2014; Hastie et al., 2020a). This would partially explain why Kirkland Lake plots as a distinct group on the Au-Ag-Cu ternary diagram.

Traditionally, most native gold research has been done using EMPA with the subject material from placer gold deposits (Desborough et al 1970a; 1970b, 1971; McTaggert and Knight, 1993; Townley et al., 2003; Chapman et al., 2010a; 2010b; 2017; 2021). Most recently this work has been applied to in-situ deposits (i.e., orogenic, epithermal, intrusion-related, and VMS; Liu et al., 2021; Liu and Beaudoin, 2021; Greenough et al., 2021) however this methodology requires evaluation and refinement (Hastie et al., 2020b) and discrimination based on deposit type remains equivocal at the moment.

It has become apparent that at least some native gold is the product of secondary processes in Au deposits (i.e., remobilization; Hastie et al., 2020a). The result of this is that the chemistry of gold may not be a primary, but instead a secondary feature and would bring into question interpretations based on primary processes. For example, Gammons and Williams-Jones (1995) suggest that the alloy composition of native gold is controlled by temperature fO_2, fS_2, Cl^-, pH and total Au/Ag content of the system, however, this assumes Au precipitation directly from a fluid and does not consider remobilized Au as part of a polymetallic melt or gold nanoparticle transport (Saunders et al. 1990; Tooth et al., 2011; Zhou et al., 2017; Saunders and Burke, 2017; Voisey et al., 2020; Petrella et al., 2020; Hastie et al., 2020a). Gold being a product of secondary processes (e.g., Hastie et al., 2020a) may also explain some of the difficulty using its chemistry to discriminate among deposit types (Liu and Beaudoin, 2021). In this context it may not be possible to use gold as a deposit type discriminator but it may still offer insight into other metallogenic processes that have spatial (i.e., regional) control on Au mineralization.

2.7.6 Refined discrimination of intrusion-related Au deposits

One of the main objectives of this study was to use a variety of parameters to see if intrusion-hosted Au deposits in the SGB could be discriminated from orogenic-type Au deposits in this belt and the contiguous AGB. Thus a detailed, field-based study of three intrusion-hosted (Rundle, Jerome, Namex) and two orogenic-type (Kenty, 4K) Au deposit settings in the SGB were complemented with stable isotopes (O and S) and whole-rock and trace-metal geochemistry to provide the basis for such evaluation. After detailed evaluation of this data, it appears that intrusion-related mineralization characterized by relatively high fO_2, as inferred by the low $\delta^{34}S_{sulfide}$ values (<-5‰), and with mineralization younger than 2690 Ma but predating shearing can be effectively discriminated from orogenic deposits.

The intrusion-related deposits of the SGB can be compared to other relevant intrusion-hosted deposits from the Timmins and Kirkland Lake areas of the AGB, as well as to late-Archean granitoid classification diagrams (Laurent et al., 2014). The tabulation of some relevant features associated with these deposits (i.e., host rocks, Au-bearing minerals, stable isotopes, age of intrusions, geochemical affinity) suggest that they belong to a distinct group of "sanukitoid-associated" deposits within the intrusion-related clan (Table 2.4), as proposed by Fayol and Jébrak (2017) for other intrusion-related Au deposits closely associated with sanukitoids. The latter intrusions are similar to the syenite-associated deposits of Robert (2001), but in fact many of the purported syenites instead have a closer chemical affinity to sanukitoids (sensu lato) and hybrid late-Archean granitoids (Fig. 2.15; Laurent et al., 2014). Importantly, this includes the

intrusions from the famed Kirkland Lake Au camp, which are closer in chemical affinity to late-Archean sanukitoids (Fig. 2.15).

2.8 Conclusions

This study has shown that detailed field mapping complemented with a variety of geochemical discriminants can be used to discriminate between intrusion-related and orogenic Au deposits. It further shows that in-situ geochemical methods offer insight into processes related to Au deposit formation that would otherwise be lost using the traditional bulk analysis methods applied over the past 50 years. Thus, the dataset presented herein that includes in-situ stable isotopes (S, O), LA-ICP-MS sulfide mapping and related data reduction, and native gold geochemistry, which follows on similar recent studies (Kerr et al., 2018; McDivitt et al., 2021), provides a template that we suggest should be widely applied in all Au deposit studies. These data were also compared to whole-rock data for host rocks, which followed detailed petrographic study, and also Au-mineralized samples from the intrusion-hosted settings.

The comparison of whole-rock and LA-ICP-MS data reveals a common Au-Ag-Te-Hg signature among Archean Au deposits. Furthermore, the Au/Ag ratios, which range from 0.1 to 10, offer an important tool for mineral exploration if the in-situ controls on these ratios can be inferred (e.g., refractory Au versus visible gold). In addition, the development of unequivocal Au associations through the in-situ analysis of native gold offer potential for resolving regional metallogenic patterns that are important for exploration, metallurgy, and interpretation of Au-forming processes.

This regional- to deposit-scale dataset combined with other existing datasets clearly shows that Archean sanukitoid-associated Au deposits represent a distinct type of deposits that can be clearly distinguished from the orogenic-type Au deposits. These Archean sanukitoid-associated deposits are shown to be characterized by: 1) having low $\delta^{34}S_{sulfide}$ values (i.e., <-5 to -25‰), which infers a high fO_2 for the ore fluid; 2) an Hg and Te geochemical signature; and 3) being <2690 Ma with associated Au mineralization predating shear zone development. This proposed deposit type is similar to the syenite-associated Au deposits of Robert (2001), but differs by the nature of the intrusions associated with those deposits.

2.9 References

Ayer, J., Amelin, Y., Corfu, F., Kamo, S., Ketchum, J., Kwok, K., and Trowell, N., 2002, Evolution of the southern Abitibi greenstone belt based on U-Pb geochronology: Autochthonous volcanic construction followed by plutonism, regional deformation and sedimentation: Precambrian Research, v. 115, p. 63-95.

Ayer, J.A., Goutier, J., Thurston, P.C., Dubé, B., and Kamber, B.S., 2010, Tectonic and metallogenic evolution of the Abitibi and Wawa subprovinces: in Summary of Field Work and Other Activities, 2010, Ontario Geological Survey, Open File Report 6260, p. 3-1 to 3-6.

Bateman, R., Ayer, J.A., and Dubé, B., 2008, The Timmins-Porcupine gold camp, Ontario: Anatomy of an Archean greenstone belt and ontogeny of gold mineralization: ECONOMIC GEOLOGY, v. 103, p. 1285-1308.

Beaudoin, G., 2011, The stable isotope geochemistry of orogenic gold deposits: In Barra, F., Reich, M., Campos, E., Tornos, F. (eds.) Lets talk ore deposits, Proceedings of the Eleventh Biennial SGA Meeting, Antofagasta, p. 556-558.

Beaudoin, G. and Chiaradia, M., 2016, Fluid mixing in orogenic deposits: Evidence from the H-O-Sr isotope composition of the Val-d'Or vein field (Abitibi, Canada): Chemical Geology, v. 437, p. 7-18.

Beaudoin, G., Mercier-Langevin, P., Dubé, B., and Taylor, B.E., 2014, Low-temperature alteration at the world-class LaRonde Penna Archean Au-rich volcanogenic massive sulfide deposit, Abitibi Subprovince, Quebec, Canada: Evidence from whole-rock oxygen isotopes: ECONOMIC GEOLOGY, v. 109, p. 167-182.

Beaudoin, G. and Pitre, D, 2005, Stable isotope geochemistry of the Archean Val-d'Or (Canada) orogenic gold vein field: Mineralium Deposita, v. 40, p. 59-75.

Beaudoin, G. and Raskevicius, T., 2014, Constraints on the genesis of the Archean oxidized, intrusion-related Canadian Malartic gold deposit, Quebec, Canada – A discussion: ECONOMIC GEOLOGY, v. 109, p. 2067-2071.

Beaudoin, G., Therrien, R., and Savard, C., 2006, 3D numerical modeling of fluid flow in the Val-d'Or orogenic gold district: major crustal shear zones drain fluids from overpressured vein fields: Mineralium Deposita, v. 41, p. 82-98.

Boyle, R.W. 1979. The geochemistry of gold and its deposits; Geological Survey of Canada, Bulletin 280, 584 p.

Burrows, D.R., Spooner, E.T.C., Wood, P.C., and Jemielita, R.A., 1993, Structural controls on formation of the Hollinger-McIntyre Au quartz vein system in the Hollinger shear zone, Timmins, southern Abitibi greenstone belt, Ontario: ECONOMIC GEOLOGY, v. 88, p. 1643-1663.

Burt, P.D., Chance, P.N., and Burns, J.G., 2011, Technical report on a resource estimate on the Jerome mine property, Osway Township, Porcupine Mining Division, Ontario, prepared for Augen Gold Corporation: Augen Gold Corp., NI 43-101 Technical Report, 92 p., www.sedar.com.

Cameron, E.M. and Hattori, K., 1987, Archean gold mineralization and oxidized hydrothermal fluids: ECONOMIC GEOLOGY, v. 82, p. 1177-1191.

Caruso, S., Fiorentini, M.L., Hollis, S.P., Laflamme, C., Baumgartner, R.J., Steadman, J.A. and Savard, D., 2018, The fluid evolution of the Nimbus Ag-Zn-(Au) deposit: An interplay between mantle plume and microbial activity: Precambrian Research, v. 317, p. 211-229.

Chapman, R.J., Mortensen, J.K., Crawford, E.C., and Lebarge, W., 2010, Microchemical studies of placer and lode gold in the Klondike District, Yukon, Canada: 1. Evidence for a small, gold-rich, orogenic hydrothermal system in the Bonanza and Eldorado Creek area: ECONOMIC GEOLOGY, v. 105, p. 1369-1392.

Chapman, R.J., Mortensen, J.K., Crawford, E.C., and Lebarge, W., 2010, Microchemical studies of placer and lode gold in the Klondike District, Yukon, Canada: 2. Constraints on the nature and location of regional lode sources: ECONOMIC GEOLOGY, v. 105, p. 1393-1410.

Chapman, R., Mileham, T., Allan, M., and Mortensen, J., 2017, A distinctive Pd-Hg signature in detrital gold derived from alkalic Cu-Au porphyry systems: Ore Geology Reviews, v. 83, p. 84-102.

Chapman, R.J., Banks, D.A., Styles, M.T., Walshaw, R.D., Piazolo, S., Morgan, D.J., Grimshaw, M.R., Spence-Jones, C.P., Mathews, T.J., and Borovinskaya, 2021, Chemical and physical heterogeneity within native gold: implications for the design of gold particle studies: Mineralium Deposita, https://doi.org/10.1007/s00126-020-01036-x.

Desborough, G.A., 1970a, Silver depletion indicated by microanalysis of gold from placer occurrences, western United States: ECONOMIC GEOLOGY, v. 65, p. 304-311.

Desborough G.A., 1970b, Distribution of silver and copper in placer gold derived from the northeastern part of the Colorado mineral belt: ECONOMIC GEOLOGY, v. 65, p. 937-944.

Desborough G.A., Heidel, R.H., Raymond, W.H. and Tripp, J., 1971, Primary distribution of silver and copper in native gold from six deposits in the western United States: Mineralium Deposita, v. 6, p. 321-334.

Dubé, B., and Gosselin, P., 2007, Greenstone-hosted quartz-carbonate vein deposits: in Goodfellow, W.D., ed., Mineral deposits of Canada: A synthesis of major deposit-types, district metallogeny, the evolution of geological provinces, and exploration methods: Geological Association of Canada, Mineral Deposits Division, Special Publication no. 5, p. 49-73.

Dubé, B., and Mercier-Langevin, P., 2021, Gold deposits of the Archean Abitibi greenstone belt, Canada: Society of Economic Geologists, Special Publication no. 23, p. 669-708.

Evans, K.A., Phillips, G.N. and Powell, R., 2006, Rock-buffering of auriferous fluids in altered rocks associated with the Golden Mile-style mineralization, Kalgoorlie gold field, Western Australia: ECONOMIC GEOLOGY, v. 101, p. 805-817.

Farquhar, J. and Wing, B.A., 2003, Multiple sulfur isotopes and the evolution of the atmosphere: Earth and Planetary Science Letters, v. 213, p. 1-13.

Fayol, N., and Jébrak, M., 2017, Archean sanukitoid gold porphyry deposits: A new understanding and genetic model from the Lac Bachelor gold deposit, Abitibi, Canada: ECONOMIC GEOLOGY, v. 112, p. 1913-1936.

Fougerouse, D., Reddy, S.M., Saxey, D.W., Rickard, W.D.A., van Riessen, A., and Micklethwaite, S., 2016, Nanoscale gold clusters in arsenopyrite controlled by growth rate not concentration: Evidence from atom probe microscopy: American Mineralogist, v. 101, p. 1916-1919.

Galley, A.G., 2003, Composite synvolcanic intrusions associated with Precambrian VMS-related hydrothermal systems: Mineralium Deposita, v. 38, p. 443-473.

Galley, A.G., Lafrance, B., 2014, Setting and evolution of the Archean synvolcanic Mooshla Intrusive Complex, Doyon-Bousquet-LaRonde mining camp, Abitibi greenstone belt: Emplacement history, petrogenesis, and implications for Au metallogenesis: ECONOMIC GEOLOGY, v. 109, p. 205-229.

Gammons, C.H., and Williams-Jones, A.E., 1995, Hydrothermal geochemistry of electrum: Thermodynamic constraints: ECONOMIC GEOLOGY, v. 90, p. 420-432.

Gemmell, T.P., and MacDonald, P.J., 2016, Geology and mineral potential of Yeo and southern Potier townships, southern Swayze area, Abitibi greenstone belt: in Summary of Field Work and Other Activities 2016, Ontario Geological Survey, Open File Report 6323, p. 7-1 to 7-13.

Goldfarb, R.J., Baker, T., Dubé, B., Groves, D.I., Hart, C.J.R., and Gosselin, P., 2005, Distribution, character, and genesis of gold deposits in metamorphic terranes: ECONOMIC GEOLOGY 100th Anniversary Volume, p. 407-450.

Goldfarb, R.J. and Groves, D.I., 2015, Orogenic gold: Common or evolving fluid and metal sources through time: Lithos, v. 233, p. 2-26.

Gourcerol, B., Kontak, D.J., Thurston, P.C., and Petrus, J.A., 2018, Application of LA ICP-MS sulphide analysis and methodology for deciphering elemental paragenesis and associations in addition to multi-stage processes in metamorphic gold settings: The Canadian Mineralogist v. 56 (1), p. 39-64.

Gourcerol, B., Kontak, D.J., Petrus, J.A, and Thurston, P.C., 2020, Application of LA ICP-MS analysis of arsenopyrite to gold metallogeny of the Meguma Terrane, Nova Scotia, Canada: Gondwana Research, v. 81, p. 265-290.

Greenough, J.D., Velasquez, A., Shaheen, M., Gagnon, J., Fryer, B.J., Tetland, M., Chen, Y., and Mossman, D.J., Laser ablation ICP MS trace element composition of native gold from the Abitibi greenstone belt, Timmins Ontario: Canadian Journal of Earth Sciences, https://doi.org/10.1139/cjes-2019-0134.

Groves, D.I., Goldfarb, R.J., Gebre-Mariam, M., Hagemann, S.G., and Robert, F., 1998, Orogenic gold deposits: A proposed classification in the context of their crustal distribution and relationship to other gold deposit types: Ore Geology Reviews, v. 13, p. 7-27.

Hagemann, S.G. and Cassidy, K.F., 2000, Archean Orogenic lode gold deposits: Reviews in Economic Geology, v. 13, p. 9-68.

Halley, S., 2020, Mapping magmatic and hydrothermal processes from routine exploration geochemical analyses, ECONOMIC GEOLOGY, v. 115, p. 489-503.

Hastie, E.C.G., 2014, Gold metallogeny of the southern Swayze greenstone belt: in Summary of Field Work and Other Activities, 2014, Ontario Geological Survey, Open File Report 6300, p. 7-1 to 7-8.

Hastie, E.C.G., 2017, Gold metallogeny of the southern Swayze area, Abitibi greenstone belt: a field trip guidebook: Ontario Geological Survey, Open File Report 6334, 19 p.

Hastie, E.C.G., Gagnon, J.E., and Samson, I.M., 2018, The Paleoproterozoic MacLellan deposit and related Au-Ag occurrences, Lynn Lake greenstone belt, Manitoba: An emerging, structurally-controlled gold camp: Ore Geology Reviews, v. 94, p. 24-45.

Hastie, E.C.G., Kontak, D.J., and Lafrance, B., 2016, Update on activities related to a gold metallogenic study of the southern Swayze greenstone belt: in Summary of Field Work and Other Activities 2016, Ontario Geological Survey, Open File Report 6323, p. 8-1 to 8-11.

Hastie, E.C.G., Kontak, D.J. and Lafrance, B., 2020a, Gold remobilization: Insights from gold deposits in the Archean Swayze greenstone belt, Abitibi Subprovince, Canada; ECONOMIC GEOLOGY v. 115, p. 241-277.

Hastie, E.C.G., Lafrance, B., and Kontak, D.J., 2015, Observations on the Kenty and Rundle deposits, Swayze greenstone belt: in Summary of Field Work and Other Activities, 2015, Ontario Geological Survey, Open File Report 6313, p. 9-1 to 9-9.

Hastie, E.C.G., Petrus, J.A., Gibson, H.L., and Tait, K.T., 2020b, Gold Fingerprinting: Using major and trace elements associated with native gold to work toward a global gold database: in Summary of Field Work, 2020, Ontario Geological Survey, Open File Report 6370, p.10-1 to 10-10.

Hastie, E.C.G., Schindler, M., Kontak, D.J. and Lafrance, B. 2021, Transport and coarsening of gold nanoparticles in an orogenic deposit by dissolution-reprecipitation and Ostwald ripening: Communications Earth & Environment, v. 2, no. 57, https://doi.org/10.1038/s43247-021-00126-6.

Heather, K.B., 2001, The geological evolution of the Archean Swayze greenstone belt, Superior Province, Canada: unpublished PhD thesis, Keele University, Keele, England, 370 p.

Helt, K.M., Williams-Jones, A.E., Clark, J.R., Wing, B.A. and Wares, R.P., 2014a, Constraints on the genesis of the Archean oxidized, intrusion-related Canadian Malartic gold deposit, Quebec, Canada: ECONOMIC GEOLOGY, v. 109, p. 713-735.

Helt, K.M., Williams-Jones, A.E., Clark, J.R., Wing, B.A. and Wares, R.P., 2014b, Constraints on the genesis of the Archean oxidized, intrusion-related Canadian Malartic gold deposit, Quebec, Canada – A reply: ECONOMIC GEOLOGY, v. 109, p. 2067-2071.

Hiebert R.S., Bekker, A., Houlé, M.G., Wing, B.A., and Rouxel, O.J., 2016, Tracing sources of crustal contamination using multiple S and Fe isotopes in the Hart komatiite-associated Ni-Cu-PGE sulfide deposit, Abitibi greenstone belt, Ontario, Canada: Mineralium Deposita, v. 51, p. 919-935.

Huston, D.L., Taylor, B.E., Bleeker, W., Stewart, B., Cook, R., and Koopman, E.R., 1995, Isotope mapping around the Kidd Creek deposit, Ontario: Application to exploration and comparison with other geochemical indicators: Exploration and Mining Geology, v. 4, p. 175-185.

Ispolatov, V., Lafrance, B., Dubé, B., Creaser, R., and Hamilton, M., 2008, Geologic and structural setting of gold mineralization in the Kirkland Lake-Larder Lake gold belt, Ontario: ECONOMIC GEOLOGY, v. 103, p. 1309-1340.

Katz, L.R., Kontak, D.J., Dubé, B., and McNicoll, V., 2017, The geology, petrology, and geochronology of the Archean Côté Gold large-tonnage, low-grade intrusion-related Au(-Cu) deposit, Swayze greenstone belt, Ontario, Canada: Canadian Journal of Earth Sciences, v. 54, p. 173-202.

Katz, L.R., Kontak, D.J., Dubé, B., McNicoll, V., Creaser, R., and Petrus, J.A., 2020, An Archean porphyry-type gold deposit: The Côté Gold Au(-Cu) deposit, Swayze greenstone belt,

Superior Province, Ontario, Canada: ECONOMIC GEOLOGY (2020), https://doi.org/10.5382/econgeo.4785.

Kerr, M.J., Hanley, J.J., Kontak, D.J., Morrison, G.G., Petrus, J., Fayek, M., and Zajacz, Z., 2018, Evidence of upgrading of gold tenor in an orogenic quartz-carbonate vein system by late magmatic-hydrothermal fluids at the Madrid deposit, Hope Bay greenstone belt, Nunavut, Canada: Geochimica et Cosmochimica Acta, v. 241, p. 180-218.

Kerrich, R. and Wyman, D., 1990, Geodynamic setting of mesothermal gold deposits: An association with accretionary tectonic regimes: Geology, v. 18, p. 882-885.

Kerrich, R., 1993, Perspectives on genetic models for lode gold deposits: Mineralium Deposita, v. 28, p. 362-365.

King, E.M., Barrie, C.T., and Valley, J.W., 1997, Hydrothermal alteration of oxygen isotope ratios in quartz phenocrysts, Kidd Creek mine, Ontario: Magmatic values are preserved in zircon: Geology, v. 25, p. 1079-1082.

Kontak, D.J., and Kyser, K., 2011, A fluid inclusion and isotopic study of an intrusion-related gold deposit (IRGD) setting in the 380 Ma South Mountain Batholith, Nova Scotia, Canada: evidence for multiple fluid reservoirs: Mineralium Deposita, v. 46, p. 337-363.

Kontak, D.J., Hanley, J.B., and Fayek, M., 2016, A Rayleigh distillation model to explain large variations in oxygen isotope data for orogenic gold veins: Abstract, Geological Association of Canada-Mineralogical Association of Canada.

Kontak, D.J., and Smith, P.K., 1989, Sulphur isotopic composition of sulphides from the Beaver Dam and other Meguma-Group-hosted gold deposits, Nova Scotia: implications for genetic models: Canadian Journal of Earth Sciences, v. 26, p. 1617-1629.

Laflamme, C., Sugiono, D., Thébaud, N., Caruso, S., Fiorentini, M., Selvaraja, V., Jeon, H., Voute, F. and Martin, L., 2018, Multiple sulfur isotopes monitor fluid evolution of an Archean orogenic gold deposit: Geochimica et Cosmochimica Acta, v. 222, p. 436-446.

Laurent, O., Martin, H., Moyen, J.F., and Doucelance, R., 2014, The diversity and evolution of late-Archean granitoids: Evidence for the onset of "modern-style" plate tectonics between 3.0 and 2.5 Ga: Lithos, v. 205, p. 208-235.

Leclerc, F. et al. Tholeiitic to calc-alkaline cyclic volcanism in the Roy Group, Chibougamau area, Abitibi Greenstone Belt – revised stratigraphy and implications for VHMS exploration. Can. J. Earth Sci. 48, 661–694 (2011).

Liu, H., and Beaudoin, G., 2021, Geochemical signatures in native gold derived from Au-bearing ore deposits: Ore Geology Reviews, v. 132, 104066.

Liu, H., Beaudoin, G., Makvandi, S., Jackson, S.E., and Huang, X, 2021, Multivariate statistical analysis of trace element compositions of native gold from orogenic gold deposits: Implication for mineral exploration: Ore Geology Reviews, v. 131, 104061.

Love, D.A. and Roberts, R.G., 1991, The geology and geochemistry of gold mineralization and associated alteration at the Rundle gold deposit, Abitibi Subprovince, Ontario: ECONOMIC GEOLOGY, v.86, p. 644-666.

MacDonald, P.J., Hastie, E.C.G., and Davis, D.W., 2017, Preliminary geology of Osway and Huffman Townships and parts of Eric, Fingal and Arbutus Townships, southern Swayze area, Abitibi greenstone belt: in Summary of Field Work and Other Activities 2017, Ontario Geological Survey, Open File Report 6333, p. 7-1 to 7-13.

MacDonald, P.J., and Piercey, S.J., 2019, Geology, lithogeochemistry, and significance of porphyry intrusions associated with gold mineralization within the Timmins-Porcupine gold camp, Canada: Canadian Journal of Earth Sciences, v. 56, p. 399-418.

Matsuhisa, Y., Goldsmith, J.R., and Clayton, R.N., 1979, Oxygen isotopic fractionation in the system quartz-albite-anorthite-water: Geochimica et Cosmochimica Acta, v. 43, p. 11341-1140.

McCuaig, T.C. and Hronsky, J.M.A., 2014, The mineral systems concept: the key to exploration targeting: Society of Economic Geologists Special Publication 18, p. 153-175.

McCuaig, T.C. and Kerrich, R., 1998, P-T-t-deformation-fluid characteristics of lode gold deposits: evidence from alteration systematics: Ore Geology Reviews, v. 12, p. 381-453.

McDivitt, J.A., Kontak, D.J., Lafrance, B., Petrus, J.A. and Fayek, M., 2020, A trace metal, stable isotope (H, O, S), and geochronological (U-Pb titanite) characterization of hybridized gold orebodies in the Missanabie-Renabie district, Wawa subprovince (Canada): Mineralium Deposita (2020), https://doi.org/10.1007/s00126-020-00983-9.

McTaggart, K.C. and Knight, J.B. 1993. Geochemistry of lode and placer gold of the Cariboo district, B.C.; British Columbia Ministry of Energy, Mines, Petroleum Resources, Open File 1993-30, p.1-26.

Mercier-Langevin, P., Hannington, M.D., Dubé, B. and Bécu, V., 2011, The gold content of volcanogenic massive sulfide deposits: Mineralium Deposita, v. 46, p. 509-539.

Mercier-Langevin, P., Lawley, C.J.M., Castonguay, S., Dubé, B., Bleeker, W., Pinet, N., Bécu, V., Pilote, J –L., Jackson, S. E., Wodicka, N., Honsberger, I.W., Davis, W.J., Petts, D.C., Yang, Z., Jautzy, J., and Lauzière, K., 2020, Targeted Geoscience Initiative 5, Gold Project: a summary of contributions to the understanding of Canadian gold systems, in Mercier-Langevin, P., Lawley, C.J.M., Castonguay, S. eds., Targeted Geoscience Initiative 5: contributions to the understanding of Canadian gold systems: Geological Survey of Canada, Open File 8712, p. 1-30.

Middlemost, E.A.K., 1994, Naming materials in the magma/igneous rock system: Earth-Science Reviews, v. 37, p. 215-224.

Monecke, T., Mercier-Langevin, P., Dubé, B., and Frieman, B.M., 2017, Geology of the Abitibi greenstone belt: Reviews in Economic Geology, v. 19, p. 7-49.

Moyen, J-F., and Martin, H., 2012, Forty years of TTG research: Lithos, v. 148, p. 312-336.

Neumayr, P., Walshe, J., Hagemann, S., Petersen, K., Roache, A., Frikken, P., Horn, L., and Halley, S., 2008, Oxidized and reduced mineral assemblages in greenstone belt rocks of the St. Ives gold camp, Western Australia: vectors to high-grade ore bodies in Archaean gold deposits?: Mineralium Deposita, v. 43, p. 363-371.

Neyedley, K., Hanley, J.J., Fayek, M., and Kontak, D.J., 2017, Textural, fluid inclusion, and stable oxygen isotope constraints on vein formation and gold precipitation at the 007 deposit, Rice Lake greenstone belt, Bissett, Manitoba, Canada: ECONOMIC GEOLOGY, v. 112, p. 629-660.

Ohmoto, H., and Rye, R.O., 1979, Isotopes of sulphur and carbon, in Barnes, H.L., ed., Geochemistry of Hydrothermal Ore Deposits, 2nd Edition, p. 509-567.

Olivo, G.R., Chang, F., and Kyser, T.K., 2006, Formation of the Auriferous and barren North Dipper veins in the Sigma mine, Val-d'Or, Canada: Constraints from structural, mineralogical, fluid inclusion and isotopic data: ECONOMIC GEOLOGY, v.101, p. 607-631.

Ontario Geological Survey, 2011, 1:250 000 scale bedrock geology of Ontario: Ontario Geological Survey, Miscellaneous Release—Data 126–Revision 1.

Ontario Geological Survey, 2019, Geochronology Inventory of Ontario—2019: Ontario Geological Survey, Geochronology Inventory of Ontario—2019, online database.

Ontario Geological Survey, 2020a, Mineral Deposit Inventory: Ontario Geological Survey Mineral Deposit Inventory (December 2020 update), online database.

Ontario Geological Survey, 2020b, Airborne magnetic and electromagnetic surveys, colour-filled contours of the residual magnetic field and electromagnetic anomalies, Biscotasing area: Ontario Geological Survey, Map 83 006, scale 1:50 000.

Paterson, W.P.E., Ravnaas, C., Lewis, S.O., Paju, G.F., Fudge, S.P., Daniels, C.M. and Pettigrew, T.K., 2020, Report of Activities 2019, Resident Geologist Program, Red Lake Regional Resident Geologist Report: Red Lake and Kenora Districts: Ontario Geological Survey, Open File Report 6363, 112p.

Pearce, J.A., Harris, N.B.W., Tindle, A.G., 1984, Trace element discrimination diagrams for the tectonic interpretation of granitic rocks: Journal of Petrology, v. 25, p. 956-983.

Peterson, E.C., and Mavrogenes, J.A., 2014, Linking high-grade gold mineralization to earthquake-induced fault-valve processes in the Porgera gold deposit, Papua New Guinea: Geology, v. 42, p. 383-386.

Petrella, L., Thébaud, N., Fougerouse, D., Evans, K., Quadir, Z., and Laflamme, C., 2019, Colloidal gold transport: a key to high-grade gold mineralization?: Mineralium Deposita, v. 55, p. 1247-1254.

Phillips, G.N., Groves, D.I., Neall, F.B., Donnelly, T.H., and Lambert, I.B., 1986, Anomalous sulfur isotope compositions in the Golden Mile, Kalgoorlie: ECONOMIC GEOLOGY, v. 81, p. 2008-2015.

Phillips, G.N., and Powell, R., 1993, Link between Gold Provinces: ECONOMIC GEOLOGY, v. 88, p. 1084-1098.

Poulsen, K.H., Robert, F. and Dubé, B., 2000, Geological classification of Canadian gold deposits: Geological Survey of Canada Bulletin 540, 106 p.

Putnis, A., 2002, Mineral replacement reactions: from macroscopic observations to microscopic mechanisms: Mineralogical Magazine, V. 66, p. 689-708.

Putnis, A., 2009, Mineral replacement reactions: Reviews in Mineralogy and Geochemistry, v. 70, p. 87-124.

Raskevicius, T., Beaudoin, G., Kyser, K., Perrouty, S., and Gaillard, N., 2020, Whole-rock δ2H and δ18O footprint of the Canadian Malartic gold deposit, Pontiac Subprovince, Québec, Canada: Mineralium Deposita, v. 55, p. 991-1008.

Robert, F., 2001, Syenite-associated disseminated gold deposits in the Abitibi greenstone belt, Canada: Mineralium Deposita, v. 36, p. 503-516.

Saunders, J.A., 1990, Colloidal transport of gold and silica in epithermal precious metal systems: Evidence from the Sleeper deposit, Nevada: Geology, v.18, p. 757-760.

Saunders, J.A., and Burke, M., 2017, Formation and aggregation of gold (electrum) nanoparticles in epithermal ores: Minerals, v. 7, no. 9: 163.

Sharman, E.R., Taylor, B.E., Minarik, W.G., Dubé, B., and Wing, B.A., 2015, Sulfur and trace element data from ore sulfides in the Noranda district (Abitibi, Canada): implications for volcanogenic massive sulfide deposit genesis: Mineralium Deposita, v. 50, p. 591-606.

Sheahan, C., Fayek, M., Quirt, D., and Jefferson, C.W., 2016, A combined ingress-egress model for the Kianna unconformity-related uranium deposit, Shea Creek project, Athabasca basin, Canada: ECONOMIC GEOLOGY, v.111, p. 225-257.

Sheppard, S.M.F., 1986, Characterization and isotopic variations in natural waters, in Valley, J.W., Taylor, H.P., O'Neill, J.R., eds., Stable isotopes in high temperature geological processes: Reviews in Mineralogy, v. 16, p. 165-184.

Shirey, S.B., and Hanson, G.N., 1984, Mantle-derived Archaean monzodiorites and trachyandesites: Nature, v. 310, p. 222-224.

Shore, M., and Fowler, A.D., 1996, Oscillatory zoning in minerals: A common phenomenon: The Canadian Mineralogist, v. 34, p. 1111-1126.

Sun, S.S., and McDonough, W.F., 1989, Chemical and isotopic systematics of oceanic basalts: implications for mantle composition and processes, in Saunders, A.D., and Norry, M.J., eds., Magmatism in ocean basins: Geological Socitey of London, Special Publications, v. 42., p. 313-345.

Taylor, H.P., 1974, The application of oxygen and hydrogen isotope studies to problems of hydrothermal alteration and ore deposition: ECONOMIC GEOLOGY, v.69, p. 843-883.

Thode, H.G., Ding, T., and Crocket, J.H., 1991, Sulphur-isotope and elemental geochemistry studies of the Hemlo gold mineralization, Ontario: sources of sulphur and implications for the mineralization process: Canadian Journal of Earth Sciences, v. 28, p. 13-25.

Thompson, P.H., 2005, A new metamorphic framework for gold exploration in the Timmins-Kirkland Lake area, western Abitibi greenstone belt: Discover Abitibi Initiative; Ontario Geological Survey, Open File Report 6162, 104p.

Thurston, P.C., Ayer, J.A., Goutier, J., and Hamilton, M.A., 2008, Depositional gaps in Abitibi greenstone belt stratigraphy: A key to exploration for syngenetic mineralization: ECONOMIC GEOLOGY, v. 103, p. 1097-1134.

Tomkins, A.G., Pattison, D.R.M., and Frost, B.R., 2007, On the initiation of metamorphic sulfide anatexis: Journal of Petrology, v. 48, no. 3, p. 511-535.

Tomkins, A.G., Pattison, D.R.M., and Zaleski, E., 2004, The Hemlo gold deposit, Ontario: An example of melting and mobilization of a precious metal-sulfosalt assemblage during amphibolite facies metamorphism and deformation: ECONOMIC GEOLOGY, v. 99, p. 1063-1084.

Tooth, B., Ciobanu, C.L., Green, L., O'Neill, B., and Brugger, J., 2011, Bi-melt formation and gold scavenging from hydrothermal fluids: An experimental study: Geochimica et Cosmochimica Acta, v. 75, p. 5423-5443.

Townley, B.K., Hérail, G., Maksaev, V., Palacios, C., de Parseval, P., Sepulveda, F., Orellana, R., Rivas, P., and Ulloa, C., 2003, Gold grain morphology as an exploration tool: application to gold exploration in covered areas: Geochemistry: Exploration, Environment, Analysis, v. 3, p. 29-38.

van Breemen, O., Heather, K.B., and Ayer, J.A., 2006, U-Pb geochronology of the Neoarchean Swayze sector of the southern Abitibi greenstone belt: Geological Survey of Canada, Current Research 2006-F1, 32 p.

van Hees, E.H., Bousquet, P., Suma-Momoh, J., Daniels, C.M., Hinz, S.L.K., Boucher, C., Sword, P., Wang, L., Fudge, S.P., Millette, A., and Patterson, C., 2020, Report of Activities 2019, Resident Geologist Program, Timmins Regional Resident Geologist Report: Timmins and Sault Ste. Marie Districts: Ontario Geological Survey, Open File Report 6366, 160p.

Velásquez, G., Béziat, D., Salvi, S., Siebenaller, L., Borisova, A.Y., Pokrovski, G.S., and de Parseval, P., 2014, Formation and deformation of pyrite and implications for gold mineralization in the El Callao District, Venezuela: ECONOMIC GEOLOGY, v. 109, p.457-486.

Voisey, C.R., Willis, D., Tomkins, A.G., Wilson, C.J.L., Micklethwaite, S., Salvemini, F., Bougoure, J., and Rickard, W.D.A., 2020, Aseismic refinement of orogenic gold systems: ECONOMIC GEOLOGY, v. 115, p. 33-50.

Wagner, T., Fusswinkel, T., Wälle, M., and Heinrich, C.A., 2016, Microanalysis of fluid inclusions in crustal hydrothermal systems using laser ablation methods: Elements, v. 12, p. 323-328.

Williams-Jones, A.E., Bowell, R.J., and Migdisov, A.A., 2009, Gold in Solution: Elements, v. 5, p. 281-287.

Winchester, J.A., and Floyd, P.A., 1977, Geochemical discrimination of different magma series and their differentiation products using immobile elements: Chemical Geology, v. 20, p. 325-343.

Zhou, H., Sun, X., Cook, N.J., Lin, H., Fu, Y., Zhong, R., and Brugger, J., 2017, Nano- to micron-scale particulate gold hosted by magnetite: A product of gold scavenging by bismuth melts: ECONOMIC GEOLOGY, v. 112, p. 993-1010.

2.10 Tables and Figures

Table 2.1. Characteristics of SGB deposits.

Deposit	Dominant Au-bearing host rock	Alteration minerals	Au host phases	Age of Mineralization (Ma)	Metamorphic grade	Preliminary Field Classification
Jerome	syenite-monzonite	quartz, orthoclase, albite, Fe-carbonate (ankerite-ferroan dolomite), pyrite (arsenian), muscovite, microcline, hematite	Au-bearing pyrite, native gold	<2684 ±3	greenschist	alkaline intrusion-hosted
Namex	monzogranite	quartz, orthoclase, albite, Fe-carbonate (ankerite-ferroan dolomite), pyrite, muscovite, tetrahedrite, microcline, hematite,	Au-bearing pyrite, Au-Ag tellurides	<2680 ±4	greenschist	intrusion-hosted (alkaline?)
Rundle	monzonite; albitite	quartz, albite, orthoclase, Fe-carbonate (ankerite), microcline, pyrite, muscovite, hematite, talc, chlorite	Au-bearing pyrite, native gold	<2680 ±5	greenschist	alkaline intrusion-hosted
Kenty	pillow basalt	quartz, albite, Fe-carbonate (ankerite), pyrite, muscovite, microcline, chlorite, rutile, hematite	Au-bearing pyrite, Au-Ag tellurides, native gold	<2685 ±2	greenschist	greenstone-hosted
4K	banded iron formation; graphitic siltstone	quartz, biotite, chlorite, pyrrhotite, pyrite, arsenopyrite, amphibole, garnet	Au-bearing arsenopyrite and pyrite	<2682 ±2	amphibolite	BIF-hosted

Table 2.2. Operating conditions, parameters, standards and analytical precision for O and S isotope analyses by SIMS.

Oxygen Isotope Analysis Parameters (Epoxy Pucks)	**Sulfur Isotope Analysis Parameters (Epoxy Pucks)**	**Sulfur Isotope Analysis Parameters (Thin Section)**
~3 nA primary ion beam of Cs+ accelerated at 10 kV	~2 nA primary ion beam of Cs+ accelerated at 10 kV	~800 pA primary ion beam of Cs+ accelerated at 10 kV
Spot size = ~20 µm	Spot size = ~20 µm	Spot size = ~15 µm
Entrance slit = 247 µm	Entrance slit = 247 µm	Entrance slit = 260 µm
Sample accelerating voltage -8.7 kV	Sample accelerating voltage -8.7 kV	Sample accelerating voltage -8.8 kV
Electrostatic analyzer in secondary column -9 kV	Electrostatic analyzer in secondary column -9 kV	Electrostatic analyzer in secondary column -9 kV
300 volt offset	300 volt offset	200 volt offset
Mass resolving power = 347	Mass resolving power = 347	Mass resolving power = 347
Detector = ETP 133H electron multiplier	Detector = ETP 133H electron multiplier	Detector = ETP 133H electron multiplier
Deadtime = 21 ns	Deadtime = 21 ns	Deadtime = 22 ns
Ions detected = ^{18}O-, ^{16}O-	Ions detected = ^{34}S-, ^{33}S-, ^{32}S-	Ions detected = ^{34}S-, ^{32}S-
Analysis = 70 cycles ~10 minutes	Analysis = 50 cycles ~12 minutes	Analysis = 50 cycles ~7 minutes
1 cycle = 1 sec on ^{16}O, 5 sec on ^{18}O	1 cycle = 1 sec on ^{32}S, 5 sec on ^{33}S & 5 sec on ^{34}S	1 cycle = 1 sec on ^{32}S, 5 sec on ^{34}S
Counts ~1 x 10^6 for ^{16}O; ~2 x 10^3 for ^{18}O	Counts ~1 x 10^6 for ^{32}S	Counts ~1 x 10^6 for ^{32}S
eGun used for charge compensation		
Field Aperture = 1800 µm, Contrast Aperture = 400 µm	Field Aperture = 1800 µm, Contrast Aperture = 400 µm	Field Aperture = 1800 µm, Contrast Aperture = 400 µm
Lprim4 Aperture = 750 µm	Lprim4 Aperture = 750 µm	Lprim4 Aperture = 200 µm
Energy window = +/-25 volts	Energy window = +/-25 volts	Energy window = +/-25 volts

Mineral	**Name**	**Isotope System**	**δ Value (‰)**	**International Reference**	**Reference**	**Spot-to-Spot Reproducibility on the Standard***
Quartz	UWQ-1	δ18O	12.3	V-SMOW	Kelly et al. (2007)	0.6 - 0.9 ‰
Pyrite	Balmat	δ34S	15.1	V-CDT	Crowe and Vaughn (1996)	0.3 - 0.6 ‰
Pyrite	Balmat	δ33S	7.9	V-CDT	Mojzsis et al. (2003)	0.7 - 0.9 ‰
Pyrrhotite	Anderson	δ34S	1.4	V-CDT	Crowe and Vaughn (1996)	0.3 - 0.5 ‰
Pyrrhotite	Anderson	δ33S	0.7	V-CDT	Mojzsis et al. (2003)	0.7 - 0.9 ‰
Chalcopyrite	Trout Lake	δ34S	0.3	V-CDT	Crowe and Vaughn (1996)	0.4 ‰
Chalcopyrite	Trout Lake	δ33S	0.0	V-CDT	Mojzsis et al. (2003)	0.7 ‰
Arsenopyrite	Kontak (Beaver Dam)	δ34S	10.0	V-CDT	This study	0.5 ‰

*Quantity of samples required multiple days of SIMS time, thus a range of spot-to-spot reproducibility values are presented

Table 2.3. A comparison of bulk versus in-situ $\delta^{18}O$ quartz values for relevant deposits.

Deposit	Bulk δ18O quartz	In-situ δ18O quartz	References
Hollinger-McIntyre	11.3 to 15.0	11.5 to 14.5	Wood, 1991; Goldfarb et al., 2005; this study
Campbell Red Lake	13.1 to 15.7	19.6 to 21.2	Goldfarb et al., 2005; this study
Kirkland Lake	11.3 to 14.0	9.9 to 15.6	Kerrich and Watson (1984); Goldfarb et al., 2005; this study
Dome	13.7 to 15.6	11.1 to 13.2	Kerrich and Fryer, 1979; Goldfarb et al., 2005; this study
Kerr Addison	12.7 to 18.5	11.9 to 13.8	Kishida and Kerrich (1987); Goldfarb et al., 2005; this study
Sigma	9.7 to 12.6	9.4 to 11.5	Beaudoin and Pitre, 2005; Olivo et al., 2006; Beaudoin and Chiaradia, 2016; this study
Siscoe	11.6 to 12.0	10.9 to 12.4	Beaudoin and Pitre, 2005; Beaudoin and Chiaradia, 2016; this study
Powell	7.7 to 10.9	8.6 to 10.2	Carrier et al., 2000; this study

Table 2.4. A comparison of relevant intrusion-hosted deposits and their characteristics.

Deposit	Dominant Au-bearing host rock	Oxygen Isotopes (Quartz)	Sulfur Isotopes (pyrite-chalcopyrite)	Au host phases	Age of Intrusion (Ma)	Closest geochemical affinity	References
Jerome	syenite-monzonite	8.9 to 16.5‰	-9.3 to -24.9‰	arsenian pyrite, native gold	2684±3	Sanukitoid	Laurent et al., 2014; MacDonald et al., 2017; this study
Rundle	monzonite; albitite	9.9 to 14.9‰	-7.2 to -10.0‰	pyrite, native gold	2688±2, 2680 ±5	Sanukitoid	Laurent et al., 2014; MacDonald et al., 2017; Ontario Geological Survey, 2019; this study
Kirkland Lake	syenite-monzonite	9.9 to 14.2.‰	-9.1 to -14.4‰*	pyrite, Au-Ag tellurides, native gold	2680-2672	Sanukitoid	Kerrich and Watson, 1984; Cameron and Hattori, 1987; Goldfarb et al, 2005; Ispolatov, 2008; Laurent et al., 2014; this study
Namex	monzogranite	8.8 to 15.9‰	-2.1 to -8.5‰	pyrite, Au-Ag tellurides	2680±4	Biotite-, Two-mica Granite	MacDonald et al., 2017; this study
Preston (incl. Preston East	tronjhemite-tonalite-granodiorite	11.6 to 15.1‰	0.8 to 3.1‰	pyrite, native gold	ca. 2690	TTG	Corfu et al., 1989; Hastie et al., 2020; this study
Paymaster	tronjhemite-tonalite-granodiorite	13.2 to 15.7‰	1.8 to 3.2‰	pyrite, chaclopyrite, native gold	2690±4	TTG	Corfu et al., 1989; Hastie et al., 2020; this study
Dome	mafic volcanic; tronjhemite-tonalite-granodiorite	11.1 to 13.2‰	0.0 to 2.8‰	pyrite, pyrrhotite, native gold	2688±2	TTG	Gray and Hucthinson 2001; Goldfarb et al., 2005; Hastie et al., 2020; this study

*bulk method from Cameron and Hattori, 1987

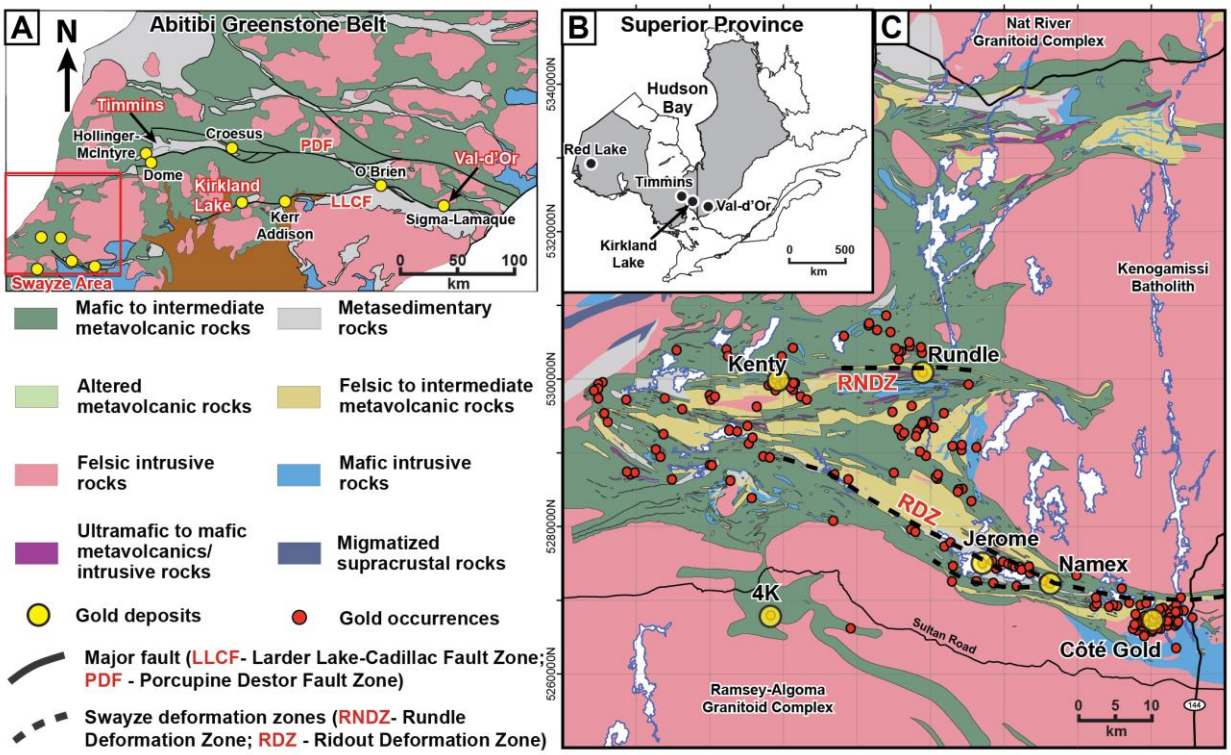

Figure 2.1. Geologic map of the Swayze area (Swayze greenstone belt; SGB), southwest Abitibi greenstone belt (AGB), Superior Province, Canada. A) Simplified geologic map of the AGB (modified after Dubé and Gosselin, 2007) highlighting the SGB (red outline) and some of the significant Au deposits and camps. B) Location of the gold camps studied within the Superior Province. C) Simplified geologic map of the SGB with Au deposits studied shown by yellow circles and gold occurrences by red circles. Location information provided as Universal Transverse Mercator (UTM) co-ordinates using North American Datum 1983 (NAD83) in Zone 17 (modified after Ontario Geological Survey, 2011; 2019; MacDonald et al., 2017 and Hastie et al., 2020a).

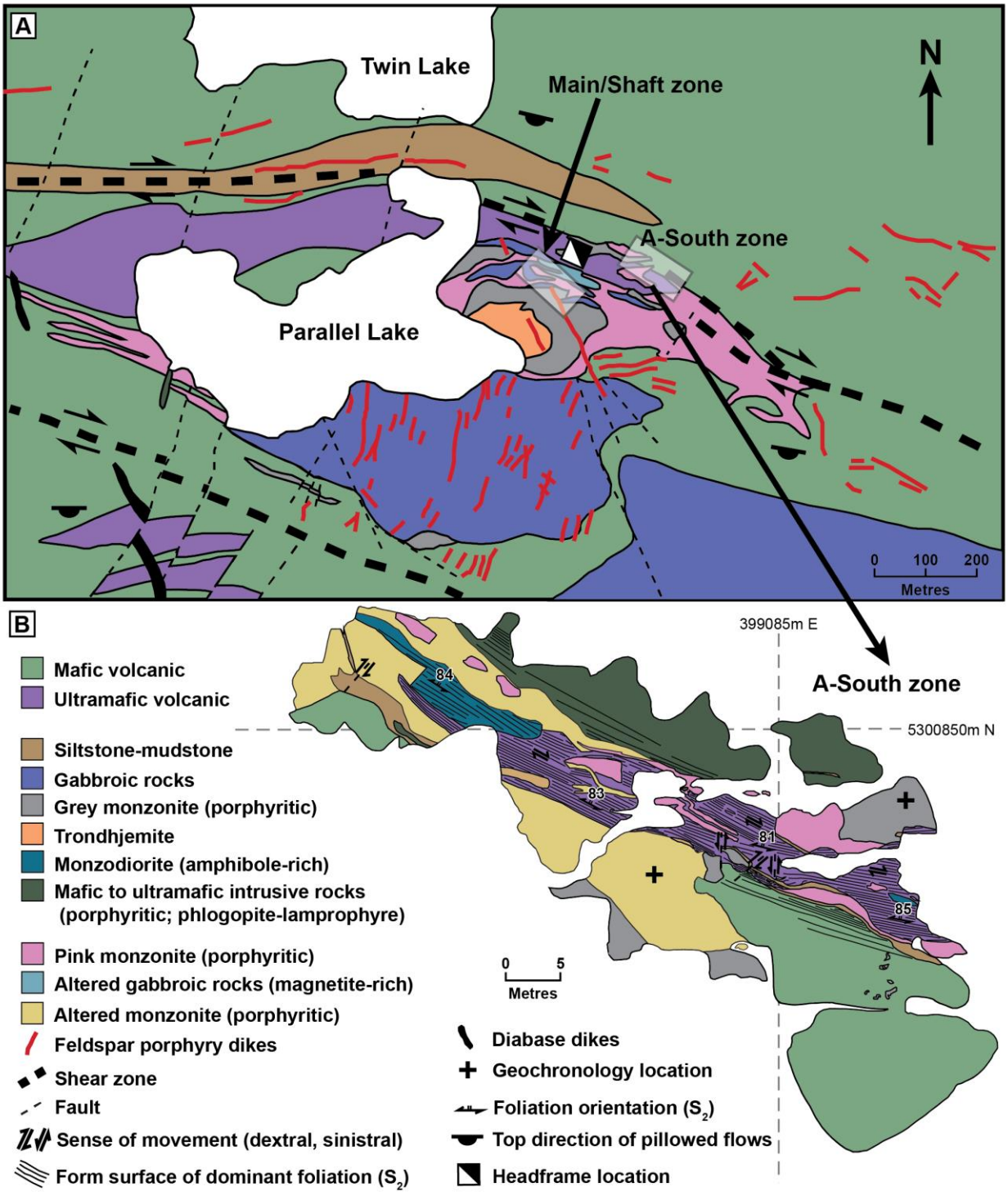

Figure 2.2. Geologic map of the Rundle deposit and associated outcrops. A) Deposit-scale geologic map of the deposit area highlighting important outcrop locations (modified after Love

and Roberts, 1991). B) Geologic outcrop map of the A-South zone (modified after Hastie et al., 2015).

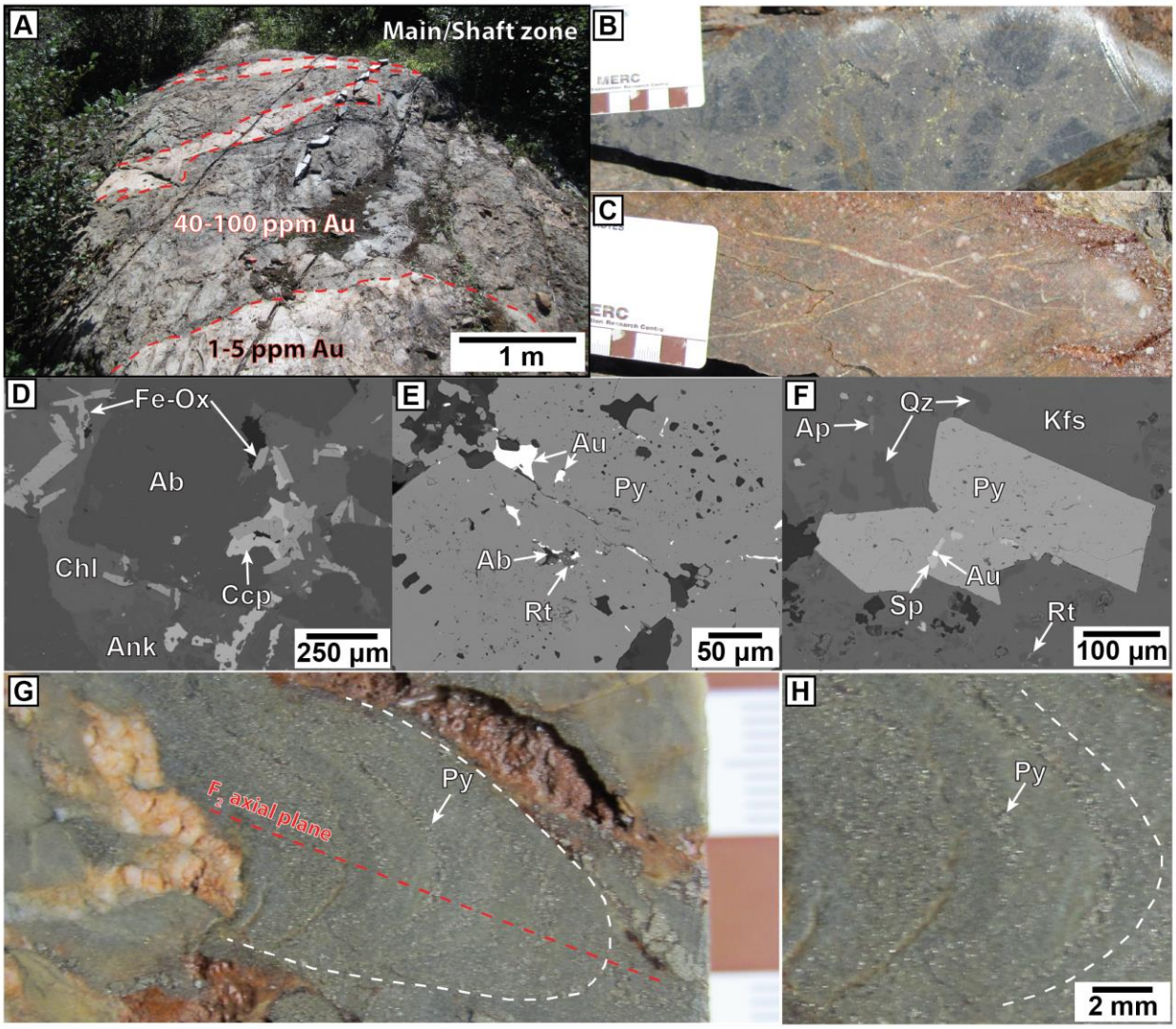

Figure 2.3. Outcrop, channel sample and back-scattered electron images of structural features and mineralized host rocks from the Rundle deposit. A) Outcrop photograph of Au-bearing host rocks from the Main/Shaft zone (gabbro, 40-100 ppm Au; pink monzonite, 1-5 ppm Au). B) Channel sample of Au-bearing gabbro showing fracture-controlled Au-pyrite mineralization (modified from Hastie et al., 2015). C) Channel sample of Au-bearing pink monzonite showing fracture-controlled Au-pyrite mineralization. D) Back-scattered electron image of gabbroic rock. E) Back-scattered electron image of pyrite-associated Au mineralization within gabbro. F) Representative back-scattered electron image of altered monzonite from A-South zone showing

pyrite-associated Au mineralization. G) Fracture-controlled Au-pyrite mineralization folded around F_2 fold hinge at the A-South zone. H) Zoomed image of folded Au-pyrite mineralization from G. Dashed white line traces fold. Scale card in photos is 9 cm long. Abbreviations: Ab, albite; Ank, ankerite; Ap, apatite; Au, gold; Ccp, chalcopyrite; Chl, chlorite; Fe, iron; Kfs, potassium feldspar; Ox, oxide; Py, pyrite; Qz, quartz; Rt, rutile; Sp, sphalerite.

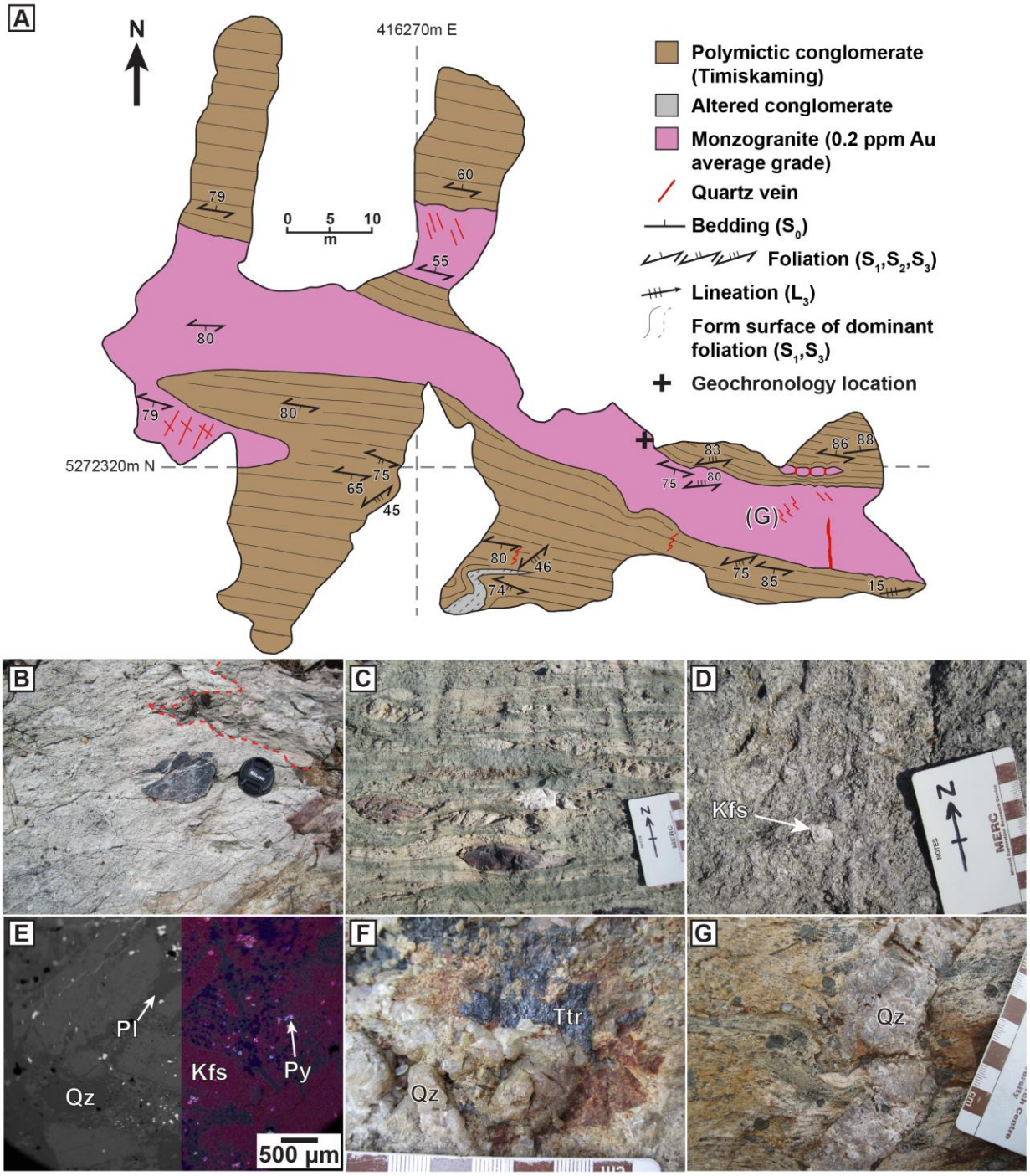

Figure 2.4. Geologic map of the Namex deposit and photographs of representative host rocks (modified from Hastie et al., 2016). A) Geologic outcrop map of the Namex East exposure. B) Monzogranite containing a conglomerate clast and showing an intrusive contact (red dashed line) with the polymictic conglomerate. C) Deformed polymictic conglomerate. D) Monzogranite

intrusion. E) Back-scattered electron image and a layered SEM-EDS elemental map of the monzogranite in split view. Different colors indicating major mineral phases are as follows: potassium feldspar = pink, quartz = blue, plagioclase = grey. F) Au-bearing monzogranite with tetrahedrite associated with a quartz extension vein (V_4). G) Sinistral quartz extension vein (V_3) in conglomerate that shows overprinting dextral fringe structures. Scale card in photos is 9 cm long. Lens cap in photo D is 5 cm in diameter. Abbreviations: Kfs, potassium feldspar; Pl, plagioclase; Py, pyrite; Qz, quartz; Ttr, tetrahedrite.

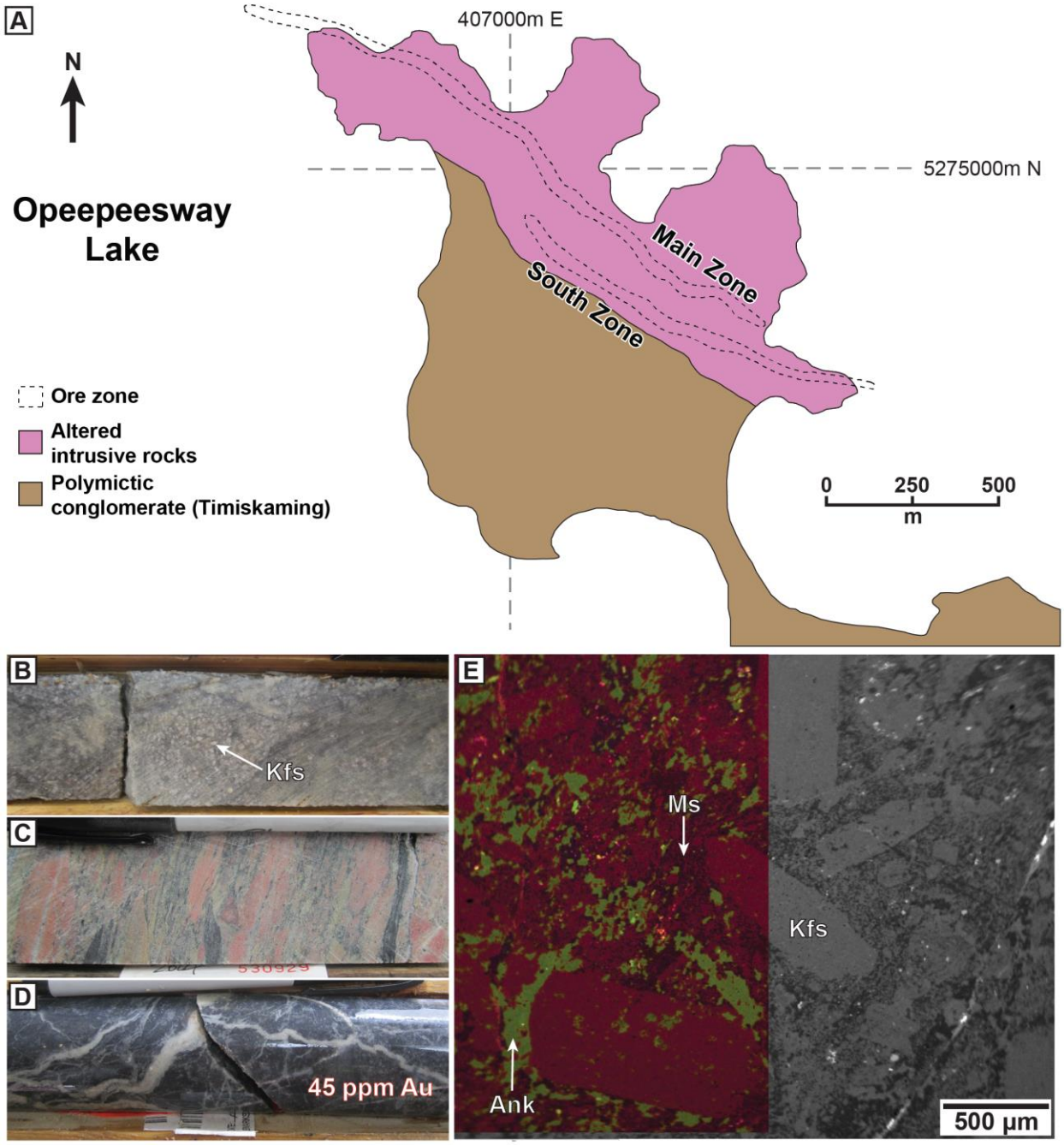

Figure 2.5. Geologic map of the Jerome deposit and photographs of representative host rocks (modified after Hastie, 2020a). A) Simplified map of the Jerome peninsula outlining the surface projection of known ore zones. B) Core sample of least altered monzonite with significant ankerite and sericite alteration. C) Core sample of deformed polymictic conglomerate containing clasts of felsic and mafic rocks and iron formation in a sericite altered matrix. D) Core sample of

heavily altered and mineralized monzonite showing stockwork quartz-ankerite ± microcline veins. E) Layered SEM-EDS elemental map and a back-scattered electron image of the least altered monzonite in split view. Different colors indicating major mineral phases are as follows: potassium feldspar = red, ankerite = green, muscovite = brown. Length of marker in photos is 14 cm. Abbreviations: Ank, ankerite; Kfs, potassium feldspar; Ms, muscovite.

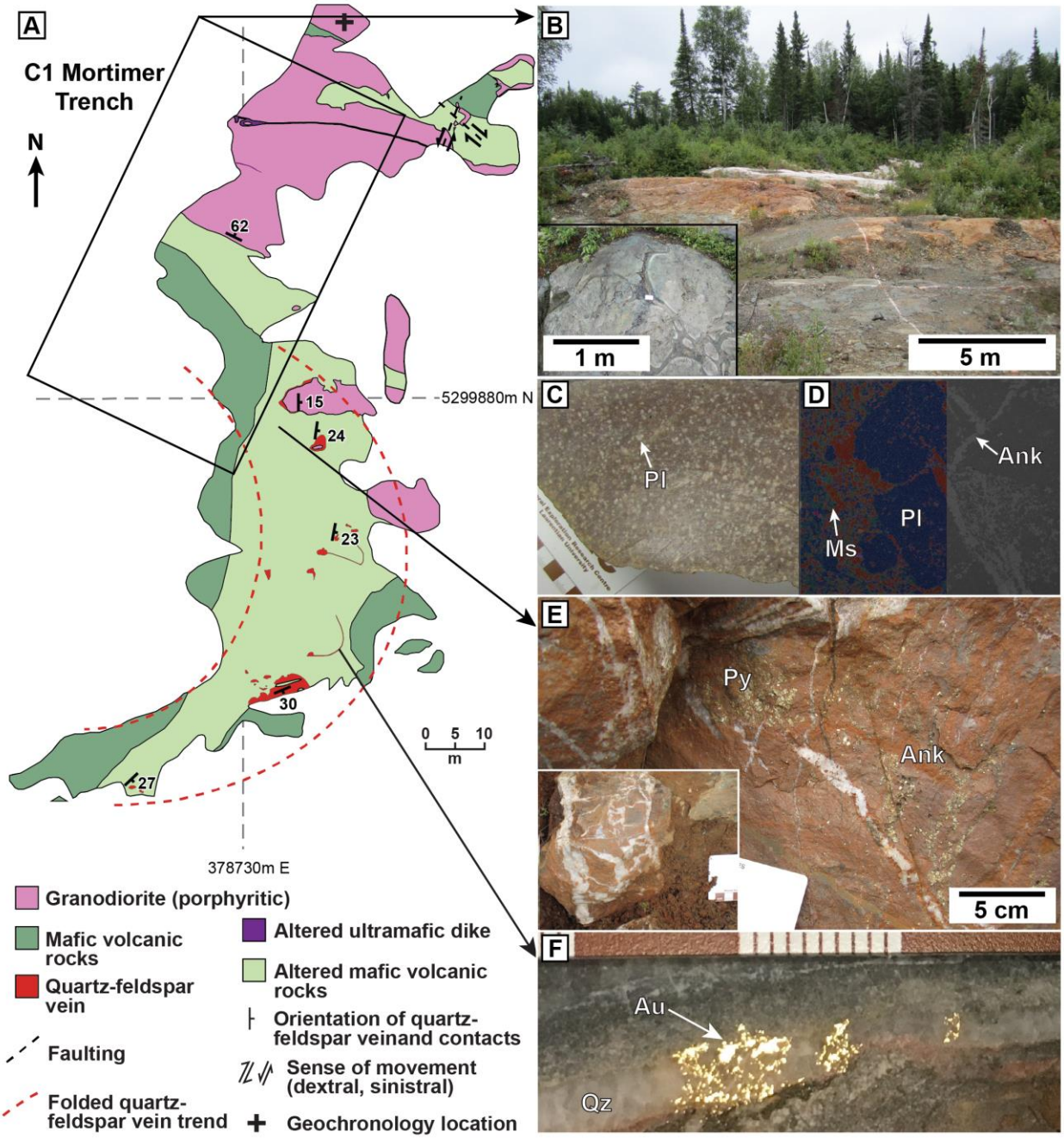

Figure 2.6. Geologic map of the Kenty deposit and photographs of representative host rocks (modified after Hastie, 2020a). A) Map of the C1 Mortimer trench at the Kenty deposit. B) Altered pillowed basalt at contact with porphyritic granodiorite. Lower left inset shows close-up of pillowed basalt. C) Channel sample of granodiorite. D) Layered SEM-EDS elemental map and a back-scattered electron image of the least altered granodiorite in split view. Different colors indicating major mineral phases are: plagioclase = blue, ankerite = red, muscovite = green. E)

Ankerite-altered pillow basalt and associated quartz-feldspar-ankerite vein with pyrite mineralization. Lower right inset shows subvertical laminated quartz-carbonate vein with entrained wallrock fragments. F) Rock slab photograph of a quartz-feldspar vein with gold lining fractures from the hinge are of the open fold in A. Scale card in photos is 9 cm long. Abbreviations: Ank, ankerite; Au, gold; Ms, muscovite; Pl, plagioclase; Py, pyrite; Qz, quartz.

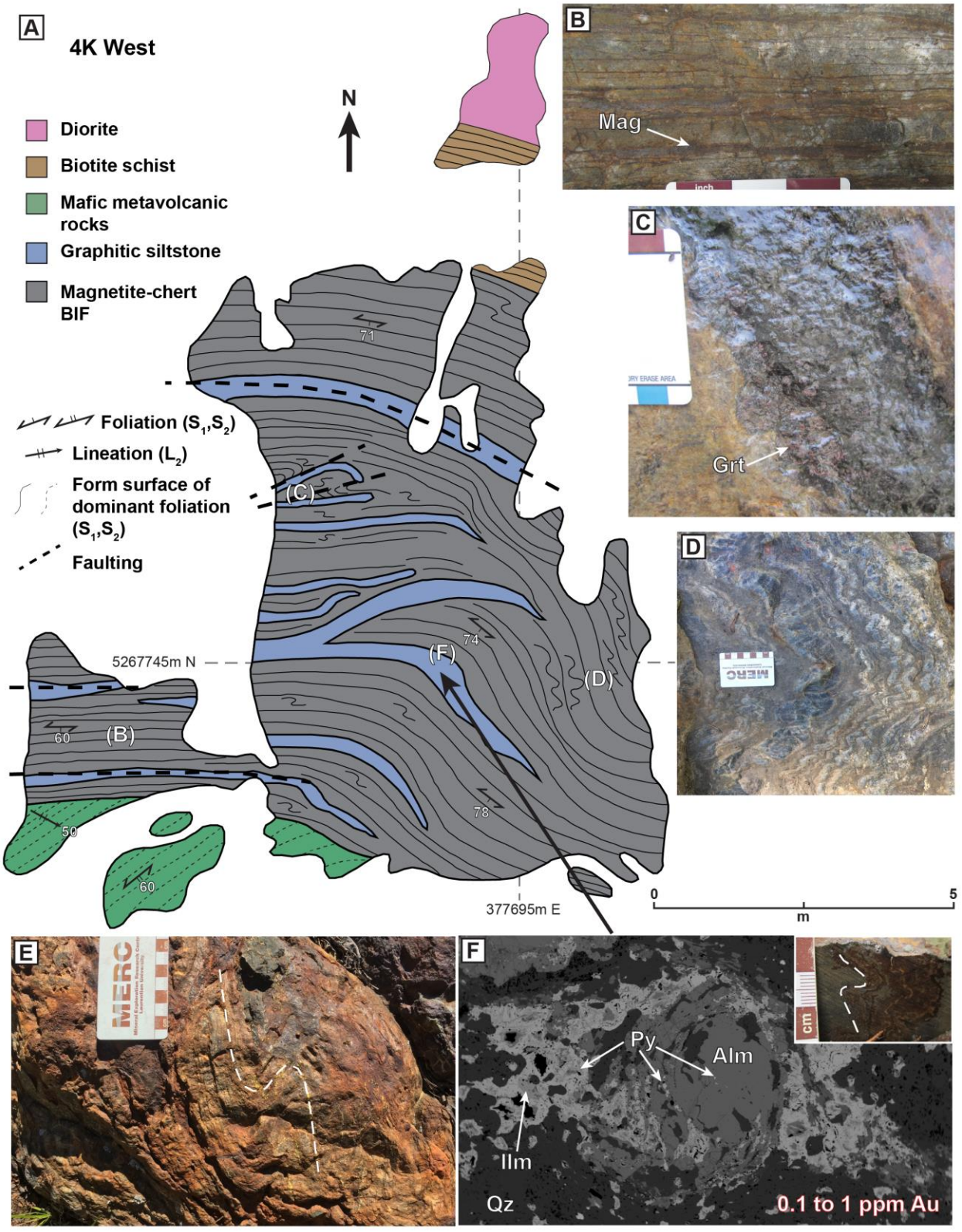
A
4K West
N
Diorite
Biotite schist
Mafic metavolcanic rocks
Graphitic siltstone
Magnetite-chert BIF
Foliation (S_1,S_2)
Lineation (L_2)
Form surface of dominant foliation (S_1,S_2)
Faulting
5267745m N
377695m E
(B)
(C)
(D)
(F)
71
74
78
60
50
60
0
5
m
B
Mag
C
Grt
D
E
F
Py
Alm
Ilm
Qz
0.1 to 1 ppm Au

Figure 2.7. Geologic map of the 4K prospect and photos of representative host rocks. A) Geologic outcrop map of the 4K West stripping. B) Magnetite-chert BIF (modified from Hastie, 2014). C) Graphitic siltstone with abundant garnet (modified from Hastie, 2014). D) Parasitic M-folds (F_2) in magnetite-chert BIF. E) Folded (F_2) magnetite-chert BIF with sulfide (pyrite-pyrrhotite-arsenopyrite) mineralization. Dashed white line traces fold. F) Back-scattered electron image of garnet (almandine) porphyroblast with pyrite as inclusions and incorporated as rings within garnet. Upper right inset shows sample location within mineralized BIF; dashed white line trace fold. Scale card in photos is 9 cm long. Abbreviations: Alm, almandine; Grt, garnet; Ilm, ilmenite; Mag, magnetite; Py, pyrite; Qz, quartz.

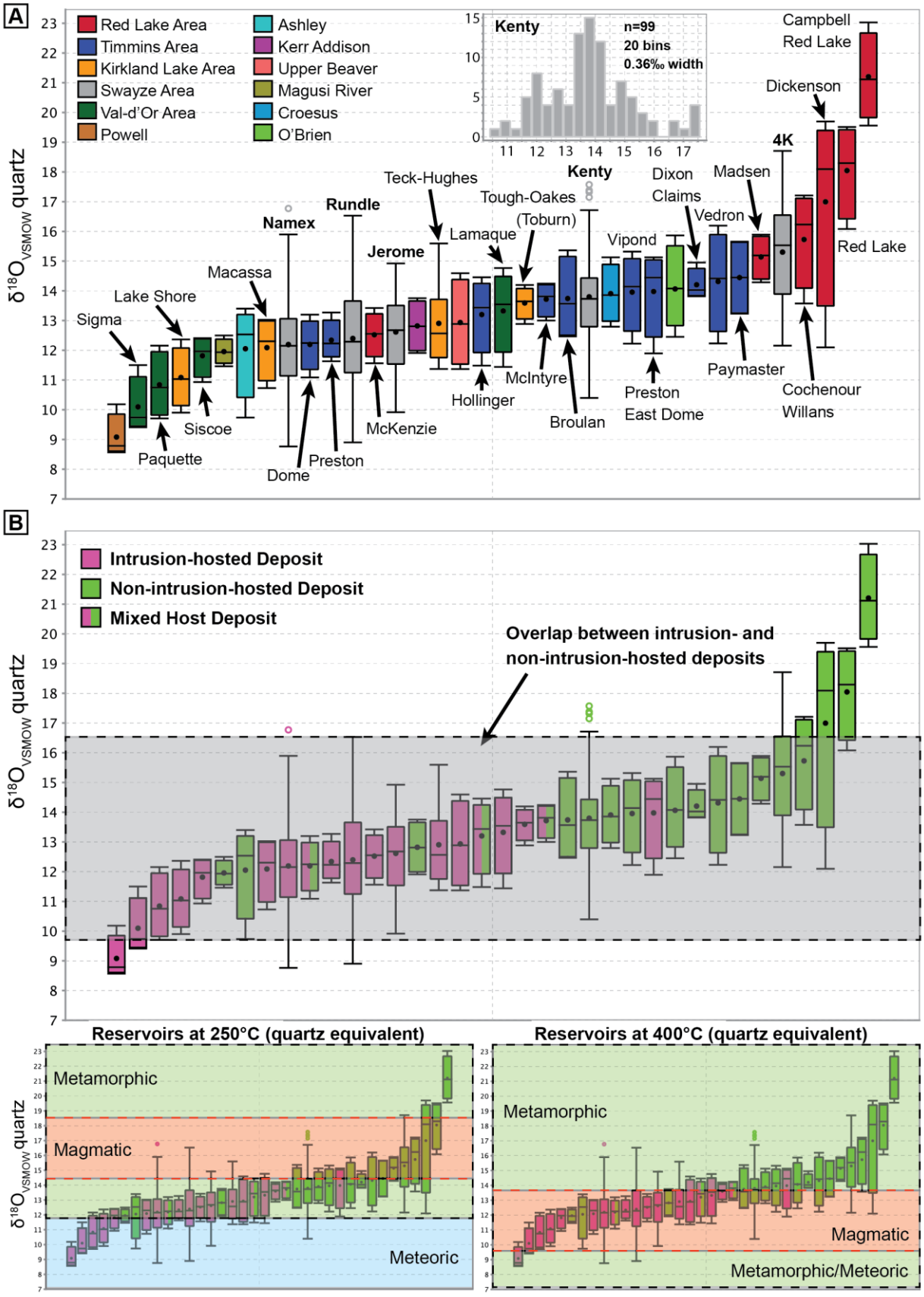
A
Red Lake Area
Timmins Area
Kirkland Lake Area
Swayze Area
Val-d'Or Area
Powell
Ashley
Kerr Addison
Upper Beaver
Magusi River
Croesus
O'Brien
Kenty
n=99
20 bins
0.36‰ width
δ18OVSMOW quartz
Sigma
Lake Shore
Paquette
Siscoe
Macassa
Dome
Namex
Preston
Rundle
McKenzie
Jerome
Teck-Hughes
Lamaque
Hollinger
Tough-Oakes
(Toburn)
McIntyre
Broulan
Kenty
Vipond
Dixon
Claims
Preston
East Dome
Vedron
Madsen
Paymaster
4K
Dickenson
Campbell
Red Lake
Red Lake
Cochenour
Willans
B
Intrusion-hosted Deposit
Non-intrusion-hosted Deposit
Mixed Host Deposit
Overlap between intrusion- and
non-intrusion-hosted deposits
δ18OVSMOW quartz
Reservoirs at 250°C (quartz equivalent)
Reservoirs at 400°C (quartz equivalent)
Metamorphic
Magmatic
Meteoric
Metamorphic
Magmatic
Metamorphic/Meteoric

Figure 2.8. Box and whisker plot of quartz $\delta^{18}O_{VSMOW}$ values for Au deposits within the SGB and Superior Craton. The central box represents the middle 50% of the data (i.e., between the lower and upper quartiles) with the mean (dot) and median (horizontal line) shown. Whiskers represent extreme values that are not outliers, with outliers shown as circles and triangles. Note that the data is sorted based on mean values from left to right. A) Data with deposit names and legend in the upper right corner. Deposits from the Kirkland Lake (orange), Timmins (blue), Red Lake (red) and Val-d'Or camps (green) have been grouped by color for comparison. Inset histogram for data from the Kenty deposit is shown to illustrate normal distribution when the mean and median plot close to each other. B) Same data with reference fluid reservoirs from (Sheppard, 1986) recalculated to quartz equivalent $\delta^{18}O$ values for 250°C and 400°C using fractionation factors of Matsuhisa et al. (1979).

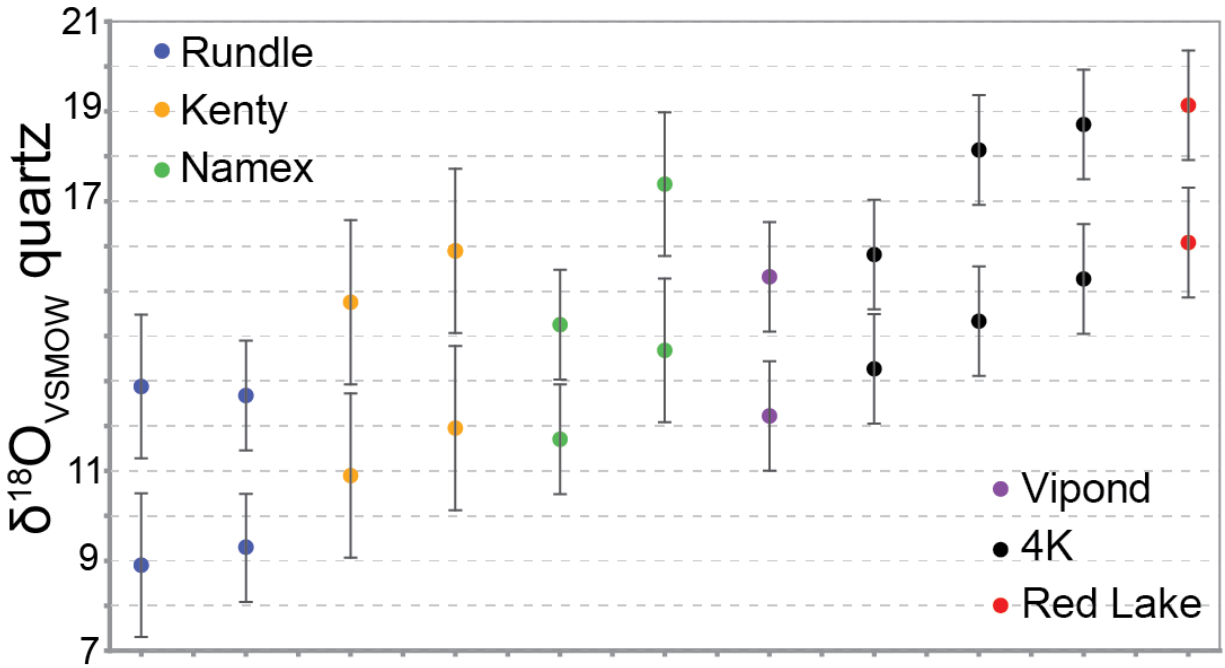

Figure 2.9. Plot of quartz $\delta^{18}O_{VSMOW}$ values for the same quartz grains in Figure 2.8 that have separation greater than 2σ precision from repeat analyses, as indicated by the black error bars.

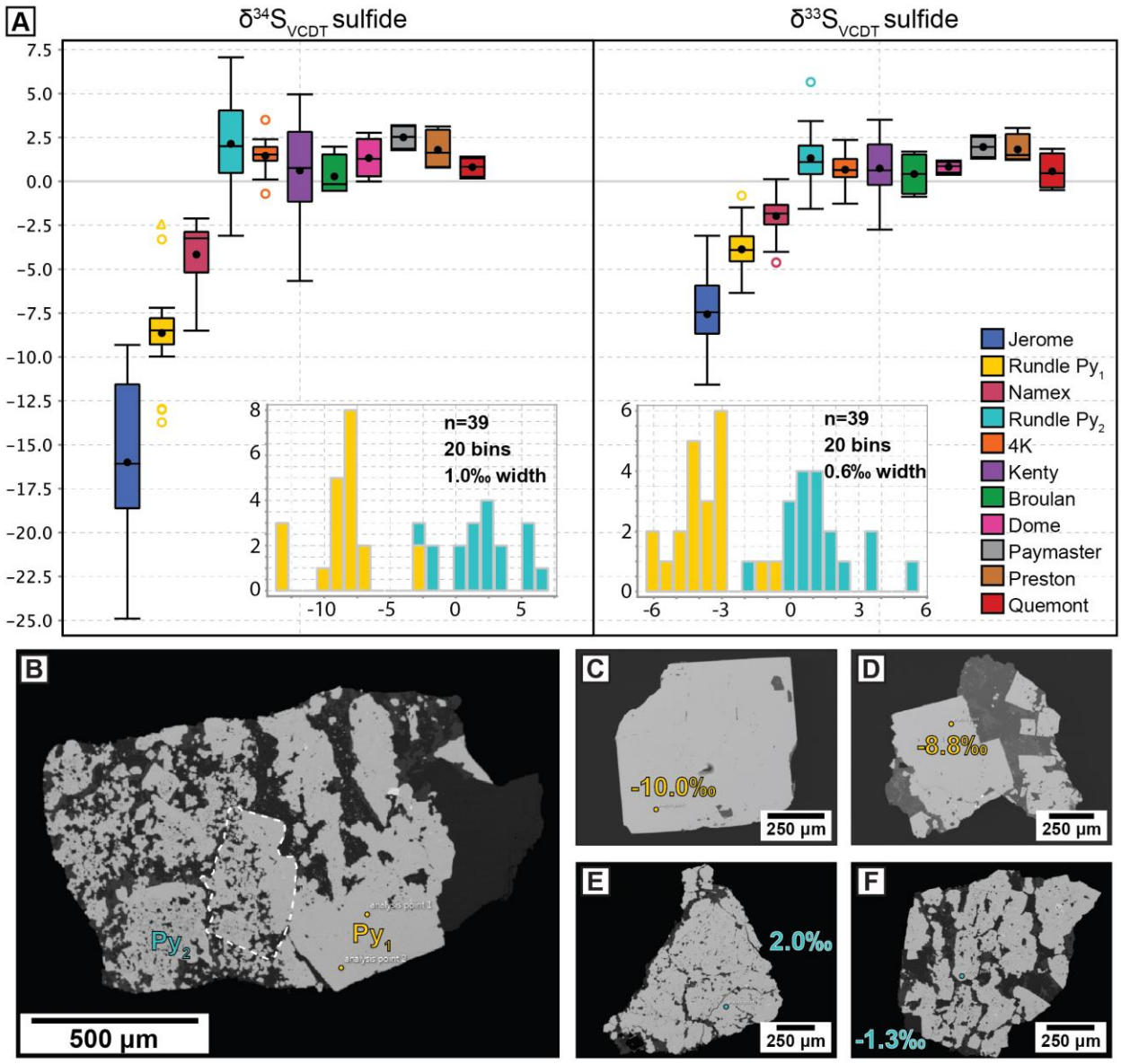

Figure 2.10. Plot of $\delta^{34}S_{VCDT}$ and $\delta^{33}S_{VCDT}$ sulfide (pyrite, pyrrhotite, arsenopyrite, chalcopyrite) data from Au deposits within the SGB and AGB and back-scattered electron (BSE) images of different pyrite generations at the Rundle deposit. Sulfides analyzed for each deposit are as follows: Kenty, Jerome, Rundle, Namex, Broulan, Dome, Preston – pyrite; 4K – pyrite, pyrrhotite, arsenopyrite; Quemont – pyrite, chalcopyrite; Paymaster – chalcopyrite. A) Box and whisker plots for the $\delta^{34}S$ and $\delta^{33}S$ data. The central box represents the middle 50% of the data (i.e., between the lower and upper quartiles) with the mean (dot) and median (horizontal line) shown. Whiskers represent extreme values that are not outliers. Outliers are shown as circles and

triangles. Data has been sorted by mean values from left to right for both $\delta^{34}S$ and $\delta^{33}S$. Histogram insets are shown for two generations of pyrite from the Rundle deposit in the bottom to illustrate bimodal distribution of the results. Yellow and teal colors correlate throughout figure for Rundle Py_1 and Py_2. B) BSE image of early pyrite (Py_1) and replacement pyrite (Py_2) at the Rundle deposit. Dashed white line encloses a partially replaced grain. C and D) Images of typical Py_1 grains, their textures and $\delta^{34}S$ values in yellow. E and F) Images of typical Py_2 grains, their textures and $\delta^{34}S$ values in teal.

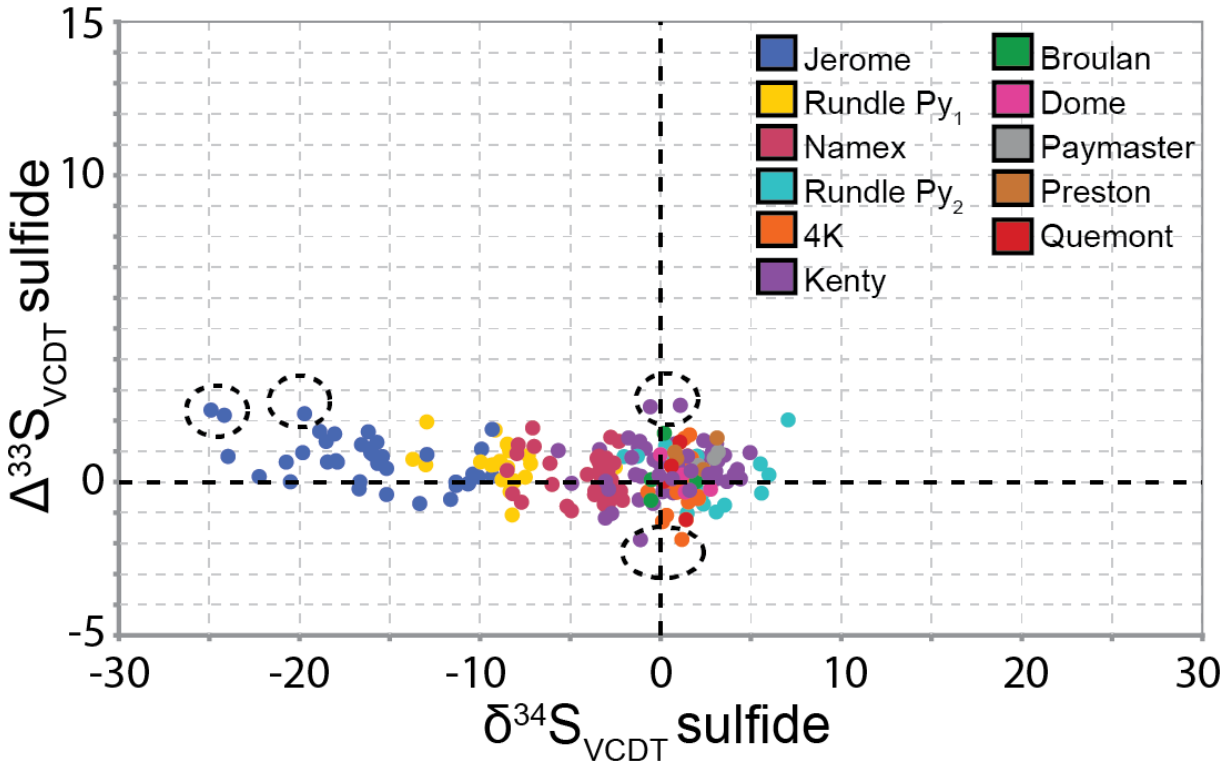

Figure 2.11. $\delta^{34}S_{VCDT}$ sulfide versus $\Delta^{33}S_{VCDT}$ sulfide data from Au deposits within the SGB and AGB. Sulfides analyzed for each deposit are as follows: Kenty, Jerome, Rundle, Namex, Broulan, Dome, Preston – pyrite; 4K – pyrite, pyrrhotite, arsenopyrite; Quemont – pyrite, chalcopyrite; Paymaster – chalcopyrite. Black dashed circles indicate outlier data discussed in the text.

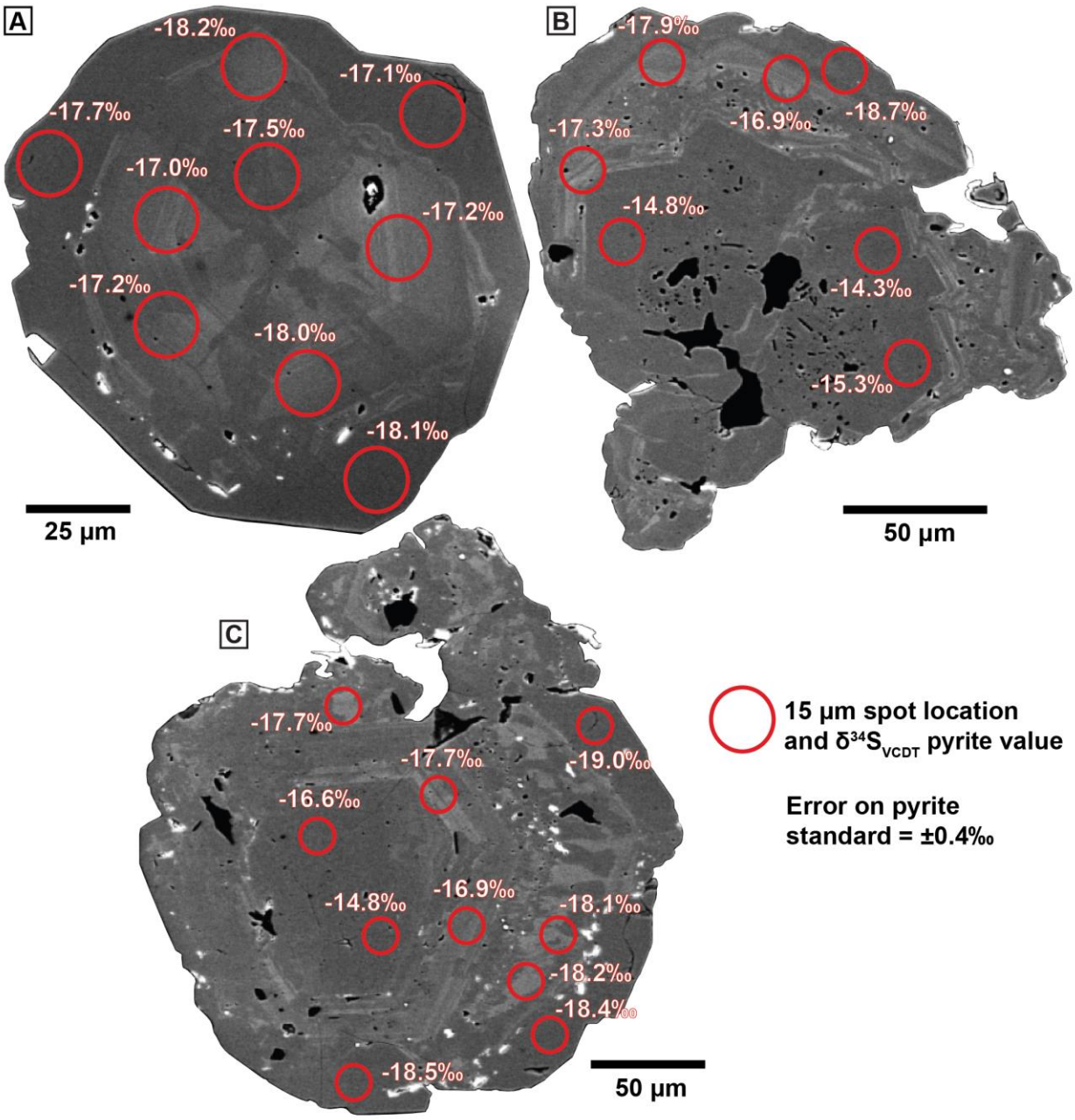

Figure 2.12. High contrast back-scattered electron images of zoned arsenian pyrite from the Jerome deposit with $\delta^{34}S_{VCDT}$ values and locations shown in red. Bright zones are As- and Au-rich while dark zones are As- and Au-poor (Hastie et al., 2020a). A) Sector zoned arsenian pyrite. B and C) Zoned arsenian pyrite with core to rim variation of ≈ 4‰ for $\delta^{34}S_{VCDT}$ values (e.g., from -14.8 to -19.0‰).

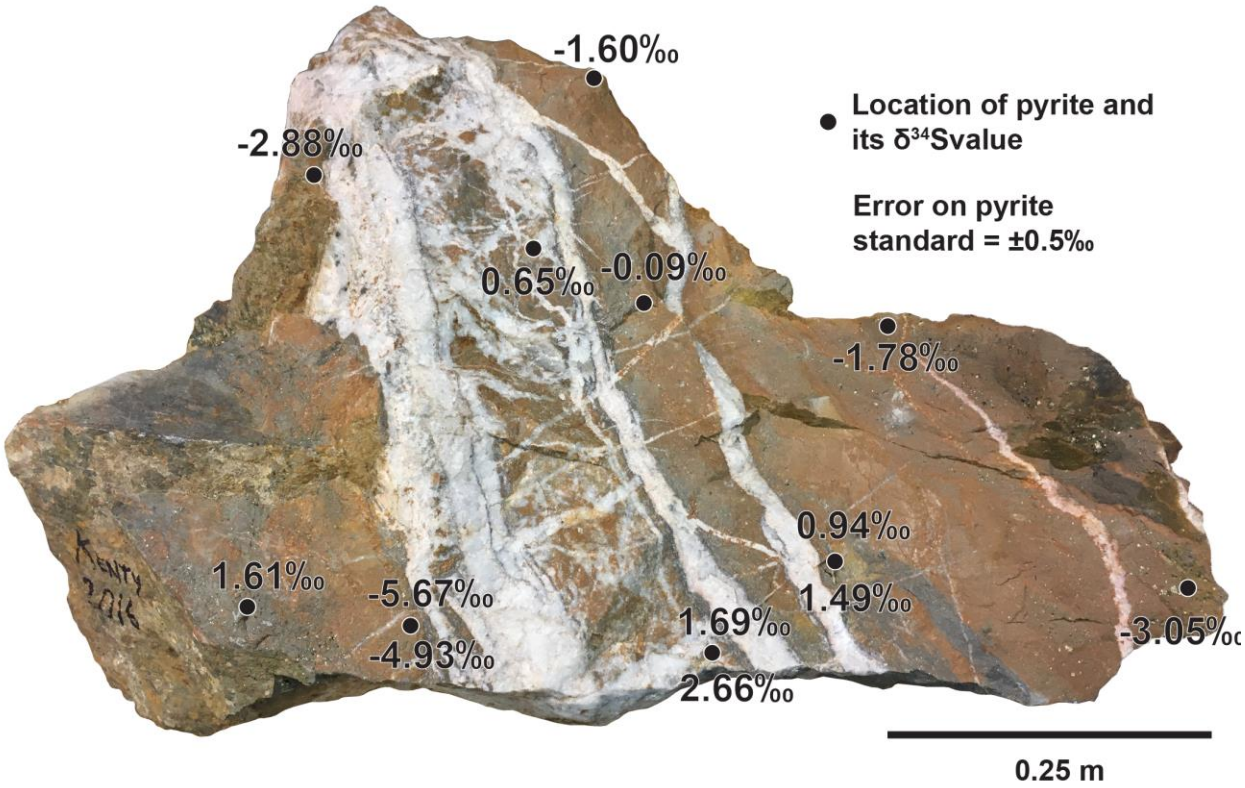

Figure 2.13. Mineralized outcrop sample from the Kenty deposit showing the locations of analysed pyrite grains and their $\delta^{34}S_{VCDT}$ values.

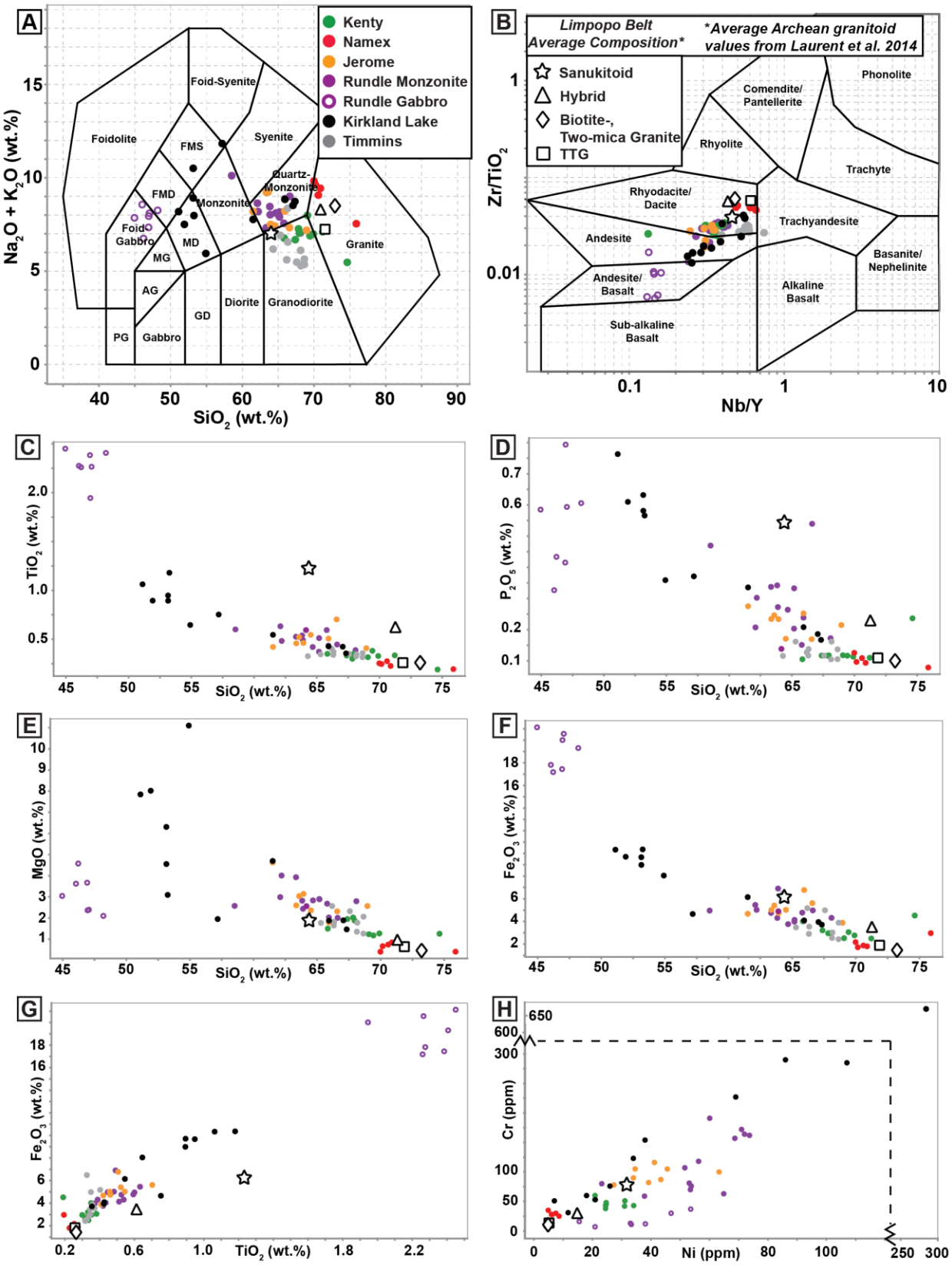
A
Kenty
Namex
Jerome
Rundle Monzonite
Rundle Gabbro
Kirkland Lake
Timmins
Foid-Syenite
Foidolite
FMS
Syenite
Quartz-Monzonite
FMD
Monzonite
Foid Gabbro
MD
MG
AG
GD
Diorite
Granodiorite
Granite
PG
Gabbro
Na2O + K2O (wt.%)
SiO2 (wt.%)
B
Limpopo Belt Average Composition*
*Average Archean granitoid values from Laurent et al. 2014
Sanukitoid
Hybrid
Biotite-, Two-mica Granite
TTG
Phonolite
Comendite/ Pantellerite
Rhyolite
Trachyte
Rhyodacite/ Dacite
Trachyandesite
Andesite
Basanite/ Nephelinite
Andesite/ Basalt
Alkaline Basalt
Sub-alkaline Basalt
Zr/TiO2
Nb/Y
C
TiO2 (wt.%)
SiO2 (wt.%)
D
P2O5 (wt.%)
SiO2 (wt.%)
E
MgO (wt.%)
SiO2 (wt.%)
F
Fe2O3 (wt.%)
SiO2 (wt.%)
G
Fe2O3 (wt.%)
TiO2 (wt.%)
H
Cr (ppm)
Ni (ppm)

Figure 2.14. Major- and trace-element geochemical data for Au-bearing intrusive rocks from the SGB Au deposits compared to referenced data for intrusions from Timmins and Kirkland Lake (Ispolatov et al., 2008; MacDonald and Piercey, 2019). In addition are shown average compositions for four groups of late-Archean granites in the Limpopo belt (TTG = square; Biotite-, two-mica granite = diamond; Hybrid = triangle; Sanukitoid = star) as described by Laurent et al. (2014). Major oxide data has been normalized to volatile-free. A) Total alkali silica diagram (SiO_2 versus Na_2O+K_2O) with plutonic subdivisions after Middlemost (1994). Abbreviations: FMD, Foid-Monzodiorite; FMS, Foid-Monzosyenite; GD, Gabbroic Diorite; AG, Alkalic Gabbro; MD, Monzodiorite; MG, Monzogabbro; PG, Peridotgabbro. B) Plot of Nb/Y versus Zr/TiO_2 with volcanic subdivisions after Winchester and Floyd (1977). C) SiO_2 versus TiO_2. D) SiO_2 versus P_2O_5. E) SiO_2 versus MgO. F) SiO_2 versus $Fe_2O_{3\ total}$. G) TiO_2 versus $Fe_2O_{3\ total}$. H) Ni versus Cr.

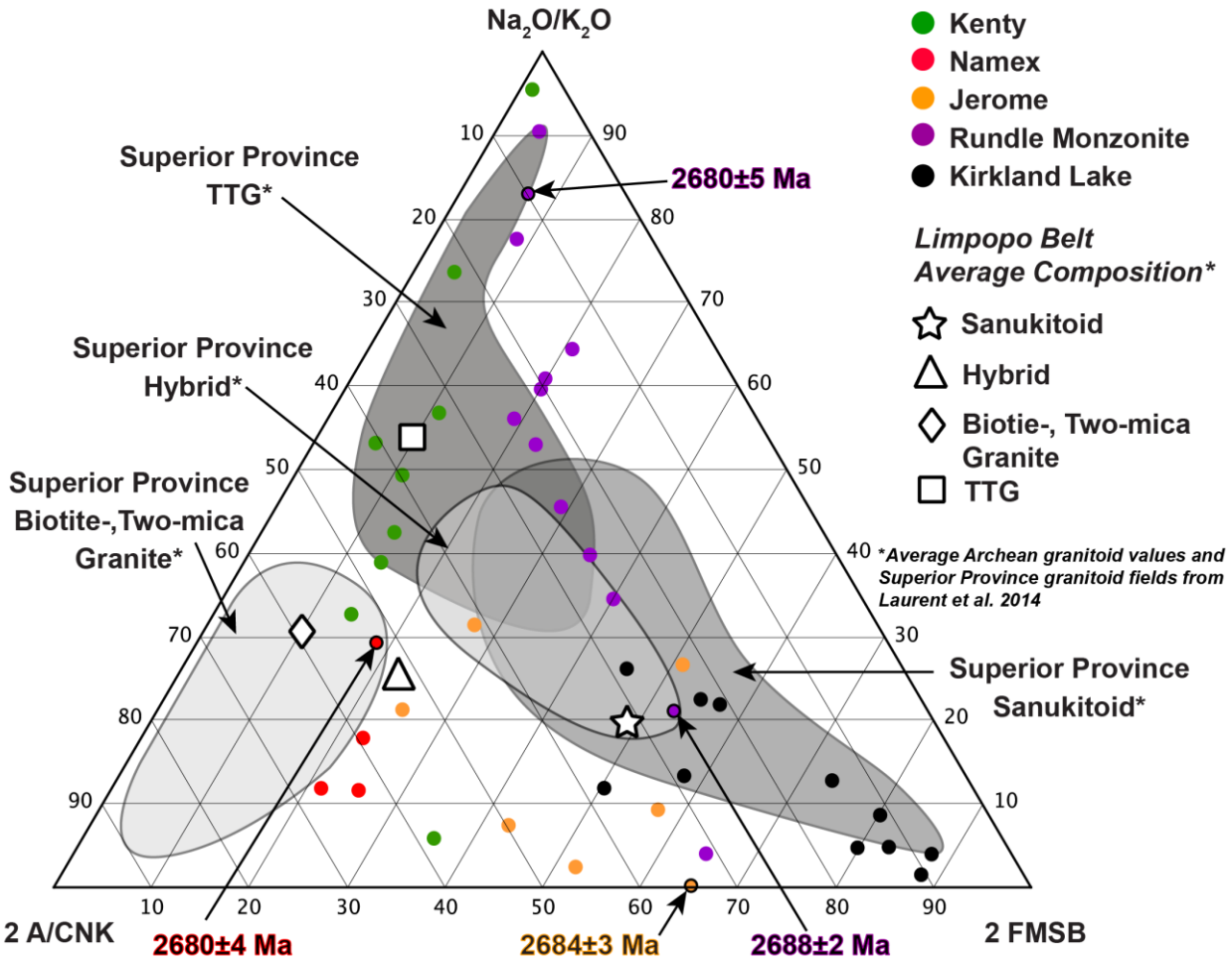

Figure 2.15. Ternary classification diagram for late-Archean granitoids (after Laurent et al., 2014) with data from the SGB Au deposits compared to referenced data from the Kirkland Lake area of the AGB (Ispolatov et al., 2008). Note that ages for select intrusive rocks are shown for reference (MacDonald et al., 2017; Ontario Geological Survey, 2019). Major oxide data has been normalized to volatile-free. The diagram also shows the average compositions for the four groups of late-Archean granites from the Limpopo belt (TTG = square; Biotite-, two-mica granite = diamond; Hybrid = triangle; Sanukitoid = star) and shaded areas for late-Archean granitoids from the Superior Province (Laurent et al. 2014).

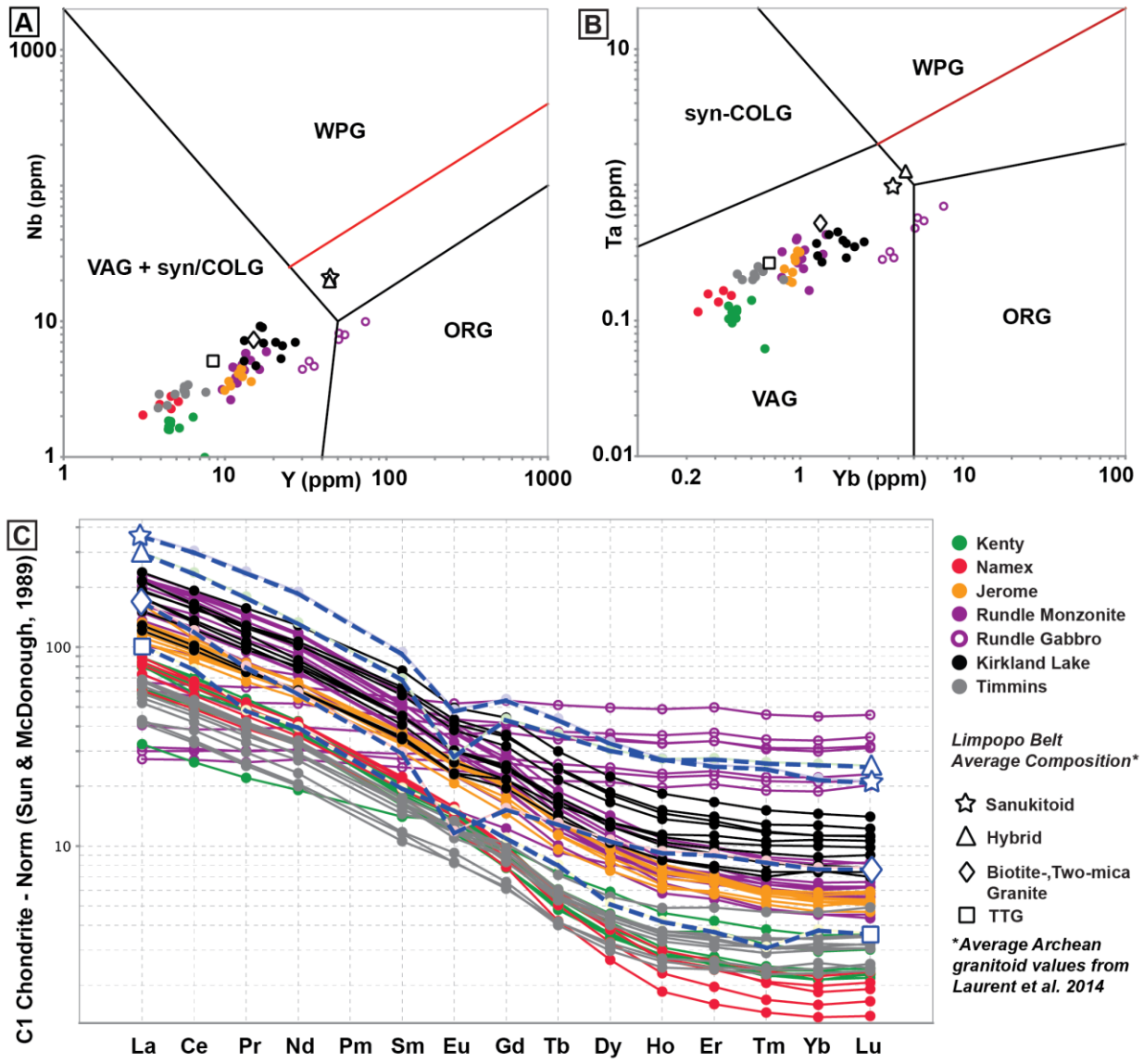

Figure 2.16. Trace-element geochemical data for Au-bearing intrusive rocks from the SGB Au deposits compared to referenced data from Timmins and Kirkland Lake areas of the AGB (Ispolatov et al., 2008; MacDonald and Piercey, 2019). The diagram also shows the average compositions for the four groups of late-Archean granites the Limpopo belt (TTG = square; Biotite-, two-mica granite = diamond; Hybrid = triangle; Sanukitoid = star) described by Laurent et al. (2014). A and B) Plots of Yb versus Ta and Y versus Nb with granite subdivisions after Pearce et al. (1984). Abbreviations: VAG, volcanic arc granite; syn-COLG, syn-collisional granite; WPG, within plate granite; ORG, ocean ridge granite. Red line is the boundary for ORG from anomalous ridges. E) Chondrite-normalized REE plot after Sun and McDonough (1989).

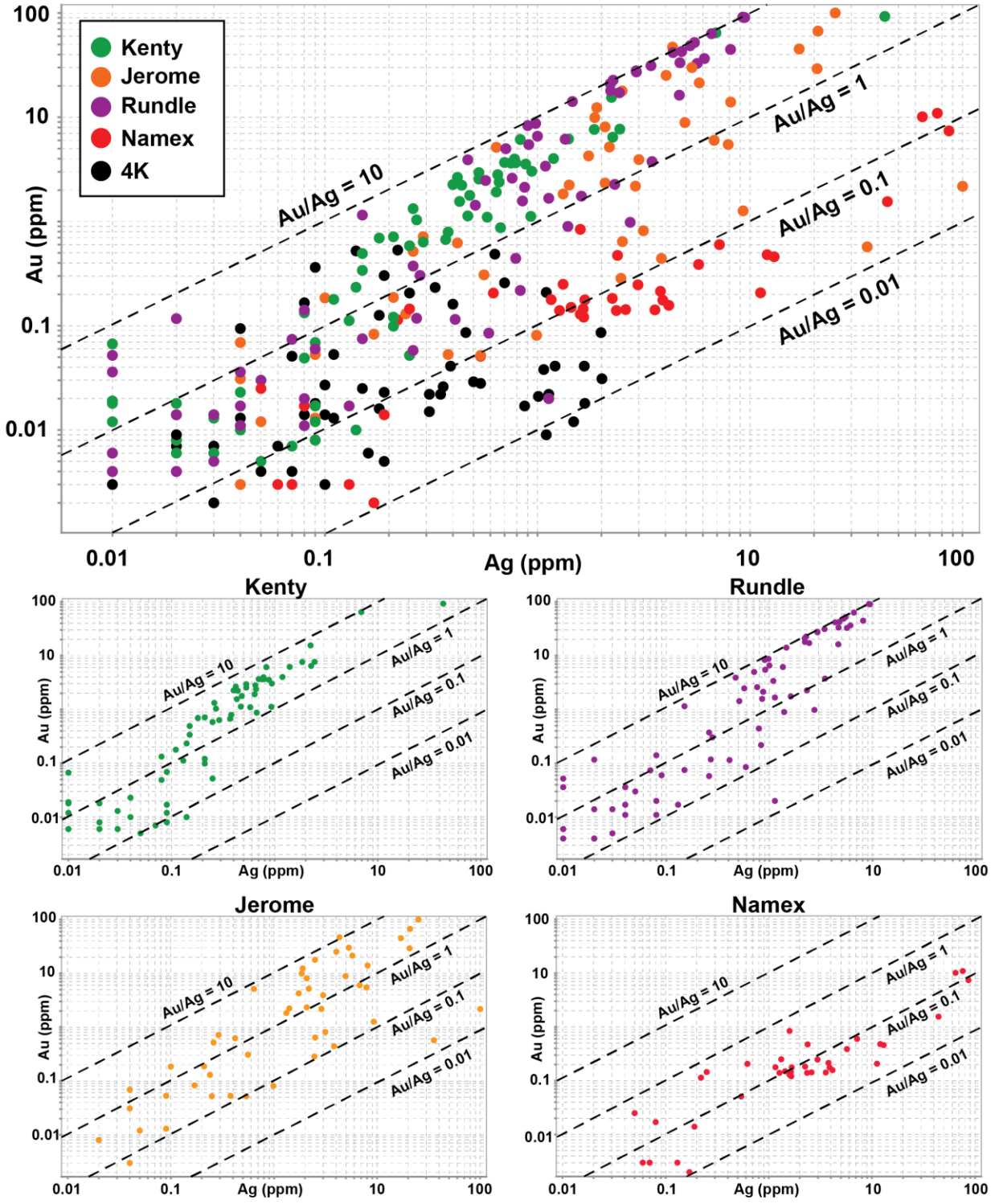

Figure 2.17. Binary plots of Ag versus Au for whole-rock data for all SGB deposits sampled in this study.

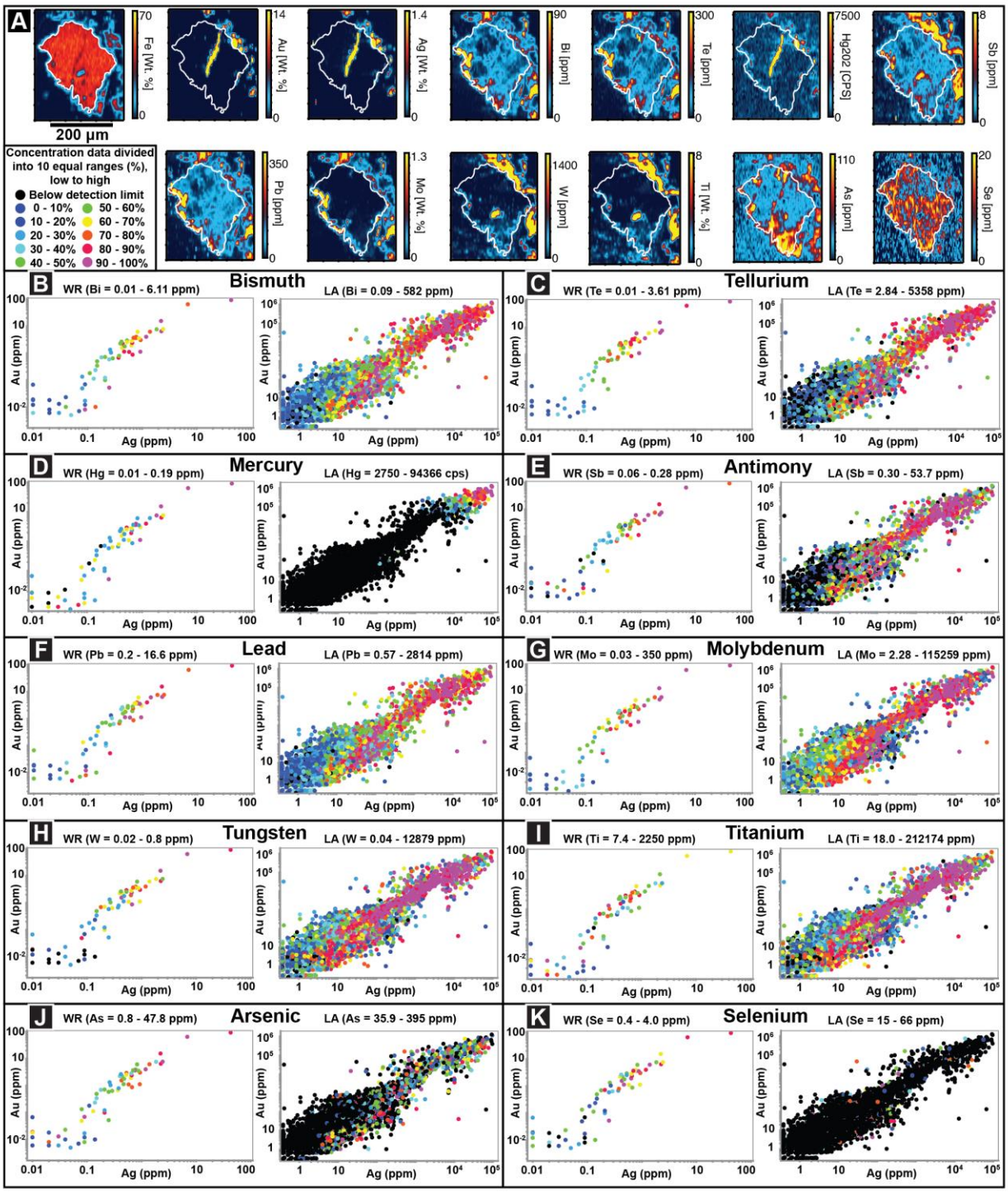

Figure 2.18. LA-ICP-MS elemental maps and side-by-side plots comparing whole rock (WR) data (left) and LA-ICP-MS (LA) time-slice data for pyrite (right) from the Kenty deposit. All plots show Ag versus Au with the third element's abundance represented using cold to hot

coding divided into ten equal ranges with each 10% division denoted by color. Data for Hg from LA-ICP-MS is not quantified and is thus displayed as counts per second (cps). A) LA-ICP-MS maps with pyrite grain outlined in white. B) Au-Ag-Bi. C) Au-Ag-Te. D) Au-Ag-Hg. E) Au-Ag-Sb. F) Au-Ag-Pb. G) Au-Ag-Mo. H) Au-Ag-W. I) Au-Ag-Ti. J) Au-Ag-As. K) Au-Ag-Se. Note the different scales the whole rock versus LA data.

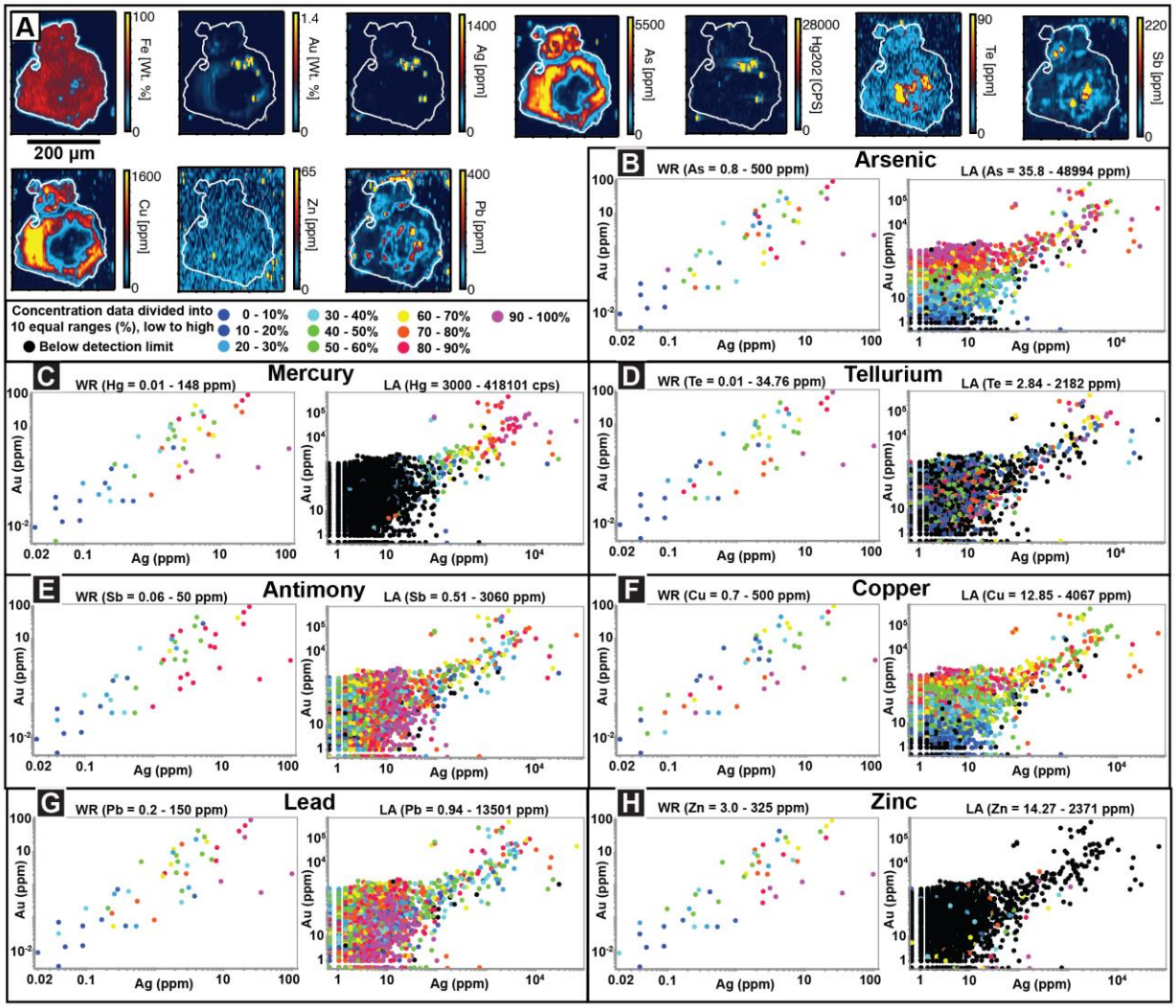

Figure 2.19. LA-ICP-MS elemental maps and side-by-side plots comparing whole rock (WR) data (left) and LA-ICP-MS (LA) time-slice data for pyrite (right) from the Jerome deposit. All plots show Ag versus Au with the third element's abundance represented using cold to hot coding divided into ten equal ranges, with each 10% division denoted by color. Data for Hg from LA-ICP-MS is not quantified and is thus displayed as counts per second (cps). A) LA-ICP-MS

maps with pyrite grain outlined in white. B) Au-Ag-As. C) Au-Ag-Hg. D) Au-Ag-Te. E) Au-Ag-Sb. F) Au-Ag-Cu. G) Au-Ag-Pb. H) Au-Ag-Zn. Note the different scales the whole rock versus LA data.

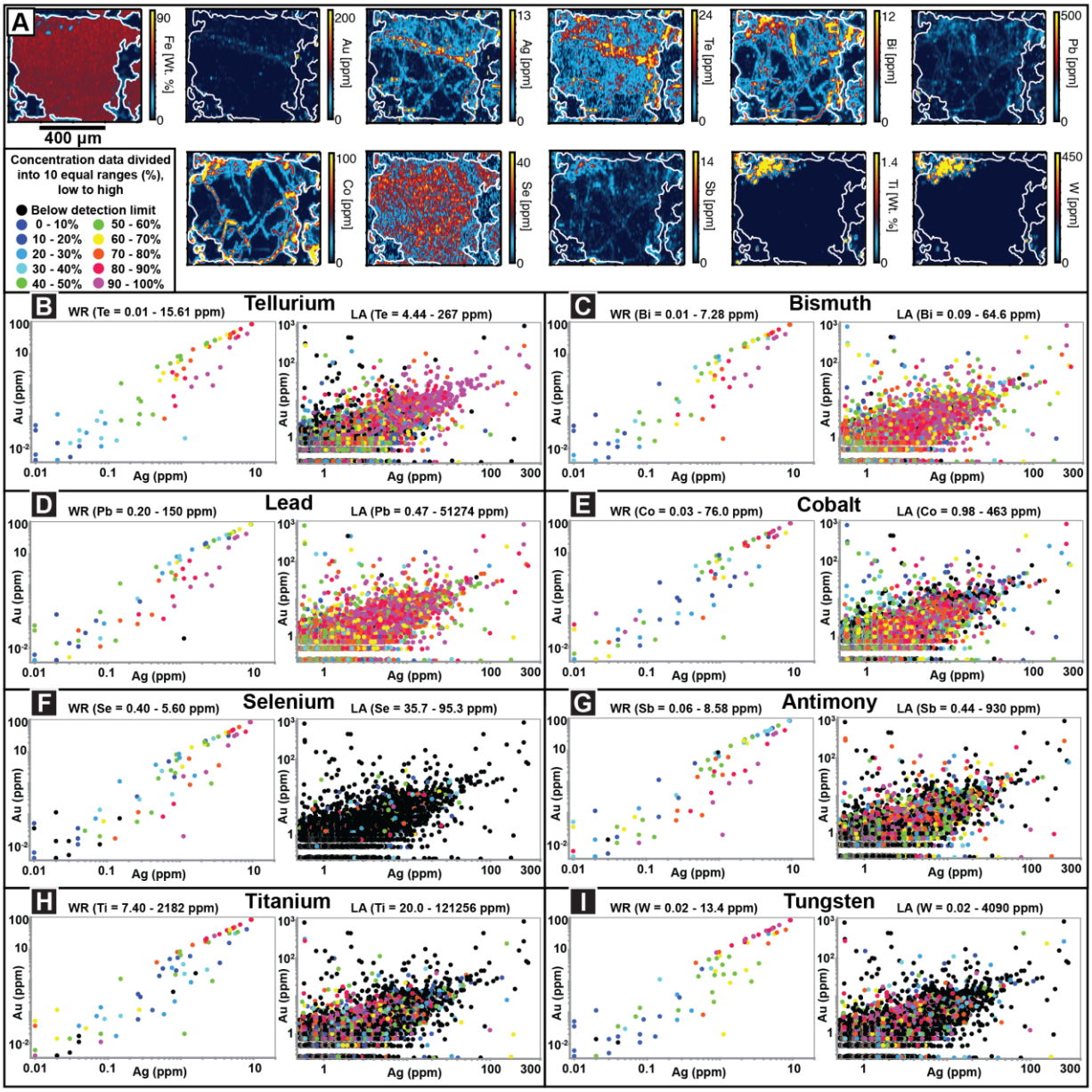

Figure 2.20. LA-ICP-MS elemental maps and side-by-side plots comparing whole rock (WR) data (left) and LA-ICP-MS (LA) time-slice data for pyrite (right) from the Rundle deposit. All plots show Ag versus Au with the third element's abundance represented using cold to hot coding divided into ten equal ranges, with each 10% division denoted by color. A) LA-ICP-MS

maps with pyrite grain outlined in white. B) Au-Ag-Te. C) Au-Ag-Bi. D) Au-Ag-Pb. E) Au-Ag-Co. F) Au-Ag-Se. G) Au-Ag-Sb. H) Au-Ag-Ti. I) Au-Ag-W. Note the different scales the whole rock versus LA data.

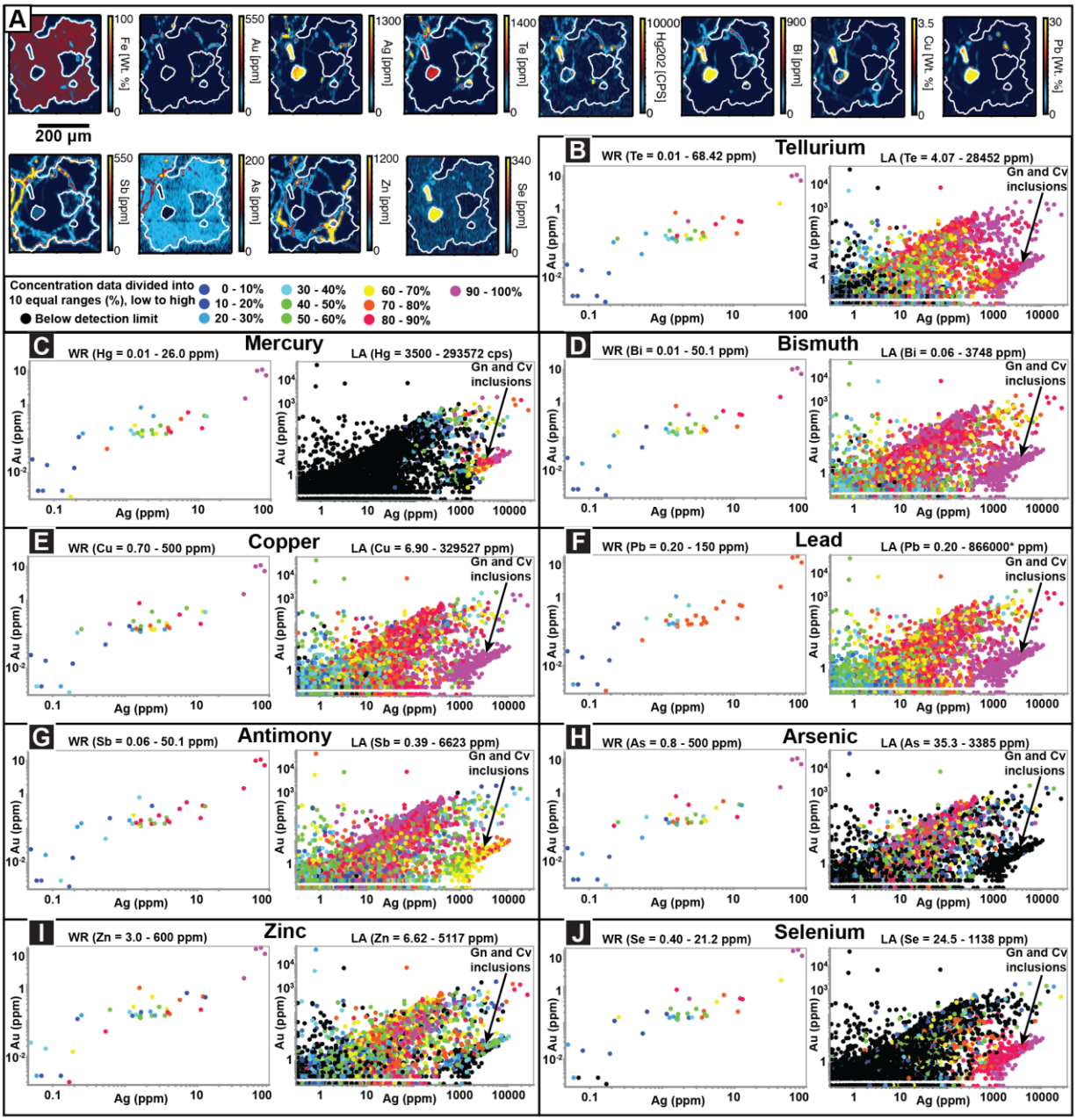

Figure 2.21. LA-ICP-MS elemental maps and side-by-side plots comparing whole rock (WR) data (left) and LA-ICP-MS (LA) time-slice data for pyrite (right) from the Namex deposit. All plots show Ag versus Au with the third element's abundance represented using cold to hot

coding divided into ten equal ranges, with each 10% division denoted by color. Data for Hg from LA-ICP-MS is not quantified and is thus displayed as counts per second (cps). A) LA-ICP-MS maps with pyrite grain outlined in white. B) Au-Ag-Te. C) Au-Ag-Hg. D) Au-Ag-Bi. E) Au-Ag-Cu. F) Au-Ag-Pb. G) Au-Ag-Sb. H) Au-Ag-As. I) Au-Ag-Zn. J) Au-Ag-Se. Note the different scales the whole rock versus LA data.

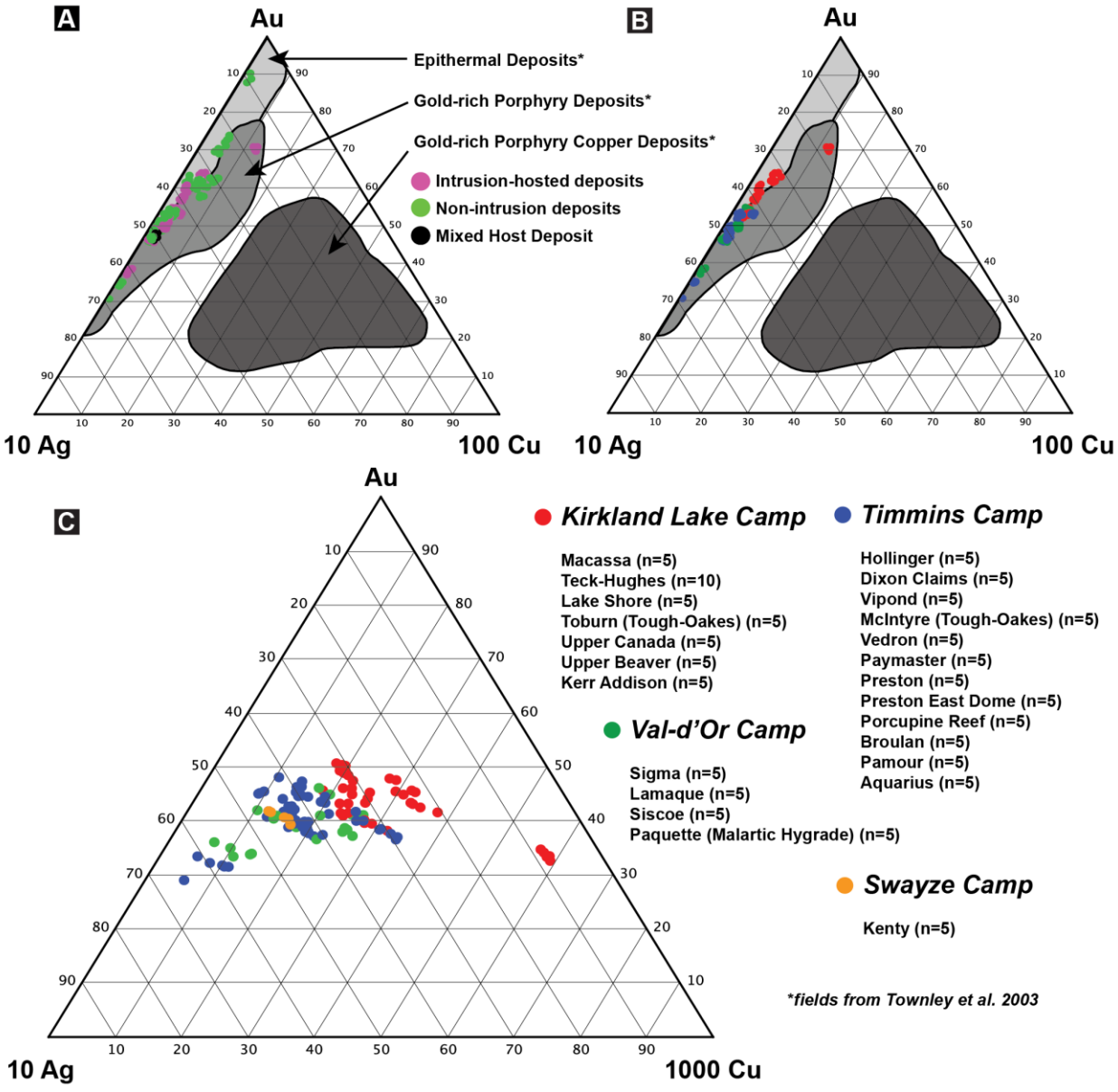

Figure 2.22. Ternary diagrams showing the Au-Ag-Cu data from EMPA analyses of native gold from across the Superior Province and specifically comparing the Timmins, Kirkland Lake and

Val-d'Or Au camps. Note the fields in A and B are for epithermal, Au-rich porphyry and Au-rich porphyry Cu deposits (modified after Townley et al., 2003). A) Au-Ag-Cu ternary for all Superior Province gold analyses from Hastie et al. (2020a). B) Au-Ag-Cu ternary for gold analyses from Kirkland Lake, Timmins and Val-d'Or Au camps only. C) Au-Ag-Cu ternary of data from (B) with increased scaling for Ag and Cu to enhance visual comparison. Kenty deposit of the SGB has also been shown for comparison. Note that no EMPA Au data exists for other deposits from the SGB.

Chapter 3

3 Au remobilization: Insights from Au deposits in the Swayze greenstone belt, Abitibi Subprovince, Canada

Evan C.G. Hastie[1, 2], Daniel J. Kontak[1], and Bruno Lafrance[1]

[1]Harquail School of Earth Sciences, Laurentian University, Sudbury, Ontario P3E 2C6;
[2]Earth Resources and Geoscience Mapping Section, Ontario Geological Survey, Sudbury, Ontario P3E 6B5

Published in Economic Geology and used with the permission of the Society of Economic Geologists; Hastie, E.C.G., Kontak, D.J. and Lafrance, B., 2020, Gold remobilization: Insights from gold deposits in the Archean Swayze greenstone belt, Abitibi Subprovince, Canada; ECONOMIC GEOLOGY v. 115, p. 241-277. DOI: https://doi.org/10.5382/econgeo.4709.

3.1 Abstract

Recognizing if and how Au is remobilized, in solid, melt, or a fluid state, is critical for understanding the origin of high-grade ore zones in Au deposits. When evidence for Au remobilization can be demonstrated, then primary versus secondary processes can be distinguished, resulting in a more complete understanding of Au deposit formation. To address this, samples from two Au deposits, Jerome and Kenty, in the Archean Swayze greenstone belt (SGB) of northern Ontario, Canada, together with archived samples from 39 high-grade Au deposits from the Abitibi greenstone belt (AGB) across Ontario and Quebec, were geochemically characterized using integrated SEM-EDS and EMPA imaging and analyses in addition to LA-ICP-MS elemental mapping. These data provided the basis to develop a model for Au remobilization and upgrading of Au widely applicable to orogenic gold settings.

Data for the Jerome deposit indicate that Au uptake into early pyrite was not due to pulsing of different fluids, but instead was predominantly controlled by S availability, whereby

the oscillatory/sector zoning in pyrite resulted from the substitution of As into S sites during rapid growth due to local chemical disequilibrium. In addition, Au-bearing pyrite from both the Jerome and Kenty deposits record textures, such as porosity development coincident with the presence of native gold and accessory sulfide phases, that is strongly suggestive of coupled dissolution-reprecipitation (CDR) reactions which liberated Au and associated elements from earlier auriferous (100 to 5000 ppm Au) pyrite. During the remobilization process, Au and Ag were decoupled which resulted in: (1) a change in Au:Ag ratios of 0.5-5 in early pyrite to ≈ 9 in the new native gold (900 Au fineness) and (2) incorporation of Ag into cogenetic secondary mineral phases (e.g., chalcopyrite, tetrahedrite, and galena). Evidence for an association of low-melting point chalcophile elements (LMCE; Hg, Te, Sb, Bi) with Au at the Jerome, Kenty, and many (>50%) of the 39 historic deposits sampled, along with native gold filling structurally favorable sites in vein quartz in all samples, indicate a fluid might not have been the only factor contributing to remobilization. This systematic Au-LMCE association strongly supports a model whereby Au is released by CDR reactions and is then remobilized either by fluid-mediated, LMCE-rich melts that began to form at 335°C and/or by local, nanoparticle (nanomelt?) transport during deformation and metamorphism. Conclusions drawn from this study have implications for Au deposits globally and can account for the common presence of coarse-grained, commonly crystalline, native gold filling fractures in quartz, the paragenetically late-stage origin of gold in veins, and also better explain the inability of Au in solution remobilization models account for locally high gold grades given the relatively low solubility of Au in hydrothermal fluids.

3.2 Introduction

Large Au deposits are often the result of multiple Au enrichment events (Groves et al., 2003; Goldfarb et al., 2005), but it is often difficult to establish whether the last of these events represents remobilized Au from pre-existing mineralization or relates to new Au introduced during a distinct epigenetic event. If evidence for Au remobilization can be shown, then resolving the various processes responsible for gold enrichment can clarify the role Au remobilization plays in forming the exceptionally high-grade ore zones that are observed in many mining districts. Elucidating this problem could help in developing more robust ore deposit models and provide a better assessment of Au endowment.

The "paradox of remobilization" as explained by Marshall and Gilligan (1987, 1993), outlines the complexity in determining the scale of metal remobilization in VMS deposits. This concept is widely applicable to other ore systems and could explain why clear evidence of Au remobilization is often lacking. This paradox states that with increasing remobilization, which is represented by changes in the metal inventory of an orebody and the distance by which metals have travelled from their source, the evidence supporting remobilization becomes more ambiguous due to increasing differences between the original ore zones and new remobilized ore zones. Applying this paradox concept to high-grade zones with coarse visible gold in giant Archean Au deposits such as Red Lake, Kirkland Lake, Croesus, Hoyle Pond, and Hollinger-McIntyre, suggests they could represent end-members in a continuum of remobilized ore given the abundance of late stage visible gold noted to cross-cut quartz (Fig. 3.1). However, finding evidence in support of such remobilization depends on having the right samples and using an analytical protocol that provides the critical textural and chemical information. If such

conclusive evidence for Au remobilization is demonstrated, then primary mineralizing processes can be separated from subsequent events and integrated into a more robust model for Au deposits.

A common feature observed in many high-grade Au deposits is the presence of coarse, often crystalline, visible gold that fills single or multiple, planar to irregular fractures in either vein quartz or the adjacent host rock (Fig. 3.1). These fractures clearly post-date the quartz veins, hence their filling with gold requires the passage of impossibly large volumes of fluids, given the relatively low solubility of Au in hydrothermal fluids (Wagner et al., 2016). In addition, these gold-filled fractures occur in contrasting types of Au deposits (e.g., orogenic versus intrusion-associated) for which different Au sources have been proposed (e.g., Robert, 2001; Goldfarb et al., 2005; Dubé and Gosselin, 2007), which makes this common textural observation an important feature that links processes among deposits.

In this contribution, we first present evidence for Au remobilization and then evaluate different mechanisms responsible for this process. We describe two Au deposits, the Jerome and Kenty, located in the Archean Swayze greenstone belt (SGB) in northern Ontario, Canada, and then discuss the nature and origin of Au in these deposits using field relationships, textures (ore petrology, SEM-EDS) and mineral chemistries (EMPA, LA-ICP-MS). These data and observations are further complemented by a suite of high-grade Au samples from 39 Archean deposits from across the provinces of Ontario and Quebec, including many from the well-studied Abitibi greenstone belt (AGB). These latter samples were collected from archived specimens at the Royal Ontario Museum (ROM), Toronto, Ontario. Collectively, as far as we are aware, these samples and data represent the largest single study of Archean Au mineralization and provide a robust foundation for evaluating the potential for Au remobilization in Archean deposits.

3.2.1 Previous Studies on Au Remobilization

Metal remobilization, including Au, can be separated into two broad categories that are largely scale dependent (Marshall and Gilligan, 1987, 1993): (1) internal remobilization (within the boundary of an orebody), whereby the original ore and host rock have maintained their spatial relationships and bulk metal grades, whereas the ore phases and internal distribution may have changed; and (2) external remobilization, whereby transport of metals (e.g., Au, Ag) over larger distances has changed the metal contents of the ore and host rock resulting in new orebodies or upgrading of existing orebodies.

Specifically for Au, two principal mechanisms are currently invoked: (1) remobilization by Au in solution (Fougerouse et al., 2016a), and (2) remobilization as part of a polymetallic melt (Frost et al, 2002; Tomkins et al., 2007) that may be fluid-mediated (Tooth et al., 2011; Zhou et al., 2017). In general, these models combine liberation mechanisms (e.g., coupled dissolution-reprecipitation (CDR), partial melting, intra-grain diffusion), which promote removal of Au from their primary host phase (e.g., sulfides), and subsequent transport (fluid and/or melt) that move Au to a new location where it is deposited and concentrated.

Of the Au remobilization mechanisms, those involving Au in solution are by far the most discussed and are essentially similar to primary Au transport involving the complexing of Au with ligands such as HS- and Cl- (Williams-Jones et al., 2009; Fougerouse et al., 2016a). Similarly, depositional mechanisms such as boiling, sulfidation reactions, oxidation, and cooling, which destabilize these complexes and precipitate Au (Williams-Jones et al., 2009), are also invoked for Au deposition accompanying secondary remobilization processes (Fougerouse et al., 2016a). There are, however, unresolved problems with remobilization of Au in solution: (1) the

models assume that the Au liberating fluid is the same as the fluid implicated in the transport of Au, hence it is a continuum model, which becomes a complex interplay of reactions and processes; and (2) this mechanism for remobilization is inefficient and has difficulty explaining the concentration of coarse-grained, visible gold in cross-cutting quartz veins given the relatively low solubility of Au in hydrothermal fluids. For example, both theoretical modeling and analysis of Au in fluids suggest values ranging from 0.001 to 1 ppm (Ulrich et al., 1999; Simmons and Brown, 2007; Williams-Jones et al., 2009; Wagner et al., 2016). Using typical microthermometrically constrained data for fluid inclusions in orogenic Au systems, such as ThCO2 (to liquid; from 15°C to 25°C), a representative salinity of 7.5 wt% eq. NaCl (i.e., Tmclathrate of 6°C) and volume of the CO2 phase (15 to 30% at ≈25°C), and the recent software package of Steele-MacInnis (2018), a fluid density of 1 ± 0.04 g/cm3 and XCO2 of 7 to 14 are calculated. These are in agreement with values reported in the literature (Ridley and Diamond, 2000; Bodnar et al., 2014). Thus, using a fluid density of 1 g/cm3 from above and assuming 1 ppm Au in solution (i.e., 0.000001 grams of Au in 1.0 gram of fluid) to calculate the volume of fluid required, a 10 Moz Au deposit (converted to grams from troy ounces) requires 0.311 km3 of fluid. This should be considered a minimum fluid volume because 1 ppm Au in solution is a concentration more typical of a magmatic system (Ulrich et al., 1999) and since metamorphic fluids contain lower Au contents of 1-100 ppb Au (Williams-Jones et al., 2009; Wagner et al., 2016), which means that even larger volumes of fluids are needed to form a 10 Moz Au deposit (311 – 3.11 km3 respectively). If generated by metamorphic devolatilization, these fluids would require a source rock volume at least an order of magnitude greater based on source rock yield estimates (Pitcairn et al., 2006; Phillips and Powell, 2010). This could possibly explain the primary enrichment of Au in a deposit, however, if gold has been transported a second time (i.e.,

remobilized) to form high-grade visible gold mineralization, an equally large volume of fluid would be needed. This is a highly unlikely remobilization mechanism due to the large volumes of fluid required and given the evidence for far more efficient mechanisms that are presented herein.

A type of fluid-mediated Au transport that can resolve this apparent mass balance problem (i.e., the large concentration of gold in narrow fractures) involves the transport of Au as colloids or nanoparticles. Here, a Au-bearing solution becomes supersaturated in Au and silica with negatively charged Au colloids becoming suspended in gel-like amorphous silica and transported to a deposition site (Saunders, 1990). Evidence in support of this mechanism was recently reported in epithermal-, seafloor- and volcanogenic massive sulfide (SMS and VMS) type systems (Hannington et al., 2016; Gartman et al., 2018; Williams-Jones et al., 2018; Hannington and Garbe-Schönberg, 2019). The inability to directly image Au nanoparticles and their associations in these deposits as well as orogenic Au deposits has, however, hindered this research.

The second mechanism for Au remobilization is a more recent idea and involves a polymetallic melt generated during metamorphism. This process appeals to the effect of low-melting point chalcophile elements (LMCE; Frost et al., 2002; Tomkins et al., 2007), such as Bi, Te, Sb and Hg, on the melting temperature of Au. In optimal conditions, these elements can depress this from 1064°C to below 300°C (Tomkins et al., 2004). Complementary to this, Tooth et al. (2011) provide experimental evidence suggesting such polymetallic melts can form in the presence of LMCE-bearing hydrothermal fluids, which can scavenge Au from preexisting mineralization aided by CDR reactions. Porous or sieve-textured Au-bearing sulfides common in many orogenic Au systems are seen as strong evidence for these types of reactions (Putnis, 2009;

Velásquez et al., 2014; Fougerouse et al., 2016a; Lawley et al., 2017; Dubosq et al., 2018). CDR dominates mineral replacement reactions and porosity development is seen as an integral part of this process because it allows the fluid to maintain contact with the reaction front (Putnis, 2009). If given enough time in contact with the fluid, the porosity would eventually clear and eliminate evidence that the reaction had taken place (Fig. 3.2). Thus, importantly the presence of mineral inclusions and porosity indicate that the host mineral (e.g., sulfide) is the product of a replacement process (Putnis 2009).

Where the fluid-mediated melt model of Tooth et al. (2011) differs from the partial melting model proposed by Frost et al. (2002) and Tomkins et al. (2007) is that CDR reactions promote melt formation at greenschist facies conditions (250 to 400°C), instead of fluid-absent partial melting that dominates at amphibolite facies conditions and above (>500°C). Regardless of the differences, these each involve polymetallic melts and can account for the abundance of coarse-grained, visible gold found in many deposits, both large and small, in addition to gold filling late fractures in quartz veins (Fig. 3.1). Potential issues with this mechanism are that LMCE-bearing minerals are not always present, and when observed do not always show textures indicating a paragenetic synchroneity.

All the mechanisms discussed above have the ability to remobilize Au. The question is which mechanism, or combination of mechanisms, can best account for the features observed in high-grade Au deposits. It is this latter aspect that is explored below.

3.2.2 Recent Advances in Au Remobilization Research

Early work on metal remobilization by Mumin et al. (1994) and Larocque et al. (1995) presented some of the first compelling evidence for Au remobilization from sulfides. This work also provided new ideas on ore zone development in Au deposits. More recent studies on Au remobilization provide: (1) evidence of early Au mineralization associated with sulfide minerals; (2) compelling evidence for remobilization of this early Au; and (3) insights into how Au is liberated, transported and deposited to form high-grade Au ore zones (Velásquez et al., 2014; Fougerouse et al., 2016a, 2016b, 2017; Zhou et al., 2017; Li et al., 2019). These studies favor Au remobilization by a fluid (Fougerouse et al., 2016a) or polymetallic melt (Zhou et al., 2017), in addition to addressing the effects of remobilization on Au fineness (Velásquez et al., 2014; Li et al., 2019). Specifically, these studies characterize Au enrichment in the primary ore, which occurs in chemically zoned auriferous sulfide minerals, and differentiate this early enrichment from paragenetically later Au-barren sulfide minerals and native gold assemblages. The main results of these studies are summarized below.

Oscillatory zoning, a common feature in auriferous pyrites, has been shown to occur in at least 75 different mineral species (Shore and Fowler, 1996). Two general hypotheses are offered for its presence in pyrite: (1) periodic and repetitive changes in the bulk fluid composition during its growth (Peterson and Mavrogenes, 2014); and (2) crystal-growth disequilibrium at the fluid-mineral interface due to its rapid growth with a commensurate substitution of trace and major elements. Importantly, the latter does not require a change in bulk fluid chemistry (Fougerouse et al., 2016b). How these models affect the uptake of Au in pyrite is an important question that is addressed in this study.

In their study of Au mineralization in the El Callao district of Venezuela, Velásquez et al. (2014) described the presence of invisible Au in early pyrite, particularly in As-rich zones, discussed the CDR liberating reactions for Au and LMCE, attributed all visible gold to remobilization, and explained its fineness of ≈ 900, which is a common feature of Au deposits globally (Morrison et al., 1991; Pal'yanova, 2008; Li et al., 2019). Investigations of the Obuasi Au deposit in the Ashanti belt of West Africa (Fougerouse et al., 2016a, 2016b, 2017) provided further insights about Au incorporation into early sulfides, its liberation from arsenopyrite via CDR reactions, and suggested that Au can become anomalously enriched in a fluid (>10 ppm) depending on sulfur concentrations. Lastly, Zhou et al. (2017) investigated Au remobilization and refinement accompanying magnetite growth at the Beiya skarn deposit in southwest China. Textural evidence and thermodynamic modeling indicated that Au was scavenged from hydrothermal fluids by Bi melts. Subsequently, fluctuating fO2 at magnetite growth interfaces led to the precipitation from this Bi-Au melt of gold and bismuth minerals that became entrapped within magnetite. This work concurs with the experimental work on Bi-melt formation and Au scavenging from hydrothermal fluids presented by Tooth et al. (2011).

3.3 Regional Geology of the Swayze Greenstone Belt

The Archean SGB of northern Ontario is the southwestern extension of the Au-rich AGB (Fig. 3.3; van Breemen et al., 2006; Thurston et al., 2008; Ayer et al., 2010). It contains intrusive and extrusive rocks of ultramafic to felsic composition, in addition to both chemical and clastic metasedimentary rocks, collectively varying in age from 2740 Ma to <2690 Ma (Heather, 2001; van Breemen et al., 2006). Ayer et al. (2002) noted a spatial relationship between ca. 2670 Ma alkaline metavolcanic rocks and Au occurrences (e.g., Kenty and Rundle deposits; Fig. 3.3B).

These metavolcanic rocks are temporally equivalent to Timiskaming alkaline metavolcanic rocks (ca. 2676-2670 Ma) in the AGB, where they are associated with coarse clastic metasedimentary rocks (Thurston et al., 2008). The majority of the SGB experienced widespread greenschist facies metamorphism but the margins of the belt have been metamorphosed to amphibolite facies near large granitoid complexes (Heather, 2001). This concurs with work done on the western AGB by Thompson (2005) who showed that rocks now at surface would have reached maximum pressures at a depth of 10 km and temperatures of 350 to 450°C. The latter occurred after the deposition of the Timiskaming assemblage (ca. 2676-2670 Ma) during final accretion of the Superior Craton (Thompson, 2005). For brevity, the prefix 'meta' is omitted for all rock types discussed in this contribution unless explicitly stated otherwise.

3.4 Analytical Techniques

Samples used in this study are from drill cores and outcrops sampled at the Jerome (n=62) and Kenty (n=97) deposit areas, which were mapped at both regional- and deposit-scales (Fig. 3.3C and D, respectively). To complement the findings from these two deposits and provide a more regional context, an additional 219 samples from 39 historic Au deposits across the AGB were examined from samples archived at the ROM. All of these samples were characterized to assess the relative timing relationships between quartz and native gold, with 41 of these samples used for geochemical analysis and comparative purposes to the SGB.

3.4.1 Petrography and SEM-EDS

Transmitted and reflected light petrographic studies were carried out on all samples and included surface area measurements of pyrite and gold in thin section using ImageJ (Schneider et al.,

2012) for mass balance calculations of gold and pyrite. This work was followed by more detailed imaging and analysis using a Zeiss EVO 50 scanning electron microscope (SEM) equipped with an Oxford X-Max 50 mm2 energy dispersive spectrometer (EDS) that utilized Oxford's Aztec© software package at the Geoscience Laboratories (Geo Labs) in Sudbury, Ontario. Analyses were performed at a working distance of 8.5 mm at 20kV and ≈750 pA, with counting times ranging from 20 to 40 seconds per spot analysis.

3.4.2 Native gold and pyrite EMPA analyses

More detailed characterization of gold and pyrite grains was carried out at the Geo Labs using a CAMECA SX-100 EPMA equipped with 5 wavelength dispersive spectrometers. The approach involved the use of dual operating conditions in order to minimize analytical time while at the same time improving the limits of detection for select elements. For native gold analysis, the operating conditions were 20kV and 30nA for major elements and 20kV and 200nA for minor elements (i.e., those expected to occur at concentrations of less than 1 wt.%). For pyrite analysis, the operating conditions were 20kV and 40nA for major elements and 20kV and 200nA for minor elements. A focused beam (<1 μm) was utilized for all analytical routines and decomposition testing on both gold and pyrite were carried out at 200nA to ensure that counting rates were not compromised over the duration of an individual analysis. The choice of x-ray lines, calibration standards, counting times and limits of detection for all native gold and pyrite analyses are outlined in Table 3.1.

The identification of potential spectral interferences were carried out by performing high-quality wavelength scans for all analyzed elements in the vicinity of each analyzed x-ray line. Pure metals were used for this application (except for HgTe) in order to maximize our ability to

identify problematic interferences. Background offsets were then chosen following close examination of superimposed wavelength scans together with the projected positions of all theoretical primary and multiple order peaks. Beam interaction depths have been estimated to be <1 μm in native gold and <3.5 μm in pyrite grains at 20kV using Electron Flight Simulator v3.1-LV©(Small World LLC), which is based on the Monte Carlo algorithms of Joy (1995). In all cases, visible micro-inclusions were avoided and the data contained no outliers in concentration to suggest any interaction with micro-inclusions beneath mineral surfaces.

For the analysis of pyrite two different routines were used in this study. The analysis of Au in Jerome pyrites was carried out on the Au Mα line using the LPET crystal. Due to the lower concentration of Au encountered in the Kenty pyrites the routine was modified in order to take advantage of combined counting on multiple spectrometers equipped with large crystals. In this case the Au Lα line was measured by combining the counts from two large LLiF crystals and a single LiF crystal. Using this approach, we were able to achieve a limit of detection for Au of approximately 60 ppm versus a detection limit of approximately 230 ppm when measuring the Au Mα line on a single LPET crystal. It is important to note that both the Au Mα and Au Lα x-ray lines have specific interferences that need to be considered. In particular, the proximity of Hg Lα to Au Lα must be taken into consideration when selecting background offsets on LiF. The close proximity of a 3rd order Fe Kα peak in the vicinity of Au Mα also needs to be taken into consideration when analyzing pyrite, therefore a differential pulse height window was used to minimize this interference.

The quality control procedures employed involved checking the performance of the calibration standards against in house reference minerals (stoichiometric end-member varieties) for pyrite or metals and HgTe in the case of native gold analysis. The determination of accuracy

for low concentrations of Au in pyrite is challenging because homogeneous pyrite standards of this nature are not available. The approach taken therefore was to evaluate the performance of the Au calibration standard (in this case pure metal) on stoichiometric Ag3AuTe2 (petzite). Using this procedure it was possible to confirm that the accuracy of Au analysis is on average within 0.4 % (relative) of the expected concentration in petzite following continued monitoring. For native gold analysis the calibrations for Au, Ag, Cu and Hg were tested against other pure metal standards (AuRM1, Alfa Aesar Ag and Cu wire) and synthetic stoichiometric HgTe (Micro-Analysis Consultants Ltd.). The average concentrations for these were all within 0.6 % (relative) to expected concentrations for these elements.

Precision testing was carried out by performing repeat analysis on the same location from select gold grains (ROM sample suite) and pyrite from Jerome and Kenty. Decomposition testing was also carried out for each of the routines to ensure that counting rates were not compromised following repeat analysis in the same location on each grain. Tabulated results of precision testing for both native gold and pyrite are given in Table 3.1. Testing on the Kenty pyrite represents 2 separate repeat analyses on the same grain with each analysis point separated by at least 20 μm. These results clearly demonstrate that individual analytical results for Au are not anomalous (i.e., due to micro-inclusions).

The results presented here are fit for purpose, that is, sufficient in analytical robustness to identify low concentrations of Au in pyrite and examine the trends in native gold chemistry across different types of gold deposits.

3.4.3 LA-ICP-MS Au-Ag traverses

To determine and isolate Au and Ag bearing phases at Jerome and Kenty, line traverses across sulfide and sulfosalt minerals were performed using a laser ablation inductively coupled plasma mass spectrometry (LA-ICP-MS) instrument at the Great Lakes Institute for Environmental Research (GLIER), University of Windsor. The traverses were completed at GLIER's Element and Heavy Isotope Analytical Laboratories using an Agilent 7900 quadrupole ICP-MS coupled with a Photon Machines, Analyte Excite 193 nm, short pulse width (<4 ns) ArF excimer laser ablation system equipped with a HelEx two-volume cell. Laser traverses used spot sizes of 25 μm and reference materials were each analyzed at a minimum of twice every 20 lines. These included USGS basaltic glasses (GSD-1G, GSE-1G; Guillong et al., 2005; Jochum et al., 2005), a doped pyrrhotite standard (Po725; Sylvester et al., 2005) and NIST610 (Jochum et al., 2011), with reference values for GSD-1G, GSE-1G and NIST610 taken from GeoReM. Background acquisition times of 60 seconds were completed prior to each line traverse, both on unknowns and reference materials. Quantification of raw data was conducted with the trace element reduction scheme in Iolite 3 (Paton et al., 2011). For the pyrite grains, Fe was used as an internal standard (Fe for chalcopyrite; Cu for tetrahedrite; Pb for galena). This preliminary LA-ICP-MS work was only for the purpose of identifying Au- and Ag-bearing phases. Au was calibrated using Po725 while Ag was calibrated using GSE-1G. During LA-ICP-MS traverses on different mineral phases GSD-1G was used as a quality control standard. In all cases average Au and Ag concentrations were within 2% of the accepted values for GSD-1G.

The only time this data was used quantitatively was to state the ranges of Ag in other sulfides (i.e., galena, chalcopyrite, tetrahedrite) and to compare with EMPA data for cross

validation purposes. The data shows reasonable agreement for Au when compared to the EMPA results. Specifically, the average Au concentrations from an LA-ICP-MS traverse that covered the same approximate region of the EMPA pyrite traverse at Jerome (Table 3.2; spot 2 to spot 12) yielded less than 7 % difference in average concentrations (i.e., 531 ppm Au by LA-ICP-MS versus 497 ppm Au by EMPA).

3.4.4 LA-ICP-MS elemental mapping and binary plots

Characterized auriferous pyrites from both deposit areas that showed potential for providing additional data were also mapped for trace elements by LA-ICP-MS. This work provides the means to assess spatial, geochemical, and elemental relationships in pyrite. It needs to be stressed that this LA-ICP-MS data (i.e., elemental maps and binary plots) are only used qualitatively to semi-quantitatively. The focus of the elemental maps and binary plots is on the relative changes and trends in major and trace elements within pyrite and not their absolute values. Pyrite mapping was completed at Laurentian University's Chemical Fingerprinting Laboratory using a Thermo X-Series II quadrupole ICP-MS coupled with a Resonetics, RESOlution M-50 193nm, 20 ns pulse width, ArF excimer laser ablation system equipped with a Laurin Technic two-volume cell. Maps were constructed from line traverses that used laser spot sizes ranging from 10 to 20 μm; the latter was dictated based on pyrite grain size and expected resolution. Reference materials included GSD-1G, GSE-1G, Po725 and NIST610 described above with each analyzed twice every 15 lines. Background acquisition times of 30 seconds were completed prior to each line traverse, both on unknowns and reference materials. Quantification of the raw data was conducted with the trace element reduction scheme in Iolite 3 (Paton et al., 2011) using Fe as the internal standard. Au, Fe and S were calibrated on Po725 while all other

elements were calibrated with GSD-1G (4 maps) or with GSE-1G (1 map), except for Te (informational value), which was calibrated on NIST610.

Calibration standards that bracketed traverse and mapping sessions were checked with regular analyses of GSE-1G for quality control. Most element concentrations were within 10% of accepted values for GSE-1G with a few exceptions. Ni and Cu were within 20% of accepted values while As and Se were higher (30-80%) due to the signal intensity of GSD-1G being very close to background for these elements. The Te in NIST610 is informational and cannot be cross validated since it is not found in GSE-1G. Concentration data for Au from LA-ICP-MS analyses showed good agreement with EMPA data gathered on pyrite. For example, Jerome maps confirm that gold is in very high concentrations in arsenic rich zones, similar to values from EMPA analysis (see Table 3.2).

The data derived from LA-ICP-MS mapping were reduced to singular points for plotting purposes from the line traverses by converting each 0.35 second increment, the time for a complete analysis at the detector and referred to as a time-slice dataset (TSD), to the equivalent of a point analysis (see details in Gourcerol et al., 2018). Such data provide a qualitative to semi-quantitative assessment of Au and Ag concentrations, in addition to other elements, and can be used to show important trends in the data when complemented by spatial distribution from the elemental maps. In addition, Au:Ag ratios in pyrite have been shown to be a useful proxy for Au fineness (Velásquez et al., 2014) and thus are used here to assess how Au and Ag relationships changed during the textural modification of pyrite (Fig. 3.2). Furthermore, by looking at other elements in the same data set, the presence of micro-inclusions in pyrite can be evaluated and their relationship to the evolution of the pyrite assessed.

3.5 Results

3.5.1 The Jerome Au Deposit

Geological setting of the Jerome Au deposit: The Jerome deposit is located in the Ridout high-strain zone approximately 20 km on strike WNW of the 8.3 Moz Côté Au(-Cu) deposit (Fig. 3.3B, C; Katz et al., 2017). The Jerome mine produced 56,878 oz of Au and 15,104 oz of Ag from 1941 to 1943 (Brown, 1948) and current inferred resources are estimated at 1.03 Moz Au at a cut-off grade of 0.3 g/t Au (Burt et al., 2011). The mineralization is hosted in altered and deformed feldspar porphyry intrusions of syenitic to monzonitic composition (Figs. 3.4A, 3.5A), which cut polymictic conglomerate (Fig. 3.4B) of the Timiskaming assemblage (<2680 ±3 Ma; Thurston et al., 2008; Hastie et al., 2016; MacDonald et al., 2017). The historical ore zones described by Fumerton and Houle (1995) consist of a stockwork of quartz-carbonate veins and breccias with associated pyrite, predominantly hosted in altered feldspar porphyry bodies.

The altered intrusions consist of subhedral to anhedral K-feldspar phenocrysts (15%; 1 to 5 mm) in a medium- to fine-grained matrix composed of orthoclase, plagioclase, muscovite, quartz, and ankerite (Figs. 3.4A, C, 3.5). A few xenoliths of the conglomerate are hosted in the porphyry (Brown, 1948; Hastie et al., 2016). The polymictic conglomerate contains moderately to strongly deformed, elongate clasts (10 to 50 cm) of mafic to felsic volcanic rocks, gabbro, iron formation, and feldspar porphyry.

Pyrite is present in and bordering the stockwork of thin quartz-ankerite veins that cut across and partially replace the feldspar phenocrysts (Figs. 3.4C, 3.5A) in the porphyry. Sericite (fine-grained, V-bearing muscovite determined by SEM-EDS) replaces both the K-feldspar and

matrix-hosted ankerite, and stringers of sericite cut the quartz-ankerite-pyrite veins (Figs. 3.4C, 3.5B-E). A simplified paragenetic sequence documenting the temporal relationships among the gangue and ore minerals is summarized in Figure 3.6.

The Jerome deposit shares similar structural characteristics with the well-exposed Namex deposit, which is located 10 km ESE along strike (Fig. 3.3B; Hastie et al., 2016). Overprinting structural relationships suggest that the Timiskaming basin underwent regional folding during north-south shortening, followed by sinistral and dextral shearing (Hastie et al., 2016).

3.5.1.1 Nature of Au mineralization and pyrite stages at the Jerome deposit

Au is primarily hosted in pyrite from the altered parts of the feldspar porphyry bodies (Fig. 3.5). In order to further investigate this relationship, more than 300 pyrite grains from high-grade ore zones were examined by high-contrast, backscattered electron imaging (BSE). This revealed that all pyrites exhibit oscillatory or relict oscillatory zoning (Figs. 3.7, 3.8). In a few rare cases, both sector and oscillatory zoning with similar elemental relationships are seen (Fig. 3.7C, D). Based on these textural features, pyrite has been separated into 2 types, Py1 and Py1a (a hybrid type; see Fig. 3.2), and are referred to as such in further discussions below.

The first type (Py1) occurs in the selvage of quartz-carbonate veins and is inclusion-poor, shows both oscillatory- and sector-type zoning, and contains invisible Au in its As-rich zones (Figs. 3.7, 3.8). The second pyrite type (Py1a) is a modification of Py1 and is seen in the quartz-ankerite veins where it is spatially associated with an increased abundance of sericite (V-bearing muscovite). Importantly, Py1a is characterized by the presence of native gold and other micro-inclusions (i.e., chalcopyrite, gersdorffite, tetrahedrite, molybdenite, galena, hematite, sericite),

having relict and dismembered oscillatory zones enriched in As, a porous texture, and irregular grain boundaries with Py1 (Figs. 3.7, 3.8).

The bright oscillatory zones in imaged Py1 (Fig. 3.8A) typically contain, as indicated by EMPA, 500 to 1000 ppm Au (up to 0.5 wt. %; see "bright zones" Table 3.2); these concentrations rival those of the Carlin-type deposits in Nevada (Reich et al., 2005). This pyrite also contains 1 to 4 wt.% As, as well as trace amounts of Cu (≈ 1000 ppm), Sb (< 400 ppm), Ag (< 200 ppm), Te (< 400 ppm), and Hg (< 700 ppm) (Table 3.2). In contrast, dark zones in Py1 contain significant amounts of Ni and Co (up to 1.1 wt. % Ni and 1600 ppm Co), but significantly less Au (<230 ppm; Table 3.2). SEM-EDS x-ray maps for As and Ni (Fig. 3.8B, C) highlight the inverse correlation between zones enriched in Ni versus As. Importantly, SEM-EDS line scans (Fig. 3.8D) across oscillatory zones show a near-perfect negative correlation between S and As. The EMPA spot analyses along the same traverse show a similar negative correlation between S and As, along with a possible negative correlation between As and Fe. The Au:Ag ratios in pyrite from select high-grade samples, as determined with SEM-EDS and EMPA, are close to 9 in the bright oscillatory zones (Fig. 3.8A), but are greater than 9 in areas of patchy zoning and porous textures (Fig. 3.8 E, F, Table 3.2). In addition to the EMPA data, LA-ICP-MS traverses were performed on Au-bearing pyrite to select appropriate grains for elemental mapping. These preliminary pyrite traverses yielded a range of Au:Ag ratios with two distinct populations at 1:1 and 9:1 (not shown).

All elements in the oscillatory zones of Py1 are represented in mineral inclusion phases of Py1a. In many cases these inclusions are multi-phase (Fig. 3.7A, B) and display triple junctions, which indicate that these phases are in textural equilibrium. Gold inclusions contain Ag and Hg, as determined by SEM-EDS, whereas chalcopyrite, gersdorffite, tetrahedrite, and

molybdenite account for the other elements found in the oscillatory zones. Silver is also present in galena (4000 to 5500 ppm) and chalcopyrite (200 to 5000 ppm) based on the preliminary LA-ICP-MS traverses, and is present in tetrahedrite inclusions (see LA-ICP-MS elemental mapping below) and concentrated in tetrahedrite (1000 to 5000 ppm; authors unpublished data) in the nearby Namex deposit (Fig. 3.3B).

3.5.1.2 LA-ICP-MS elemental mapping

Two LA-ICP-MS maps of arsenian pyrite grains shown in Figures 3.9 and 3.10 exhibit primary zoning. The images are ordered with respect to the spatial association among elements, with decreasing spatial overlap from left to right and top to bottom, with the exception of Au and Ag, which have been placed adjacent to each other to facilitate comparison.

The maps show enrichment of As, Cu, Sb, Au, Ag, Pb, Mo, Hg, Te, Bi, and Se in zones that correspond to the light oscillatory bands seen in BSE imaging (Fig. 3.9) in contrast to enrichment of Ni and Co in the dark bands. These data agree well with values from EMPA analyses (Table 3.2). These maps also reveal that As, Cu, Se and Te show the best spatial overlap with Au, whereas Ag, Sb, Bi, Pb, Mo and Tl less so due to increasing development of porosity and presence of inclusions. The pyrite grain in Figure 3.10 shows similar patterns, except that Ag and Hg only show spatial overlap with gold inclusions. This Ag-Hg association with gold grains supports the SEM-EDS results described above. The inferred elemental paragenesis indicates that Au and expected associated elements are cogenetic while remaining spatially separated from Ni and Co. Lastly, Cr, V, and Mo appear most enriched near porous areas, shown by the relative elemental changes from Figure 3.9 to 3.10. High V highlights the presence of sericite (V-bearing muscovite) as discrete grains both surrounding and filling pores in the pyrite grains.

3.5.2 The Kenty Au Deposit

3.5.2.1 Geological setting of the Kenty Au deposit

The Kenty Au deposit is located in the NE corner of Swayze Township in the SGB (Fig. 3.3B, D). It was discovered in 1931 and had sporadic production until 1948 (Fumerton and Houle, 1995). The Au mineralization is coincident with the presence of Fe-carbonate alteration, disseminated pyrite and quartz veining, as exposed at three stripped outcrops (C1 Mortimer, Salo and Mortimer Camp). This study focused primarily on the C1 Mortimer trench (Fig. 3.3D) and the Mortimer Camp stripping (not shown) located approximately 2 km ESE from the C1 Mortimer trench.

The C1 Mortimer trench area consists of pillowed basalts intruded by ultramafic dikes (<2 m width) and feldspar porphyry (≈ 40 by 50 m) of granodioritic composition (Figs. 3.3D, 3.11A). A 5 to 15 m wide zone of Fe-carbonate alteration at the contact of the porphyry and pillowed basalts is cross-cut by quartz-feldspar (albite and orthoclase) veins with entrained wall-rock fragments of altered basalt. The quartz veins cut all rock types and are surrounded by a centimeter- to decameter-scale alteration halo of ankerite-albite-sericite-pyrite ± chlorite (Fig. 3.11A, B). The main vein dips shallowly (≈ 30°) and is deformed by an open upright fold (Fig. 3.3D). It is cross-cut by numerous smaller, mutually cross-cutting, subvertical, quartz-feldspar veins (1 to 3 cm width) that define a conjugate set of 210° and 310° striking veins (Fig. 3.11C). Whole-rock assays of the altered wall rock and quartz veins from this locality vary from 1 to 85 ppm Au (authors unpublished data). Other subvertical quartz-feldspar veins, varying in width from 5 to 30 cm and striking NW, are also enriched (1 to 35 ppm) in Au.

Structural features in the area include a closely spaced foliation, defined by chlorite and sericite, which occurs within 10 cm of the large, shallowly dipping quartz-feldspar vein. A mineral stretching lineation defined by feldspar and sericite along the contact between this vein and the feldspar porphyry body plunges 25° towards the SE (150°). The late open fold plunges ~30° towards the ESE (110°) parallel to the stretching lineation. This fold also overprints the foliation, the shallowly dipping quartz-feldspar vein, and the alteration halo between the porphyry and pillowed basalt (Fig. 3.3D).

3.5.2.2 Nature of Au mineralization and pyrite stages at the Kenty deposit

Two distinct generations of Au mineralization are observed: invisible Au in pyrite, and visible gold in the form of inclusions and lining fractures that cut vein quartz (Fig. 3.11D). Invisible and visible gold are associated with pyrite in the alteration halo to the main quartz-feldspar vein at the C1 Mortimer trench (Fig. 3.3D, 3.11D). The pyrite grains are all modified to some extent and are mantled by hematite and chlorite; the latter minerals increase with proximity to the veins. Pyrite grains also differ in regards to their texture, morphology, and trace-element composition with decreasing distance from the vein (i.e., distal, medial and proximal), hence they are described as such below.

Distal pyrite grains are present more than 1 meter from the vein. These grains are euhedral with texturally uniform portions (Py1) and some small ilmenite inclusions (<2 μm), and modified porous portions (Py1a) containing inclusions of ilmenite, chalcopyrite, galena, rutile, hematite and gold (Fig. 3.12A, D).

Medial pyrite grains occur at a distance of 10 cm to 1 m from the vein. These grains are subhedral with locally preserved crystal faces and are typically seen in association with micro-

folded, rutile-rich foliation planes (Figs. 3.11E, F, 3.12F, I). They typically contain more pores and mineral inclusions (chalcopyrite, galena, rutile, hematite and gold) than the distal pyrite (Fig. 3.12B, E).

Proximal pyrite grains occur within 10 cm of the vein contact. These grains are similar to medial pyrite grains by their association with micro-folded rutile-rich foliation planes (Fig. 3.12C, F, I). They differ by their anhedral shape and irregular grain boundaries, and by a greater abundance of pores and inclusions of chalcopyrite, hematite, rutile, and native gold. The latter two minerals are also present lining microfractures cutting pyrite grains (Fig. 3.12F, I). Analysis of medial and proximal pyrite types by EMPA indicates that Au in pyrite ranges from 130-1500 ppm and does not have an obvious association with As, as did the pyrites from Jerome (Table 3.2).

Visible gold lines conjugate fracture sets in hinge area of the main, folded quartz-feldspar vein (Figs. 3.3D, 3.11D, 3.12C, F). The fractures have similar orientations to the 210°-310° conjugate quartz-feldspar vein network on the same outcrop. Visible gold is also seen intergrown with the micro-folded rutile described above (Fig. 3.12C, F, I). The axial plane of these micro-folds is parallel to the plane bisecting the angle between the conjugate fractures, suggesting that the folds and conjugate fractures formed during the same shortening event.

At the Mortimer Camp stripping, visible gold is associated with Au-Ag tellurides coating late-stage fractures, which cut subvertical, NW striking, quartz-feldspar veins (Fig. 3.13A). The fractures are coated with specular hematite (Fig. 3.13B) and cut across the host basalt and sub-vertical quartz-feldspar veins lacking visible alteration and pyrite mineralization (Fig. 3.13A). Where fractures cut the quartz-feldspar veins (Fig. 3.13) native gold is intergrown with petzite

(Ag_3AuTe_2) > hessiste (Ag_2Te) ± calaverite ($AuTe_2$) (Fig. 3.13C, D). Gold and petzite exhibit curvilinear grain boundaries between each other and petzite has low interfacial angles against quartz (Fig. 3.13D).

Visible gold present as inclusions in distal, medial and proximal pyrite, as discrete grains lining fractures in proximal pyrite and quartz at the C1 Mortimer Trench, and as fracture-fill grains intergrown with tellurides at the Mortimer camp stripping, all contain similar concentrations of Ag (9 to 10 wt. %), Cu (250 to 600 ppm) and Hg (500 to 800 ppm). This gold typically has a fineness of ≈ 900 (Table 3.3). A simplified paragenetic sequence documenting the temporal relationships between gangue and ore minerals is summarized in Figure 3.14.

3.5.2.3 LA-ICP-MS elemental mapping

Element distribution maps for distal pyrite (Figs. 3.12A, 3.15) show a very strong spatial correlation between Ni and Co, and a weak correlation of these elements with As and Cu. Zones enriched in Ni and Co have sharp boundaries and distribution patterns that mimic the outline of the host pyrite and internal oscillatory bands. In marked contrast, Ti, Sb, Te, Au, and Ag display patchy and mottled distribution patterns in zones corresponding with porosity and mineral inclusions in the grain (Fig. 3.12A, D). The Au:Ag ratios range from 0.5 to 1 in these zones based on the element mapping.

Element distribution maps for medial pyrite (Figs. 3.12B, 3.15B) show similar, but less defined, distribution patterns compared to those in distal pyrite grain. One of the most notable differences between distal and medial pyrite is the depletion of Au, Ag, Cu, Sb and Te in the outer zone or rim. The Au:Ag ratios based on the element mapping have also changed, ranging from 0.5 to 5, which is similar to the Au:Ag ratio of ≈5 from an EMPA traverse (Kenty EMPA

points 1 to 5; Table 3.2) in a separately analyzed medial pyrite (Fig. 3.12G). In addition, Ti, which is spatially associated with Au and Ag, also shows an increasing spatial relationship with Ni and Co.

In contrast to the distal and medial pyrite, elemental distribution maps for proximal pyrite show little Au and Ag throughout the pyrite (Fig. 3.15C). Instead, Au and Ag are localized to a single fracture in the grain; As and possibly Te are the only metals that also show an association with this fracture. Peripheral to the grain, Au and Ag are associated with Te, Sb and Ti, but this should be considered a qualitative assessment since quantifying the data relies on the internal standards of Fe. Whereas Ni, Co and As still show a strong spatial correlation in the pyrite grain, their distribution is more heterogeneous compared to that in the distal and medial pyrites. Finally Ti shows very little association with other elements, which relates to its concentration in late rutile trails outside of the pyrite (Figs. 3.12F, I). This contrasts to the distal pyrite where Ti, while patchy, is still in the pyrite. The Au:Ag ratio is close to 9 based on the elemental mapping data where these elements are concentrated both near and within the fracture.

3.5.3 LA-ICP-MS Au-Ag Binary Plots for Jerome and Kenty Pyrite Data

Data derived from LA-ICP-MS element mapping of pyrite from Jerome and Kenty areas are used to assess inter-element relationships related to changes during its textural evolution as noted above. In Figures 3.16, 3.17, and 3.18, these data are reduced to singular points and displayed in a series of binary plots, as described in the methods section.

Figure 3.16 shows an Au-Ag binary for the two mapped pyrite grains from the Jerome deposit (Figs. 3.9, 3.10) along with their BSE images and element maps for Au, Ag and V. The less altered pyrite is characterized by its relative lack of porosity, fewer inclusions, and absence

of significant V, which is used as a proxy for sericite (V-bearing muscovite) associated with late alteration. In contrast, the more altered pyrite shows an increase in porosity, presence of inclusions, and V distribution that correlates with sericite inclusions and sericite occurring outside the grain. The inset plot in the lower right of Figure 3.16 highlights how Au and Ag are associated with the different zones and inclusions phases and thus reflects how these elements relate to the modification of the pyrite grains. The following points are noted: (1) the less altered pyrite has the lowest, but uniform Au and Ag contents; (2) the altered pyrite has more inclusions of native gold with a relatively uniform Au:Ag ratio of about 9; (3) the highest Au values, of between 100 and 1000 ppm, represent modified primary zones where Ag has been removed. This is also seen by the change is Au and Ag distribution in the element maps; and (4) higher Ag concentrations represent mineral inclusions (e.g., tetrahedrite, chalcopyrite, galena) in both the less and more altered pyrite and is consistent with both SEM-EDS and petrographic observations

Figure 3.17 also shows a Au-Ag binary plot but for point data for the three different pyrite grains from the Kenty area (Fig. 3.15) with data color coded to reflect the different types of pyrite (i.e., distal, medial, and proximal). The plot shows marked contrasts in Au-Ag chemistry for these pyrite grains: (1) high Au and Ag values observed in the proximal grain, which is consistent with it hosting higher abundances of gold inclusions (e.g., Fig. 3.12I); and (2) the medial and distal grains showing lower and less uniform Au:Ag ratios than the proximal grain. Similar to the samples from the Jerome deposit, the data trending towards lower Au:Ag ratios are interpreted to reflect the presence of inclusions other than gold, such as galena and chalcopyrite, which are Ag-bearing. As done for the Jerome data, the inset plot in the lower right of Figure 3.17 highlights how Au and Ag are associated with the different zones and inclusions

phases and thus reflects how these elements relate to the modification of the pyrite grains. The same points are noted for these data as highlighted for Jerome.

Figure 3.18 combines the point data for pyrite from both deposits in order to summarize the overall Au-Ag relationships, elemental zoning, inclusion phase spatial variations, and associated elemental trends (see inset plot for summary of this). The two pyrite generations (Py1 and Py1a) show distinct Au and Ag values and ratios (Fig. 3.18A) that reflect a progression from least modified pyrite (Py1) having low Au:Ag ratios to more modified pyrite (Py1a) with higher Au:Ag ratios. The consistently high Au:Ag ratios (i.e., near 9) are due to the presence of gold inclusions in Py1a, while high Au with almost no Ag (Au:Ag >9) is due to Ag removal from Au-rich zones in pyrite. Color-coding the data points for As, Pb, Cu, and Sb concentrations (Fig. 3.18B-E) highlights the correlations of As, Cu, and Sb with higher Au values that are consistent with their concentrations in the oscillatory and relict/dismembered oscillatory zones of pyrite from the Jerome deposit. The data also show a distinct correlation between Pb and Cu, and to a lesser extent Sb, with higher Ag values due to their incorporation in micro-inclusions (galena, chalcopyrite and tetrahedrite); note however that the high Sb and Cu in the oscillatory zones noted above mask the low level Sb and Cu color scheme in the plot related to the Ag-bearing inclusions.

3.5.4 Characterizing Gold from the Superior Craton (ROM samples)

In order to compare mineral associations, elemental relationships, and textural features of Au from the Jerome and Kenty deposits with other deposits of the AGB, 41 high-grade samples with visible gold from 39 deposits across the AGB were selected for detailed textural, mineralogical (SEM-EDS) and chemical (EMPA) analyses. The results are summarized in Table 3.3.

All of the 219 archived samples from Au deposits in the AGB and elsewhere in Ontario and Quebec show gold filling late fractures in a quartz-dominated host (e.g., Fig. 3.1) or less commonly in metasedimentary, metavolcanic or felsic intrusive host rocks. Thus, it is noted that where coarse visible gold is present, its setting and texture are similar across the suite of samples, regardless of the Au deposit type or host. Gold in all 41 sub-samples (Table 3.3) contain both Hg (up to 4 wt. %) and Cu (up to 1600 ppm). Other elements analyzed (e.g., Sb, Te, and Bi) generally yielded values below detection limits (Table 3.3). In half of the 41 sub-samples, elements such as Te, Sb, Bi, Pb, Hg, Ni, Cu, As were present in various tellurides (petzite, calaverite, hessite, altaite, coloradoite, tellurobismuthite, melonite, and montbrayite), sulfosalts (tetrahedrite, tetradymite, ullmannite, and zinkenite), antimonides (aurostibite), and native Te. In all cases, these minerals are paragenetically associated with native gold. Thus many of the LMCE discussed previously are present in the studied samples. Of particular note are the gold samples from the Kirkland Lake and Red Lake districts, as they contain many of the Te and Sb phases respectively (Table 3.3). Lastly, gold from most of the deposits has a fineness of ≈ 900 or greater with a Au:Ag ratio of 9:1.

3.6 Discussion and Implications

The Au-mineralized samples from the Jerome and Kenty deposits provide strong evidence for multiple stages of Au mineralization that commence with early invisible Au in pyrite and end with visible gold in late fractures. How early Au was incorporated into pyrite and subsequently liberated and transported to form coarse visible gold (Fig. 3.1) is addressed below.

3.6.1 Interpretation of Au Stages at the Jerome Deposit

Oscillatory zoning is exceptionally well developed in Py1, mainly due to varying As content (Figs. 3.7, 3.8). This zoning crosses irregular internal boundaries between Py1 and Py1a (Fig. 3.8A, F) and, in addition, is present in Py1a as relict and dismembered patches of oscillatory-zoned pyrite (Fig. 3.8A, E). These zones contain between 500 to 5000 ppm Au with Au:Ag ratios close to 9, whereas other similarly zoned pyrites from the same sample have Au:Ag ratios closer to 1. In contrast to Py1, Py1a shows porous and inclusion-rich textures (Figs. 3.7, 3.8), which are strong evidence for CDR reactions (Putnis, 2002, 2009; Velásquez et al., 2014; Fougerouse et al., 2016b; Fig. 3.2). These textures suggest that a fluid dissolved earlier Py1 and it was re-precipitated as Py1a. Commensurate with this process, elements previously bound in Py1 were liberated, decoupled, and re-precipitated as inclusions and lattice-bound elements in Py1a, as evident in both the SEM images (Figs. 3.7, 3.8) and elemental maps (Figs. 3.9, 3.10). Chalcopyrite, tetrahedrite, gersdorffite and tetrahedrite inclusions that resulted from this process occur in isolation but are also commonly found as multi-phase inclusions showing textural equilibrium (Fig. 3.7A, B). This suggests that these phases are coeval and their textures are consistent with formation from a melt, which has also been the interpretation for similar LMCE-bearing, multi-phase inclusions elsewhere (Frost et al., 2002).

Inclusions in Py1a provide further insight into the composition of the fluid involved in the CDR reactions. The formation of Ccp and Hem inclusions in Py1a indicates Fe^{2+} was oxidized to Fe^{3+} in the presence of a fluid. This fluid reacted with Py1 and via CDR reactions liberated Au and other elements. This internal remobilization of elements culminated in

formation of native gold and associated mineral inclusions now hosted in the new pyrite (Py1a) that replaced the precursor pyrite (Py1).

The remobilization of Au from pyrite can be assessed by comparing the concentration of Au in early pyrite (Py1) to the total amount of native gold observed. If we assume a concentration of 100 ppm Au in pyrite, a pyrite density of 5.02 g/cm^3, and a gold density of 19.32 g/cm, then 1 cm^3 of gold could be created from 38,486 cm^3 (33.76 x 33.76 x 33.76 cm) of pyrite. This is similar to calculations performed by others (Mumin et al., 1994; Velasquez et al., 2014). To assess this from thin section requires a two-dimensional approach therefore a grain of pyrite 33.76 x 33.76 cm can yield a gold grain 1 x 1 cm (i.e., pyrite area is ≈1100 times greater than gold area). The total area of pyrite and gold from thin sections (n=10) were calculated using the measure and threshold tools in ImageJ. This assumes that the thin sections are representative of the relative amounts of pyrite versus visible gold at the Jerome deposit and that the Py1a represents only 50 % of the total pyrite based on petrographic observations (e.g., Fig. 3.8A). The measured area of Py1a is over 20,000 times greater than that of gold inclusions. This means that the amount of Py1a observed can account for the visible gold in these sections, particularly since pyrite at Jerome contains up to 10 times more gold than used in this calculation (Table 3.2) and this also highlights the strong possibility that some Au has been lost from the system.

3.6.2 Interpretation of Au Stages at the Kenty Deposit

The increased abundance of pyrite and ankerite in the alteration halo to the main quartz-feldspar vein at the C1 Mortimer trench suggests pyrite mineralization is linked to the emplacement of the vein. The early pyrite (Py1) exhibits oscillatory zoning defined by Ni-Co-As-rich bands, has somewhat patchy but relatively homogenous Au associated with Ag, Te, Sb, and Ti, and has

Au:Ag ratios <1 (e.g., distal pyrite as an analogue); as such, it represents the first stage of Au mineralization at the Kenty deposit.

The replacement of oscillatory zones in Py1 by pore- and inclusion-rich pyrite (Py1a) represents the second stage of Au mineralization during which Au was liberated from Py1 and precipitated as inclusions in Py1a and native gold exterior to pyrite (e.g., medial and proximal pyrites as an analogue). There is also a gradual shift in the Au:Ag ratios from <1 in Py1(i.e., distal) to ≥ 9 in highly modified Py1a (i.e., proximal), which indicates that Ag has been removed during dissolution and the result is native gold both inside and outside the pyrite with a higher fineness (i.e., 900). Evidence for a fluid that could have oxidized Ag relative to gold is shown by chalcopyrite inclusions and hematite rims on pyrite indicating oxidation of $Fe^{2+}$to Fe^{3+} similar to Jerome.

The presence of pores, which form by dissolution, and inclusions, which form by precipitation, are indicative of CDR reactions in the presence of a fluid (Putnis 2009). Further evidence for the coupling of these reactions is given by the presence of other elements such as Ag, Te, Sb, Cu, As and Ti, which were liberated during the dissolution of the oscillatory bands and porosity development. These elements were subsequently incorporated into newly formed inclusions of galena, chalcopyrite and rutile that occlude pores.

That native gold lines conjugate fractures cutting the quartz-feldspar vein along with the presence of rutile-gold intergrowths outside the pyrite grains also suggest that Au was also mobilized from pyrite grains. The rutile-gold intergrowths are overprinted by micro-folds with axial planes parallel to that of the folded quartz-feldspar vein. Because the shortening direction for the formation of the folds and conjugate fractures is the same, and gold fills the fractures and

was therefore mobilized during their formation, it follows that gold was mobilized during folding and deformation of the quartz-feldspar vein. The latter acted as a planar anisotropy that localized deformation and micro-fracturing. In addition, this vein-host rock contact also focused the flow of fluids that caused the gradual changes in the textures and chemistries of pyrite as these fluids penetrated the wall rocks to the vein.

At the Mortimer Camp stripping, the presence of native gold and Au-Ag tellurides in fractures cutting quartz-feldspar veins indicate their late timing relative to quartz. The lack of alteration or pyrite mineralization associated with these fractures suggests that a mechanism other than remobilization by Au in solution was responsible for the deposition of gold along these fractures. First the curvilinear and lobate grain boundaries between native gold and petzite (Fig. 3.13D), and the presence of both hessite and calaverite in the same fractures indicate that gold and telluride minerals formed at the same time. Petzite has low interfacial angles with quartz (Fig. 3.13D), suggesting that it crystallized from a melt that wetted quartz grain boundaries (Frost et al., 2002). Second, the modal proportions of these minerals (i.e., petzite > Au > hessiste > calaverite) place this assemblage in the melting field of the Au-Ag-Te system at temperatures of 335°C (Cabri, 1965; Tomkins et al., 2004), well below the expected metamorphic temperatures for the region (350-450°C; Heather, 2001; Thompson, 2005). Collectively this evidence strongly suggests that Au was transported as a Au-Ag-Te melt. These elements were likely liberated from pyrite elsewhere, as shown by the progressive loss of Au, Ag, and Te from pyrite during CDR at the nearby C1 Mortimer trench.

As with Jerome but requiring a larger scale approach, the remobilization of Au from pyrite can be generally tested at Kenty from field observations and mass balance calculations. We have used the approximate dimensions of pyrite bearing altered rock as 50 x 10 x 2 m and a

modal abundance of 3% pyrite based on outcrop measurements and conservative visual estimates (e.g., Fig. 3.11A, B). The assumption made in this case is that the C1 Mortimer trench is representative of the relative amounts of pyrite versus visible gold. From the earlier calculations using 100 ppm Au in pyrite and the densities for pyrite and gold, we know that 38,486 cm^3 (or 1.93 x 10^5 g) of pyrite are required to yield 1 cm3 (19.32 g) of gold. The amount of visible gold recovered and estimated at the C1 Mortimer trench is approximately 2 cm^3 (or 38.64 g) based on observations. This means that 3.86 x 10^5 g of pyrite are required to account for this gold. If we reduce the volume of pyrite by 50% to account for Au still in pyrite and use the outcrop dimensions and pyrite modal abundance noted above the calculated amount of pyrite is 7.53 x10^7 g. As with Jerome the pyrite at Kenty can more than account for the abundance of visible gold observed since the pyrite contains several times more gold than used in the calculation (Table 3.2). This again highlights the strong possibility that some Au has been removed from the observed system due to remobilization.

3.6.3 Incorporation of Au into Early Pyrite

The strongly zoned arsenian pyrite associated with early Au at the Jerome deposit is used to address how invisible Au was incorporated into the early pyrite. The SEM-EDS line scan across Py1 in Figure 3.8D shows that chemical zoning and Au incorporation are predominantly controlled by As substituting for S since they have a near-perfect negative correlation. The following discussion addresses two separate but related phenomena: (1) the origin of oscillatory zoning and sector zoning in pyrite; and (2) how this relates to primary Au enrichment in pyrite.

Different models have addressed formation of oscillatory zoning in pyrite, especially auriferous pyrite. Peterson and Mavrogenes (2014) suggested that oscillatory zoning results from

periodic and repetitive changes in fluid chemistry, such as pulses of Au- and As-rich fluids, possibly related to seismic events. In contrast, Fougerouse et al. (2016b) later argued for growth-rate controlled Au incorporation in arsenian pyrite by local disequilibrium at fluid-mineral interfaces, whereby Au is incorporated due to local S depletion at fluid-mineral growth interfaces during rapid crystal growth. Substitution of As into S sites would distort the structure of pyrite and promote the deposition and concentration of Au along the pyrite growth interface. When S concentrations are restored in the fluid next to the growth interfaces, its incorporation into pyrite resumes without As substitution and therefore Au deposition terminates. The latter process would generate oscillatory zoning with As-Au-rich and S depleted zones alternating with stoichiometric zones lacking As and Au. These findings are corroborated by the experimental studies of Kusebauch et al. (2018) on As substitution for S in Au-rich pyrite.

The significance of having both oscillatory and sector zoning in pyrite, as observed at the Jerome deposit, has been overlooked in other studies, such as Peterson and Mavrogenes (2014) where both textural varieties of pyrite noted herein were documented. Sector zoning is a rapid growth phenomenon centered about a nucleation point or "seed" that promotes growth of crystal faces having distinct stereochemical properties, which is a differing spatial arrangement of their outward facing atoms (Hollister, 1970; Dowty, 1976; Chouinard et al., 2005). Crystal faces accept different substitutions of trace elements (e.g., As) according to their outward facing atomic arrangements and these differ between adjacent sectors (Hollister, 1970; Dowty, 1976; Chouinard et al., 2005). As substitution in S sites and incorporation of Au can occur at the same time as other trace elements (e.g., Ni-Co substituting for Fe) are added to adjacent crystal faces; both oscillatory and sector zoning can develop simultaneously during the growth of pyrite. Although it is conceivable that oscillatory zones could be due to pulses of Au- and As-rich

fluids, as suggested by Peterson and Mavrogenes (2014), sector zoning depends on atomic arrangement along crystal faces rather than fluid chemistries. Thus, our observations support the incorporation of Au in As-enriched zones of pyrite due to local disequilibrium at fluid-mineral interfaces likely during the rapid growth of pyrite, as suggested by Fougerouse et al. (2016b).

3.6.4 Application of Indicator Elements to Au Remobilization and Exploration

Examination of the Jerome, Kenty, and archived samples from the ROM deposits indicate that of the elements associated with primary Au-Ag mineralization (i.e., As, Cu, Sb, Bi, Pb, Te and Hg), it is Te and Hg that show the strongest associations with "Au-dominant" deposits. Hg is in all analyzed gold samples (Table 3.3). Tellurides can contain Au (i.e., petzite (Ag3AuTe2) and calaverite (AuTe2)), have a close spatial association with native gold, and in many cases show mutual boundary textures indicating similar timing with gold. They are also associated with many large, high-grade Au deposits from the ROM suite of samples (Sigma, Lamaque, Robb-Montbray, Vipond, Ashley, Preston East Dome, Powell, Upper Canada, Vedron, and Kirkland Lake: Macassa, Tough Oakes, Lakeshore, Teck Hughes; Table 3.3). The other noted elements (As, Cu, Sb, Bi, Pb) are commonly hosted in secondary phases within and exterior to pyrite, which highlights the decoupling of Ag from Au as noted in the pyrites of this study (Figs. 3.16, 3.17, 3.18). Using these other elements to target Au has been a valid exploration model for many years, but these are just as likely to find Cu and Ag mineralization as they are to find Au mineralization.

The conclusions inferred from the textures, mineralogical features and geochemistry of the Kenty and Jerome samples provides the basis to assess the data for the ROM samples (Table 3.3). Thus, extrapolating from the conclusions inferred above it follows that the chemistry of the

coarse gold (i.e., 900 fineness in almost all samples; Table 3.3) and its associated mineralogy together suggest this gold most likely originated from similar Au remobilization and Au-Ag decoupling processes as the visible gold at the studied deposits. These implications are significant and suggest the widespread occurrence of coarse gold reflects remobilization from an earlier stage of Au enrichment. Our data would strongly suggest that the origin of this gold is from auriferous pyrite (i.e., invisible Au).

The Au:Ag ratios, Au fineness and associated elements defined above (Hg and Te) provide the basis to apply such chemical indicators to other datasets, such as whole-rock geochemistry. The Au and Ag data has the potential to predict the host phase for Au present in a whole-rock sample. Considering that remobilized Au has a fineness of ≈ 900 in Au deposits, particularly in metamorphic terranes (Figs. 3.16, 3.17, 3.18 and Table 3.3), then Au:Ag ratios in whole-rock samples close to 9 would indicate that Au is likely in the form of native gold. In contrast, Au:Ag ratios in whole-rock samples close to 1 would indicate that Au is likely bound in a sulfide phase or only internally remobilized on the scale of the sample as a mixture of native gold and Ag-rich minerals (e.g., tetrahedrite, galena or chalcopyrite). Furthermore, Au:Ag ratios between 9 and 1 would likely indicate a combination of these. This is important from a metallurgical and recovery standpoint and provides important and readily obtained information in the initial stages of a Au exploration program.

3.6.5 Au Remobilization Processes

Three mechanisms may explain the remobilization of Au at the deposits studied: (1) Au concentrations in solution may be higher than previously considered (i.e., fluid-only transport mechanism); (2) gold may be remobilized by solid-state ductile flow; or (3) Au may be

transported as a fluid-mediated, polymetallic melt and/or local Au nanoparticle transport (nanomelts?). These possible models are discussed below.

More traditional fluid-only transport mechanisms, whereby Au is complexed with ligands such as HS- and Cl-, face issues when trying to explain coarse visible gold by remobilization. This is not a particularly efficient remobilization mechanism when considering the massive volumes of fluid required (see calculations in Previous Studies on Au Remobilization section). To account for this Fougerouse et al. (2016a) have suggested remobilization by a fluid that contained higher than normal Au concentrations in solution, however empirical evidence shows that metamorphic fluids contain less than 100 ppb Au (Wagner et al., 2016), therefore we consider this option unlikely. In addition, there is no evidence of new quartz having precipitated within the gold-filled fractures at Kenty nor formation of any associated alteration minerals in or adjacent to these fractures (Fig. 3.12C, F), both of which would provide corroborating evidence for fluid flux related to gold deposition.

Solid-state gold remobilization by ductile flow has been previously discussed (Tomkins et al., 2004) and may potentially be significant, particularly where fractures cut quartz veins or other competent phases (e.g., magnetite, pyrite, arsenopyrite). Solid-state mechanical remobilization of common sulfide minerals (i.e., chalcopyrite, pyrrhotite, sphalerite) is a well-known process and is facilitated at temperatures greater than 250 to 300°C by their high ductility (Cox, 1987; Marshall and Gilligan, 1987, 1993). Because native gold is ductile at room temperature, it would presumably flow easily at greenschist facies conditions. Conjugate fractures at the Kenty deposit, however, are contractional structures that formed during shortening because the plane bisecting the angle between the two sets of fractures is parallel to

the axial plane of the fold. Thus, gold would be forced out rather than forced in during the formation of the conjugate fractures.

Remobilization of Au at the Jerome deposit shares many of the characteristics of the partial melting model of Tomkins et al. (2004, 2007), such as the multi-phase inclusions (chalcopyrite-tetrahedrite-gersdorffite-gold), the LMCE chemistry of the inclusions (i.e., Sb in tetrahedrite and Hg in gold), and the presence of LMCE (Sb, Te, Bi ± Hg) in primary growth zones of pyrite. However, at Jerome our observations suggest it is the dissolution via CDR processes by an oxidizing fluid rather than partial melting of the pyrite that is likely responsible for the liberation of Au. Once liberated, Au could form a melt with LMCE in the presence of the hydrothermal fluid with external transport dependent on fluid pathways available in the host rock. Thus, the liberation of Au from Py1 and its remobilization and deposition as inclusions in Py1a likely resulted from fluid-mediated melt migration. However because this remobilization was on such a small-scale (internal remobilization; Marshall and Gilligan, 1987, 1993), it is difficult to confirm that a similar process operated at other deposits without first identifying multi-phase LMCE-bearing inclusions forming as a result of CDR reactions.

Data from the Jerome deposit shows that pyrite can have significant concentrations of LMCE in its structure. This may imply that, whereas Au deposits may not exhibit significant LMCE dominant minerals, there can be significant amounts of LMCE present in pyrite and other sulfides. Thus, without detailed characterization of these phases it is both difficult to know if LMCE are present and to conclusively evaluate if Au could have been remobilized via fluid-mediated melt migration. The recent widespread application of LA-ICP-MS elemental mapping to sulfides (e.g., pyrite, arsenopyrite) in Au deposits suggests that LMCE are in fact common

(Neyedley et al., 2017; Dubosq et al., 2018; Gourcerol et al., 2018; Kerr et al., 2018), therefore supporting the conclusions herein.

Gold associations and textures at the Mortimer Camp stripping of the Kenty deposit suggest that it was transported and deposited from a polymetallic melt. In this area there are annealed conjugate fractures, which cut quartz veins within Fe-rich basalt and have significant Au and Au-Ag telluride mineralization associated with them (Fig. 3.13). These annealed fractures have no associated pyrite mineralization or alteration haloes of ankerite (Fig. 3.13) as seen elsewhere at the Kenty deposit and in host basalts away from mineralization. This lack of evidence for fluid-rock interaction strongly suggests that gold was not deposited from Au in solution. The low wetting angles (<60°) of petzite with quartz (Fig. 3.13D), the curvilinear grain boundaries of native gold and Au-Ag tellurides, and their modal proportions (petzite > Au > hessiste > calaverite), suggest that these minerals crystallized from a polymetallic melt at regional greenschist facies metamorphic temperatures estimated for the SGB (Heather, 2001; Thompson, 2005). Recent experimental work shows that polymetallic melts can form in the presence of LMCE-bearing hydrothermal fluids (Tooth et al. 2014), which highlights that Au-Ag-Te melts can form in the presence of a fluid during CDR of pyrite.

Gold at the nearby C1 Mortimer trench was remobilized out of pyrite into conjugate fractures that cut a folded quartz vein. Similar to the Mortimer Camp stripping, native gold along the fractures contains Hg and Cu, pyrite grains contain similar concentrations of Au and Te, but Au-Ag telluride minerals are lacking, which raises the possibility that a different process may be responsible for remobilization of this gold. Although the lack of evidence for tellurides does not preclude a polymetallic melt mechanism, it does allow for the possibility of other mechanisms (e.g., nanoparticle gold transport).

Our ongoing research has identified gold nanoparticles of <3 nm size at the C1 Mortimer trench of the Kenty deposit (Hastie et al., 2019). As others have also identified gold nanoparticles in hydrothermal fluids (Hannington and Garbe-Schönberg, 2019), this raises the possibility that nanoparticle transport could be a viable mechanism for remobilization. A significant factor that may be of importance to this issue at the C1 Mortimer trench is the effect of particle size-dependent melting and nanoparticle transport. The melting temperature of Au drops significantly for particle sizes below 50 Å, or 5 nm in diameter (Buffat and Borel, 1976), although this research has had difficulty predicting melting for smaller particles (Castro et al., 1990). In fact, particles <3 nm in diameter can melt at temperatures of ~300°C (Castro et al., 1990; Burda et al., 2005), thus significantly lower than the melting temperature of bulk Au (1064 °C), however the behavior of gold nanoparticles <2 nm is still poorly understood. This particle size-dependent melting phenomenon is best explained as a function of increased surface area to volume ratios of small gold particles relative to larger ones. Having smaller gold particles would increase the free energy in the system and facilitate the change to a more favored liquid phase in an effort to reduce surface energy, since surface energy is lower in the liquid compared to the solid phase (Burda et al., 2005). Importantly, it has also been shown that the effect of increasing pressures on the melting temperature of Au is negligible (Akella and Kennedy, 1971). Increasing the pressure by 5 kbars, well within the temperature and pressure range for most orogenic gold deposits formation, is equivalent to the Au melting temperature increasing by ≈30°C. Unless increased pressure affects particle size-dependent melting in a way we have yet to comprehend, this minor temperature increase would not dramatically effect particle size-dependent melting.

If LMCE are removed from the system prior to polymetallic melt formation or are lacking in Au-rich pyrite, then size-dependent melting could be a significant process for

remobilizing Au from pyrite containing gold nanoparticles <3 nm in size (Hastie et al., 2019). Reich et al. (2006) previously considered this possibility and showed that pyrite can act as a buffer that promotes solid-state dissolution of gold nanoparticles before a phase transition from solid to liquid Au can occur. During their heating experiment, gold nanoparticles <2 nm in size began to dissolve into their host pyrite matrix at 370°C and coarsened into larger gold nanoparticles above this temperature by solid-state Ostwald ripening (Reich et al., 2006). However, if pyrite has undergone dissolution by a fluid at 250 to 400°C, the liberated gold nanoparticles could have melted in the presence of this fluid according to the particle size-dependent melting curve (Buffat and Borel, 1976; Castro et al., 1990; Burda et al., 2005). Thus, Au could still be mobilized via fluid-mediated melt migration (i.e., Au-Ag-only nanomelt) until coming into contact with other gold nanoparticles (or nanomelts), which would facilitate coarsening into bulk gold. This particle size-dependent melting, or evidence for nanoparticle transport in general, could help explain local, high-grade Au-Ag remobilization that lacks LMCE versus regional, high-grade Au-Ag-Te mineralization such as at the Kenty deposit.

The concept of an open versus relatively closed system can further help explain the possible Au remobilization mechanisms. These processes rely upon the ability of Au to come into contact with LMCE or not. In the former case, polymetallic melts that coexist with a fluid can migrate further from the original site of mineralization (external remobilization). In contrast, where nanoparticle gold is not in contact with LMCE, hence lacking the ability to form a polymetallic melt as above, it will only migrate locally (internal remobilization). In both cases, the dominant deposition site for the remobilized Au is fractured quartz, a favorable structural trap (Fig. 3.1), particularly in the hinges of folds.

3.6.6 A Model for Au Remobilization

A schematic diagram summarizing pyrite textural evolution and related Au mineralization is presented in Figure 3.19. The diagram merges observations from this study with the various remobilization models and concepts presented above. In this regard, we note that aspects related to Au at the nano-scale should be considered conceptual until future research better defines the behavior of gold nanoparticles or nanomelts in orogenic Au deposits.

Initial fracturing of the Fe-rich host rock allowed for the ingress of hydrothermal fluids and commensurate alteration, which resulted in formation of ankerite and oscillatory zoned, auriferous pyrite grains (Py1; Fig. 3.19A). These fractures were subsequently sealed with quartz, feldspar, and ankerite to form the veins (Fig. 3.19B). Deformation and metamorphism allowed continued fluid infiltration via conjugate fractures (Fig. 3.19C). These later fluids dissolved the early pyrite and promoted development of its porous texture which allowed Au and other trace elements (e.g., LMCE) to be liberated and mobilized from pyrite. Commensurate with this were the formation of modified pyrite grains (Py1a) and the formation of mineral inclusions and gold that could precipitate in the modified pyrite (Py1a; Fig. 3.19D) or pores created in Py1. Furthermore, elements could also be transported to the exterior of the pyrite (Fig. 3.19E, F). Note that in this model, we do not note the development of completely new pyrite grains devoid of inclusions or vestiges of the precursor pyrite (Py1), although in theory this should happen and indeed is observed where CDR occurs (Putnis, 2002, 2009).

Gold transported as nanoparticles (or nanomelts?) in the proposed model (Fig. 3.19E) would only account for local, centimeter- to meter-scale, remobilization unless other influences, such as LMCE, maintained these elements in the melt phase. In this case, gold would have

precipitated as a result of agglomeration when Au domains exceeded >3 nm. This accounts for native gold found in fractures crossing pyrite grains, micro-folded gold-rutile trails and intergrowths in host rocks, and gold in fractures cutting quartz veins. In contrast, regional, meter- to kilometer-scale transport of Au-Ag-Te melts migrated away from primary mineralization to form native Au, petzite, hessite and calaverite in fractures that cross-cut quartz veins (Fig. 3.19F). The competency contrast between host rocks and quartz veins (or other rheologically similar host rocks) would allow fractures to preferentially form in the quartz while the host rock underwent ductile deformation.

These mechanisms best explain many of the observations of this and other studies: (1) the porous textures of early Au-bearing sulfides (i.e., pyrite, arsenopyrite) observed in many deposits; (2) the presence of gold filling late fractures in quartz veins; and 3) abundance of coarse, visible gold in many large deposits. Although a fluid is required to initiate the CDR process which liberates Au from the pyrite structure between 250°C to 400°C, the remobilization of Au may not necessarily involve the transport of Au in a fluid as a dissolved species (e.g., Au(HS)2- or AuCl2-). Indeed, evidence for LMCE presented in this study at both the Jerome (Sb), Kenty (Te), and many historic Au districts such as Red Lake (Sb) and Kirkland Lake (Te) suggest that fluid-mediated, Au-rich, Te- and Sb-bearing melts may be a significant contributor to the upgrading of Au deposits during remobilization processes.

3.7 Conclusions

This study has shown that the presence of high-grade Au zones with visible Au from two deposits in the Archean Swayze greenstone belt formed by the conjunction of several processes: (1) fluid-assisted liberation of Au from early hydrothermal pyrite enriched in LMCE; (2) remobilization of Au by fluid-mediated, LMCE-rich melts and/or Au-Ag nanoparticles (nanomelts?); and (3) deposition of gold in fractures cutting across quartz veins and in other structurally favorable sites. The Au fineness varies from ≈ 400 to 500 in the earliest stage pyrite to ≈ 900 in the later coarse visible gold seen in fractures and quartz veins.

More specifically, our study has furthered the understanding of primary Au mineralization and remobilization by: (1) disproving the fluid pulse model for As-Au oscillatory zoning in pyrite since it fails to explain sector zoning in the same pyrite grains; (2) showing that LMCE that can cause melting are present in significant concentrations in pyrite; (3) presenting evidence for Archean Au remobilization by fluid-mediated Au-Ag-Te melts at greenschist facies conditions (Kenty deposit); (4) suggesting that fluid-mediated LMCE melts may have played an important role in the formation of high grade Au zones in giant mining districts (Kirkland Lake, Te melts; Red Lake, Sb melts); and (5) explaining for the first time why a gold fineness of ≈ 900 is common in high-grade deposits across the Au-rich Abitibi greenstone belt and elsewhere in Ontario and Quebec, this commonality being due to Au remobilization from early Au-bearing pyrite and other Au-bearing sulfides.

Our results have important implications for Au exploration in terms of host minerals, associated elements, and structural traps. Specific implications from this study indicate that: (1) readily obtained Au:Ag ratios from whole-rock samples could indicate the host phase for Au,

which is important for selecting projects that are viable from a metallurgical and recovery standpoint; (2) Hg and Te should be considered high-priority indicator elements when exploring for Au-dominant systems; and (3) a good understanding of local deformation features, specifically fold hinges, conjugate fracture sets and other favorable structural traps, is integral for understanding high-grade ore zone geometry. Collectively, these features should be considered paramount when targeting high-grade ore zones in Au systems.

3.8 References

Akella, J., and Kennedy, G.C., 1971, Melting of gold, silver and copper – Proposal for a new high-pressure calibration scale: Journal of Geophysical Research, v. 76, no. 20, p. 4969-4977.

Ayer, J.A., Goutier, J., Thurston, P.C., Dubé, B., and Kamber, B.S., 2010, Tectonic and metallogenic evolution of the Abitibi and Wawa subprovinces: in Summary of Field Work and Other Activities, 2010, Ontario Geological Survey, Open File Report 6260, p. 3-1 to 3-6.

Ayer, J.A., Ketchum, J.W.F., and Trowell, N.F., 2002, New geochronological and neodymium isotopic results from the Abitibi greenstone belt, with emphasis on the timing and the tectonic implications of Neoarchean sedimentation and volcanism: in Summary of Field Work and Other Activities, 2002, Ontario Geological Survey, Open File Report 6100, p. 5-1 to 5-16.

Bodnar R.J., Lecumberri-Sanchez P., Moncada D. and Steele-MacInnis M., 2014, Fluid Inclusions in Hydrothermal Ore Deposits. In: Holland H.D. and Turekian K.K. (eds.) Treatise on Geochemistry, Second Edition, v. 13, p. 119-142. Oxford: Elsevier.

Brown, W.L., 1948, Jerome Mine: in Structural Geology of Canadian Ore Deposits – A Symposium. Special Volume 1. Canadian institute of Mining and Metallurgy. Mercury Press Limited, Montreal, Quebec, p. 438-441.

Buffat, Ph., and Borel, J-P., 1976, Size effect on the melting temperature of gold particles: Physical Review A, v. 13, p. 2287-2298.

Burda, C., Chen, X., Narayanan, R., and El-Sayed, M.A., 2005, Chemistry and properties of nanocrystals of different shapes: Chemical Reviews, v. 105, p. 1025-1102.

Burt, P.D., Chance, P.N., and Burns, J.G., 2011, Technical report on a resource estimate on the Jerome mine property, Osway Township, Porcupine Mining Division, Ontario, prepared for Augen Gold Corporation: Augen Gold Corp., NI 43-101 Technical Report, filed August 29, 2011 with SEDAR®, see SEDAR Home Page, 92 p.

Cabri, L.J., 1965, Phase relations in the Au-Ag-Te system and their mineralogical significance: ECONOMIC GEOLOGY, v. 60, p. 1569-1606.

Castro, T., Reifenberger, R., Choi, E., and Andres, R.P., 1990, Size-dependent melting temperature of individual nanometer-sized metallic clusters: Physical Review B, v. 42, p. 8548-8556.

Chouinard, A., Paquette, J., and Williams-Jones, A.E., 2005, Crystallographic controls on trace-element incorporation in auriferous pyrite from the Pascua epithermal high-sulfidation deposit, Chile-Argentina: The Canadian Mineralogist, v. 43, p. 951-963.

Cox, S.F., 1987, Flow mechanisms in sulphide minerals: Ore Geology Reviews, v.2, p. 133-171.

Dowty, E., 1976, Crystal structure and crystal growth: II. Sector zoning in minerals: American Mineralogist, v. 61, p. 460-469.

Dubé, B., and Gosselin, P., 2007, Greenstone-hosted quartz-carbonate vein deposits: in Goodfellow, W.D., ed., Mineral deposits of Canada: A synthesis of major deposit-types, district metallogeny, the evolution of geological provinces, and exploration methods: Geological Association of Canada, Mineral Deposits Division, Special Publication no. 5, p. 49-73.

Dubosq, R., Lawley, C.J.M., Rogowitz, A., Schneider, D.A., and Jackson, S., 2018, Pyrite deformation and connections to gold mobility: Insight from micro-structural analysis and trace element mapping: Lithos, 310-311, 86-104.

Fougerouse, D., Micklethwaite, S., Tomkins, A.G., Mei, Y., Kilburn, M., Guagliardo, P., Fisher, L.A., Halfpenny, A., Gee, M., Paterson, D., and Howard, D.L., 2016a, Gold remobilisation and formation of high grade ore shoots driven by dissolution-reprecipitation replacement and Ni substitution into auriferous arsenopyrite: Geochimica et Cosmochimica Acta, v. 178, p. 143-159.

Fougerouse, D., Reddy, S.M., Saxey, D.W., Rickard, W.D.A., van Riessen, A., and Micklethwaite, S., 2016b, Nanoscale gold clusters in arsenopyrite controlled by growth rate not concentration: Evidence from atom probe microscopy: American Mineralogist, v. 101, p. 1916-1919.

Fougerouse, D., Micklethwaite, S., Ulrich, S., Miller, J., Godel, B., Adams, D.T., and McCuaig, T.C., 2017, Evidence for two stages of mineralization in West Africa's largest gold deposit: Obuasi, Ghana: ECONOMIC GEOLOGY, v. 112, p. 3-22.

Frost, B.R., Mavrogenes, J.A., and Tomkins, A.G., 2002, Partial meting of sulphide ore deposits during medium- and high-grade metamorphism: The Canadian Mineralogist, v. 40, p. 1-18.

Fumerton, S., and Houle, K., 1995, Mineral prospects of the Swayze greenstone belt, Volume 1 — parts of NTS 41 O, and Volume 2 — parts of NTS 41 P, 42 A and 42 B: Ontario Geological Survey, Open File Report 5912, v.1, p. 1-372.

Gartman, A., Hannington, M., Jamieson, J.W., Peterkin, B., Garbe-Schönberg, Findlay, A.J., Fuchs, S., and Kwasnitschka, 2018, Boiling-induced formation of colloidal gold in black smoker hydrothermal fluids: Geology, v. 46, no. 1, p. 39-42.

Goldfarb, R.J., Baker, T., Dubé, B., Groves, D.I., Hart, C.J.R., and Gosselin, P., 2005, Distribution, character, and genesis of gold deposits in metamorphic terranes: ECONOMIC GEOLOGY 100th Anniversary Volume, p. 407-450.

Gourcerol, B., Kontak, D.J., Thurston, P.C., and Petrus, J.A., 2018, Application of LA ICP-MS sulphide analysis and methodology for deciphering elemental paragenesis and associations in addition to multi-stage processes in metamorphic gold settings: The Canadian Mineralogist v. 56 (1), p. 39-64.

Groves, D.I., Goldfarb, R.J., Robert, F., and Hart, C.J.R., 2003, Gold deposits in metamorphic belts: Overview of current understanding, outstanding problems, future research, and exploration significance: ECONOMIC GEOLOGY, v.98, p.1-29.

Guillong, M., Hametner, K., Reusser, E., Wilson, S.A., and Günther, D., 2005, Preliminary characterisation of new glass reference materials (GSA-1G, GSC-1G, GSD-1G and GSE-1G) by

laser ablation-inductively coupled plasma-mass spectrometry using 193 nm, 213 nm and 266 nm wavelengths: Geostandards and Geoanalytical Research, v. 29, no. 3, p. 315-331.

Hannington, M., Hardardóttir, V., Garbe-Schönberg, D., and Brown, K.L., 2016, Gold enrichment in active geothermal systems by accumulating colloidal suspensions: Nature Geoscience v. 9, p. 299-302.

Hannington, M., and Garbe-Schönberg, D., 2019, Detection of gold nanoparticles in hydrothermal fluids: ECONOMIC GEOLOGY, v. 114, p. 397-400.

Hastie, E.C.G., 2014, Gold metallogeny of the southern Swayze greenstone belt: in Summary of Field Work and Other Activities, 2014, Ontario Geological Survey, Open File Report 6300, p. 7-1 to 7-8.

Hastie, E.C.G., 2017, Gold metallogeny of the southern Swayze area, Abitibi greenstone belt: a field trip guidebook: Ontario Geological Survey, Open File Report 6334, 19 p.

Hastie, E.C.G., Lafrance, B., and Kontak, D.J., 2015, Observations on the Kenty and Rundle deposits, Swayze greenstone belt: in Summary of Field Work and Other Activities, 2015, Ontario Geological Survey, Open File Report 6313, p. 9-1 to 9-9.

Hastie, E.C.G., Kontak, D.J., and Lafrance, B., 2016, Update on activities related to a gold metallogenic study of the southern Swayze greenstone belt: in Summary of Field Work and Other Activities 2016, Ontario Geological Survey, Open File Report 6323, p. 8-1 to 8-11.

Hastie, E.C.G., Kontak, D.J., Lafrance, B., and Schindler, M., 2019, On the nature and origin of Dubéesque gold in the Abitibi and beyond: GAC-MAC, Quebec City, 2019, Abstracts, p. 104-105.

Heather, K.B., 2001, The geological evolution of the Archean Swayze greenstone belt, Superior Province, Canada: unpublished PhD thesis, Keele University, Keele, England, 370 p.

Hollister, L.S., 1970, Origin, mechanism, and consequences of compositional sector-zoning in staurolite: American Mineralogist, v. 55, p. 742-766.

Jochum, K.P., Weis, U., Stoll, B., Kuzmin, D., Yang, Q., Raczek, I., Jacob, D.E., Stracke, A., Birbaum, K., Frick, D.A., Günther, D., and Enzweiler, J., 2011, Determination of reference values for NIST SRM 610-617 glasses following ISO guidelines: Geostandards and Geoanalytical Research, v.35, no. 4, p. 397-429.

Jochum, K.P., Willbold, M., Raczek, I., Stoll, B., and Herwig, K., 2005, Chemical characterisation of the USGS reference glasses GSA-1G, GSC-1G, GSD-1G, GSE-1G, BCR-2G, BHVO-2G and BIR-1G using EMPA, ID-TIMS, ID-ICP-MS and LA-ICP-MS: Geostandards and Geoanalytical Research, v.29, no. 3, p. 285-302.

Joy, D.C., 1995, Monte Carlo Modeling for Microscopy and Microanalysis: Oxford University Press, 224 p.

Katz, L.R., Kontak, D.J., Dubé, B., and McNicoll, V., 2017, The geology, petrology, and geochronology of the Archean Côté Gold large-tonnage, low-grade intrusion-related Au(-Cu)

deposit, Swayze greenstone belt, Ontario, Canada: Canadian Journal of Earth Sciences, v. 54, p. 173-202.

Kerr, M.J., Hanley, J.J., Kontak, D.J., Morrison, G.G., Petrus, J., Fayek, M., and Zajacz, Z., 2018, Evidence of upgrading of gold tenor in an orogenic quartz-carbonate vein system by late magmatic-hydrothermal fluids at the Madrid deposit, Hope Bay greenstone belt, Nunavut, Canada: Geochimica et Cosmochimica Acta, v. 241, p. 180-218.

Kusebauch, C., Oelze, M., and Gleeson, S.A., 2018, Partitioning of arsenic between hydrothermal fluid and pyrite during experimental siderite replacement: Chemical Geology, v. 500, p. 136-147.

Larocque, A.C.L., Hodgson, C.J., Cabri, L.J., and Jackman, J.A., 1995, Ion microprobe analysis of pyrite, chalcopyrite and pyrrhotite from the Mobrun VMS deposit in northwestern Quebec: Evidence for metamorphic remobilization of gold: The Canadian Mineralogist, v. 33, p. 373-388.

Lawley, C.J.M., Jackson, S., Yang, Z., Davis, W., and Eglington, B., 2017, Tracing the transition of gold from source to sponge to sink: ECONOMIC GEOLOGY, v. 112, p. 169-183.

Li, W., Cook, N.J., Ciobanu, C.L., Xie, G., Wade, B.P., and Gilbert, S.E., 2019, Trace element distributions in (Cu)-Pb-Sb sulfosalts from the Gutaishan Au-Sb deposit, South China: Implications for formation of high fineness native gold.

MacDonald, P.J., Hastie, E.C.G., and Davis, D.W., 2017, Preliminary geology of Osway and Huffman Townships and parts of Eric, Fingal and Arbutus Townships, southern Swayze area, Abitibi greenstone belt: in Summary of Field Work and Other Activities 2017, Ontario Geological Survey, Open File Report 6333, p. 7-1 to 7-13.

Marshall, B., and Gilligan, L.B., 1987, An introduction to remobilization: information from ore-body geometry and experimental considerations: Ore Geology Reviews, v. 2, p. 87-131.

Marshall, B., and Gilligan, L.B., 1993, Remobilization, syn-tectonic processes and massive sulphide deposit: Ore Geology Reviews, v. 8, p. 39-64.

Morrison, G.W., Rose, W.J., and Jaireth, S., 1991, Geological and geochemical controls on the silver content (fineness) of gold in gold-silver deposits: Ore Geology Reviews, v. 6, p. 333-364.

Mumin, A.H., Fleet, M.E., and Chryssoulis, S.L., 1994, Gold mineralization in As-rich mesothermal gold ores of the Bogosu-Prestea mining district of the Ashanti gold belt, Ghana: Remobilization of "invisible" gold: Mineralium Deposita, v. 29, p. 445-460.

Neyedley, K., Hanley, J.J., Fayek, M., and Kontak, D.J., 2017, Textural, fluid inclusion, and stable oxygen isotope constraints on vein formation and gold precipitation at the 007 deposit, Rice Lake greenstone belt, Bissett, Manitoba, Canada: ECONOMIC GEOLOGY, v. 112, p. 629-660.

Ontario Geological Survey, 2011, 1:250 000 scale bedrock geology of Ontario: Ontario Geological Survey, Miscellaneous Release—Data 126–Revision 1.

Pal'yanova, G., 2008, Physiochemical modeling of the coupled behavior of gold and silver in hydrothermal processes: Gold fineness, Au/Ag ratios and their possible implications: Chemical Geology, v. 255, p. 399-413.

Peterson, E.C., and Mavrogenes, J.A., 2014, Linking high-grade gold mineralization to earthquake-induced fault-valve processes in the Porgera gold deposit, Papua New Guinea: Geology, v. 42, p. 383-386.

Phillips, G.N., and Powell, R., 2010, Formation of gold deposits: a metamorphic devolatilization model: Journal of Metamorphic Geology, v. 28, p. 689-718.

Pitcairn, I.K., Teagle, D.A.H., Craw, D., Olivo, G.R., Kerrich, R., and Brewer, T.S., 2006, Sources of metals and fluids in orogenic gold deposits: Insights from the Otago and Alpine schists, New Zealand: ECONOMIC GEOLOGY, v. 101, p. 1525-1546.

Putnis, A., 2002, Mineral replacement reactions: from macroscopic observations to microscopic mechanisms: Mineralogical Magazine, V. 66, p. 689-708.

Putnis, A., 2009, Mineral replacement reactions: Reviews in Mineralogy and Geochemistry, v. 70, p. 87-124.

Reich, M., Utsunomiya, S., Kesler, S.E., Wang, L., Ewing, R.C., and Becker, U., 2006, Thermal behavior of metal nanoparticles in geologic materials: Geology, v. 34, no. 12, p.1033-1036.

Ridley J.R., and Diamond L.W., 2000, Fluid chemistry of lode-gold deposits and implications for genetic models. In: Hagemann S.G., Brown P. (Eds.), Gold in 2000. Reviews in Economic Geology. Society of Economic Geologists, Inc., v. 13, p. 141-162.

Robert, F., 2001, Syenite-associated disseminated gold deposits in the Abitibi greenstone belt, Canada: Mineralium Deposita, v. 36, p. 503-516.

Saunders, J.A., 1990, Colloidal transport of gold and silica in epithermal precious metal systems: Evidence from the Sleeper deposit, Nevada: Geology, v.18, p. 757-760.

Schneider, C.A., Rasband, W.S., and Eliceiri, K.W., 2012, NIH Image to ImageJ: 25 years of image analysis: Nature Methods v. 9, p. 671-675.

Shore, M., and Fowler, A.D., 1996, Oscillatory zoning in minerals: A common phenomenon: The Canadian Mineralogist, v. 34, p. 1111-1126.

Simmons, S.F., and Brown, K.L., 2007, The flux of gold and related metals through a volcanic arc, Taupo Volcanic Zone, New Zealand: Geology, v. 35, no. 12, p.1099-1102.

Steele-MacInnis, M., 2018, Fluid inclusions in the system H2O-NaCl-CO2: An algorithm to determine composition, density and isochore: Chemical Geology, v. 498, p. 31-44.

Thompson, P.H., 2005, A new metamorphic framework for gold exploration in the Timmins-Kirkland Lake area, western Abitibi greenstone belt: Discover Abitibi Initiative; Ontario Geological Survey, Open File Report 6162, 104p.

Sylvester, P.C., Cabri, L.J., Turbett, M.N., McMahon, G., Laflamme, J.G.H., and Peregoedova, A., 2005, Synthesis and evaluation of a fused pyrrhotite standard reference material for platinum-group element and gold analyses by laser ablation-ICPMS: Geological Survey of Finland, Espoo, Finland, 10th International Platinum Symposium, Extended abstracts, p. 16-20.

Thurston, P.C., Ayer, J.A., Goutier, J., and Hamilton, M.A., 2008, Depositional gaps in Abitibi greenstone belt stratigraphy: A key to exploration for syngenetic mineralization: ECONOMIC GEOLOGY, v. 103, p. 1097-1134.

Tomkins, A.G., Pattison, D.R.M., and Frost, B.R., 2007, On the initiation of metamorphic sulfide anatexis: Journal of Petrology, v. 48, no. 3, p. 511-535.

Tomkins, A.G., Pattison, D.R.M., and Zaleski, E., 2004, The Hemlo gold deposit, Ontario: An example of melting and mobilization of a precious metal-sulfosalt assemblage during amphibolite facies metamorphism and deformation: ECONOMIC GEOLOGY, v. 99, p. 1063-1084.

Tooth, B., Ciobanu, C.L., Green, L., O'Neill, B., and Brugger, J., 2011, Bi-melt formation and gold scavenging from hydrothermal fluids: An experimental study: Geochimica et Cosmochimica Acta, v. 75, p. 5423-5443.

Ulrich, T., Günther, D., and Heinrich, C.A., 1999, Gold concentrations of magmatic brines and the metal budget of porphyry copper deposits: Letters to Nature, v. 399, p. 676-679.

van Breemen, O., Heather, K.B., and Ayer, J.A., 2006, U-Pb geochronology of the Neoarchean Swayze sector of the southern Abitibi greenstone belt: Geological Survey of Canada, Current Research 2006-F1, 32 p.

Velásquez, G., Béziat, D., Salvi, S., Siebenaller, L., Borisova, A.Y., Pokrovski, G.S., and de Parseval, P., 2014, Formation and deformation of pyrite and implications for gold mineralization in the El Callao District, Venezuela: ECONOMIC GEOLOGY, v. 109, p.457-486.

Wagner, T., Fusswinkel, T., Wälle, M., and Heinrich, C.A., 2016, Microanalysis of fluid inclusions in crustal hydrothermal systems using laser ablation methods: Elements, v. 12, p. 323-328.

Williams-Jones, A.E., Bowell, R.J., and Migdisov, A.A., 2009, Gold in Solution: Elements, v. 5, p. 281-287.

Williams-Jones, A.E., McLeish, D.F., and Vasyukova, O.V., 2018, Colloidal processes in the formation of Bonanza-grade gold ores: V.M. Goldschmidt Conference, Programs and Abstracts 28, Goldschmidt 2018.

Zhou, H., Sun, X., Cook, N.J., Lin, H., Fu, Y., Zhong, R., and Brugger, J., 2017, Nano- to micron-scale particulate gold hosted by magnetite: A product of gold scavenging by bismuth melts: ECONOMIC GEOLOGY, v. 112, p. 993-1010.

3.9 Tables and Figures

Table 3.1. Listing of analytical parameters, choice of standards, limits of detection for gold and pyrite routines, and precision test results for native gold and pyrite. Notes (1) Fe was analyzed at normal operating conditions for native gold analyses to betray any contamination from Fe sulfides (i.e., pyrite, pyrrhotite, chalcopyrite, arsenopyrite).

Gold Routine

X-ray	Calibration Standard	Analyzing Crystal	Peak Counting Time (s)	Gun Voltage (kV)	Beam Current (nA)	L.O.D.
Au Lα	Au (metal)	LLIF	15	20	30	0.113
Ag Lα	Ag (metal)	PET	15	20	30	0.122
Fe Kα	Fe (metal)	LIF	15	20	30	0.029
Cu Kα	Cu (metal)	LIF	30	20	200	0.011
Sb Lα	Sb (metal)	PET	30	20	200	0.020
Te Lα	HgTe (synthetic)	PET	30	20	200	0.019
Hg Lα	HgTe (synthetic)	LLIF	30	20	200	0.037
Bi Lα	Bi (metal)	LLiF	30	20	200	0.082

Macassa (n=7)

Element	Wt %	Error 2σ (+/-)
Au	94.193	0.484
Ag	5.879	0.300
Fe	b.d.l.	
Cu	0.036	0.006
Sb	b.d.l.	
Te	b.d.l.	

Campbell Red Lake (n=7)

Element	Wt %	Error 2σ (+/-)
Au	90.505	0.273
Ag	9.408	0.350
Fe	b.d.l.	
Cu	0.016	0.008
Sb	b.d.l.	
Te	b.d.l.	

Hg	0.354	0.041
Bi	b.d.l.	
Total	100.462	

Hg	0.461	0.029
Bi	b.d.l.	
Total	100.390	

Jerome Pyrite Routine: Using Au Mα

X-ray	Calibration Standard	Analyzing Crystal	Peak Counting Time (s)	Gun Voltage (kV)	Beam Current (nA)	L.O.D.
S Kα	FeS_2 (natural)	PET	15	20	40	0.015
Fe Kα	FeS_2 (natural)	LiF	15	20	40	0.021
Co Kα	Co (metal)	LiF	10	20	200	0.013
Ni Kα	NiO (synthetic)	LLiF	15	20	200	0.007
Cu Kα	$CuFeS_2$ (natural)	LIF	15	20	200	0.008
As Lα	FeAsS (natural)	TAP	30	20	200	0.012
Ag Lα	Ag (metal)	LPET	15	20	200	0.013
Sb Lα	Sb (metal)	PET	10	20	200	0.021
Te Lα	HgTe (synthetic)	PET	10	20	200	0.022
Au Mα	Au (metal)	LPET	15	20	200	0.023
Hg La	HgTe (synthetic)	LiF	20	20	200	0.064
Bi Mα	Bi metal	PET	10	20	200	0.048

Pyrite Precision (Using Au Mα)

Jerome 4 (n=7)

Element	Wt %	Error 2σ (+/-)
S	51.257	0.243
Fe	45.569	0.249
Co	b.d.l.	
Ni	0.012	0.005
Cu	0.158	0.013
As	2.802	0.029
Ag	b.d.l.	
Sb	b.d.l.	
Te	b.d.l.	
Au	0.223	0.022
Hg	b.d.l.	
Bi	b.d.l.	
Total	100.020	

Jerome 5 (n=7)

Element	Wt %	Error 2σ (+/-)
S	51.755	0.220
Fe	45.725	0.244
Co	b.d.l.	
Ni	b.d.l.	
Cu	0.102	0.008
As	2.233	0.061
Ag	b.d.l.	
Sb	b.d.l.	
Te	b.d.l.	
Au	0.230	0.032
Hg	b.d.l.	
Bi	b.d.l.	
Total	100.045	

Kenty Pyrite Routine: Using Au Lα

X-ray	Calibration Standard	Analyzing Crystal	Peak Counting Time (s)	Gun Voltage (kV)	Beam Current (nA)	L.O.D.
S Kα	FeS_2 (natural)	PET	15	20	40	0.015
Fe Kα	FeS_2 (natural)	LiF	15	20	40	0.021
Co Kα	Co (metal)	LiF	15	20	200	0.011
Ni Kα	NiO (synthetic)	LLiF	15	20	200	0.007
Cu Kα	$CuFeS_2$ (natural)	LLiF	15	20	200	0.008
As Lα	FeAsS (natural)	TAP	30	20	200	0.012
Ag Lα	Ag (metal)	LPET	30	20	200	0.010
Sb Lα	Sb (metal)	PET	15	20	200	0.018
Te Lα	HgTe (synthetic)	PET	15	20	200	0.019
Au Lα	Au (metal)	LLiF(x2) + LiF(x1)	100 (x3)	20	200	0.006
Hg La	HgTe (synthetic)	LiF	15	20	200	0.073

Pyrite Precision (Using Au Lα)

Kenty 1a (n=7)

Element	Wt %	Error 2σ (+/-)
S	53.161	0.277
Fe	46.496	0.223
Co	0.017	0.009
Ni	0.113	0.008
Cu	b.d.l.	
As	b.d.l.	
Ag	0.013	0.006
Sb	b.d.l.	
Te	b.d.l.	
Au	0.068	0.008
Hg	b.d.l.	
Total	99.869	

Kenty 1b (n=7)

Element	Wt %	Error 2σ (+/-)
S	53.348	0.332
Fe	46.493	0.226
Co	0.016	0.011
Ni	0.105	0.005
Cu	b.d.l.	
As	b.d.l.	
Ag	b.d.l.	
Sb	b.d.l.	
Te	b.d.l.	
Au	0.091	0.006
Hg	b.d.l.	
Total	100.054	

Table 3.2. Results from EMPA analyses of pyrite grains from the Jerome (Sample 530972) and Kenty (Sample 228874B) deposits. For Jerome, locations for oscillatory traverse points 1 through 40 can be found labeled in Figure 13.8D and for Kenty traverse points 1 through 5 can be found labeled in Figure 3.12. b.d.l. = below detection limit and n.a. = not analyzed.

Deposit and Sample Description	S (wt.%)	Fe (wt.%)	Co (wt.%)	Ni (wt.%)	Cu (wt.%)	As (wt.%)	Ag (wt.%)	Sb (wt.%)	Te (wt.%)	Au (wt.%)	Hg (wt.%)	Bi (wt.%)	Total (wt.%)
Detection Limit	**0.015**	**0.021**	**0.013**	**0.007**	**0.008**	**0.012**	**0.013**	**0.021**	**0.022**	**0.023**	**0.064**	**0.048**	
Jerome Oscillatory (Dark Zone 1)	**53.116**	**46.098**	**0.046**	**0.180**	b.d.l.	**0.140**	b.d.l.	b.d.l.	b.d.l.	b.d.l.	b.d.l.	b.d.l.	99.580
Jerome Oscillatory (Dark Zone 2)	**53.315**	**46.248**	**0.039**	**0.373**	b.d.l.	**0.371**	b.d.l.	b.d.l.	b.d.l.	b.d.l.	b.d.l.	b.d.l.	100.346
Jerome Oscillatory (Intermediate Zone 1)	**53.223**	**46.078**	**0.090**	**0.098**	b.d.l.	**0.087**	b.d.l.	b.d.l.	b.d.l.	b.d.l.	b.d.l.	b.d.l.	99.576
Jerome Oscillatory (Intermediate Zone 2)	**51.955**	**44.618**	**0.130**	**1.126**	b.d.l.	**1.960**	b.d.l.	b.d.l.	b.d.l.	b.d.l.	b.d.l.	b.d.l.	99.789
Jerome Oscillatory (Bright Zone 1)	**51.171**	**44.801**	**0.019**	**0.058**	**0.211**	**3.214**	b.d.l.	b.d.l.	b.d.l.	**0.122**	b.d.l.	b.d.l.	99.596
Jerome Oscillatory (Bright Zone 2)	**51.166**	**45.131**	b.d.l.	**0.034**	**0.161**	**2.882**	b.d.l.	b.d.l.	b.d.l.	**0.059**	b.d.l.	b.d.l.	99.433
Jerome Oscillatory (Bright Zone 3)	**50.039**	**44.530**	b.d.l.	**0.017**	**0.057**	**4.202**	**0.018**	**0.047**	b.d.l.	**0.507**	b.d.l.	b.d.l.	99.417
Jerome Oscillatory (Bright Zone 4)	**51.564**	**45.315**	b.d.l.	**0.014**	**0.134**	**2.361**	b.d.l.	b.d.l.	b.d.l.	**0.104**	b.d.l.	b.d.l.	99.492
Jerome Oscillatory (Dark Zone 3)	**53.398**	**45.867**	**0.160**	**0.373**	b.d.l.	**0.387**	b.d.l.	b.d.l.	b.d.l.	b.d.l.	b.d.l.	b.d.l.	100.185
Jerome Oscillatory (Bright Zone 5)	**50.176**	**44.513**	**0.015**	**0.013**	**0.183**	**4.222**	b.d.l.	**0.023**	b.d.l.	**0.393**	b.d.l.	b.d.l.	99.538
Jerome Oscillatory (Bright Zone 6)	**51.274**	**45.466**	b.d.l.	**0.026**	**0.038**	**2.710**	b.d.l.	b.d.l.	b.d.l.	**0.378**	b.d.l.	b.d.l.	99.892
Jerome Oscillatory (Bright Zone 7)	**51.175**	**45.167**	**0.019**	**0.025**	**0.210**	**3.180**	b.d.l.	b.d.l.	b.d.l.	**0.140**	b.d.l.	b.d.l.	99.916
Jerome Oscillatory (Intermediate Zone 3)	**52.452**	**45.632**	**0.049**	**0.703**	b.d.l.	**1.065**	b.d.l.	b.d.l.	b.d.l.	b.d.l.	b.d.l.	b.d.l.	99.901
Jerome Oscillatory (Dark Zone 4)	**53.243**	**45.983**	**0.107**	**0.203**	b.d.l.	**0.091**	b.d.l.	b.d.l.	b.d.l.	b.d.l.	b.d.l.	b.d.l.	99.627
Jerome Oscillatory (Bright Zone 8)	**50.199**	**44.584**	**0.021**	**0.020**	**0.034**	**4.117**	b.d.l.	**0.023**	b.d.l.	**0.415**	b.d.l.	b.d.l.	99.413
Jerome Oscillatory Traverse (Point 1)	**52.547**	**46.252**	b.d.l.	**0.011**	**0.082**	**0.770**	b.d.l.	b.d.l.	b.d.l.	b.d.l.	b.d.l.	b.d.l.	99.662

Jerome Oscillatory Traverse (Point 2)	**52.497**	**46.093**	**0.016**	**0.026**	**0.063**	**0.877**	b.d.l.	b.d.l.	b.d.l.	**0.025**	b.d.l.	b.d.l.	99.597
Jerome Oscillatory Traverse (Point 3)	**52.039**	**45.813**	**0.025**	**0.035**	**0.089**	**1.179**	b.d.l.	b.d.l.	b.d.l.	**0.051**	b.d.l.	b.d.l.	99.231
Jerome Oscillatory Traverse (Point 4)	**51.829**	**45.701**	**0.015**	**0.031**	**0.118**	**1.542**	b.d.l.	b.d.l.	b.d.l.	**0.041**	b.d.l.	b.d.l.	99.277
Jerome Oscillatory Traverse (Point 5)	**52.088**	**46.031**	**0.019**	**0.027**	**0.112**	**1.449**	b.d.l.	b.d.l.	b.d.l.	**0.026**	b.d.l.	b.d.l.	99.752
Jerome Oscillatory Traverse (Point 6)	**52.157**	**45.633**	**0.016**	**0.034**	**0.109**	**1.371**	b.d.l.	b.d.l.	b.d.l.	**0.043**	b.d.l.	b.d.l.	99.363
Jerome Oscillatory Traverse (Point 7)	**52.247**	**45.782**	**0.030**	**0.040**	**0.100**	**1.332**	b.d.l.	b.d.l.	b.d.l.	**0.072**	b.d.l.	b.d.l.	99.603
Jerome Oscillatory Traverse (Point 8)	**52.129**	**45.736**	**0.023**	**0.035**	**0.097**	**1.275**	b.d.l.	b.d.l.	b.d.l.	**0.037**	b.d.l.	b.d.l.	99.332
Jerome Oscillatory Traverse (Point 9)	**50.469**	**45.182**	**0.022**	**0.056**	**0.116**	**2.190**	b.d.l.	b.d.l.	b.d.l.	**0.047**	b.d.l.	b.d.l.	98.082
Jerome Oscillatory Traverse (Point 10)	**50.504**	**44.839**	**0.045**	**0.100**	**0.213**	**3.521**	b.d.l.	b.d.l.	b.d.l.	**0.082**	b.d.l.	b.d.l.	99.304
Jerome Oscillatory Traverse (Point 11)	**50.425**	**44.938**	**0.030**	**0.058**	**0.176**	**2.986**	b.d.l.	b.d.l.	b.d.l.	**0.081**	b.d.l.	b.d.l.	98.694
Jerome Oscillatory Traverse (Point 12)	**51.977**	**45.651**	b.d.l.	**0.038**	**0.102**	**2.213**	b.d.l.	b.d.l.	**0.037**	**0.042**	b.d.l.	b.d.l.	100.060
Jerome Oscillatory Traverse (Point 13)	**52.348**	**45.862**	**0.025**	**0.039**	**0.060**	**1.501**	b.d.l.	b.d.l.	b.d.l.	b.d.l.	b.d.l.	b.d.l.	99.835
Jerome Oscillatory Traverse (Point 14)	**52.644**	**46.281**	**0.017**	**0.025**	**0.043**	**0.644**	b.d.l.	b.d.l.	b.d.l.	b.d.l.	b.d.l.	b.d.l.	99.654
Jerome Oscillatory Traverse (Point 15)	**52.778**	**46.135**	b.d.l.	**0.026**	**0.027**	**0.619**	b.d.l.	**0.033**	b.d.l.	b.d.l.	b.d.l.	b.d.l.	99.618
Jerome Oscillatory Traverse (Point 16)	**52.562**	**46.178**	**0.022**	**0.030**	**0.037**	**0.746**	b.d.l.	b.d.l.	b.d.l.	b.d.l.	b.d.l.	b.d.l.	99.575
Jerome Oscillatory Traverse (Point 17)	**52.212**	**45.951**	b.d.l.	**0.029**	**0.070**	**1.122**	b.d.l.	b.d.l.	b.d.l.	b.d.l.	b.d.l.	b.d.l.	99.384
Jerome Oscillatory Traverse (Point 18)	**52.371**	**45.918**	**0.019**	**0.036**	**0.083**	**1.412**	b.d.l.	b.d.l.	b.d.l.	**0.024**	b.d.l.	b.d.l.	99.863
Jerome Oscillatory Traverse (Point 19)	**52.396**	**45.924**	**0.025**	**0.053**	**0.063**	**1.187**	b.d.l.	b.d.l.	b.d.l.	b.d.l.	b.d.l.	b.d.l.	99.648
Jerome Oscillatory Traverse (Point 20)	**52.551**	**46.067**	**0.027**	**0.044**	**0.049**	**0.930**	b.d.l.	b.d.l.	b.d.l.	b.d.l.	b.d.l.	b.d.l.	99.668
Jerome Oscillatory Traverse (Point 21)	**51.348**	**45.702**	b.d.l.	**0.037**	**0.059**	**1.471**	b.d.l.	b.d.l.	b.d.l.	**0.035**	b.d.l.	b.d.l.	98.652
Jerome Oscillatory Traverse (Point 22)	**51.018**	**45.491**	**0.018**	**0.036**	**0.088**	**2.756**	b.d.l.	b.d.l.	b.d.l.	**0.065**	b.d.l.	b.d.l.	99.472
Jerome Oscillatory Traverse (Point 23)	**50.929**	**45.486**	**0.014**	**0.020**	**0.109**	**2.774**	**0.016**	b.d.l.	b.d.l.	**0.107**	b.d.l.	b.d.l.	99.455
Jerome Oscillatory Traverse (Point 24)	**51.915**	**45.669**	**0.021**	**0.036**	**0.171**	**2.633**	b.d.l.	b.d.l.	b.d.l.	**0.076**	b.d.l.	b.d.l.	100.521
Jerome Oscillatory Traverse (Point 25)	**52.909**	**45.884**	b.d.l.	**0.011**	**0.050**	**0.710**	b.d.l.	b.d.l.	b.d.l.	b.d.l.	b.d.l.	b.d.l.	99.564

Jerome Oscillatory Traverse (Point 26)	**52.874**	**46.345**	**0.019**	**0.013**	**0.058**	**0.477**	b.d.l.	b.d.l.	b.d.l.	b.d.l.	b.d.l.	b.d.l.	99.786
Jerome Oscillatory Traverse (Point 27)	**52.780**	**46.042**	**0.014**	**0.029**	**0.073**	**1.032**	b.d.l.	b.d.l.	**0.025**	b.d.l.	b.d.l.	b.d.l.	99.995
Jerome Oscillatory Traverse (Point 28)	**53.360**	**46.244**	b.d.l.	b.d.l.	**0.027**	**0.168**	b.d.l.	b.d.l.	b.d.l.	b.d.l.	b.d.l.	b.d.l.	99.799
Jerome Oscillatory Traverse (Point 29)	**53.121**	**46.073**	b.d.l.	**0.019**	**0.033**	**0.166**	b.d.l.	b.d.l.	b.d.l.	b.d.l.	b.d.l.	b.d.l.	99.412
Jerome Oscillatory Traverse (Point 30)	**53.138**	**46.231**	b.d.l.	b.d.l.	**0.024**	**0.115**	b.d.l.	b.d.l.	b.d.l.	b.d.l.	b.d.l.	b.d.l.	99.508
Jerome Oscillatory Traverse (Point 31)	**52.601**	**46.317**	b.d.l.	b.d.l.	**0.028**	**0.235**	b.d.l.	b.d.l.	b.d.l.	b.d.l.	b.d.l.	b.d.l.	99.181
Jerome Oscillatory Traverse (Point 32)	**52.382**	**46.151**	**0.014**	**0.009**	**0.065**	**0.794**	b.d.l.	b.d.l.	b.d.l.	b.d.l.	b.d.l.	b.d.l.	99.415
Jerome Oscillatory Traverse (Point 33)	**52.284**	**45.853**	b.d.l.	b.d.l.	**0.110**	**1.165**	b.d.l.	b.d.l.	b.d.l.	**0.024**	b.d.l.	b.d.l.	99.436
Jerome Oscillatory Traverse (Point 34)	**51.956**	**46.005**	b.d.l.	**0.015**	**0.145**	**1.319**	b.d.l.	b.d.l.	b.d.l.	**0.045**	b.d.l.	b.d.l.	99.485
Jerome Oscillatory Traverse (Point 35)	**51.918**	**45.829**	**0.022**	**0.031**	**0.159**	**1.744**	**0.015**	b.d.l.	b.d.l.	**0.026**	b.d.l.	b.d.l.	99.744
Jerome Oscillatory Traverse (Point 36)	**52.129**	**45.656**	**0.019**	**0.040**	**0.154**	**1.750**	b.d.l.	b.d.l.	b.d.l.	**0.027**	**0.068**	b.d.l.	99.843
Jerome Oscillatory Traverse (Point 37)	**52.270**	**45.645**	b.d.l.	**0.028**	**0.164**	**1.662**	b.d.l.	b.d.l.	b.d.l.	**0.033**	b.d.l.	b.d.l.	99.802
Jerome Oscillatory Traverse (Point 38)	**51.852**	**45.600**	**0.019**	**0.045**	**0.141**	**1.614**	b.d.l.	b.d.l.	b.d.l.	**0.032**	b.d.l.	b.d.l.	99.303
Jerome Oscillatory Traverse (Point 39)	**52.499**	**45.633**	**0.018**	**0.045**	**0.154**	**1.569**	b.d.l.	b.d.l.	b.d.l.	**0.030**	b.d.l.	b.d.l.	99.948
Jerome Oscillatory Traverse (Point 40)	**52.416**	**45.766**	**0.033**	**0.059**	**0.141**	**1.545**	b.d.l.	b.d.l.	b.d.l.	b.d.l.	b.d.l.	b.d.l.	99.960
Deposit and Sample Description	**S (wt.%)**	**Fe (wt.%)**	**Co (wt.%)**	**Ni (wt.%)**	**Cu (wt.%)**	**As (wt.%)**	**Ag (wt.%)**	**Sb (wt.%)**	**Te (wt.%)**	**Au (wt.%)**	**Hg (wt.%)**	**Bi (wt.%)**	**Total (wt.%)**
Detection Limit	**0.015**	**0.021**	**0.011**	**0.007**	**0.008**	**0.012**	**0.010**	**0.018**	**0.019**	**0.006**	**0.073**	**n.a.**	
Kenty C1 Medial Pyrite Traverse (Point 1)	**53.484**	**46.437**	**0.064**	**0.197**	b.d.l.	b.d.l.	**0.019**	b.d.l.	b.d.l.	**0.096**	b.d.l.	n.a.	100.297
Kenty C1 Medial Pyrite Traverse (Point 2)	**53.561**	**46.417**	**0.012**	**0.137**	b.d.l.	b.d.l.	**0.012**	b.d.l.	b.d.l.	**0.077**	b.d.l.	n.a.	100.216
Kenty C1 Medial Pyrite Traverse (Point 3)	**53.549**	**46.649**	b.d.l.	**0.149**	b.d.l.	b.d.l.	**0.015**	b.d.l.	b.d.l.	**0.077**	b.d.l.	n.a.	100.439
Kenty C1 Medial Pyrite Traverse (Point 4)	**53.304**	**46.406**	**0.032**	**0.211**	b.d.l.	b.d.l.	**0.019**	b.d.l.	b.d.l.	**0.082**	b.d.l.	n.a.	100.054
Kenty C1 Medial Pyrite Traverse (Point 5)	**53.318**	**46.544**	**0.014**	**0.173**	b.d.l.	b.d.l.	**0.016**	b.d.l.	b.d.l.	**0.084**	b.d.l.	n.a.	100.149
Kenty C1 Mortimer Pyrite	**53.404**	**46.328**	**0.044**	**0.127**	b.d.l.	**0.016**	**0.018**	b.d.l.	b.d.l.	**0.128**	b.d.l.	n.a.	100.065

Kenty C1 Mortimer Pyrite	**53.463**	**46.406**	**0.033**	**0.145**	b.d.l.	b.d.l.	b.d.l.	b.d.l.	b.d.l.	**0.151**	b.d.l.	n.a.	100.198
Kenty C1 Mortimer Pyrite	**53.366**	**46.574**	**0.021**	**0.045**	b.d.l.	b.d.l.	**0.011**	b.d.l.	b.d.l.	**0.029**	b.d.l.	n.a.	100.046
Kenty C1 Mortimer Pyrite	**53.581**	**46.477**	**0.031**	**0.013**	b.d.l.	b.d.l.	**0.017**	b.d.l.	b.d.l.	**0.044**	b.d.l.	n.a.	100.163
Kenty C1 Mortimer Pyrite	**53.623**	**46.458**	**0.026**	b.d.l.	b.d.l.	b.d.l.	**0.011**	b.d.l.	b.d.l.	**0.062**	b.d.l.	n.a.	100.180
Kenty C1 Mortimer Pyrite	**53.547**	**46.577**	**0.021**	**0.033**	b.d.l.	b.d.l.	**0.011**	b.d.l.	b.d.l.	**0.013**	b.d.l.	n.a.	100.202
Kenty C1 Mortimer Pyrite	**53.863**	**46.459**	**0.107**	**0.035**	b.d.l.	b.d.l.	b.d.l.	b.d.l.	b.d.l.	b.d.l.	b.d.l.	n.a.	100.464
Kenty C1 Mortimer Pyrite	**53.759**	**46.863**	b.d.l.	b.d.l.	b.d.l.	b.d.l.	b.d.l.	b.d.l.	b.d.l.	b.d.l.	b.d.l.	n.a.	100.622
Kenty C1 Mortimer Pyrite	**53.518**	**46.723**	**0.028**	**0.018**	**0.022**	b.d.l.	**0.015**	b.d.l.	b.d.l.	**0.009**	b.d.l.	n.a.	100.333
Kenty C1 Mortimer Pyrite	**53.621**	**47.075**	b.d.l.	b.d.l.	b.d.l.	b.d.l.	**0.014**	b.d.l.	b.d.l.	**0.050**	b.d.l.	n.a.	100.760
Kenty C1 Mortimer Pyrite	**53.428**	**46.791**	**0.049**	b.d.l.	b.d.l.	**0.019**	**0.015**	b.d.l.	b.d.l.	**0.075**	b.d.l.	n.a.	100.377
Kenty C1 Mortimer Pyrite	**53.452**	**46.739**	**0.032**	**0.070**	b.d.l.	b.d.l.	**0.015**	b.d.l.	b.d.l.	**0.066**	b.d.l.	n.a.	100.374
Kenty C1 Mortimer Pyrite	**53.851**	**46.764**	**0.012**	**0.013**	b.d.l.	b.d.l.	b.d.l.	b.d.l.	b.d.l.	**0.014**	b.d.l.	n.a.	100.654
Kenty C1 Mortimer Pyrite	**53.573**	**46.893**	b.d.l.	b.d.l.	b.d.l.	b.d.l.	**0.019**	b.d.l.	b.d.l.	**0.014**	b.d.l.	n.a.	100.499
Kenty C1 Mortimer Pyrite	**53.840**	**46.905**	b.d.l.	**0.015**	**0.009**	b.d.l.	**0.018**	b.d.l.	b.d.l.	**0.027**	b.d.l.	n.a.	100.814
Kenty C1 Mortimer Pyrite	**53.759**	**46.888**	**0.037**	**0.017**	b.d.l.	b.d.l.	b.d.l.	b.d.l.	b.d.l.	**0.021**	b.d.l.	n.a.	100.722
Kenty C1 Mortimer Pyrite	**53.781**	**46.771**	b.d.l.	**0.018**	b.d.l.	b.d.l.	b.d.l.	b.d.l.	b.d.l.	**0.013**	b.d.l.	n.a.	100.583
Kenty C1 Mortimer Pyrite	**53.473**	**46.493**	b.d.l.	**0.015**	b.d.l.	b.d.l.	**0.016**	b.d.l.	b.d.l.	**0.029**	b.d.l.	n.a.	100.026
Kenty C1 Mortimer Pyrite	**53.354**	**46.807**	**0.012**	**0.008**	b.d.l.	b.d.l.	b.d.l.	b.d.l.	b.d.l.	**0.063**	b.d.l.	n.a.	100.244

Table 3.3. List of samples used in this study, both from the Kenty and the ROM samples, with results of EMPA analyses of native Au. Also listed are the associated elements and other mineral phases in the subsamples studied, as determined by SEM-EDS and EMPA. b.d.l. = below detection limit.

Deposit-Analysis Number (ROM Catalogue Number)	Fe (wt.%)	Cu (wt.%)	Ag (wt.%)	Sb (wt.%)	Te (wt.%)	Au (wt.%)	Hg (wt.%)	Bi (wt.%)	Total (wt.%)	Au Fineness = (Au/All Elements)*1000	Associated Mineral Phases	Associated Major Elements from Other Minerals
Detection Limit	**0.029**	**0.011**	**0.122**	**0.020**	**0.019**	**0.113**	**0.037**	**0.082**				
Lamaque-1 (11985)	b.d.l.	**0.016**	**13.596**	b.d.l.	b.d.l.	**86.112**	b.d.l.	b.d.l.	99.72	863.50	petzite, altaite, chalcopyrite, tellurobismuthite (Sb-bearing)	Bi, Te, Cu, Sb, Pb, Fe, Au, Ag
Lamaque-2 (11985)	**0.035**	**0.034**	**13.317**	b.d.l.	b.d.l.	**86.275**	**0.092**	b.d.l.	99.75	864.89		
Lamaque-3 (11985)	b.d.l.	**0.034**	**13.552**	b.d.l.	b.d.l.	**86.878**	**0.053**	**0.103**	100.62	863.43		
Lamaque-4 (11985)	b.d.l.	**0.024**	**13.654**	b.d.l.	**0.045**	**86.746**	**0.065**	b.d.l.	100.53	862.85		
Lamaque-5 (11985)	**0.034**	**0.028**	**14.247**	b.d.l.	b.d.l.	**85.864**	**0.044**	b.d.l.	100.22	856.78		
Croesus-1 (LM47273)	b.d.l.	**0.049**	**9.18**	b.d.l.	b.d.l.	**91.12**	**0.055**	b.d.l.	100.40	907.53	chalcopyrite	Cu, Fe
Croesus-2 (LM47273)	b.d.l.	**0.05**	**8.949**	b.d.l.	b.d.l.	**91.305**	**0.056**	b.d.l.	100.36	909.77		
Croesus-3 (LM47273)	b.d.l.	**0.056**	**8.957**	b.d.l.	b.d.l.	**90.607**	**0.083**	b.d.l.	99.70	908.77		
Croesus-4 (LM47273)	b.d.l.	**0.04**	**8.91**	b.d.l.	b.d.l.	**90.754**	b.d.l.	b.d.l.	99.70	910.23		
Croesus-5 (LM47273)	b.d.l.	**0.034**	**9.062**	b.d.l.	b.d.l.	**91.087**	**0.084**	b.d.l.	100.27	908.44		
Temiskamingue-1 (M15626)	b.d.l.	**0.107**	**5.784**	b.d.l.	b.d.l.	**94.85**	**0.063**	b.d.l.	100.80	940.93	chalcopyrite	Cu, Fe
Temiskamingue-2 (M15626)	b.d.l.	**0.119**	**5.649**	b.d.l.	b.d.l.	**93.878**	**0.05**	b.d.l.	99.70	941.64		
Temiskamingue-3 (M15626)	b.d.l.	**0.078**	**5.599**	b.d.l.	b.d.l.	**94.645**	**0.044**	b.d.l.	100.37	943.00		
Temiskamingue-4 (M15626)	b.d.l.	**0.109**	**5.872**	b.d.l.	b.d.l.	**94.467**	b.d.l.	b.d.l.	100.45	940.46		
Temiskamingue-5 (M15626)	b.d.l.	**0.073**	**5.548**	b.d.l.	b.d.l.	**93.78**	b.d.l.	b.d.l.	99.40	943.45		

Dome-1 (M22582)	b.d.l.	**0.035**	**9.525**	b.d.l.	b.d.l.	**90.087**	**0.1**	b.d.l.	99.75	903.15	pyrite (As-bearing)	Cu, Fe, As
Dome-2 (M22582)	b.d.l.	**0.033**	**9.741**	b.d.l.	b.d.l.	**90.579**	**0.106**	b.d.l.	100.46	901.65		
Dome-3 (M22582)	b.d.l.	**0.045**	**9.745**	b.d.l.	**0.022**	**90.556**	**0.115**	b.d.l.	100.48	901.21		
Dome-4 (M22582)	b.d.l.	**0.031**	**9.47**	b.d.l.	b.d.l.	**90.372**	**0.103**	b.d.l.	99.98	903.94		
Dome-5 (M22582)	b.d.l.	**0.033**	**9.593**	b.d.l.	b.d.l.	**90.399**	**0.134**	b.d.l.	100.16	902.55		
O'Brien1 (M21973)	b.d.l.	**0.058**	**3.459**	b.d.l.	b.d.l.	**96.295**	**0.155**	b.d.l.	99.97	963.27	no associated phases in subsample	no associated phases in subsample
O'Brien2 (M21973)	b.d.l.	**0.057**	**3.632**	b.d.l.	b.d.l.	**96.158**	**0.103**	b.d.l.	99.95	962.06		
O'Brien3 (M21973)	b.d.l.	**0.053**	**3.664**	b.d.l.	b.d.l.	**96.32**	**0.1**	b.d.l.	100.14	961.88		
O'Brien4 (M21973)	**0.046**	**0.069**	**3.512**	b.d.l.	b.d.l.	**93.989**	**0.104**	b.d.l.	97.72	961.82		
O'Brien5 (M21973)	b.d.l.	**0.062**	**3.443**	b.d.l.	b.d.l.	**96.143**	**0.128**	b.d.l.	99.78	963.59		
Paymaster1 (M27622)	b.d.l.	**0.047**	**8.203**	b.d.l.	b.d.l.	**91.199**	**0.61**	b.d.l.	100.06	911.45	gersdorffite, chalcopyrite, pyrite	Cu, Fe, Ni, As
Paymaster2 (M27622)	b.d.l.	**0.039**	**7.643**	b.d.l.	b.d.l.	**89.467**	**0.623**	b.d.l.	97.77	915.06		
Paymaster3 (M27622)	b.d.l.	**0.031**	**8.238**	b.d.l.	b.d.l.	**91.63**	**0.602**	b.d.l.	100.50	911.73		
Paymaster4 (M27622)	b.d.l.	**0.034**	**7.934**	b.d.l.	b.d.l.	**91.211**	**0.602**	b.d.l.	99.78	914.11		
Paymaster5 (M27622)	b.d.l.	**0.029**	**8.097**	b.d.l.	**0.022**	**91.628**	**0.611**	b.d.l.	100.39	912.75		
Stadacona1 (M31176)	b.d.l.	**0.117**	**4.769**	b.d.l.	b.d.l.	**95.043**	**0.191**	b.d.l.	100.12	949.29	no associated phases in subsample	no associated phases in subsample
Stadacona2 (M31176)	b.d.l.	**0.12**	**4.696**	b.d.l.	b.d.l.	**95.163**	**0.196**	b.d.l.	100.18	949.97		
Stadacona3 (M31176)	b.d.l.	**0.115**	**4.671**	b.d.l.	b.d.l.	**95.274**	**0.199**	b.d.l.	100.26	950.28		
Stadacona4 (M31176)	b.d.l.	**0.119**	**4.435**	b.d.l.	b.d.l.	**94.351**	**0.202**	b.d.l.	99.11	952.01		
Stadacona5 (M31176)	b.d.l.	**0.124**	**4.459**	b.d.l.	b.d.l.	**95.437**	**0.169**	b.d.l.	100.19	952.57		
Robb-Montbray1 (M37291)	b.d.l.	**0.06**	**5.146**	b.d.l.	b.d.l.	**94.911**	**0.051**	b.d.l.	100.17	947.52	montbrayite, chalcopyrite, pyrite, altaite	Bi, Sb, Te, Pb, Cu, Fe
Robb-Montbray2 (M37291)	b.d.l.	**0.054**	**5.437**	b.d.l.	b.d.l.	**93.157**	b.d.l.	b.d.l.	98.65	944.34		
Robb-Montbray3 (M37291)	b.d.l.	**0.052**	**5.758**	b.d.l.	b.d.l.	**94.752**	**0.049**	b.d.l.	100.61	941.77		

Robb-Montbray4 (M37291)	b.d.l.	**0.048**	**5.917**	b.d.l.	b.d.l.	**93.973**	b.d.l.	b.d.l.	99.94	940.31		
Robb-Montbray5 (M37291)	b.d.l.	**0.042**	**5.804**	b.d.l.	b.d.l.	**94.364**	b.d.l.	b.d.l.	100.21	941.66		
Kerr Addison1 (M38711)	b.d.l.	**0.038**	**5.988**	b.d.l.	b.d.l.	**94.096**	**0.301**	b.d.l.	100.42	937.00	no associated phases in subsample	no associated phases in subsample
Kerr Addison2 (M38711)	b.d.l.	**0.035**	**5.461**	b.d.l.	b.d.l.	**90.809**	**0.345**	b.d.l.	96.65	939.57		
Kerr Addison3 (M38711)	b.d.l.	**0.043**	**5.991**	b.d.l.	b.d.l.	**93.369**	**0.353**	b.d.l.	99.76	935.97		
Kerr Addison4 (M38711)	b.d.l.	**0.038**	**5.865**	b.d.l.	b.d.l.	**94.04**	**0.364**	b.d.l.	100.31	937.52		
Kerr Addison5 (M38711)	b.d.l.	**0.038**	**5.9**	b.d.l.	b.d.l.	**94.113**	**0.33**	b.d.l.	100.38	937.56		
Lake Shore1 (M38713)	b.d.l.	**0.037**	**7.287**	b.d.l.	b.d.l.	**92.757**	**0.136**	b.d.l.	100.22	925.56	altaite, coloradoite, chalcopyrite	Pb, Hg, Te, Cu, Fe
Lake Shore2 (M38713)	b.d.l.	**0.05**	**7.156**	b.d.l.	b.d.l.	**92.914**	**0.093**	b.d.l.	100.21	927.17		
Lake Shore3 (M38713)	b.d.l.	**0.047**	**7.392**	b.d.l.	b.d.l.	**92.486**	**0.085**	b.d.l.	100.01	924.77		
Lake Shore4 (M38713)	b.d.l.	**0.053**	**7.897**	b.d.l.	b.d.l.	**92.011**	**0.06**	b.d.l.	100.02	919.92		
Lake Shore5 (M38713)	b.d.l.	**0.077**	**7.284**	b.d.l.	b.d.l.	**92.927**	**0.086**	b.d.l.	100.37	925.81		
Sigma1 (M47792)	b.d.l.	**0.04**	**7.156**	b.d.l.	b.d.l.	**91.343**	**0.049**	**0.084**	98.67	925.72	tellurobismuthite	Bi, Te
Sigma2 (M47792)	b.d.l.	**0.035**	**7.282**	b.d.l.	b.d.l.	**92.689**	b.d.l.	b.d.l.	100.01	926.83		
Sigma3 (M47792)	b.d.l.	**0.06**	**7.239**	b.d.l.	b.d.l.	**92.776**	b.d.l.	b.d.l.	100.08	927.06		
Sigma4 (M47792)	b.d.l.	**0.059**	**7.591**	b.d.l.	b.d.l.	**92.73**	b.d.l.	b.d.l.	100.38	923.79		
Sigma5 (M47792)	b.d.l.	**0.056**	**7.621**	b.d.l.	b.d.l.	**92.951**	b.d.l.	b.d.l.	100.63	923.71		
Aquarius1 (M55935)	b.d.l.	**0.046**	**10.023**	b.d.l.	b.d.l.	**90.045**	**0.202**	b.d.l.	100.32	897.61	no associated phases in subsample	no associated phases in subsample
Aquarius2 (M55935)	b.d.l.	**0.047**	**9.932**	b.d.l.	b.d.l.	**90.142**	**0.212**	b.d.l.	100.33	898.43		
Aquarius3 (M55935)	b.d.l.	**0.051**	**10.033**	b.d.l.	**0.020**	**89.924**	**0.191**	b.d.l.	100.22	897.27		
Aquarius4 (M55935)	b.d.l.	**0.027**	**10.278**	b.d.l.	b.d.l.	**89.727**	**0.21**	b.d.l.	100.24	895.10		

Aquarius5 (M55935)	b.d.l.	**0.038**	**10.262**	b.d.l.	b.d.l.	**89.707**	**0.188**	b.d.l.	100.20	895.32		
Tough Oakes1 (M8553)	b.d.l.	**0.064**	**7.592**	b.d.l.	b.d.l.	**92.246**	**0.133**	b.d.l.	100.04	922.14	altaite	Pb, Te
Tough Oakes2 (M8553)	b.d.l.	**0.063**	**7.496**	b.d.l.	b.d.l.	**92.97**	**0.117**	b.d.l.	100.65	923.73		
Tough Oakes3 (M8553)	b.d.l.	**0.067**	**7.387**	b.d.l.	b.d.l.	**92.38**	**0.157**	b.d.l.	99.99	923.88		
Tough Oakes4 (M8553)	b.d.l.	**0.054**	**7.635**	b.d.l.	b.d.l.	**92.798**	**0.168**	b.d.l.	100.66	921.94		
Tough Oakes5 (M8553)	b.d.l.	**0.051**	**7.815**	b.d.l.	**0.021**	**91.82**	**0.16**	b.d.l.	99.87	919.42		
Brouland1 (M21177)	b.d.l.	**0.019**	**8.978**	b.d.l.	b.d.l.	**91.108**	**0.148**	b.d.l.	100.25	908.78	sphalerite, pyrite	Zn, Fe
Brouland2 (M21177)	b.d.l.	**0.027**	**8.87**	b.d.l.	b.d.l.	**91.649**	**0.113**	b.d.l.	100.66	910.49		
Brouland3 (M21177)	b.d.l.	**0.032**	**8.962**	b.d.l.	b.d.l.	**91.174**	**0.158**	b.d.l.	100.33	908.78		
Brouland4 (M21177)	b.d.l.	**0.031**	**9.059**	b.d.l.	b.d.l.	**90.918**	**0.113**	b.d.l.	100.12	908.08		
Brouland5 (M21177)	b.d.l.	**0.034**	**9.056**	b.d.l.	b.d.l.	**91.097**	**0.17**	b.d.l.	100.36	907.73		
Cochenour Willlans1 (M21859)	b.d.l.	**0.025**	**5.671**	b.d.l.	b.d.l.	**94.659**	**0.094**	b.d.l.	100.45	942.36	arsenopyrite, pyrite, sphalerite, unidentified Pb-Sb-sulfosalt	Pb, Sb, As, Fe, Zn
Cochenour Willlans2 (M21859)	b.d.l.	**0.036**	**5.585**	b.d.l.	b.d.l.	**95.002**	b.d.l.	b.d.l.	100.62	944.14		
Cochenour Willlans3 (M21859)	b.d.l.	**0.034**	**5.601**	b.d.l.	b.d.l.	**94.633**	**0.091**	b.d.l.	100.36	942.94		
Cochenour Willlans4 (M21859)	b.d.l.	**0.03**	**5.399**	b.d.l.	b.d.l.	**94.398**	**0.093**	b.d.l.	99.92	944.74		
Cochenour Willlans5 (M21859)	b.d.l.	**0.023**	**5.236**	b.d.l.	b.d.l.	**94.52**	**0.097**	b.d.l.	99.88	946.37		
Paquette1 (M25238)	b.d.l.	**0.041**	**10.068**	b.d.l.	b.d.l.	**90.349**	**0.043**	b.d.l.	100.50	898.99	chalcopyrite	Cu, Fe
Paquette2 (M25238)	b.d.l.	**0.022**	**10.223**	b.d.l.	b.d.l.	**90.283**	**0.054**	b.d.l.	100.58	897.61		
Paquette3 (M25238)	b.d.l.	**0.054**	**10.241**	b.d.l.	b.d.l.	**90.66**	b.d.l.	b.d.l.	100.96	898.02		
Paquette4 (M25238)	b.d.l.	**0.03**	**9.916**	b.d.l.	b.d.l.	**90.057**	**0.063**	b.d.l.	100.07	899.98		
Paquette5 (M25238)	b.d.l.	**0.03**	**10.239**	b.d.l.	b.d.l.	**90.218**	**0.056**	b.d.l.	100.54	897.31		

Teck-Hughes1 (M24804)	b.d.l.	**0.056**	**6.661**	b.d.l.	b.d.l.	**94.311**	**0.048**	b.d.l.	101.08	933.07	altaite, calaverite, native Te, galena all phases intergrown (myrmekitic)	Pb, Te, Au, Ag
Teck-Hughes2 (M24804)	b.d.l.	**0.043**	**6.658**	b.d.l.	b.d.l.	**94.008**	**0.042**	b.d.l.	100.75	933.07		
Teck-Hughes3 (M24804)	b.d.l.	**0.055**	**6.393**	b.d.l.	b.d.l.	**94.481**	**0.068**	b.d.l.	101.00	935.48		
Teck-Hughes4 (M24804)	b.d.l.	**0.046**	**6.442**	b.d.l.	b.d.l.	**94.706**	**0.04**	b.d.l.	101.23	935.52		
Teck-Hughes5 (M24804)	b.d.l.	**0.048**	**6.647**	b.d.l.	b.d.l.	**93.822**	**0.09**	b.d.l.	100.61	932.56		
Upper Beaver1 (M42652)	b.d.l.	**0.164**	**2.216**	b.d.l.	b.d.l.	**94.112**	**4.034**	b.d.l.	100.53	936.20	pyrite	Fe
Upper Beaver2 (M42652)	b.d.l.	**0.163**	**2.351**	b.d.l.	b.d.l.	**93.6**	**3.967**	b.d.l.	100.08	935.24		
Upper Beaver3 (M42652)	b.d.l.	**0.169**	**2.359**	b.d.l.	b.d.l.	**93.606**	**4.036**	b.d.l.	100.17	934.47		
Upper Beaver4 (M42652)	b.d.l.	**0.152**	**2.312**	b.d.l.	b.d.l.	**93.534**	**4.028**	b.d.l.	100.03	935.10		
Upper Beaver5 (M42652)	b.d.l.	**0.157**	**2.306**	b.d.l.	b.d.l.	**93.749**	**4.012**	b.d.l.	100.22	935.39		
Dixon Claims1 (M48036)	b.d.l.	**0.021**	**15.74**	b.d.l.	b.d.l.	**85.201**	**0.214**	b.d.l.	101.18	842.11	altaite, unidentified Pb-Bi-Ag telluride	Pb, Te, Bi, Ag
Dixon Claims2 (M48036)	b.d.l.	**0.027**	**15.539**	b.d.l.	b.d.l.	**85.322**	**0.247**	b.d.l.	101.14	843.64		
Dixon Claims3 (M48036)	b.d.l.	**0.028**	**15.437**	b.d.l.	b.d.l.	**84.372**	**0.228**	b.d.l.	100.07	843.17		
Dixon Claims4 (M48036)	b.d.l.	**0.03**	**15.398**	b.d.l.	**0.020**	**84.973**	**0.217**	b.d.l.	100.64	844.34		
Dixon Claims5 (M48036)	b.d.l.	**0.014**	**15.466**	b.d.l.	b.d.l.	**85.064**	**0.206**	b.d.l.	100.75	844.31		
Red Lake1 (M52649)	b.d.l.	**0.068**	**2.841**	b.d.l.	b.d.l.	**96.293**	**1.109**	b.d.l.	100.31	959.94	aurostibite (Ni-bearing), pyrite, ullmannite	Sb, Ni, Au, Fe
Red Lake2 (M52649)	b.d.l.	**0.065**	**2.944**	b.d.l.	b.d.l.	**96.148**	**1.082**	b.d.l.	100.24	959.19		
Red Lake3 (M52649)	b.d.l.	**0.063**	**2.776**	b.d.l.	b.d.l.	**96.657**	**1.043**	**0.106**	100.65	960.38		
Red Lake4 (M52649)	b.d.l.	**0.074**	**3.165**	b.d.l.	b.d.l.	**96.428**	**1.063**	b.d.l.	100.73	957.29		
Red Lake5 (M52649)	b.d.l.	**0.064**	**3.078**	b.d.l.	b.d.l.	**95.963**	**1.056**	b.d.l.	100.16	958.09		
Dickenson1 (M26912)	b.d.l.	**0.03**	**8.737**	b.d.l.	b.d.l.	**91.862**	**0.072**	b.d.l.	100.70	912.23		

Dickenson2 (M26912)	b.d.l.	**0.044**	**8.767**	b.d.l.	b.d.l.	**91.707**	**0.056**	b.d.l.	100.57	911.84	chalcopyrite, ullmannite, pyrite, pyrrhotite, zinkenite	Cu, Ni, Sb, Fe, Pb
Dickenson3 (M26912)	b.d.l.	**0.044**	**8.685**	b.d.l.	b.d.l.	**91.396**	**0.075**	b.d.l.	100.20	912.14		
Dickenson4 (M26912)	b.d.l.	**0.031**	**8.689**	b.d.l.	b.d.l.	**91.654**	**0.054**	b.d.l.	100.43	912.63		
Dickenson5 (M26912)	b.d.l.	**0.033**	**8.834**	b.d.l.	b.d.l.	**91.858**	**0.066**	b.d.l.	100.79	911.37		
Teck-Hughes1 (M13815)	b.d.l.	**0.054**	**4.915**	b.d.l.	b.d.l.	**95.13**	**0.051**	b.d.l.	100.15	949.88	altaite, barite, melonite	Pb, Te, Ni, Ba
Teck-Hughes2 (M13815)	b.d.l.	**0.066**	**4.707**	b.d.l.	b.d.l.	**95.362**	**0.059**	b.d.l.	100.19	951.77		
Teck-Hughes3 (M13815)	b.d.l.	**0.086**	**4.737**	b.d.l.	b.d.l.	**95.368**	**0.083**	b.d.l.	100.27	951.07		
Teck-Hughes4 (M13815)	b.d.l.	**0.068**	**4.662**	b.d.l.	b.d.l.	**95.456**	**0.062**	b.d.l.	100.25	952.20		
Teck-Hughes5 (M13815)	b.d.l.	**0.057**	**4.814**	b.d.l.	b.d.l.	**95.839**	**0.044**	b.d.l.	100.75	951.22		
Vipond1 (M15118)	b.d.l.	b.d.l.	**18.666**	b.d.l.	b.d.l.	**81.828**	**0.326**	b.d.l.	100.82	811.62	altaite	Pb, Te
Vipond2 (M15118)	b.d.l.	b.d.l.	**18.413**	b.d.l.	b.d.l.	**81.644**	**0.338**	b.d.l.	100.40	813.23		
Vipond3 (M15118)	b.d.l.	b.d.l.	**18.448**	b.d.l.	b.d.l.	**81.871**	**0.313**	b.d.l.	100.63	813.57		
Vipond4 (M15118)	b.d.l.	**0.016**	**18.3**	b.d.l.	**0.028**	**81.728**	**0.334**	b.d.l.	100.41	813.98		
Vipond5 (M15118)	b.d.l.	b.d.l.	**18.22**	b.d.l.	b.d.l.	**81.904**	**0.325**	**0.087**	100.54	814.67		
Ashley1 (M19881)	b.d.l.	**0.026**	**16.052**	b.d.l.	b.d.l.	**84.575**	**0.068**	b.d.l.	100.72	839.70	hessite (Pb- and Hg-bearing)	Te, Ag, Hg, Pb
Ashley2 (M19881)	b.d.l.	**0.016**	**15.971**	b.d.l.	b.d.l.	**84.516**	**0.08**	b.d.l.	100.58	840.26		
Ashley3 (M19881)	b.d.l.	**0.024**	**15.799**	b.d.l.	b.d.l.	**83.934**	**0.084**	b.d.l.	99.84	840.68		
Ashley4 (M19881)	b.d.l.	**0.025**	**15.757**	b.d.l.	b.d.l.	**84.03**	**0.072**	b.d.l.	99.88	841.28		
Ashley5 (M19881)	b.d.l.	**0.023**	**15.825**	b.d.l.	b.d.l.	**84.449**	**0.042**	b.d.l.	100.34	841.64		
O'Brien1 (M25293)	b.d.l.	**0.035**	**8.334**	b.d.l.	b.d.l.	**91.786**	b.d.l.	b.d.l.	100.16	916.44	no associated phases in subsample	no associated phases in subsample
O'Brien2 (M25293)	b.d.l.	**0.042**	**8.762**	b.d.l.	b.d.l.	**91.564**	**0.052**	b.d.l.	100.42	911.81		
O'Brien3 (M25293)	b.d.l.	**0.017**	**8.537**	b.d.l.	b.d.l.	**92.007**	**0.04**	b.d.l.	100.60	914.57		
O'Brien4 (M25293)	b.d.l.	**0.041**	**8.397**	b.d.l.	b.d.l.	**92.102**	b.d.l.	b.d.l.	100.54	916.07		

O'Brien5 (M25293)	b.d.l.	**0.042**	**8.533**	b.d.l.	b.d.l.	**92.014**	b.d.l.	b.d.l.	100.59	914.75		
Preston East Dome1 (M22584)	b.d.l.	**0.018**	**9.311**	b.d.l.	b.d.l.	**91.461**	**0.057**	b.d.l.	100.85	906.93	pyrrhotite, chalcopyrite, tellurobismuthite	Cu, Fe, Bi, Te
Preston East Dome2 (M22584)	b.d.l.	**0.018**	**9.147**	b.d.l.	b.d.l.	**90.59**	**0.041**	b.d.l.	99.80	907.75		
Preston East Dome3 (M22584)	b.d.l.	**0.033**	**9.111**	b.d.l.	b.d.l.	**90.865**	**0.068**	b.d.l.	100.08	907.95		
Preston East Dome4 (M22584)	**0.035**	**0.042**	**9.442**	b.d.l.	b.d.l.	**90.754**	**0.076**	b.d.l.	100.35	904.38		
Preston East Dome5 (M22584)	b.d.l.	**0.033**	**9.084**	b.d.l.	b.d.l.	**90.861**	**0.073**	b.d.l.	100.05	908.15		
Hollinger1 (M22631)	b.d.l.	**0.038**	**9.618**	b.d.l.	b.d.l.	**90.317**	**0.043**	b.d.l.	100.02	903.03	pyrite (As- and Sb-bearing)	Fe, As, Sb
Hollinger2 (M22631)	b.d.l.	**0.039**	**9.887**	b.d.l.	b.d.l.	**90.551**	**0.056**	b.d.l.	100.53	900.71		
Hollinger3 (M22631)	b.d.l.	**0.048**	**10.061**	b.d.l.	b.d.l.	**90.401**	**0.089**	b.d.l.	100.60	898.63		
Hollinger4 (M22631)	b.d.l.	**0.043**	**9.306**	b.d.l.	b.d.l.	**90.483**	**0.065**	b.d.l.	99.90	905.76		
Hollinger5 (M22631)	b.d.l.	**0.054**	**9.688**	b.d.l.	b.d.l.	**90.636**	b.d.l.	b.d.l.	100.38	902.95		
Preston1 (M22637)	b.d.l.	**0.073**	**7.344**	b.d.l.	b.d.l.	**92.125**	**0.098**	b.d.l.	99.64	924.58	no associated phases in subsample	no associated phases in subsample
Preston2 (M22637)	b.d.l.	**0.073**	**7.453**	b.d.l.	b.d.l.	**92.294**	**0.126**	b.d.l.	99.95	923.44		
Preston3 (M22637)	b.d.l.	**0.084**	**7.212**	b.d.l.	b.d.l.	**92.086**	**0.107**	b.d.l.	99.49	925.59		
Preston4 (M22637)	b.d.l.	**0.085**	**7.411**	b.d.l.	b.d.l.	**92.063**	**0.122**	b.d.l.	99.68	923.58		
Preston5 (M22637)	b.d.l.	**0.08**	**7.318**	b.d.l.	b.d.l.	**92.762**	**0.105**	b.d.l.	100.27	925.17		
Porcupine Reef1 (M38695)	b.d.l.	**0.028**	**7.495**	b.d.l.	b.d.l.	**92.91**	b.d.l.	b.d.l.	100.43	925.09	sphalerite, pyrite, chalcopyrite	Zn, Fe, Cu
Porcupine Reef2 (M38695)	b.d.l.	**0.063**	**7.574**	b.d.l.	b.d.l.	**92.992**	**0.065**	b.d.l.	100.69	923.51		
Porcupine Reef3 (M38695)	b.d.l.	**0.04**	**7.549**	b.d.l.	b.d.l.	**93.033**	**0.075**	b.d.l.	100.70	923.89		
Porcupine Reef4 (M38695)	b.d.l.	**0.06**	**7.745**	b.d.l.	b.d.l.	**92.091**	**0.05**	b.d.l.	99.95	921.41		
Porcupine Reef5 (M38695)	b.d.l.	**0.056**	**7.324**	b.d.l.	b.d.l.	**92.89**	**0.066**	b.d.l.	100.34	925.79		

Campbell Red Lake1 (M38697)	b.d.l.	**0.018**	**9.241**	b.d.l.	b.d.l.	**90.315**	**0.507**	b.d.l.	100.08	902.42	pyrrhotite, sphalerite, chalcopyrite, arsenopyrite, galena, unidentified sulfosalts (Pb-Sb-Ni-As-Ti-Fe)	Fe, Ti, Sb, As, Ni, Se, Pb, Zn
Campbell Red Lake2 (M38697)	b.d.l.	**0.023**	**9.195**	b.d.l.	b.d.l.	**90.11**	**0.527**	b.d.l.	99.86	902.41		
Campbell Red Lake3 (M38697)	**0.035**	**0.035**	**9.438**	b.d.l.	b.d.l.	**90.54**	**0.532**	**0.084**	100.66	899.43		
Campbell Red Lake4 (M38697)	b.d.l.	**0.033**	**9.654**	b.d.l.	b.d.l.	**90.405**	**0.534**	b.d.l.	100.63	898.43		
Campbell Red Lake5 (M38697)	b.d.l.	**0.023**	**9.384**	b.d.l.	b.d.l.	**90.167**	**0.57**	b.d.l.	100.14	900.37		
Madsen1 (M38701)	b.d.l.	b.d.l.	**1.012**	b.d.l.	b.d.l.	**98.265**	**0.042**	b.d.l.	99.32	989.39	native As	As
Madsen2 (M38701)	b.d.l.	**0.023**	**1.012**	b.d.l.	b.d.l.	**99.646**	b.d.l.	b.d.l.	100.68	989.72		
Madsen3 (M38701)	b.d.l.	**0.012**	**0.923**	b.d.l.	b.d.l.	**98.376**	b.d.l.	b.d.l.	99.31	990.59		
Madsen4 (M38701)	b.d.l.	b.d.l.	**1.01**	b.d.l.	b.d.l.	**99.072**	b.d.l.	b.d.l.	100.08	989.91		
Madsen5 (M38701)	b.d.l.	**0.018**	**1.164**	b.d.l.	b.d.l.	**98.121**	**0.065**	b.d.l.	99.37	987.45		
Macassa1 (M38715)	b.d.l.	**0.036**	**5.978**	b.d.l.	b.d.l.	**93.656**	**0.354**	b.d.l.	100.02	936.34	unidentified Hg- and Au-Ag tellurides	Hg, Te, Au, Ag,
Macassa2 (M38715)	b.d.l.	**0.033**	**5.818**	b.d.l.	b.d.l.	**94.148**	**0.381**	b.d.l.	100.38	937.92		
Macassa3 (M38715)	b.d.l.	**0.035**	**5.697**	b.d.l.	b.d.l.	**93.853**	**0.362**	b.d.l.	99.95	939.03		
Macassa4 (M38715)	b.d.l.	**0.053**	**6.034**	b.d.l.	b.d.l.	**94.134**	**0.366**	b.d.l.	100.59	935.85		
Macassa5 (M38715)	b.d.l.	**0.04**	**5.945**	b.d.l.	b.d.l.	**93.973**	**0.381**	b.d.l.	100.34	936.56		
Siscoe1 (M38721)	b.d.l.	**0.061**	**8.573**	b.d.l.	b.d.l.	**91.767**	b.d.l.	b.d.l.	100.40	914.00	no associated phases in subsample	no associated phases in subsample
Siscoe2 (M38721)	b.d.l.	**0.045**	**8.624**	b.d.l.	b.d.l.	**91.682**	**0.042**	b.d.l.	100.39	913.23		
Siscoe3 (M38721)	b.d.l.	**0.06**	**8.808**	**0.027**	b.d.l.	**91.057**	b.d.l.	b.d.l.	99.95	911.01		
Siscoe4 (M38721)	b.d.l.	**0.059**	**8.51**	b.d.l.	b.d.l.	**91.349**	b.d.l.	b.d.l.	99.92	914.24		
Siscoe5 (M38721)	b.d.l.	**0.066**	**8.742**	b.d.l.	b.d.l.	**91.322**	b.d.l.	b.d.l.	100.13	912.03		
Quemont1 (M38723)	b.d.l.	**0.079**	**5.104**	b.d.l.	b.d.l.	**95.088**	**0.043**	b.d.l.	100.31	947.90	pyrite, chalcopyrite,	Cu, Fe, Zn
Quemont2 (M38723)	b.d.l.	**0.109**	**5.183**	b.d.l.	b.d.l.	**95.258**	b.d.l.	b.d.l.	100.55	947.37		

											sphalerite	
Quemont3 (M38723)	b.d.l.	**0.089**	**4.377**	b.d.l.	b.d.l.	**88.532**	b.d.l.	b.d.l.	93.00	951.98		
Quemont4 (M38723)	b.d.l.	**0.081**	**5.171**	b.d.l.	b.d.l.	**95.157**	b.d.l.	b.d.l.	100.41	947.69		
Quemont5 (M38723)	b.d.l.	**0.094**	**5.256**	b.d.l.	b.d.l.	**94.741**	b.d.l.	b.d.l.	100.09	946.55		
Magus' River1 (M38724)	b.d.l.	**0.026**	**15.762**	b.d.l.	b.d.l.	**84.505**	**0.046**	b.d.l.	100.34	842.19	no associated phases in subsample	no associated phases in subsample
Magus' River2 (M38724)	b.d.l.	**0.016**	**15.599**	b.d.l.	b.d.l.	**85.142**	b.d.l.	b.d.l.	100.76	845.02		
Magus' River3 (M38724)	b.d.l.	**0.027**	**15.91**	b.d.l.	b.d.l.	**85.121**	**0.059**	b.d.l.	101.12	841.81		
Magus' River4 (M38724)	b.d.l.	**0.014**	**15.258**	b.d.l.	b.d.l.	**84.134**	b.d.l.	b.d.l.	99.41	846.37		
Magus' River5 (M38724)	b.d.l.	**0.016**	**15.653**	b.d.l.	b.d.l.	**84.553**	**0.056**	b.d.l.	100.28	843.19		
Powell1 (M38726)	b.d.l.	**0.04**	**8.008**	b.d.l.	b.d.l.	**92.373**	**0.044**	b.d.l.	100.47	919.45	tetradymite	Bi, Te
Powell2 (M38726)	b.d.l.	**0.059**	**8.276**	b.d.l.	b.d.l.	**92.082**	b.d.l.	b.d.l.	100.42	917.00		
Powell3 (M38726)	b.d.l.	**0.046**	**8.035**	b.d.l.	b.d.l.	**92.326**	**0.073**	b.d.l.	100.48	918.85		
Powell4 (M38726)	**0.041**	**0.032**	**8.071**	b.d.l.	b.d.l.	**92.221**	**0.046**	b.d.l.	100.41	918.44		
Powell5 (M38726)	b.d.l.	**0.049**	**7.9**	b.d.l.	b.d.l.	**92.063**	**0.047**	b.d.l.	100.06	920.09		
Upper Canada1 (M42651)	b.d.l.	**0.065**	**5.105**	b.d.l.	b.d.l.	**94.936**	**0.318**	b.d.l.	100.42	945.35	tetrahedrite, altaite	Pb, Te, Sb, Cu, Zn
Upper Canada2 (M42651)	b.d.l.	**0.072**	**5.153**	b.d.l.	b.d.l.	**94.116**	**0.294**	b.d.l.	99.64	944.61		
Upper Canada3 (M42651)	b.d.l.	**0.061**	**5.214**	b.d.l.	b.d.l.	**94.758**	**0.28**	b.d.l.	100.31	944.62		
Upper Canada4 (M42651)	b.d.l.	**0.071**	**5.188**	b.d.l.	b.d.l.	**94.54**	**0.333**	b.d.l.	100.13	944.15		
Upper Canada5 (M42651)	b.d.l.	**0.077**	**5.097**	b.d.l.	b.d.l.	**94.993**	**0.332**	**0.092**	100.59	944.35		
Vedron1 (M46421)	b.d.l.	**0.042**	**7.803**	**0.024**	b.d.l.	**92.217**	**0.064**	b.d.l.	100.15	920.79	sphalerite, altaite	Zn, Fe, Pb, Te
Vedron2 (M46421)	b.d.l.	**0.029**	**7.642**	b.d.l.	b.d.l.	**91.448**	**0.087**	b.d.l.	99.21	921.80		
Vedron3 (M46421)	b.d.l.	**0.028**	**7.906**	b.d.l.	b.d.l.	**92.729**	b.d.l.	b.d.l.	100.66	921.18		
Vedron4 (M46421)	**0.034**	**0.02**	**7.927**	b.d.l.	b.d.l.	**92.432**	b.d.l.	b.d.l.	100.41	920.52		
Vedron5 (M46421)	b.d.l.	**0.032**	**8.143**	b.d.l.	b.d.l.	**92.014**	**0.088**	b.d.l.	100.28	917.60		

Outpost Island1 (M48035)	b.d.l.	**0.102**	**0.728**	b.d.l.	b.d.l.	**99.486**	b.d.l.	b.d.l.	100.32	991.73	no associated phases in subsample	no associated phases in subsample
Outpost Island2 (M48035)	b.d.l.	**0.072**	**0.699**	b.d.l.	b.d.l.	**99.468**	b.d.l.	b.d.l.	100.24	992.31		
Outpost Island3 (M48035)	b.d.l.	**0.079**	**0.721**	b.d.l.	b.d.l.	**99.777**	b.d.l.	b.d.l.	100.58	992.05		
Outpost Island4 (M48035)	b.d.l.	**0.079**	**0.674**	b.d.l.	b.d.l.	**98.98**	b.d.l.	b.d.l.	99.73	992.45		
Outpost Island5 (M48035)	b.d.l.	**0.072**	**0.674**	b.d.l.	b.d.l.	**98.461**	**0.045**	b.d.l.	99.25	992.03		
McIntyre1 (M9689)	b.d.l.	**0.035**	**9.467**	b.d.l.	b.d.l.	**91.009**	**0.044**	b.d.l.	100.56	905.07	chalcopyrite	Cu, Fe
McIntyre2 (M9689)	b.d.l.	**0.042**	**9.516**	b.d.l.	b.d.l.	**91.336**	**0.072**	b.d.l.	100.97	904.62		
McIntyre3 (M9689)	b.d.l.	**0.042**	**9.688**	b.d.l.	b.d.l.	**90.942**	**0.063**	b.d.l.	100.74	902.78		
McIntyre4 (M9689)	b.d.l.	**0.043**	**9.818**	b.d.l.	b.d.l.	**90.334**	b.d.l.	b.d.l.	100.20	901.58		
McIntyre5 (M9689)	b.d.l.	**0.045**	**9.893**	b.d.l.	b.d.l.	**90.413**	**0.073**	b.d.l.	100.42	900.31		
Kenty1 (this study)	b.d.l.	**0.038**	**10.098**	b.d.l.	b.d.l.	**90.515**	b.d.l.	b.d.l.	100.65	899.30	pyrite, rutile, petzite, hessite, calaverite, sphalerite, chalcopyrite, galena, hematite	Te, Au, Ag, Fe, Zn, Cu, Ti, Pb
Kenty2 (this study)	b.d.l.	**0.026**	**9.949**	b.d.l.	b.d.l.	**90.577**	**0.059**	b.d.l.	100.61	900.27		
Kenty3 (this study)	b.d.l.	**0.035**	**9.748**	b.d.l.	b.d.l.	**90.228**	**0.053**	b.d.l.	100.06	901.70		
Kenty4 (this study)	b.d.l.	**0.027**	**9.951**	b.d.l.	b.d.l.	**90.657**	**0.082**	b.d.l.	100.72	900.12		
Kenty5 (this study)	b.d.l.	**0.033**	**9.773**	b.d.l.	b.d.l.	**90.043**	**0.071**	b.d.l.	99.92	901.15		

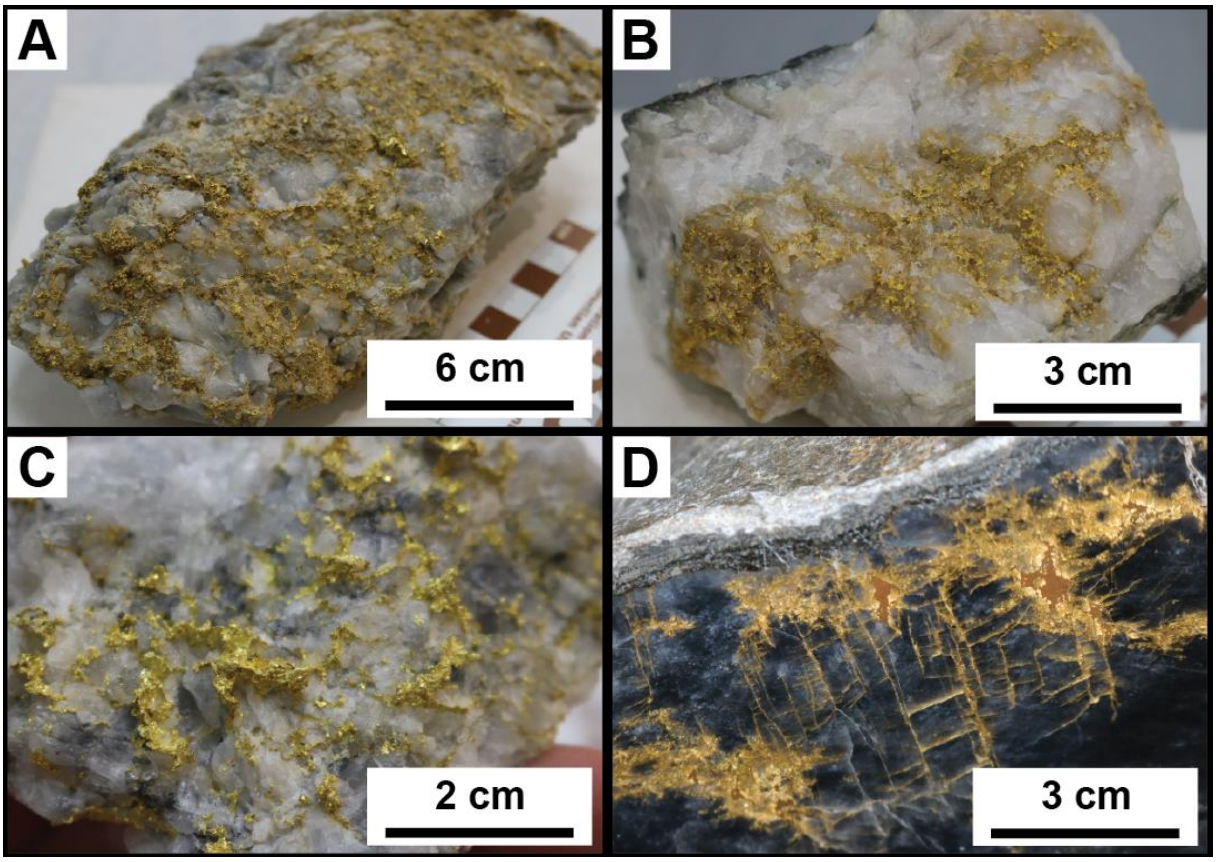

Figure 3.1 Hand sample photographs of gold samples from Archean deposits in Ontario (ON) and Quebec (QC), Canada showing that gold occupies cross-cutting features in the host quartz. A) Gold in quartz from the Croesus deposit, Munro Township east of Matheson, ON (Sample LM47273). B) Gold in quartz from the Kerr Addison deposit, Virginiatown, ON (Sample M38709). C) Gold in quartz from the McIntyre deposit, Timmins, ON. D) Gold in smoky quartz from the O'Brien deposit, Cadillac, QC (Sample 9919). Photos were taken with the permission of the Ontario Geological Survey and the Royal Ontario Museum (ROM); the sample numbers refer to the ROM sample catalogue. Scale card with cm units.

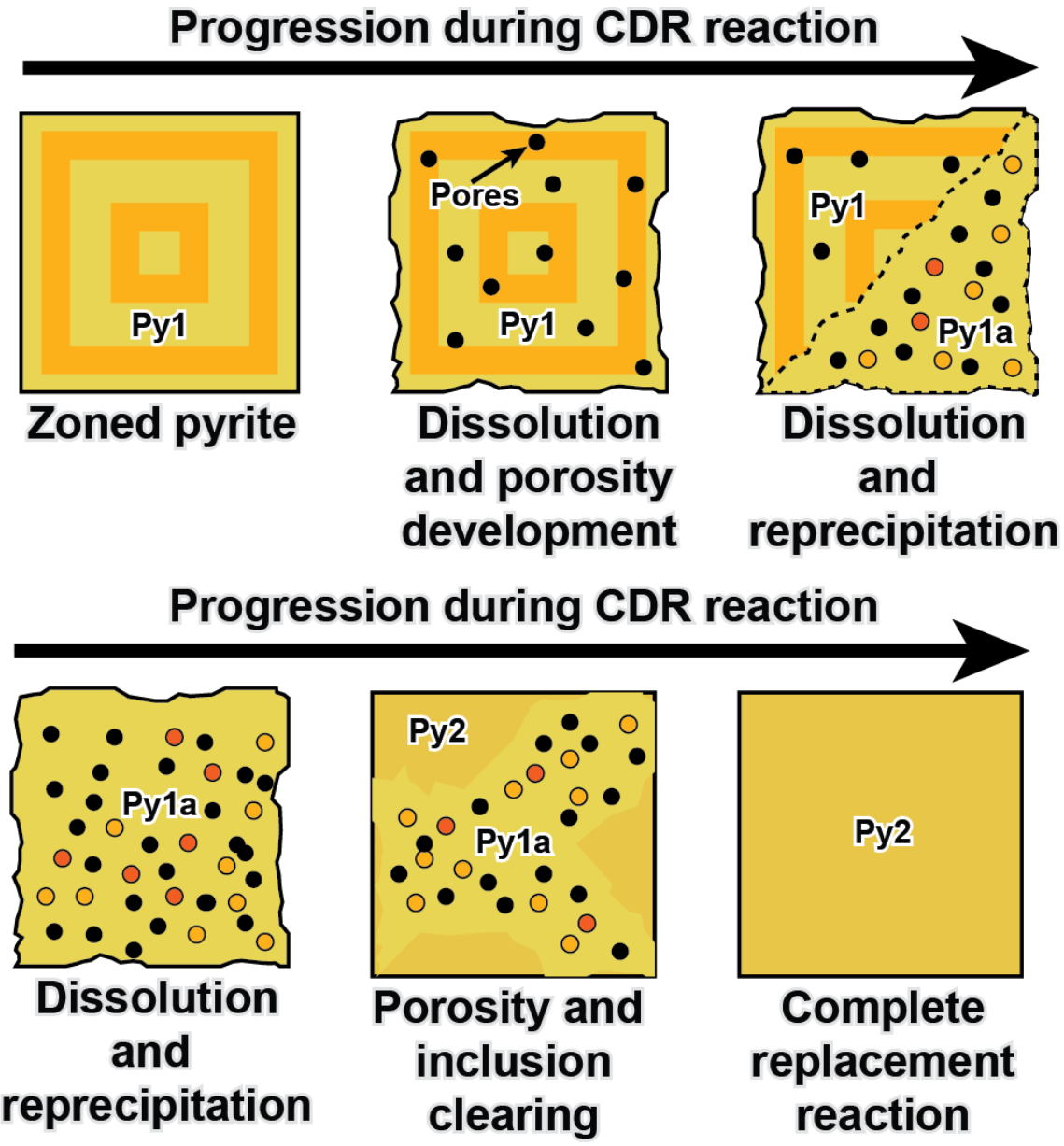

Figure 3.2 Schematic diagram illustrating CDR reactions and textures that develop at various stages of the process (constructed using concepts from Putnis, 2009). Note Py1a is a hybrid phase between the first generation pyrite (Py1) and the replacement pyrite (Py2). As such, the textures and microstructures (inclusions and porosity) are retained or "frozen in" if the product phase (pyrite) loses contact with the hydrothermal fluid (Putnis, 2009).

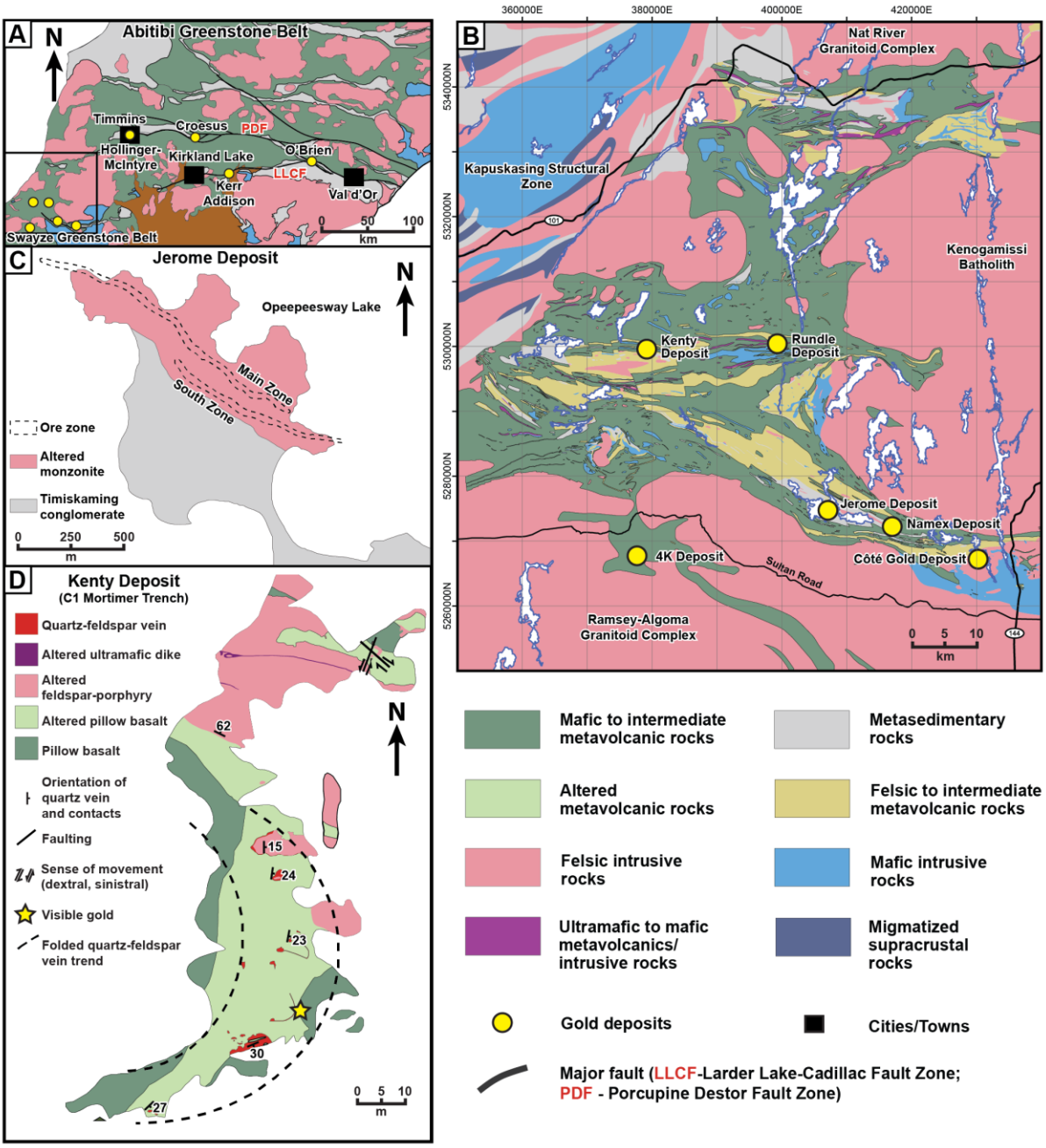

Figure 3.3. Geologic maps of the Abitibi greenstone belt and deposit areas mapped at various scales. The names of Au deposits mentioned in the text are indicated by filled yellow circles. A) Simplified geologic map of the Abitibi greenstone belt (modified after Dubé and Gosselin, 2007) highlighting significant Au deposits. Also shown is the location of the Swayze greenstone belt (enclosed by black rectangle). B) Simplified geologic map of the Swayze greenstone belt.

Location information provided as Universal Transverse Mercator (UTM) co-ordinates using North American Datum 1983 (NAD83) in Zone 17 (modified after Ontario Geological Survey, 2011 and Hastie, 2014). C) Simplified geologic map of the Jerome peninsula outlining a surface projection of known ore zones (modified after Hastie, 2017). D) Geologic outcrop map of the C1 Mortimer trench at the Kenty deposit (modified after Hastie et al., 2015).

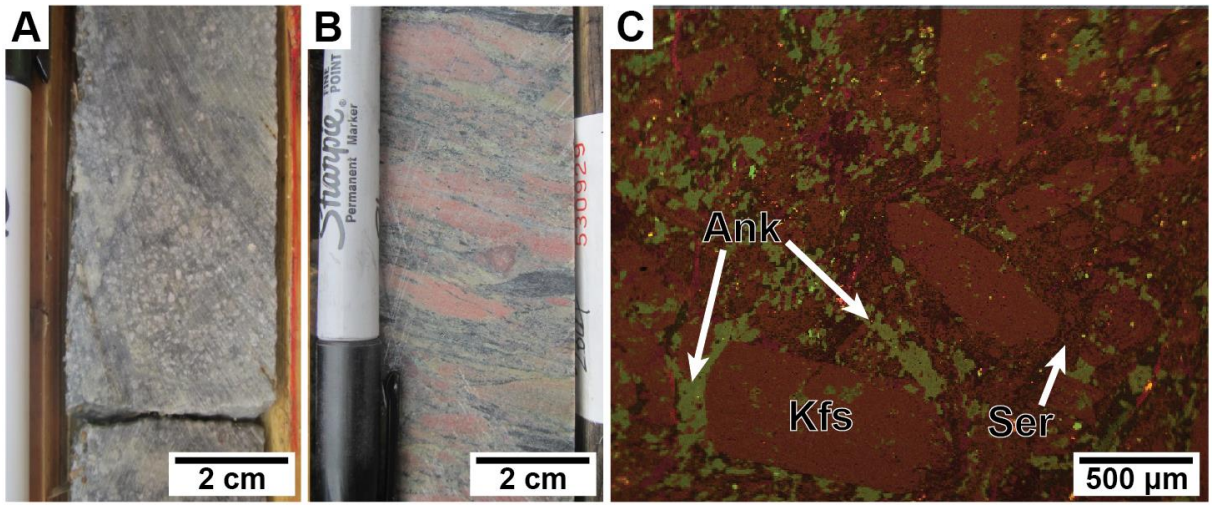

Figure 3.4. Photographs of the host rocks and mineral relationships at the Jerome Au deposit. A) Core sample of least altered feldspar porphyry, although still containing significant Ank and Ser alteration (modified after Hastie, 2014) Length of marker is 14 cm. B) Core sample of deformed polymictic conglomerate containing felsic, mafic and iron formation clasts along with sericite alteration of the matrix (modified after Hastie, 2014). Length of marker is 14 cm. C) Layered SEM-EDS elemental map of feldspar porphyry shown in A showing relict potassium feldspar phenocrysts along with an altered matrix of ankerite, sericite, and potassium feldspar. Different colors indicating major mineral phases are: Ank (green), Kfs (red), Ser (brown). Abbreviations: Ank, ankerite; Kfs, potassium feldspar; Ser, sericite.

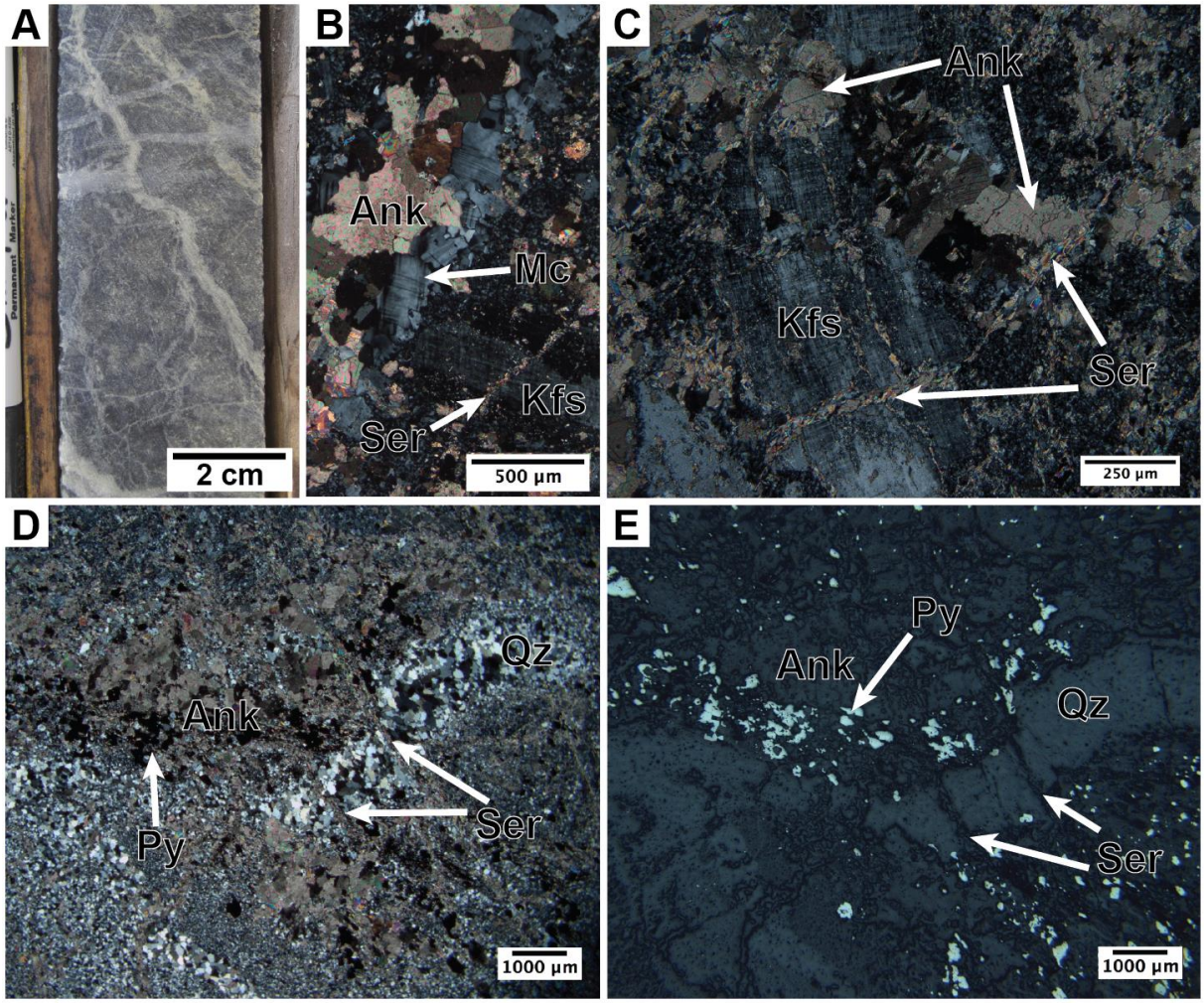

Figure 3.5. Photographs showing the most altered host rocks and mineral relationships at the Jerome Au deposit. A) Core sample of heavily altered and mineralized feldspar porphyry showing stockwork quartz-ankerite ±microcline veins (modified after Hastie, 2014). Length of marker is 14 cm. B) Photomicrograph in crossed nicols showing an ankerite-microcline vein cross-cutting both potassium feldspar phenocrysts in altered feldspar porphyry rocks. C) Photomicrograph in crossed nicols showing ankerite replacement of potassium feldspar, and sericite cross-cutting both ankerite and potassium feldspar in altered feldspar porphyry rocks. D) Photomicrograph in crossed nicols showing folded and fractured quartz-ankerite vein with Py that has been cross-cut by sericite in altered feldspar porphyry rocks. E) Same as D in reflected

light. Abbreviations: Ank, ankerite; Kfs, potassium feldspar; Mc, microcline; Py, pyrite; Qz, quartz; Ser, sericite.

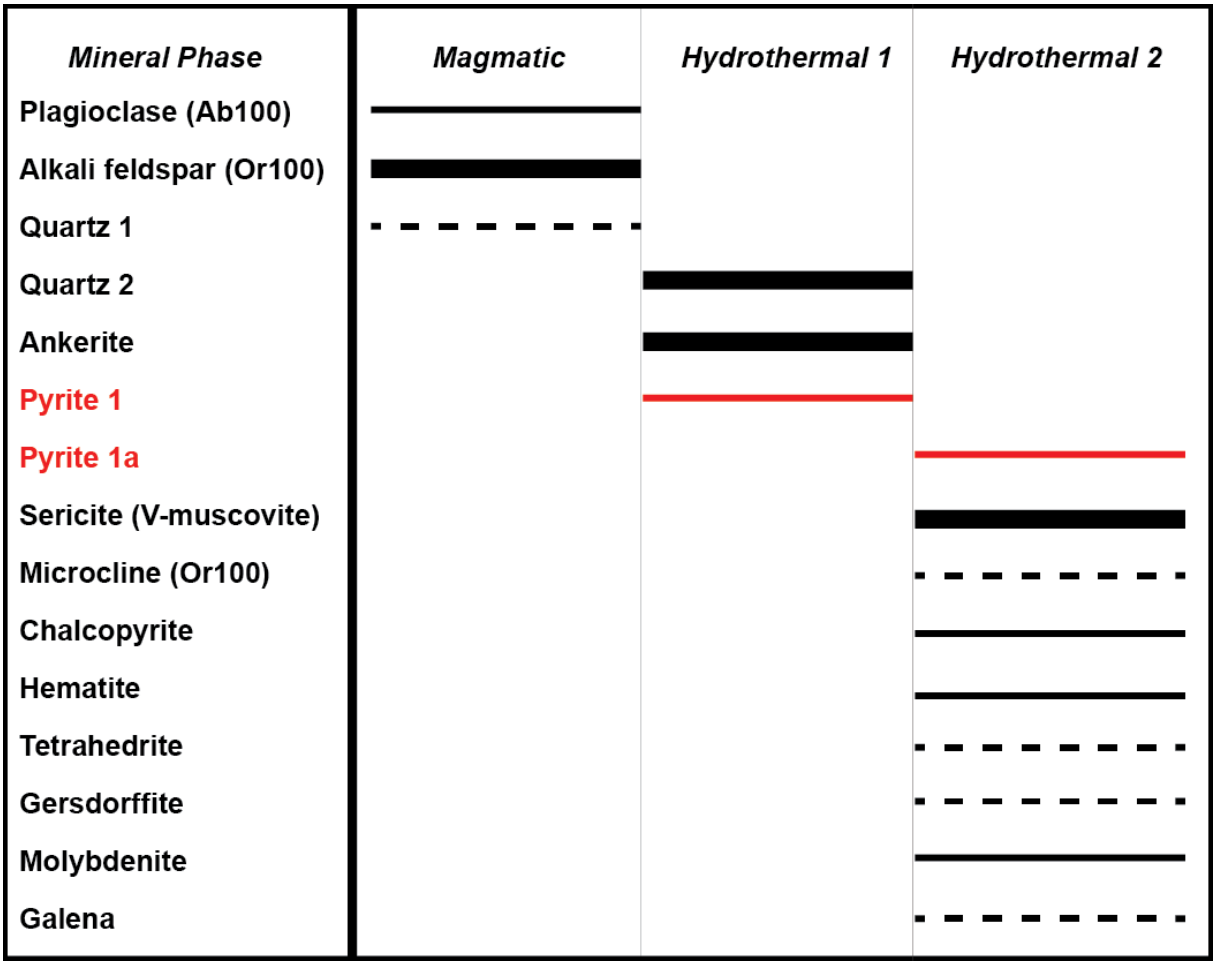

Figure 3.6. Simplified paragenesis for the Jerome Au deposit. Mineral abundance is indicated by black lines (thick=most abundant, thin=less abundant, dashed=least abundant). Red lines and letters indicate Au-bearing phases.

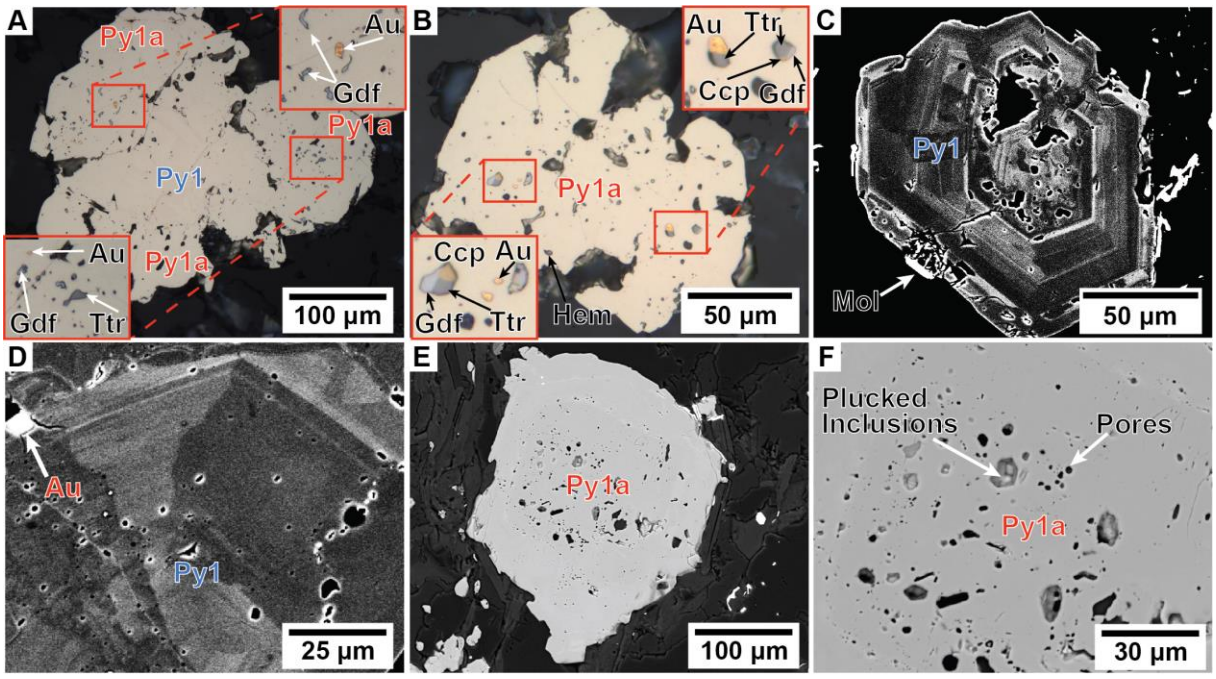

Figure 3.7. Reflected light (RL) photomicrographs and backscattered electron (BSE) images showing the two generations of pyrite (Py1 and Py1a), their textures, and inclusions from the Jerome deposit. Red-boxed insets are higher magnification insets of porous and inclusion-rich areas. A) RL photomicrograph of inclusion-poor Py1 surrounded by porous and inclusion-rich Py1a that hosts gold, gersdorffite and tetrahedrite. B) RL photomicrograph of Py1a showing multi-phase inclusions of gold, chalcopyrite, gersdorffite, and tetrahedrite, as well as inclusions of hematite. C) High-contrast, BSE image of Py1 showing oscillatory and sector zoning. Light zones in pyrite are As-, Cu-, and Au-rich whereas dark zones are Ni- and Co-rich. D) High-contrast, BSE image of Py1 showing oscillatory and sector zoning. Light and dark zones in pyrite have the same metal enrichments and depletion as in C. E) BSE image showing ¬an example of porosity versus plucked inclusions in Py1a. F) Higher magnification of E, showing detail of the porous and plucked texture. Porous texture is seen by round <10 µm holes in Py whereas angular and larger features indicate possible plucking of inclusion phases.

Abbreviations: Au, gold; Ccp, chalcopyrite; Gdf, gersdorffite; Hem, hematite; Py, pyrite; Ttr, tetrahedrite.

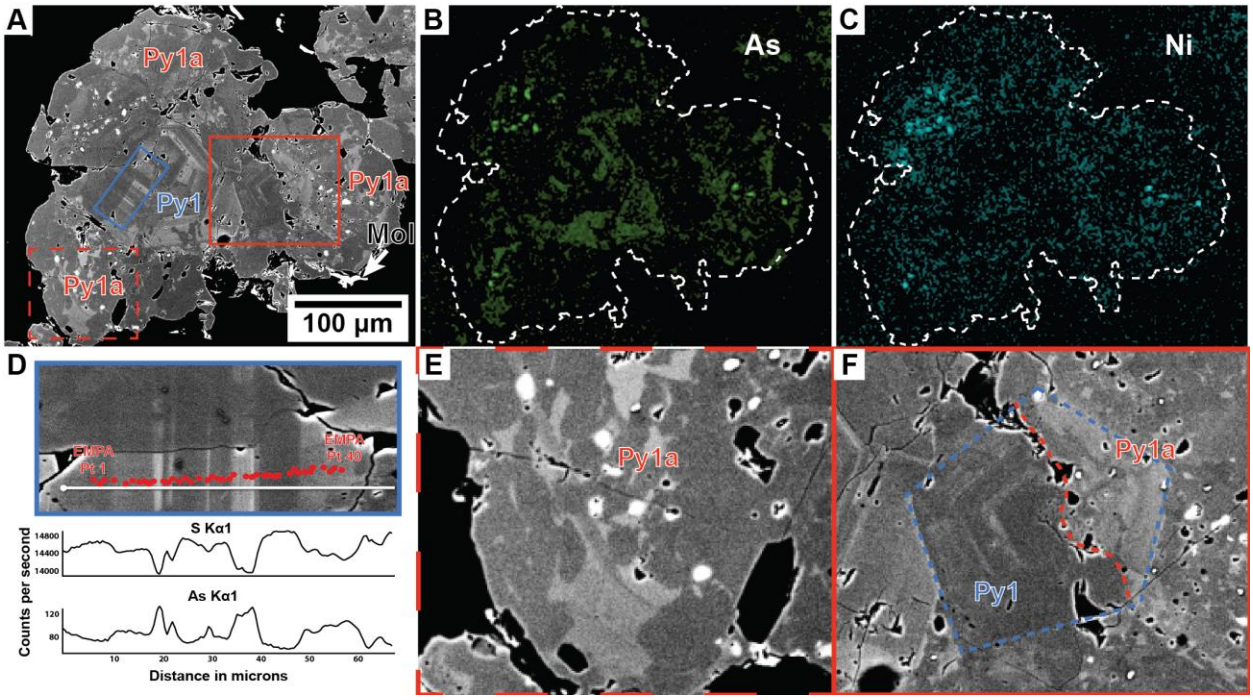

Figure 3.8. High-contrast, SEM backscatter electron (BSE) images and SEM elemental line scan/maps showing chemical zoning and textural relationships between pyrite generations at the Jerome deposit. Rectangles (solid red, dashed red, and solid blue) in A enclose areas of interest that are seen in larger magnification in D, E, and F. A) High-contrast, BSE Image of Py1 surrounded by Py1a. Same grain as shown in Figure 3.6A. Light zones are As-, Cu- and Au-rich and dark zones are Ni- and Co-rich. B) SEM elemental map showing As distribution in green that correlates to light areas of oscillatory zoning in Py1, patchy light zoning in Py1a, and gersdorffite and tetrahedrite inclusions in Py1a. Large grain in Figure 3.6A outlined by white broken line. C) SEM elemental map showing Ni distribution in teal that correlates to dark areas of oscillatory zoning in Py1, patchy dark zoning in Py1a, and gersdorffite inclusions in Py1a. Large grain in Figure 3.6A outlined by white broken line. D) High contrast, BSE image (top) of

area enclosed by blue rectangle in A with red dots indicating the location of some EMPA analyses found in Table 3.2 and a white line indicating the location of an SEM line scan showing data in counts per second for S and As (bottom). E) Higher magnification of area enclosed by dashed red rectangle in the lower left of A showing patchy and dismembered zoning in Py1a. F) Higher magnification of area enclosed by solid red rectangle in right of A showing irregular boundaries between Py1 and Py1a (dashed red) and oscillatory zoning can be seen crossing these boundaries (dashed blue). Abbreviations: Gdf, gersdorffite; Mol, molybdenite; Py, pyrite; Ttr, tetrahedrite.

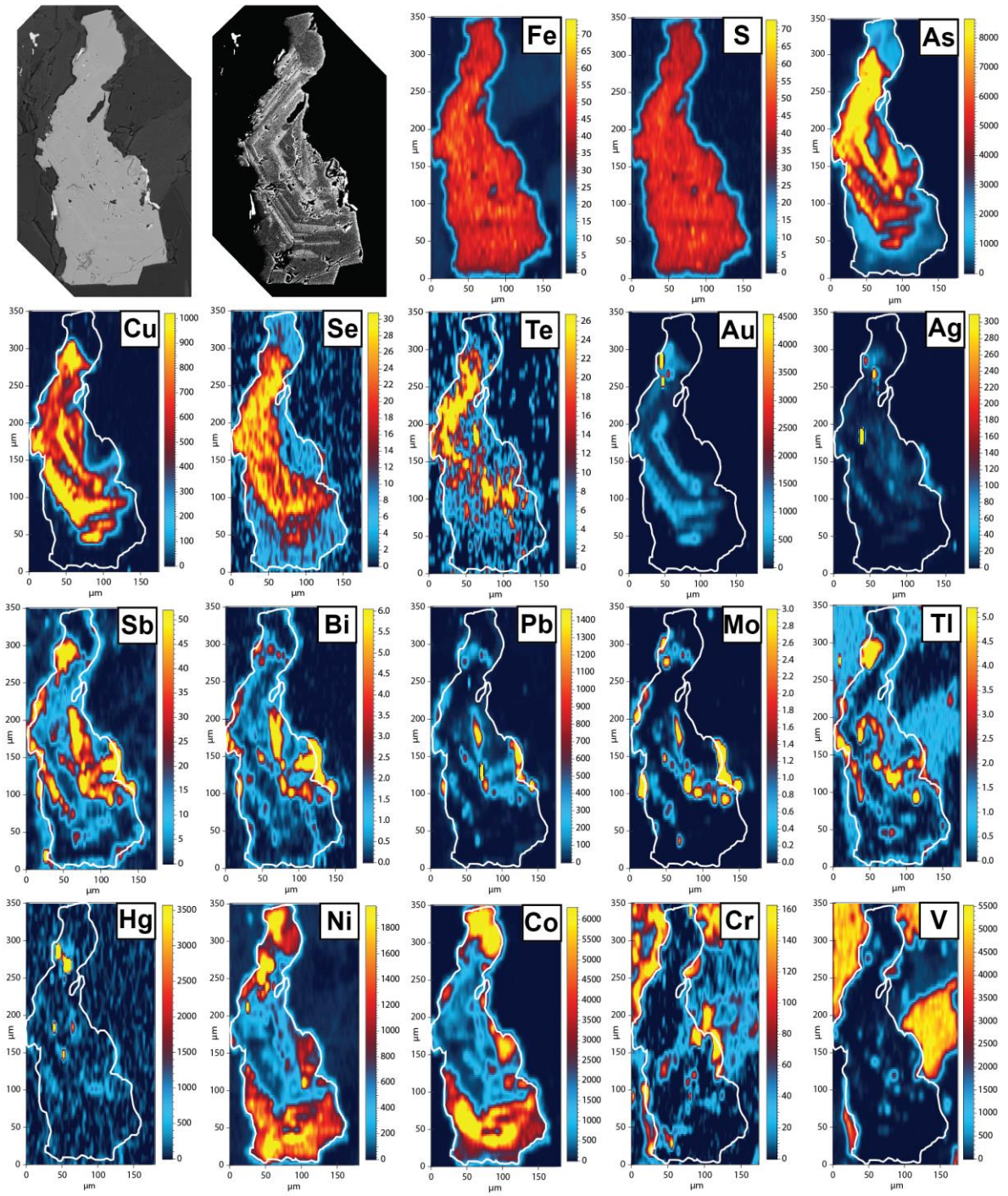

Figure 3.9. SEM backscatter electron images and LA-ICP-MS elemental maps of a pyrite grain from the Jerome Au deposit. Hot colors indicate higher element concentrations in wt% for Fe, Mo, S, and in ppm for the other elements.

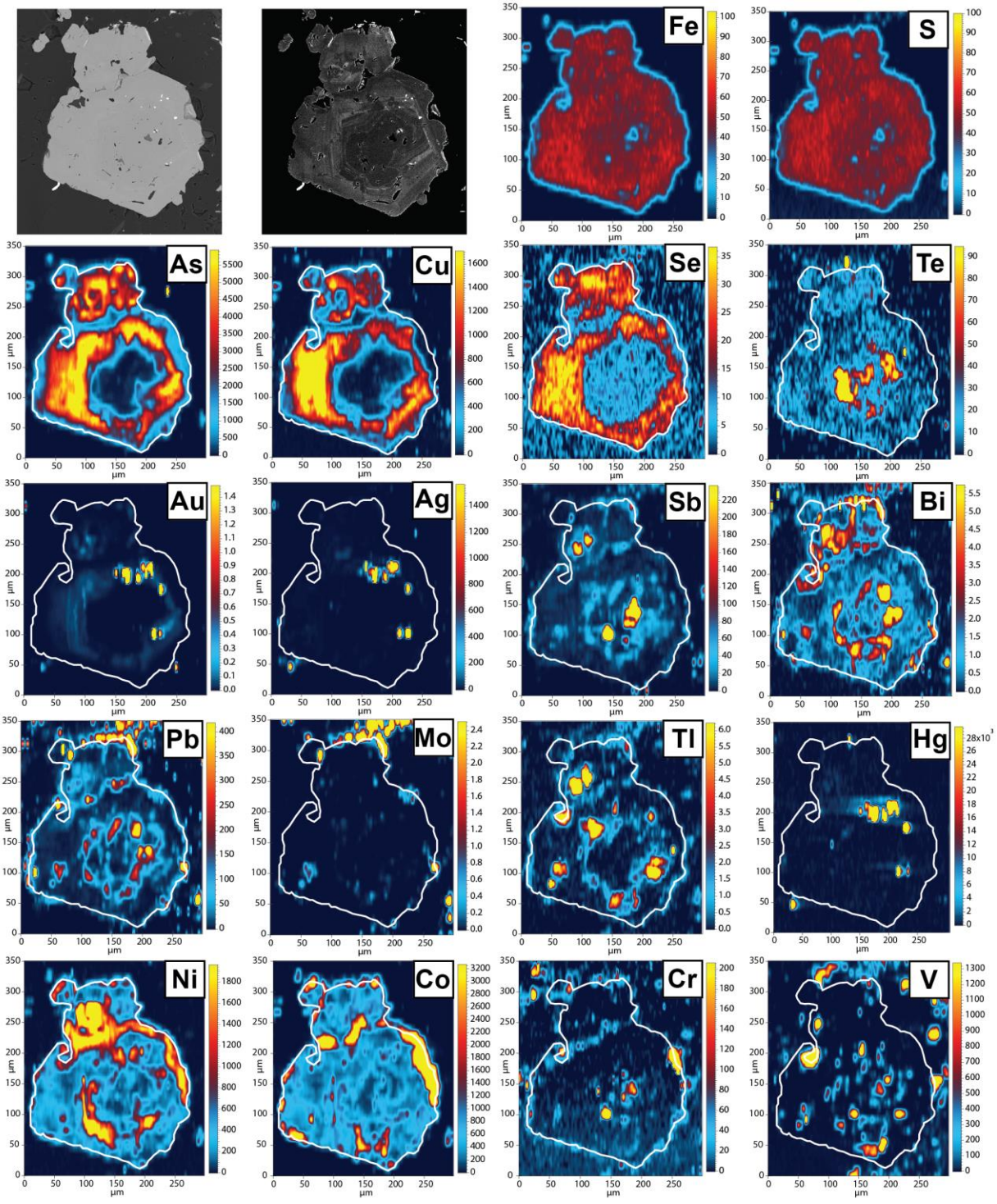

Figure 3.10. SEM backscatter electron images and LA-ICP-MS elemental maps of a pyrite grain from the Jerome Au deposit. Hot colors indicate higher element concentrations in wt% for Au, Fe, Mo, S, and in ppm for the other elements.

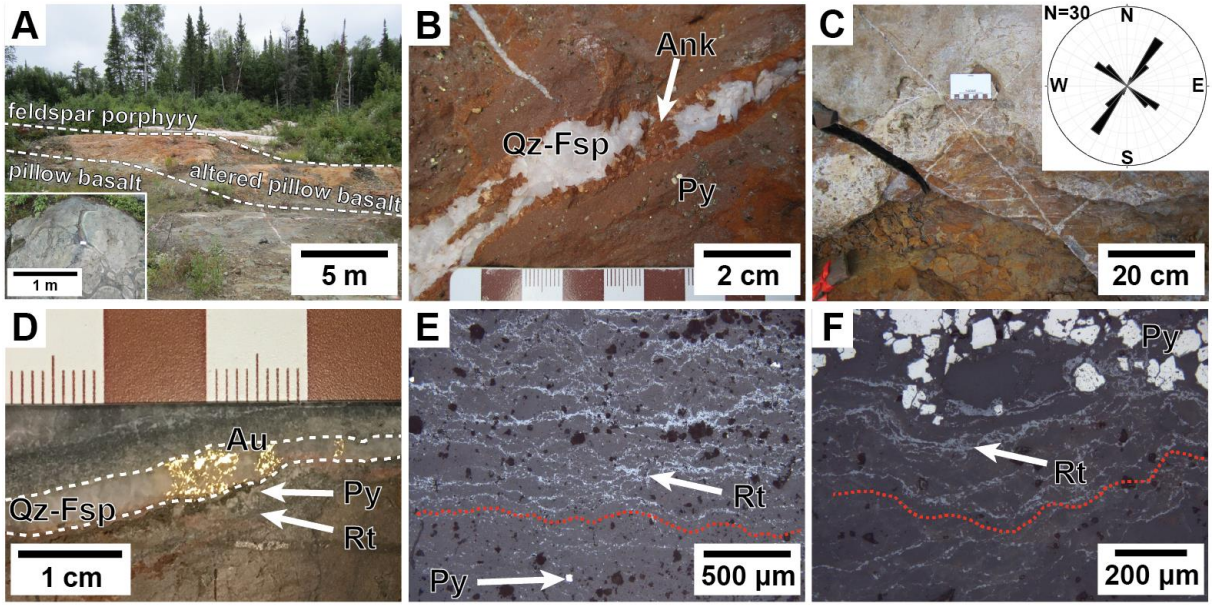

Figure 3.11. Photographs of the host rocks, alteration, and Au mineralization at the C1 Mortimer trench of the Kenty Au deposit. A) Outcrop photograph showing altered pillowed basalt at contact with feldspar porphyry. Lower left inset shows close-up of pillowed basalt. Top of photo is north. B) Field photograph of ankerite altered pillow basalt and associated quartz-feldspar-ankerite vein with pyrite mineralization. C) Field photograph of late conjugate vein sets (≈ 210° and 310°) cross-cutting shallowly dipping vein. Rose diagram inset in upper right corner summarizes conjugate set measurements. Top of photo is NNW. D) Photograph of rock slab of the shallowly dipping quartz-feldspar vein with fracture-fill native gold from the hinge of an open fold in Figure 3.2D. E) Reflected light (RL) photomicrograph of micro-folded rutile foliation planes in altered basalt. The dark pits are due to plucking of weathered pyrite during the polishing process. F) Reflected light (RL) photomicrograph of micro-folded rutile-rich foliation planes and associated pyrite in altered basalt. Abbreviations: Ank, ankerite; Au, gold; Fsp, feldspar; Py, pyrite; Qz, quartz; Rt, rutile.

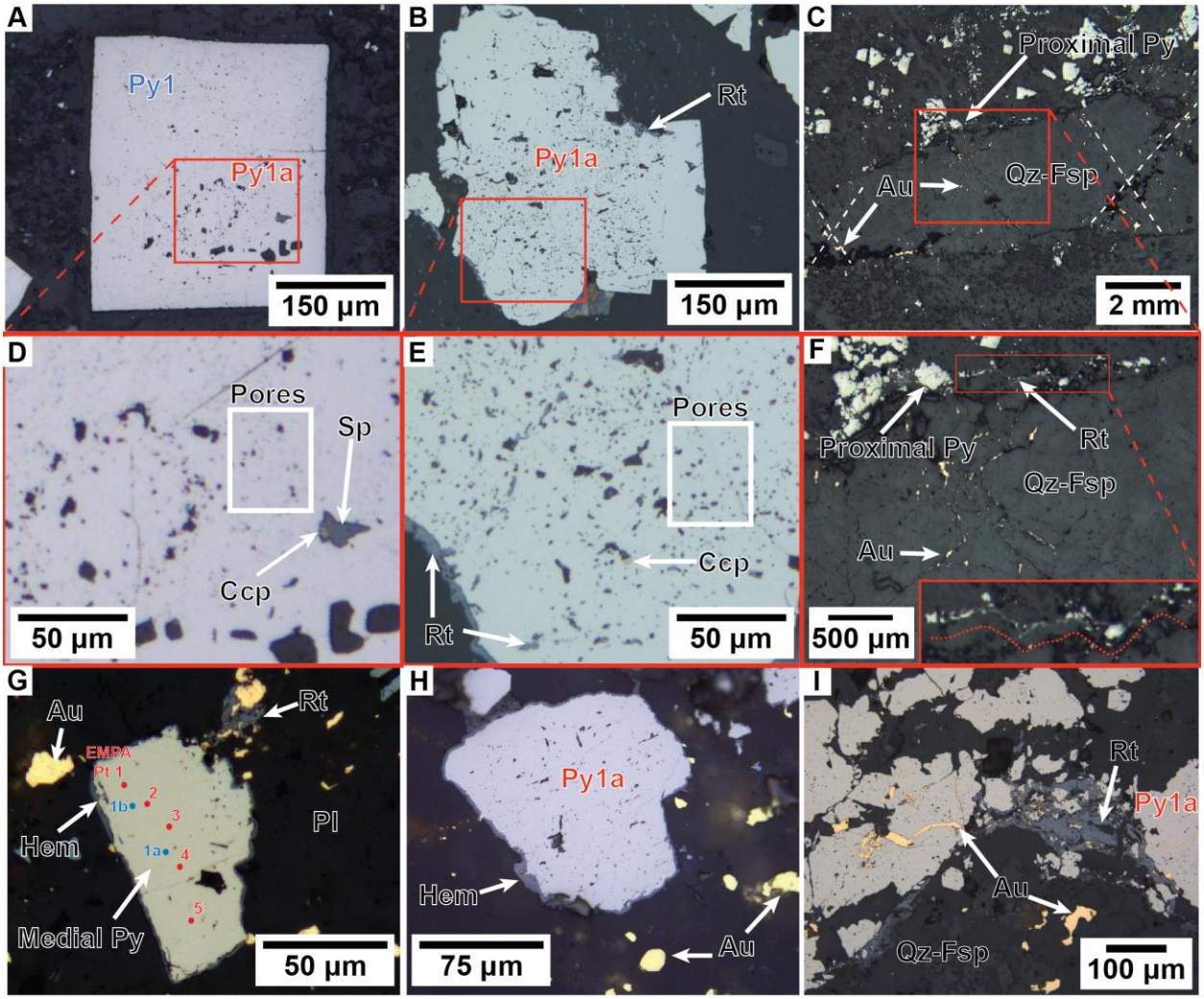

Figure 3.12. Reflected light (RL) photomicrographs of distal, medial, and proximal pyrite grains. Red rectangles and dashed lines link the upper row photomicrographs with the middle row, higher magnification, photomicrographs. A) Distal, euhedral pyrite with pores and inclusions. B) Medial Py with higher abundance of pores and inclusions. C) RL Proximal, anhedral shaped pyrites in addition to presence of native gold filling conjugate fractures in quartz vein (white dashed lines). D) Higher magnification of red rectangle area in A showing pores and inclusions of chalcopyrite and sphalerite. E) Higher magnification of red rectangle in B showing pores and inclusions of chalcopyrite and rutile, as well as rutile rims on pyrite. F) Higher magnification of red rectangle in C showing proximal pyrite mapped by LA-ICP-MS adjacent to

quartz-feldspar vein with native gold filling conjugate fractures in the vein. Dashed red line in lower right of image shows micro-folded trails of rutile that are axial planar to the conjugate fractures within the vein and the hinge of open fold (see Fig. 3.2D). G) A medial pyrite with Hem replacement rim, and spatial association with native gold and rutile. Blue dots indicate locations of precision tests from Table 3.1, while the red dots indicate the location of EMPA traverse data found in Table 3.2. H) Proximal pyrite with hematite replacement rim, and spatial association with native gold. I) Higher magnification of F showing proximal pyrite grain (right) along with gold and rutile. Note that gold is seen as inclusions and fractures in the pyrite as well as outside the pyrite where it is seen forming gold-rutile intergrowths which at a larger scale F shows previously mentioned micro-folding. Abbreviations: Au, gold; Ccp, chalcopyrite; Fsp, feldspar; Gdf, gersdorffite; Hem, hematite; Kfs, potassium feldspar (Or100); Pl, plagioclase (Ab100); Py, pyrite; Qz, quartz; Rt, rutile; Sp, Sphalerite.

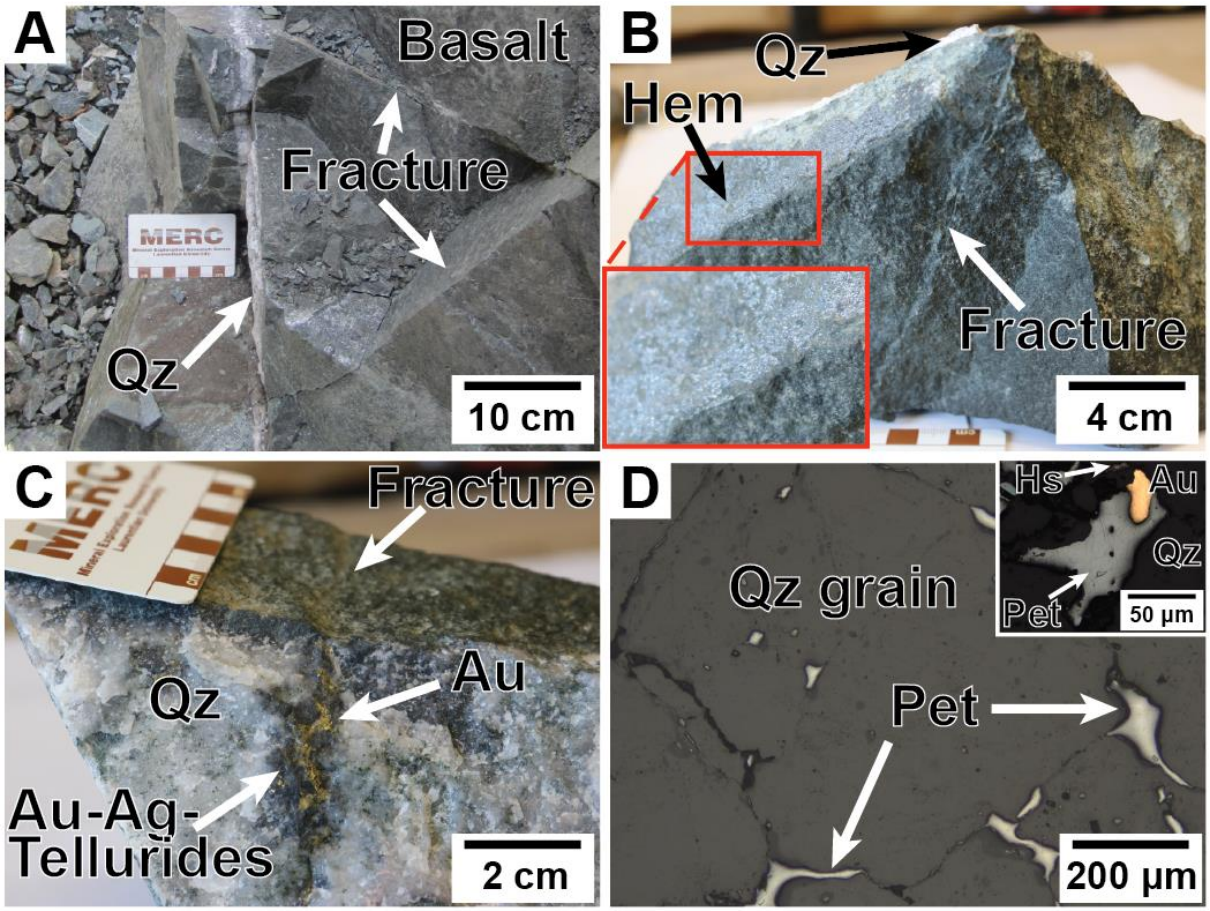

Figure 3.13. Pictures of mineralized quartz vein hosted in basalt from the Mortimer Camp outcrop. A) Representative outcrop photograph, looking north, of a narrow vertical quartz vein cutting the basalt and later conjugate fractures cutting both the basalt and the vein. B) Photograph of hand sample from the outcrop in A showing hematite coating the conjugate fractures (red rectangle inset in lower left). C) Photograph of the same hand sample shown in B rotated to expose the vein surface and enclosed native gold and Au-Ag tellurides. D) Reflected light photomicrograph from the same sample showing low interfacial angles of petzite against quartz and curvilinear grain boundaries between gold and petzite. Abbreviations: Au, gold; Hem, hematite; Hs, Hessite; Pet, petzite; Qz, quartz.

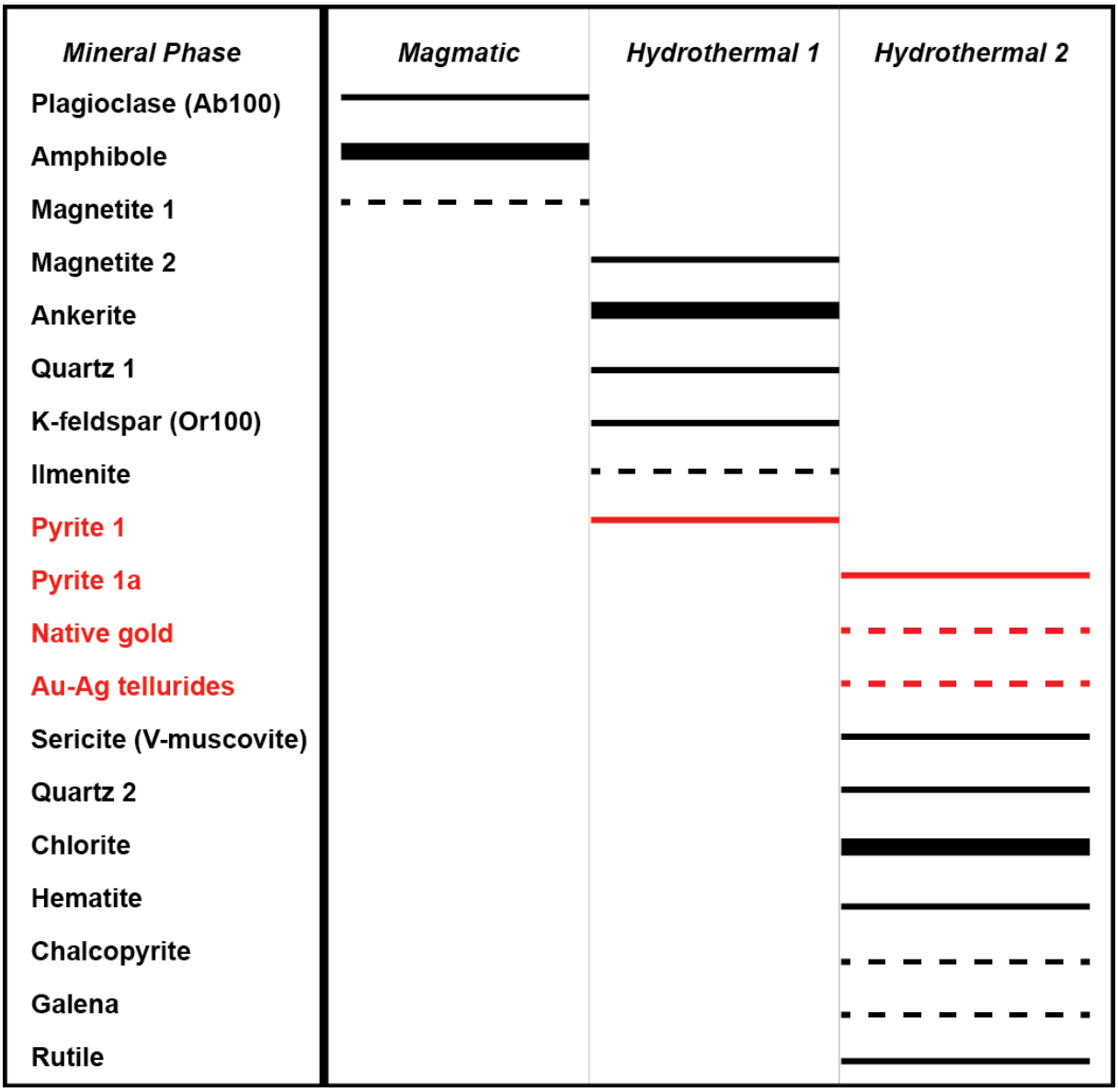

Figure 3.14. Mineral paragenesis for the Kenty Au deposit. Mineral abundance is indicated by black lines (thick=most abundant, thin=less abundant, dashed=least abundant). Red lines indicate Au-bearing phases.

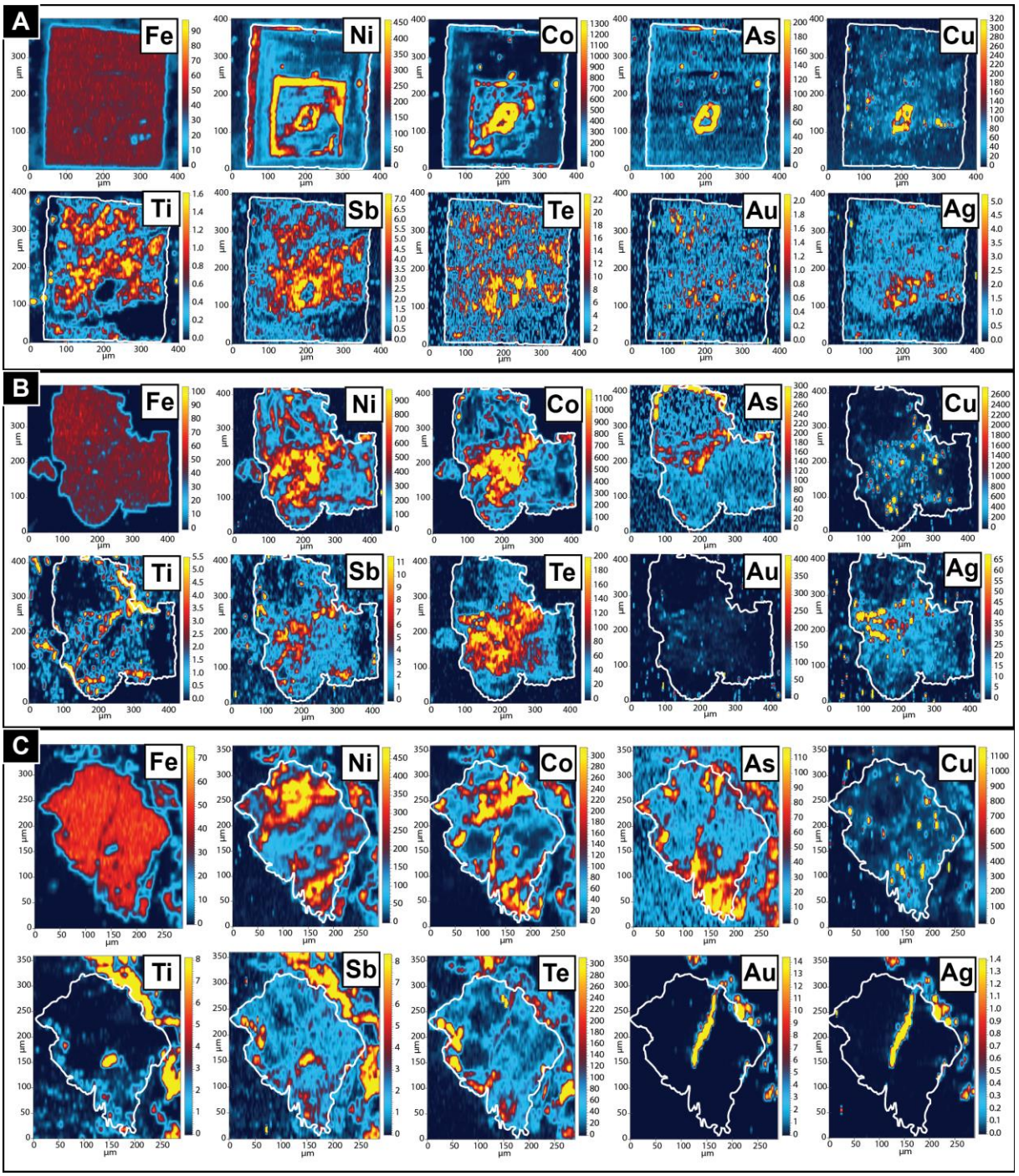

Figure 3.15. LA-ICP-MS elemental maps for distal to proximal pyrite grains from the Kenty Au deposit. Hot colors indicate higher concentrations with all data measured in ppm except for Fe, and Au and Ag in C, which are measured in wt. %. White lines delineate outlines of the pyrite grains. A) Distal pyrite. B) Medial pyrite. C) Proximal pyrite.

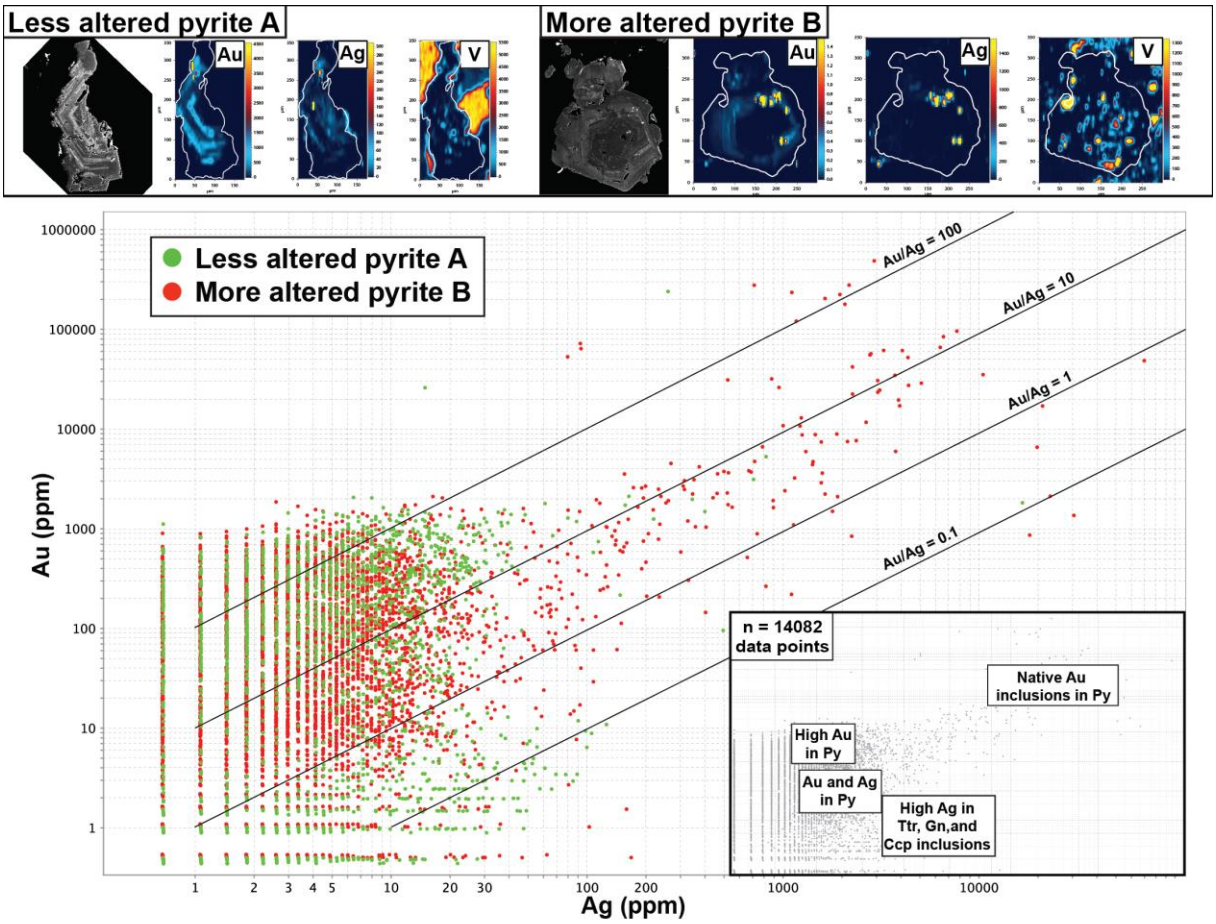

Figure 3.16. Selected SEM backscatter electron images and relevant LA-ICP-MS elemental maps from the Jerome Au deposit, along with a binary Ag versus Au plot of time-slice data generated from the LA-ICP-MS elemental mapping. Data from least altered pyrite A and more altered pyrite B are shown as green and red dots, respectively. The lower right inset shows the number of data points, with fields corresponding to Au in pyrite, Ag in other inclusion phases (tetrahedrite, galena, chalcopyrite), and native Au inclusions. Abbreviations: Au, gold; Ccp, chalcopyrite; Gn, galena; Py, pyrite; Ttr, tetrahedrite.

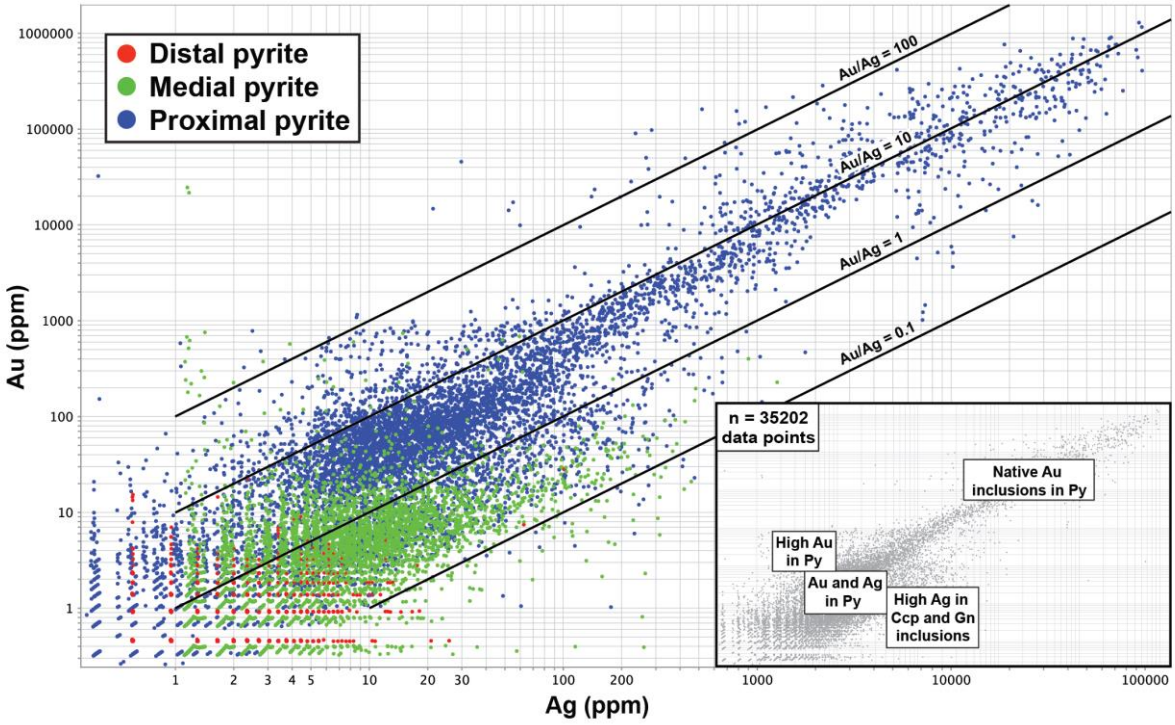

Figure 3.17. Binary Ag versus Au plot of time-slice data generated from LA-ICP-MS elemental mapping of distal (red dots), medial (green dots) and proximal (blue dots) pyrite grains from the Kenty Au deposit. Lower right inset shows the number of data points, with fields corresponding to Au in pyrite, Ag in other inclusion phases (galena, chalcopyrite), and native Au inclusions. Abbreviations: Au, gold; Ccp, chalcopyrite; Gn, galena; Py, pyrite.

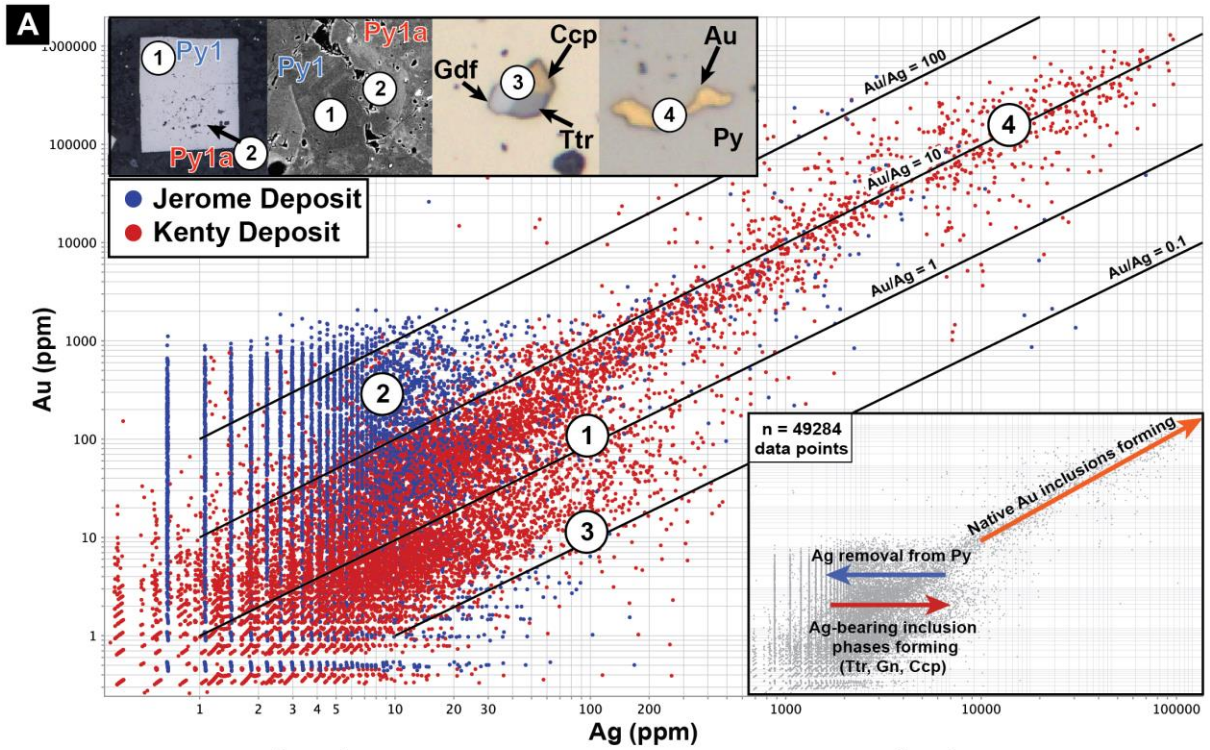
A
Py1
Py1a
Py1
Py1a
Gdf
Ccp
Ttr
Au
Py
Jerome Deposit
Kenty Deposit
Au/Ag = 100
Au/Ag = 10
Au/Ag = 1
Au/Ag = 0.1
n = 49284
data points
Native Au inclusions forming
Ag removal from Py
Ag-bearing inclusion
phases forming
(Ttr, Gn, Ccp)
Au (ppm)
Ag (ppm)

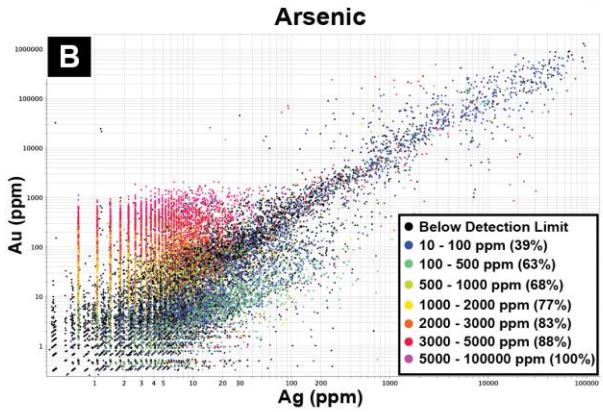
Arsenic
B
Below Detection Limit
10 - 100 ppm (39%)
100 - 500 ppm (63%)
500 - 1000 ppm (68%)
1000 - 2000 ppm (77%)
2000 - 3000 ppm (83%)
3000 - 5000 ppm (88%)
5000 - 100000 ppm (100%)
Au (ppm)
Ag (ppm)

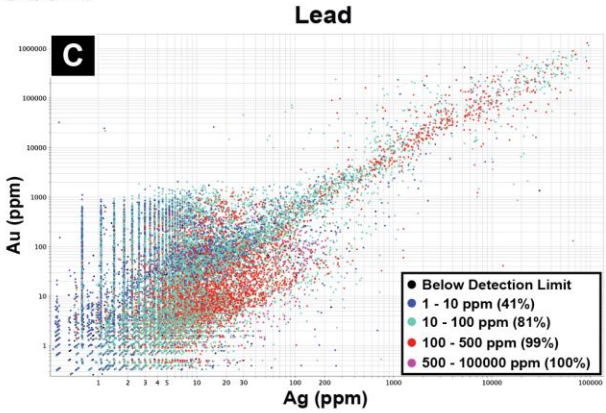
Lead
C
Below Detection Limit
1 - 10 ppm (41%)
10 - 100 ppm (81%)
100 - 500 ppm (99%)
500 - 100000 ppm (100%)
Au (ppm)
Ag (ppm)

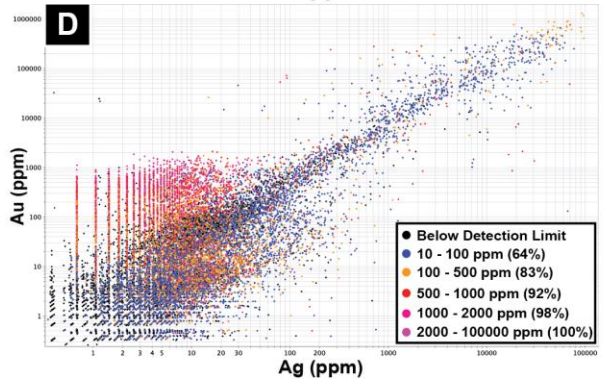
Copper
D
Below Detection Limit
10 - 100 ppm (64%)
100 - 500 ppm (83%)
500 - 1000 ppm (92%)
1000 - 2000 ppm (98%)
2000 - 100000 ppm (100%)
Au (ppm)
Ag (ppm)

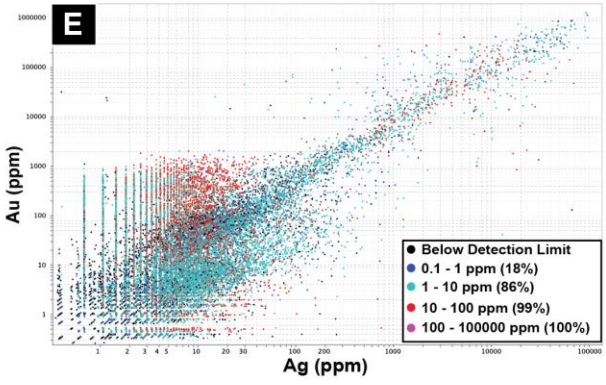
Antimony
E
Below Detection Limit
0.1 - 1 ppm (18%)
1 - 10 ppm (86%)
10 - 100 ppm (99%)
100 - 100000 ppm (100%)
Au (ppm)
Ag (ppm)

Figure 3.18. Binary plots of Ag versus Au using combined time-slice data generated from LA-ICP-MS elemental mapping of pyrite grains at both deposits. A) Ag versus Au combined plot (Jerome, blue data points; Kenty, red data points). The upper left inset of the large plot shows numbered, backscatter electron images and reflected light photomicrographs and their corresponding locations within the plot to generalize where different trends with respect to Au, Ag, and mineral phases occur. The lower right inset of the large plot shows arrows to indicate the combined behavior of Au compared to Ag at both deposits. The four smaller Ag versus Au plots below highlight geochemical trends and mineral phase relationships seen at both deposits. B) Arsenic, C) Lead, D) Copper, and E) Antimony. Individual concentration legends are shown with each respective plot in the lower right corner. Abbreviations: Au, gold; Ccp, chalcopyrite; Gn, galena; Gdf, gersdorffite; Py, pyrite; Ttr, tetrahedrite.

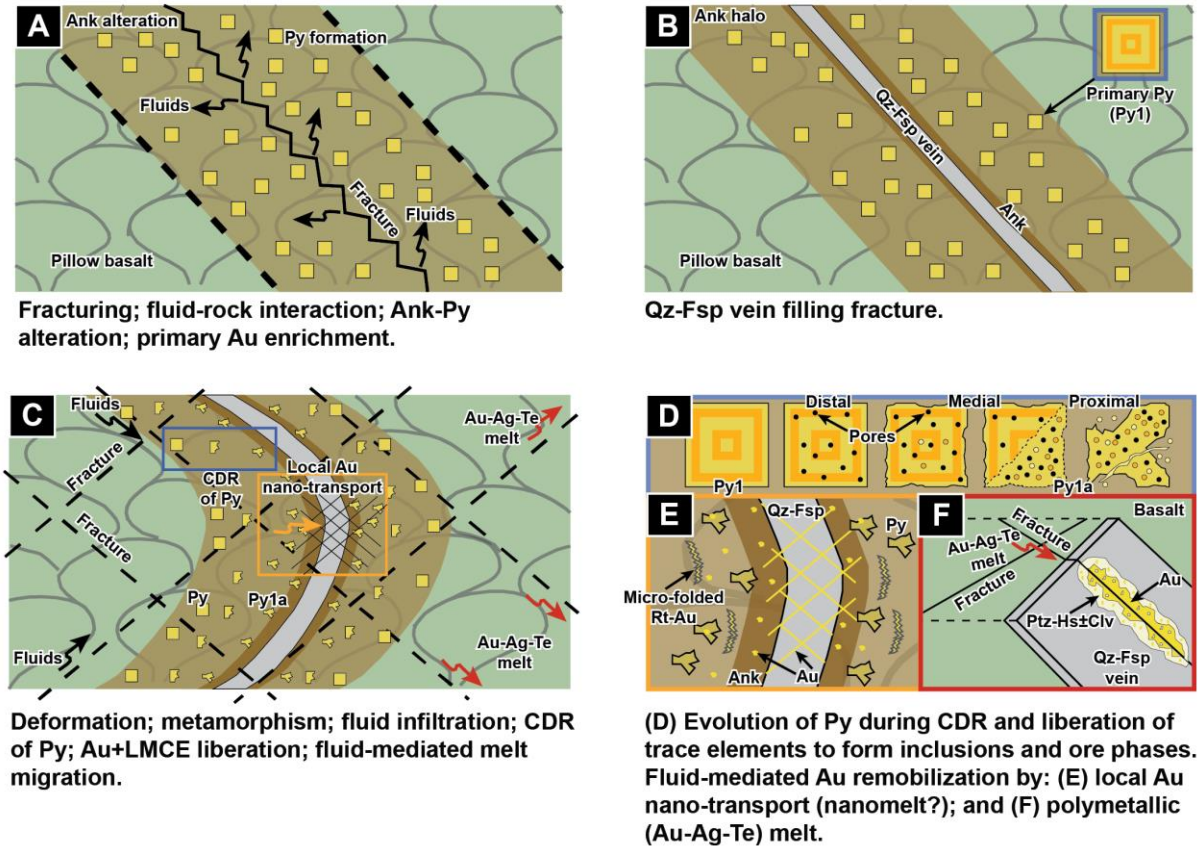

Figure 3.19. Conceptual model for the remobilization of Au from pyrite based on the Kenty deposit; see text for discussion. Order of stages shown is from A to E. Abbreviations: Ank, ankerite; CDR, coupled dissolution-reprecipitation; Clv, calaverite; Fsp, feldspar; Hs, hessite; LMCE, low-melting point chalcophile elements; Ptz, petzite; Py, pyrite; Qz, quartz; Rt, rutile; Te, tellurium.

Chapter 4

4 Transport and coarsening of gold nanoparticles in an orogenic deposit by dissolution-reprecipitation and Ostwald ripening

E.C.G. Hastie[1, 2], M. Schindler[3] D.J. Kontak[1], and B. Lafrance[1]

[1]Mineral Exploration Research Centre, Harquail School of Earth Sciences, Laurentian University, Sudbury, Ontario P3E 2C6;
[2]Earth Resources and Geoscience Mapping Section, Ontario Geological Survey, Sudbury, Ontario P3E 6B5
[3]Department of Geological Sciences, University of Manitoba, Winnipeg, Manitoba R3T 2N2

Accepted and soon be published; Transport and coarsening of gold nanoparticles in an orogenic deposit by dissolution-reprecipitation and Ostwald ripening, Communications Earth & Environment, Nature Research, Springer Nature, London UK.

4.1 Abstract

The role of nanoparticle gold in the formation of gold deposits has long been debated. To date, evidence in support of this process is limited to epithermal-, Carlin- and seafloor massive-sulphide-type deposits where gold nanoparticles are associated with primary fluid related processes. At the Kenty orogenic deposit in Ontario, Canada, gold has been remobilized from early pyrite through secondary coupled dissolution-reprecipitation processes to form high-grade gold external to pyrite. Here we report gold nanoparticles and related textures that help document this gold coarsening process. A combination of focused ion beam technology and transmission electron microscopy provides a rare glimpse of gold coarsening frozen in time, which includes nanoparticles trapped in iron oxides and rutile and non-oriented attachment of gold nanoparticles to bulk gold suggesting coarsening via Ostwald ripening. The processes documented are applicable to orogenic deposits formed through Earth's history, and may explain the formation of ultra high-grade ore zones.

4.2 Introduction

Orogenic gold deposits represent one of the most important Au resources on the planet, particularly those formed in Archean terranes[1,2]. As the name suggests, these epigenetic deposits formed during collisional orogeny[3] and, regardless of age and setting, are known for spectacular high-grade ore zones with coarse gold[1,4,5,6]. There is, however, a growing recognition that the formation of such high-grade coarse gold is difficult to explain using conventional Au-in-solution processes[4,5,6,7]. This has therefore catalyzed in recent years an increased scrutiny of other possible mechanisms, such as Au enrichment via nanoparticle processes, to account for formation of coarse gold[5,6,8,9,10].

The aqueous transport of primary gold nanoparticles has for some time been shown to be a factor in high-grade, 'bonanza-type' gold ore zones in epithermal deposits[8,10,11] and thus may also a factor in forming high-grade gold in other deposit types[5,6,9,11,12,13,14,15]. However, until now documenting gold nanoparticles as part of Au remobilization due to secondary processes, as in orogenic deposits, has not been demonstrated. To do so is important, as it would show that such processes are also important for upgrading ore zones versus being exclusive to primary processes.

4.2.1 Geological setting, the Kenty Au deposit and Au remobilization

The Abitibi greenstone belt (AGB) is one of the most gold endowed Archean terranes in the world and accounts for a significant portion of the total gold endowment in the Superior Province of Canada[16]. The Swayze area, which is the southwestern extension of the AGB (Fig. 4.1), contains volcanic and plutonic rocks with a wide range of compositions (ultramafic to felsic) as well as metasedimentary rocks (both chemical and clastic). These rocks were deposited

and emplaced between ca. 2750 Ma to 2670 Ma[19,20]. Metamorphosed rocks in the western AGB attained temperatures of 350 to 450°C and maximum pressures of about 3 kbar (10 km depth) during the final construction of the Superior Craton at ca. 2670 Ma to 2640 Ma[21]. Although metamorphosed, the prefix 'meta' is herein omitted from the rock names for simplicity.

The Kenty orogenic Au deposit (Fig. 4.1) is located in the central part of the Swayze area. It was discovered in the 1930s and is characterized by high-grade ore zones with coarse gold. Kenty is an excellent natural laboratory to study gold remobilization processes because it has a simple mineralization history and has escaped the multitude of overprinting events that complicate the interpretation of ore-forming processes in many orogenic deposits[4]. The Au mineralization is hosted in altered pillow basalts and granitoid rocks[4], the latter dated at 2684.7 ± 1.5 Ma (U-Pb zircon). Two generations of Au mineralization are present: (1) early Au in pyrite localized to ankerite alteration zones marginal (i.e., <1-2 m) to quartz veins; and (2) later coarse gold lining fractures that cut the quartz veins[4]. The late coarse gold commonly lines conjugate fractures that formed in the hinge of the folded quartz veins with microfolded gold-rutile intergrowths in the wallrocks of the veins[4].

Our previous research[4] has interpreted the late coarse gold at Kenty to be a product of remobilization from earlier pyrite based on: (1) textures indicative of dissolution-reprecipitation processes[22] that increase towards the quartz veins hosting coarse gold. These textures reflect the destruction of primary chemical zonation, porosity development and the formation of secondary inclusions (e.g., native gold, sulfides, and tellurides) consistent with trace elements (e.g., Au, Ag, Te, Cu) enriched in the primary zones; (2) SEM-EDS (energy dispersive spectroscopy) imaging and laser ablation inductively-coupled mass spectrometry (LA-ICP-MS) elemental mapping of pyrite that shows progressive loss of Au and associated elements commensurate with the degree

of pyrite modification and its proximity to quartz veins; (3) elements that are spatially associated with Au in pyrite (e.g., Ag, Cu, Te) are also associated with, and incorporated into, late coarse gold phases exterior to pyrite (e.g., Cu and Ag in native gold, petzite, hessite, calaverite); and (4) the Au content of primary pyrite (i.e., 100s to 1000s ppm) is sufficient to account for abundance of coarse gold hosted in late fractures[4]. A summary of this dissolution-reprecipitation model (Fig. 4.2) highlights the progressive loss of Au from pyrite with its increasing textural and chemical modification.

This research further demonstrated that the liberated Au from pyrite was likely remobilized at temperatures as low as 335°C via fluid-mediated polymetallic melts enriched in low melting point chalcophile elements (LMCE), such as Te[4,23,24,25,26,27,28]. Indeed, a number of recent studies provide substantive evidence to support Au concentration by LMCE-rich melts in the presence of a fluid[26,27]. Seemingly enigmatic are areas at the Kenty deposit, as with many Au deposits worldwide, where zones hosting coarse gold lack evidence for LMCE-rich phases. We previously suggested that LMCE-rich melts may operate in conjunction with nanoparticle transport to account for Au upgrading at the Kenty deposit[4], but we only provided evidence for the former mechanism. Thus convincing evidence for the presence of gold nanoparticles in this Archean orogenic Au setting remains to be demonstrated.

4.3 Results and Discussion

4.3.1 Gold nanoparticles, associated mineral phases and textures

Here we report on the occurrence of gold nanoparticles within samples from the high-grade ore assemblage at the Kenty Au deposit (Fig. 4.1). To demonstrate this, we chose a mineralized sample (Fig. 4.3a-d) with evidence of gold remobilization[4]. The sample contains early-stage

auriferous pyrite (≈ 800 ppm Au) in spatial association with late-stage coarse gold. Sample sections were extracted from a thin section by focused ion beam-scanning electron microscopy (FIB-SEM) and thinned to foils for subsequent transmission electron microscopy (TEM) studies. The foils were extracted from the interior of the above-described pyrite grain and across its interface with gold-hematite-albite-rutile grains (Fig. 4.3d).

TEM examination of the FIB section from the interior of the pyrite (Supplementary Fig. 4.1) indicates the presence of nano-size Au-Ag-Te-Pb domains with droplet-like morphologies (Fig. 4.3e, f). The spatial overlap of Au-Ag-Te in the droplet suggests a telluride phase (e.g., petzite); as Pb is concentrated towards the upper part of the droplet it may be part of another phase (altaite?). In addition to the droplets, bright sub-nanometer-size domains in the pyrite (Fig. 4.3e, f) and LA-ICP-MS elemental maps of pyrite grains (Fig. 4.2; distal and medial) also suggest that finely dispersed elemental Au, Ag and Te occur throughout the pyrite.

The FIB section extracted along the pyrite margin (Fig. 4.3d) contains gold surrounded by grains of Fe-oxide, pyrite, albite and rutile (Fig. 4.4). On the lower left side of the FIB section, a large grain of Fe-oxide is in contact with pyrite (Fig. 4.4a, b). This Fe-oxide grain also connects to Fe-oxides on the margins of gold, albite and rutile and is also in the interior of the latter two minerals (Fig. 4.4b). The Fe-oxides are present prior to extraction (Fig. 4.3d) and thinning (Fig. 4.4b, c) and remain throughout the thinning process even when the gap in the area between gold and albite widens (Fig. 4.4d).

The larger Fe-oxide grain (Fig. 4.4a, b) is composed of intergrown hematite, goethite, and magnetite/maghemite (Fig. 4.5a, b) and it contains gold nanoparticles ranging in size from 1 to 5 nm (Fig. 4.5c-e). A portion of the Fe-oxide on the margin of gold that was previously attached to

the larger Fe-oxide grain (Fig. 4.4) is composed of hematite (Fig. 4.5f, g). This hematite also contains gold nanoparticles that range in size from 1 to 5 nm (Fig. 4.5h-j).

Observing the Fe-oxide between the gold and albite (Fig. 4.4), a thin layer (5 to 10 nm thick) of the Fe-oxide remained after FIB thinning on the gold surface. This thin layer contains gold nanoparticles whose lattice orientation is different from that of the coarse gold (Fig. 4.6a-c).

The Fe-oxide filling that occurs between the gold and rutile grain boundary (Fig. 4.4a, b) also contains gold nanoparticles. At the far end of this grain boundary, gold nanoparticles up to 10 nm in size occur within rutile in close proximity to the gold surface (Fig. 4.6d-f).

4.3.2 Discussion on gold nanoparticles and their chemical behavior

Documenting the nature and origin of gold nanoparticles in an Archean orogenic deposit (i.e., Kenty) is an important step towards understanding how high-grade ore zones form in such Au deposits in general given that most previous research on this topic is restricted to epithermal, Carlin and seafloor massive sulfide deposits[8,9,10,12,13]. Although mechanisms have been suggested for nanoparticle aggregation previously[8,10], evidence for nanoparticle processes related to secondary remobilized gold has been lacking until now. The following discussion aims to resolve some of these aspects.

Caution must be exercised when preparing samples by FIB milling since redeposition of material is possible[29] and some TEM observations may be equivocal (e.g., Supplementary Fig. 4.2). Although this is a possibility, the gold nanoparticles presented in Figures 4.3, 4.5 and 4.6 are interpreted to be natural based on the following evidence: (1) separate and distinct gold nanoparticles are found in pyrite (Fig. 4.3e-f), Fe-oxides (Fig. 4.5) and rutile (Fig. 4.6d-f) with 3-dimensional features that confirm that the gold nanoparticles are not surface redeposition; (2)

pyrite, Fe-oxide and rutile also have an association with gold at the micro-scale (Fig. 4.3c, d)[4]; (3) the Fe-oxide was present at the margin of gold and adjacent to pyrite (Fig. 4.4a-c) from the very beginning of the FIB sample thinning; (4) the gap in the FIB section widened during the FIB milling process, hence material was being removed and not added during this process (Fig. 4.4); (5) the Fe-oxide between gold and albite narrowed during the FIB milling process (Fig. 4.4b-d), reinforcing the first two points; and (6) the Fe-oxides adjacent to pyrite and on the margin of gold include goethite, hematite and magnetite/maghemite, as confirmed by selected area electron diffraction (SAED; Fig 4.5a, b). A combination of Fe^{2+}, Fe^{3+} and hydrous Fe-oxides within the same assemblage would simply not form at the same time as a redeposition during FIB milling, which precludes this being an artifact of the process.

4.3.3 Model on the formation, transport and coarsening of gold nanoparticles

An oxidizing fluid was responsible for the dissolution-reprecipitation of pyrite at the Kenty deposit (Figs 4.2, 4.3c, d)[4]. Once Au supersaturates in a fluid[6,8,9,10], gold nanoparticles would remain suspended in solution as long as their surface charges create larger net repulsive forces than net attractive forces. This phenomenon is best explained by Derjaguin-Landau-Verwey-Overbeak theory (DLVO)[30], which is commonly used to predict nanoparticle behaviour, although quantum effects for particles <20 nm have yet to be resolved[31].

The surface charge of any nanoparticle is mainly affected by pH and counter-ion activity, although particle size and compositional variations (e.g., fluctuating Ag content of gold) can also affect the surface charge[30,31]. Gold nanoparticles generally have a negative charge in near neutral to basic solutions and a positive one in highly acidic solutions[10,32,33,34] with gold aggregation initiated where the pH favors a point of zero charge (PZC). The PZC for gold at 25°C occurs at a

pH of ≈3, however no data currently constrains the PZC for gold at conditions relevant to ore deposit formation.

Two alternative models can explain the charge-dependent transport and coarsening of gold nanoparticles at the Kenty deposit based on the evidence presented above and the aforementioned summary of current research on nanoparticle behavior. Dissolution of the early auriferous pyrite by an oxidizing fluid liberated Au (Fig. 4.2) and lowered the pH of the transporting fluid such that:

(1) A fluid with a pH below the PZC of gold would promote the transport of positively-charged gold nanoparticles. The dissolution of another phase (e.g., plagioclase) would be required to raise the pH of the fluid close to the PZC of gold to promote aggregation. This represents an intriguing mechanism, as both transport and aggregation of the gold nanoparticles is promoted by the dissolution of minerals. Albitization is a common process in gold deposits[1,3,35] and Kenty is no exception[4], as indicated by likely dissolution of original plagioclase (~An30) based on the presence of end-member albite with associated alteration phases now seen (i.e., pyrite-muscovite(sericite)-carbonate)[4].

(2) A fluid with a pH above the PZC of gold would promote the transport of negatively-charged gold nanoparticles. Adsorption of counter-ions, such as Fe^{3+} aqueous species (dominant under acidic to near-neutral pH conditions) on the surface of the gold nanoparticles, would have cancelled their negative charge and thus promoted gold attachment and coarsening. This is a reasonable model given the replacement of Au-rich pyrite by Fe-oxides (Fig. 4.3d) that contain gold nanoparticles (Figs. 4.5, 4.6a-c).

Recent studies on epithermal deposits have provided evidence for diffusion-limited Au aggregation resulting in "fractal" dendrites[8]. These textures form through oriented attachment of Au nanoparticles, but data from the Kenty deposit only shows non-oriented attachment (Fig. 4.6a). Thus, gold coarsening most likely occurred through a different mechanism.

Studies on nanoparticle attachment[36,37] have provided evidence for crystallization of minerals via non-oriented attachment of nanoparticles. These studies showed that when non-oriented attachment occurs near flat or negatively curved surfaces, nanoparticles dissolve and a net transfer of monomers to the larger crystal occurs (i.e., Ostwald ripening)[36,37]. Thus the non-oriented attachment observed at Kenty (Fig. 4.6a) supports an interpretation whereby gold coarsened through dissolution of gold nanoparticles and the mass transfer of Au monomers to the coarse gold lattice. The implication of this conclusion is that non-oriented attachment and Ostwald ripening may play an important role in the coarsening of gold in orogenic deposits. This also offers an alternative for gold coarsening by oriented attachment reported in epithermal environments[8].

There is only a limited understanding of gold nanoparticle behavior in natural systems due to the changing properties of minerals at the nanoscale and different nanoparticle-host-interactions[38]. For example, the melting temperature of gold decreases dramatically from 1064°C to <400°C for isolated nanoparticles <3 nm[13,39,40,41], but becomes unpredictable for nanoparticles <2 nm where quantum effects need to be considered. In addition, the thermal stability of gold nanoparticles is also governed by their host mineral[13,38]. In isolation, gold nanoparticles are stable until they reach the size-dependent melting curve[39,40,41], but in arsenian pyrite it has been shown that gold nanoparticles <4 nm in diameter would be unstable at temperatures relevant to orogenic deposits (i.e., 250-400°C), and would coarsen through solid-state Ostwald ripening to

become stable[13]. Assuming As does not greatly affect the stability of gold nanoparticles[13], then the minimum temperatures obtained at the Kenty deposit (335°C)[4] would indicate that gold nanoparticles within pyrite would need to be a minimum of 4 nm to be stable[13]. However, gold nanoparticles between 1-5 nm in diameter occur in Fe-oxides indicating that this type of matrix affects the thermal stability of gold nanoparticles differently than pyrite. Thus, our observations (Figs. 4.5, 4.6) offer rare evidence of nanoparticles trapped prior to their coarsening into larger gold domains.

Considering that LMCE and Au can form a polymetallic melt in the presence of a fluid[26,27] and that we have evidence at Kenty for polymetallic melt formation from previous research[4], as well as droplet-like polymetallic nano-domains within primary pyrite from this work (Fig. 4.3e, f), we suggest that fluid-mediated polymetallic melts and gold nanoparticle transport are both relevant to upgrading orogenic Au deposits. Where LMCE are absent from the system, then nanoparticle transport would become the dominant mechanism.

All aspects influencing the behavior of gold nanoparticles, their transport, and how they aggregate in different environments must be examined in detail if we want to better understand and resolve the processes that govern the formation of high-grade gold zones. However, many unanswered questions remain regarding nanoparticle processes in Au deposits, but discovering direct evidence for gold nanoparticles associated with gold remobilization in an Archean orogenic deposit serves to highlight that this mechanism is not restricted to a specific geologic time period or deposit setting. Future research should aim to: (1) understand the role of Ag in the behavior of gold nanoparticles because almost all natural gold contains significant Ag and many epithermal deposits are host to electrum (i.e. <80 wt.% Au, >20 wt.% Ag); (2) examine the nature of gold within precursor pyrite to understand if there is a conversion of elemental Au to

nanoparticles or simply nanoparticle liberation during dissolution; (3) clarify the relationship among gold nanoparticles and other elements, nanoparticles and minerals; and (4) determine the roles temperature and particle size play in the formation and aggregation of gold nanoparticles, specifically for conditions relevant to ore deposit formation.

4.3.4 Implications for Au deposits and relevant disciplines

High-grade, 'bonanza-type' ore zones can form in ancient to recent Au deposit types due to the transport and aggregation of gold nanoparticles[5,6,8,9,10]. This mechanism can operate alone or in conjunction with fluid-mediated polymetallic melts to upgrade Au deposits. Dissolution of minerals, Au remobilization, counter-ion activity and pH fluctuation are likely controls for gold nanoparticle formation, transport and aggregation. The underlying mechanism for gold coarsening may, however, differ between orogenic (attachment, dissolution and monomer transfer) and epithermal (diffusion-limited aggregation and orthokinetic aggregation)[8] deposits. The existence of these different gold coarsening processes has far-reaching implications for other disciplines given that gold nanoparticle research is a critical component of material science [42,43], nanomedicine[44,45] and nanotechnology[46,47]. A more complete understanding of natural gold nanoparticles and their interaction with other natural materials may enhance laboratory manipulation for a variety of disciplines.

4.4 Methods

4.4.1 Geological Sampling

Rock sampling and bedrock mapping was carried out by the lead author as an employee of the Ontario Geological Survey. The Universal Transverse Mercator (UTM) coordinates for the location of the sample used in this study are 378743m E, 5299846m N using NAD83 in zone 17.

The sample location can also be seen with reference to the detailed outcrop map (Fig. 4.1b) and is shown by a yellow star.

4.4.2 SEM-EDS

This work was performed with a Zeiss EVO 50 SEM at the Geoscience Laboratories in Sudbury, Ontario, Canada. The SEM is equipped with an Oxford X-Max 50 mm2 EDS, and used Oxford's Aztec© software package. Operating conditions were 20kV and ≈750 pA with variable counting times for each spot analysis (20 to 40 seconds) and used a working distance of 8.5 mm.

4.4.3 TEM of FIB sections

Extraction of FIB sections were conducted with a FEI Helios 650 NanoLab FIB at the 4D LABS at Simon Fraser University, Vancouver, British Columbia, Canada. FIB sections were lifted with a platinum gas-glue and thinned with ion gas milling (Ga ions) to electron transparency. The FIB sections were analyzed with a field emission TEM FEI Talos F200x at the Manitoba Institute for Materials, at the University of Manitoba, Winnipeg, Manitoba, Canada. Imaging in bright and dark field mode was performed with an accelerating voltage of 200 kV and with a 16 MB ceta camera and a Fischicone high angle annular dark field (HAADF) detector. Compositional analysis was performed in STEM-EDS mode with 4 SDD detectors. Micro-scale phases were identified in previous research[4] and confirmed here at the nano-scale using a combination of Selected Area Electron Diffraction (SAED) and Fast Fourier Transform (FFT) patterns, chemical distribution maps, semi-quantitative chemical analyses, and textural features of phases previously described in the literature. TEM and STEM-EDS chemical distribution maps were processed with the TEM Imaging & Analysis (TIA) (a trademark of FEI) and Esprit 1 (a trademark of Bruker Nano).

4.4.3.1 Quality control during TEM-STEM examinations

TEM and STEM imaging can cause significant damage to the sample due to beam-sample interactions. The two main damage types that samples experience are displacement effects and breaking of chemical bonds[48]. Imaging in TEM and STEM mode can generate similar integrated doses and dose rates but in TEM mode, a defined area for the entire image is illuminated whereas a smaller area of the sample is illuminated with a similar peak dose/rate in STEM mode than the larger area in TEM mode (during the same acquisition time)[48]. Thus, an individual nanoparticle in, for example, a FIB section is exposed to a higher peak dose/rate in STEM than TEM mode.

In this study, the Au nanoparticles were exposed to the highest peak dose/rate during the recording of chemical distribution maps with STEM-EDS (maximum 30 minutes). For this reason, STEM images were recorded prior and during the recording of STEM-EDS chemical distribution maps. Additionally, TEM images were taken from the same area after the recording of the STEM-EDS chemical distribution maps. STEM and TEM images taken before, during or after the recording of the chemical maps were then compared to identify potential damage to the samples. Beside the drift of the sample, especially detectable at high magnification, no changes in the number, morphology and texture of any mineralogical feature were observed during recording of the STEM-EDS chemical distribution maps.

4.5 References

1. Goldfarb, R.J. et al. Distribution, character, and genesis of gold deposits in metamorphic terranes. Econ. Geol. 100th Anniversary Volume, 407–450 (2005).

2. Goldfarb, R.J. & Groves, D.I. Orogenic gold: Common or evolving fluid through time. Lithos 233, 2–26 (2015).

3. Groves, D.I., Goldfarb, R.J., Gebre-Mariam, M., Hagemann, S.G. & Robert, F. Orogenic gold deposits: A proposed classification in the context of their crustal distribution and relationship to other gold deposit types. Ore Geol. Rev. 13, 7–27 (1998).

4. Hastie, E.C.G., Kontak D.J. & Lafrance, B. Gold remobilization: insights from Au deposits in the Swayze greenstone belt, Abitibi Subprovince, Canada. Econ. Geol. 115, 241–277 (2020).

5. Voisey, C.R. et al. Aseismic refinement of orogenic gold systems. Econ. Geol. 115, 33–50 (2020).

6. Petrella, L. et al. Colloidal gold transport: a key to high-grade gold mineralization? Miner. Deposita 55, 1247–1254 (2020).

7. Williams-Jones, A.E., Bowell, R.J., & Migdisov, A.A. Gold in Solution. Elements 5, p. 281–287 (2009).

8. Saunders, J.A. & Burke, M. Formation and aggregation of gold (electrum) nanoparticles in epithermal ores. Minerals 7, 163–174 (2017).

9. Gartman, A. et al. Boiling-induced formation of colloidal gold in black smoker hydrothermal fluids. Geology 46, 39–42 (2018).

10. Saunders, J.A. Colloidal transport of gold and silica in epithermal precious-metal systems: evidence from the Sleeper deposit, Nevada. Geology 18, 757–760 (1990).

11. Deditius, A.P. et al. Trace metal nanoparticles in pyrite. Ore Geol. Rev. 42, 32–46 (2011).

12. Palenik, C.S. et al. “Invisible” gold revealed: direct imaging of gold nanoparticles in a Carlin-type deposit. Am. Mineral. 89, 1359–1366 (2004).

13. Reich, M. et al. Thermal behavior of metal nanoparticles in geologic materials. Geology 34, 1033–1036 (2006).

14. Hough, R.M., Noble, R.R.P. & Reich, M. Natural gold nanoparticles. Ore Geol. Rev. 42, 55–61 (2011).

15. Ciobanu, C.L. et al. Gold-telluride nanoparticles revealed in arsenic-free pyrite, Am. Mineral. 97, 1515–1518 (2012).

16. Mercier-Langevin, P. et al. Targeted Geoscience Initiative 5, Gold Project: A summary of contributions to the understanding of Canadian gold systems; in Targeted Geoscience Initiative 5: Contributions to the Understanding of Canadian Gold Systems, (eds.) Mercier-Langevin, P., Lawley, C.J.M., & Castonguay, S. Geological Survey of Canada Open File 8712, 1–30 (2020).

17. Ontario Geological Survey. 1:250 000 scale bedrock geology of Ontario. Ontario Geological Survey Miscellaneous Release–Data 126–Revision 1 (2011).

18. Hastie, E.C.G., Lafrance, B. & Kontak, D.J. Observations on the Kenty and Rundle deposits, Swayze greenstone belt. Ontario Geological Survey Open File Report 6313, 9-1 to 9-9 (2015).

19. Monecke, T., Mercier-Langevin, P., Dubé, B., & Frieman, B. Geology of the Abitibi greenstone belt. Rev. Econ. Geol. 19, 7–49 (2017).

20. Katz, L.R., Kontak, D.J., Dubé, B. & McNicoll, V. The geology, petrology, and geochronology of the Archean Côté Gold large-tonnage, low-grade intrusion-related Au(-Cu) deposit, Swayze greenstone belt, Ontario, Canada. Can. J. Earth Sci. 54, 173–202 (2017).

21. Thompson, P.H. A New Metamorphic Framework for Gold Exploration in the Timmins-Kirkland Lake Area, Western Abitibi Greenstone Belt: Discover Abitibi Initiative. Ontario Geological Survey, Open File Report 6162, 1–104 (Ontario Geological Survey, 2005).

22. Putnis, A. Mineral replacement reactions. Rev. Mineral. Geochem. 70, 87–124 (2009).

23. Tomkins, A.G, & Mavrogenes, J. A. Mobilization of gold as a polymetallic melt during Pelite Anatexis at the Challenger Deposit, South Australia: A metamorphosed Archean gold deposit. Econ. Geol. 97, 1249-1271 (2002).

24. Tomkins A.G., Pattison, D.R.M., & Zaleski, E. The Hemlo gold deposit, Ontario: an example of melting and mobilization of a precious metal-sulfosalt assemblage during amphibolite facies metamorphism and deformation. Econ. Geol. 99, 1063–1084 (2004).

25. Ciobanu C. L., Birch W. D., Cook N. J., Pring A. & Grundler P. V. Petrogenetic significance of Au–Bi–Te–S associations: The example of Maldon, Central Victorian gold province, Australia. Lithos 116, 1–17 (2010).

26. Tooth, B., Ciobanu, C.L., Green, L., O'Neill, B., and Brugger, J., 2011, Bi-melt formation and gold scavenging from hydrothermal fluids: An experimental study. Geochim. Cosmochim. Acta 75, 5423–5443 (2011).

27. Zhou, H. et al. Nano- to micron-scale particulate gold hosted by magnetite: a product of gold scavenging by bismuth melts. Econ. Geol. 112, 993–1010 (2017).

28. Cabri, L.J. Phase relations in the Au-Ag-Te system and their mineralogical significance. Econ. Geol. 60, 1569–1606 (1965).

29. Capitani, G. Bizarre artefacts in transmission electron microscopy preparation and observation of geological samples. Eur. J. Mineral. 31, 857–873 (2019).

30. Hotze, E.M., Phenrat, T. & Lowry, G.V. Nanoparticle aggregation: challenges to understanding transport and reactivity in the environment. J. Environ. Qual. 39, 1909–1924 (2010).

31. Batista, C.A.S., Larson, R.G. & Kotov N.A. Nonadditivity of nanoparticle interactions. Science 350, 1242477 (2015).

32. Boyle, R.W. The geochemistry of gold and its deposits. Geological Survey of Canada Bulletin 280, 1–584 (Geological Survey of Canada, 1979).

33. Morrison, I.D. & Ross, S. Colloidal dispersions: suspensions, emulsions and foams. Wiley Interscience, 1–656 (Wiley Interscience, New York, 2002).

34. Csapó, E. et al. Surface and structural properties of gold nanoparticles and their biofunctionalized derivatives in aqueous electrolytes solution. J. Dispersion Sci. Technol. 35, 815–825 (2014).

35. Kontonikas-Charos, A. et al. Feldspar evolution in the Roxby Downs Granite, host to Fe-oxide Cu-Au-(U) mineralisation at Olympic Dam, South Australia. Ore Geol. Rev. 80, 838–859 (2019).

36. Nielsen, M.H. et al. Investigating processes of nanocrystal formation and transformation via liquid cell TEM. Microsc. Microanal. 20, 425–436 (2014).

37. De Yoreo, J.J. et al. Crystallization by particle attachment in synthetic, biogenic, and geologic environments. Science 349, aaa6760 (2015).

38. Becker, U., Reich, M. & Biswas, S. Nanoparticle-host interactions in natural systems; in Nanoscopic Approaches in Earth and Planetary Sciences, (eds.) Brenker, F.E., & Jordan G. European Mineralogical Union (EMU) 8, Chapter 8 (2010).

39. Buffat, P. & Borel, J.-P. Size effect on the melting temperature of gold particles. Phys. Rev. A 13, 2287-2298 (1976).

40. Castro, T., Reifenberger, R., Choi, E., & Andres, R.P. Size-dependent melting temperature of individual nanometer-sized metallic clusters. Phys. Rev. B 42, 8548–8556 (1990).

41. Burda, C., Chen, X., Narayanan, R., & El-Sayed, M.A. Chemistry and properties of nanocrystals of different shapes. Chem. Rev. 105, 1025–1102 (2005).

42. El-Zoka, A.A., Howe, J.Y., Newman, R.C. & Perovic, D.D. In situ STEM/SEM study of the coarsening of nanoporous gold. Acta Mater. 162, 67–77 (2019).

43. Welborn, S.S. & Detsi, E. Small-angle X-ray scattering of nanoporous materials. Nanoscale Horiz. 5, 12–24 (2020).

44. Park, S. et al. Reversibly pH-responsive gold nanoparticles and their applications for photothermal cancer therapy. Sci. Rep. 9, 20180 (2019).

45. Sindhwani, S. et al. The entry of nanoparticles into solid tumours. Nat. Mater. (2020).

46. Chen, Y., Zhao, Y., Yoon, S.J., Gambhir, S.S. & Emelianov, S. Miniature gold nanorods for photoacoustic molecular imaging in the second near-infrared optical window. Nat. Nanotechnol. 14, 465–472 (2019).

47. Han, G. et al. Controlled fabrication of gold nanotip arrays by nanomolding-necking technology. Nanotechnology 31, 144001 (2020).

48. Nicholls, D. et al. Minimising damage in high resolution scanning transmission electron microscope images of nanoscale structures and processes. Nanoscale 12, 21248 (2020).

4.6 Figures

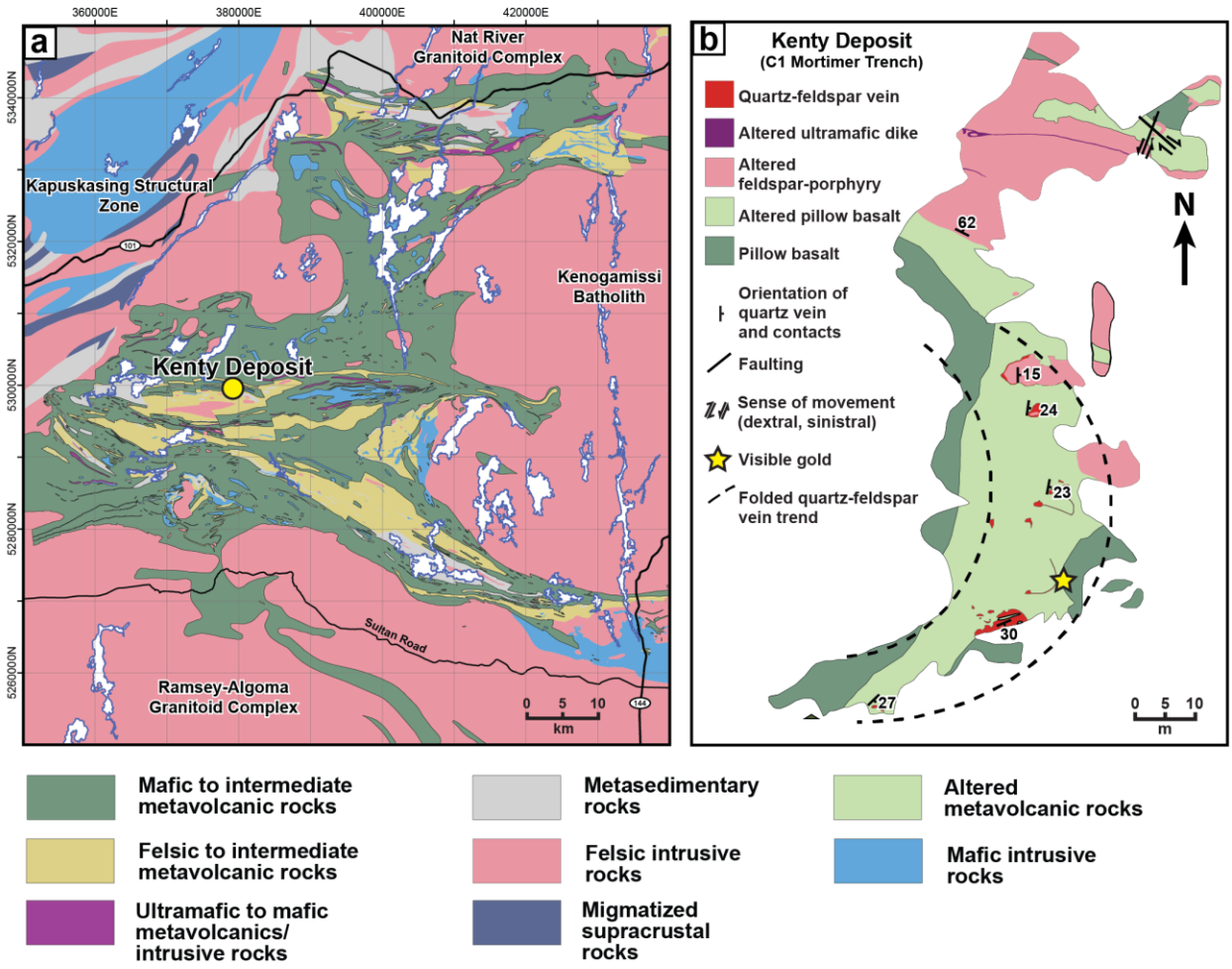

Figure 4.1. Location and geologic maps of the Swayze area and Kenty deposit. a, Simplified geologic map of the Swayze area, southwestern Abitibi greenstone belt. Location information provided as Universal Transverse Mercator (UTM) co-ordinates using North American Datum 1983 (NAD83) in Zone 17. b, Geologic outcrop map of the C1 Mortimer trench at the Kenty deposit. All maps are modified from previous Ontario Geological Survey and Society of Economic Geologists, Inc. publications[4,17,18].

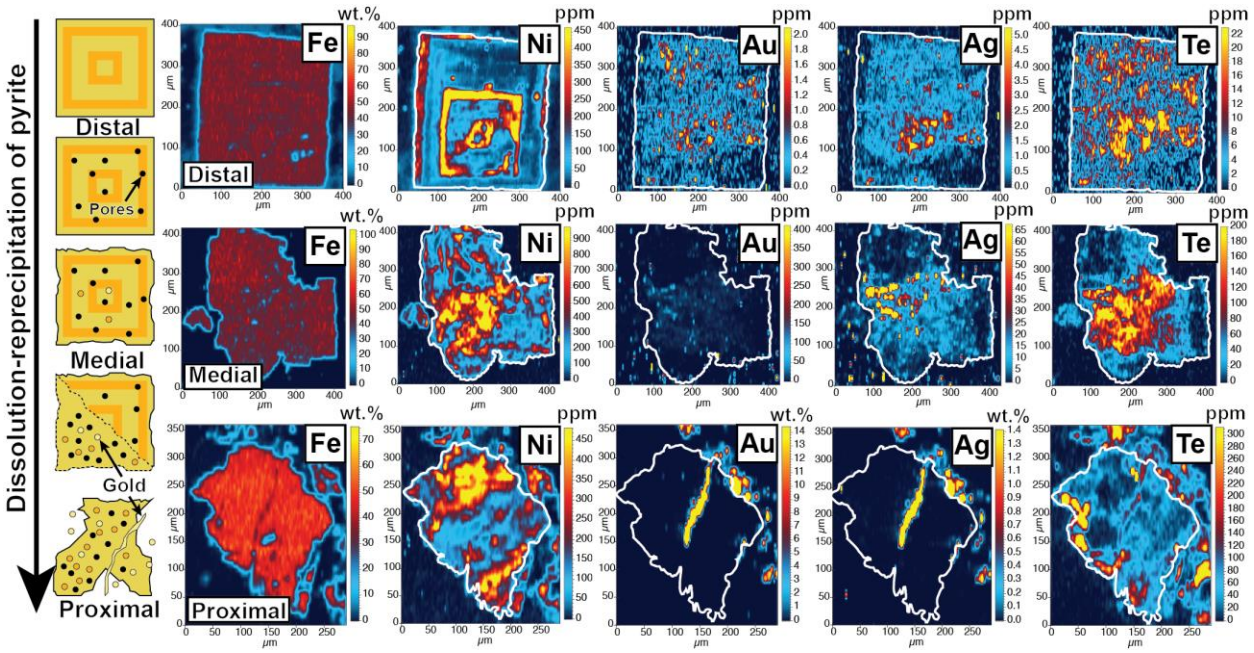

Figure 4.2. Summary of dissolution-reprecipitation and Au remobilization at the Kenty deposit (modified from previous research in Society of Economic Geologists, Inc. publication[4]). Schematic diagram of dissolution-reprecipitation textures in relation to LA-ICP-MS elemental maps for Fe, Ni, Au, Ag, and Te for distal, medial and proximal pyrite. Increasing pyrite modification highlights textures consistent with dissolution-reprecipitation[22] and gold remobilization from pyrite[4]. Abbreviations: Au, gold; Ag, silver; Fe, iron; Ni, nickel; Te, tellurium.

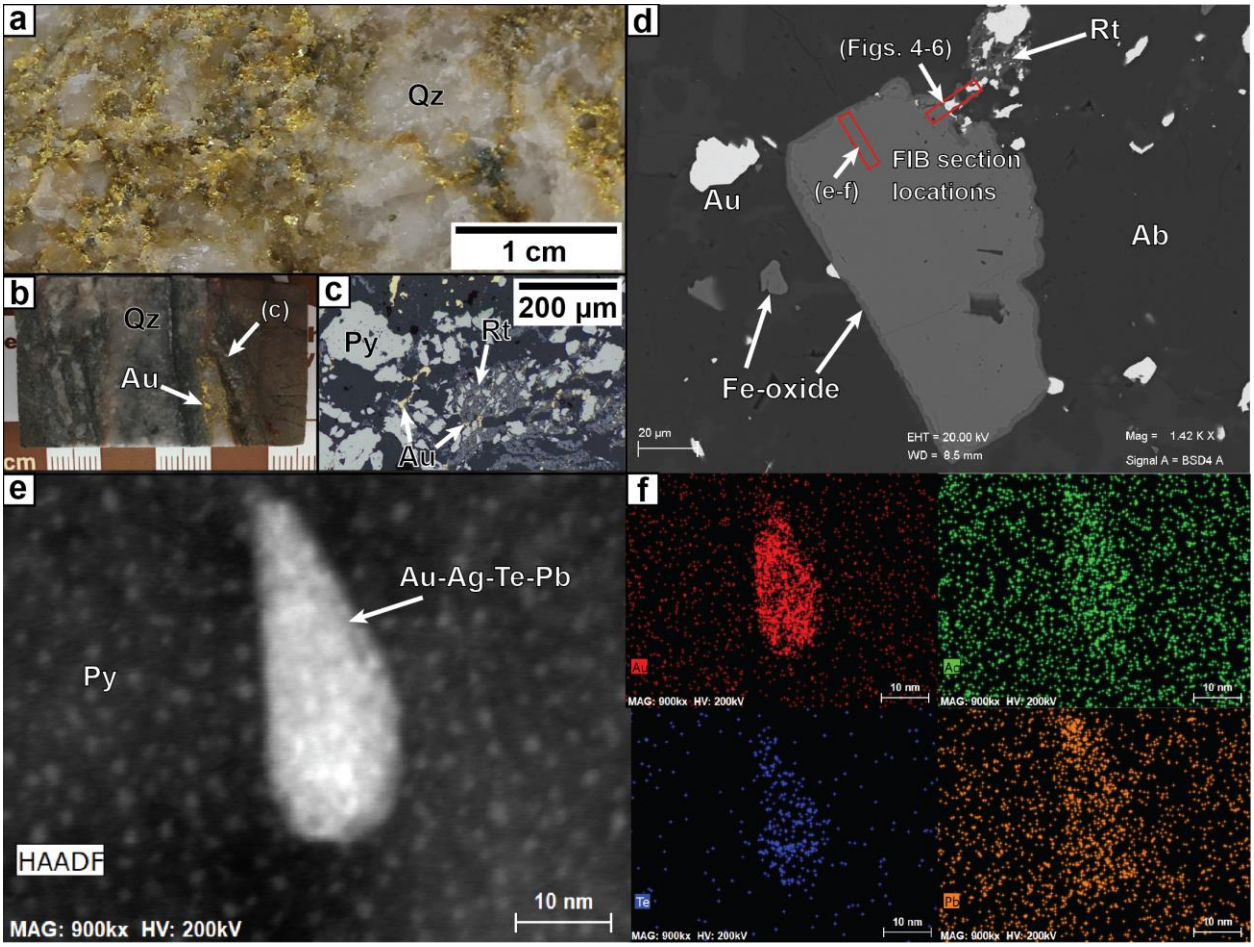

Figure 4.3. Hand specimen, SEM and STEM-EDS images of gold and associated mineral phases. a, Gold in quartz from the Kenty deposit, Swayze area, Ontario (Sample M17410). Photo taken with the permission of the Royal Ontario Museum (ROM); sample number refers to the ROM sample catalogue. b, Gold in quartz sample from the Kenty deposit used in this study. c, Reflected light image of porous pyrite, native gold and rutile. Native gold crosscuts pyrite and is intergrown with rutile. d, SEM backscattered electron image of Au-bearing pyrite, native gold, and associated minerals with FIB section locations shown with red rectangles. e, STEM image of nano-size Au-bearing polymetallic phase with droplet-like morphology hosted in the pyrite shown in d. f, STEM-EDS element maps of Au, Ag, Te and Pb for image shown in e. Abbreviations: Ab, albite; Ag, silver; Au, gold; Fe, iron; Pb, lead; Py, pyrite; Qz, quartz; Rt,

rutile; Te, tellurium. Some images have been cropped and rotated to highlight on specific features.

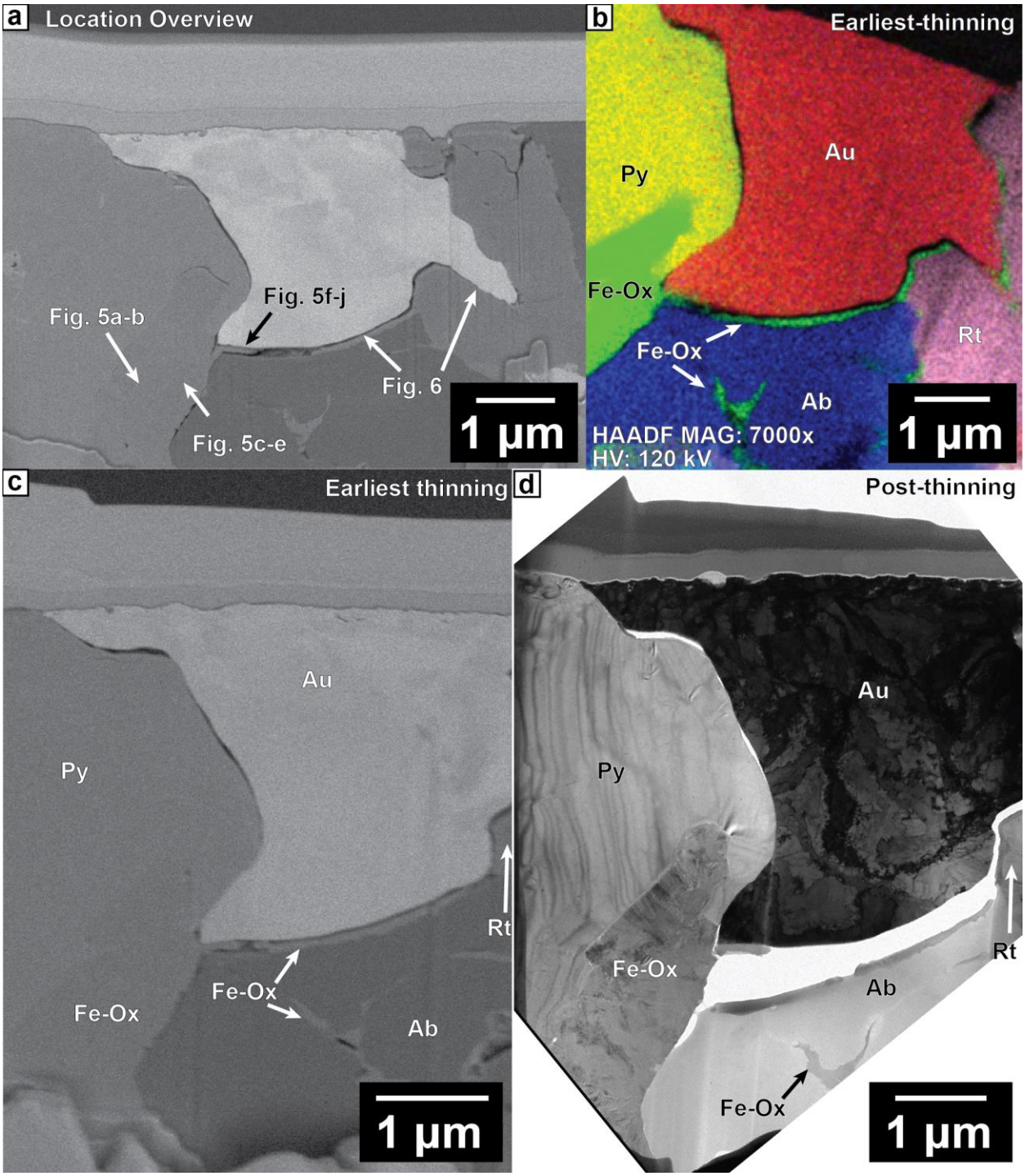

Figure 4.4. SEM/TEM images and STEM-EDS phase map for the FIB section from the location shown in Fig. 4.3d. a, SEM backscattered electron image of entire FIB section showing locations for Fig. 4.5 and 4.6. b, STEM-EDS phase map highlighting different minerals shown in a. c-d,

SEM backscattered electron image showing FIB section at earliest stage of thinning and TEM image showing FIB section after thinning. Abbreviations: Ab, albite; Au, gold; Fe, iron; Hem, hematite; Ox, oxide; Py, pyrite; Rt, rutile. Some images have been cropped and rotated or reflected to produce similar orientations and aid comparison.

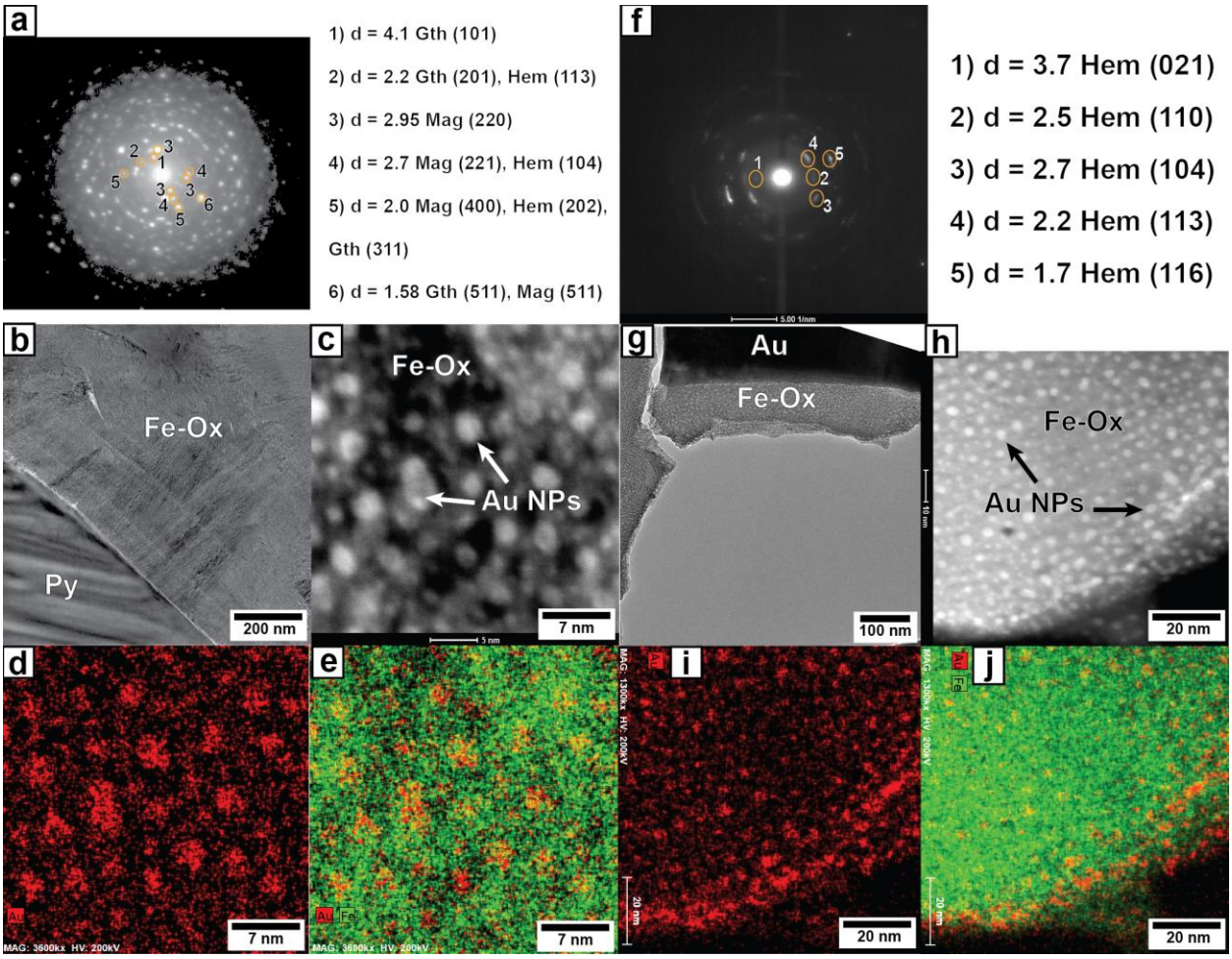

Figure 4.5. SAED patterns, STEM/TEM images and STEM-EDS elemental maps of Fe-oxides from locations shown in Fig. 4.4a. a, SAED pattern for Fe-oxides (hematite, magnetite/maghemite, goethite) shown in b. Numbers and circles refer to diffraction legend. b, TEM image of Fe-oxides in contact with pyrite. c, STEM image of gold nanoparticles in Fe-oxide. d-e, STEM-EDS elemental maps highlighting gold nanoparticles within Fe-oxides from c.

Au is in red, Fe in green. f. SAED pattern for Fe oxide (hematite) shown in g. Numbers and circles refer to diffraction legend. g, TEM image of Fe-oxide in contact with gold. h, STEM image of gold nanoparticles in Fe-oxide. i-j, STEM-EDS elemental maps highlighting gold nanoparticles within Fe-oxide from h. Au is in red, Fe in green. Abbreviations: Au, gold; Fe, iron; Hem, hematite; Mag, magnetite/maghemite; NP, nanoparticle; Ox, oxide. Some images have been cropped and rotated or reflected to produce similar orientations and aid comparison.

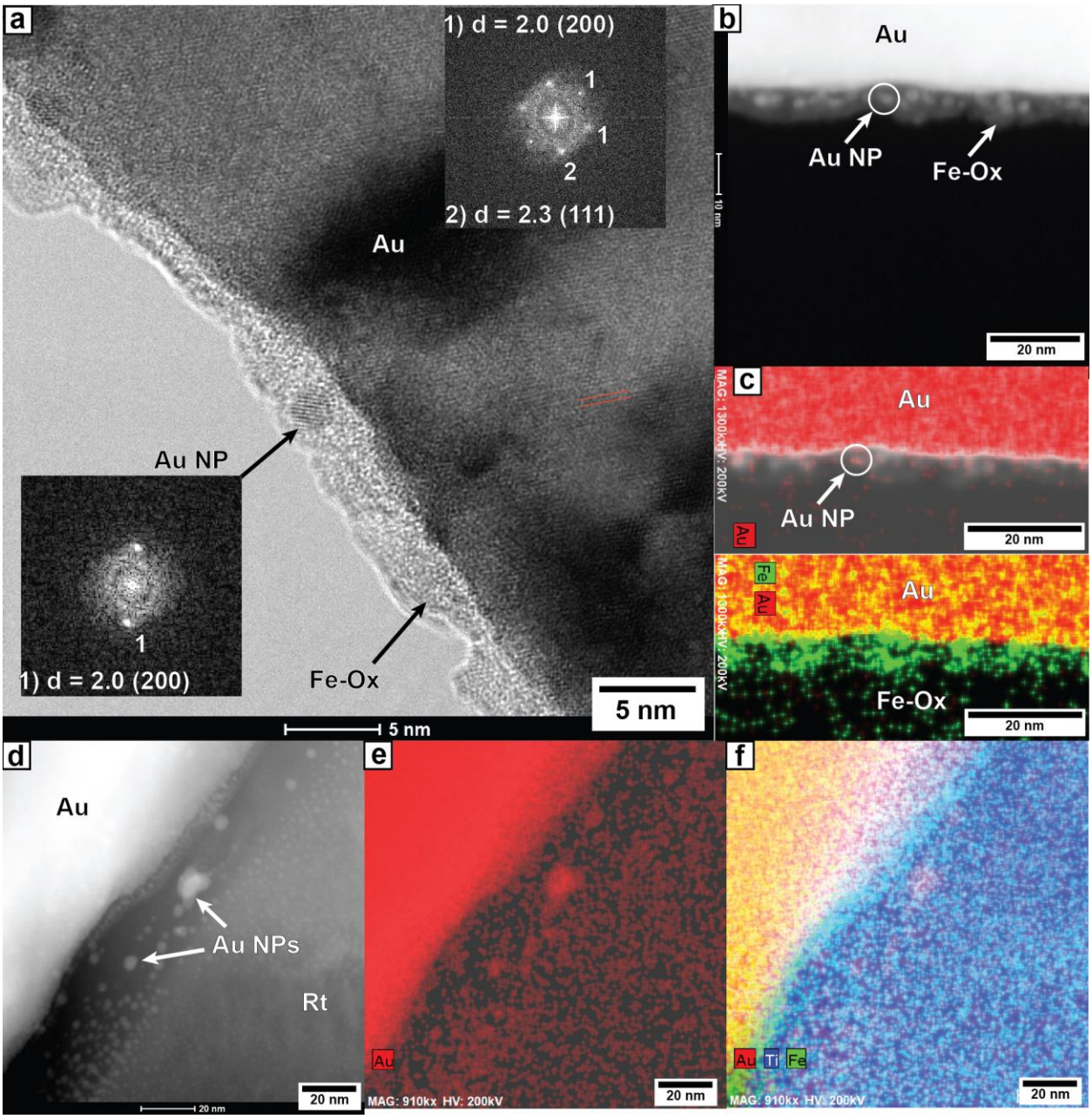

Figure 4.6. High-resolution TEM image with Fast Fourier Transform (FFT) patterns, STEM images and STEM-EDS elemental maps from locations shown in Fig. 4.4a. a, High resolution TEM image of Fe-oxide on coarse gold surface with FFT patterns for gold nanoparticles and coarse gold. Numbers refer to FFT legend provided with FFT. b, STEM image of Fe-oxide and gold nanoparticles on coarse gold surface. c, STEM-EDS elemental maps highlighting gold

nanoparticles within Fe-oxides on the surface of coarse gold from b. Au is in red, Fe in green. d, STEM image of gold nanoparticles within rutile at the margin of coarse gold-Fe-oxide-rutile. e-f, STEM-EDS elemental maps highlighting gold nanoparticles within rutile. Au is in red, Fe in green, Ti in blue. Abbreviations: Au, gold; Fe, iron; Mag, magnetite/maghemite; NP, nanoparticle; Ox, oxide; Rt, rutile; Ti, titanium. Some images have been cropped and rotated or reflected to produce similar orientations and aid comparison.

4.7 Supplementary Figures

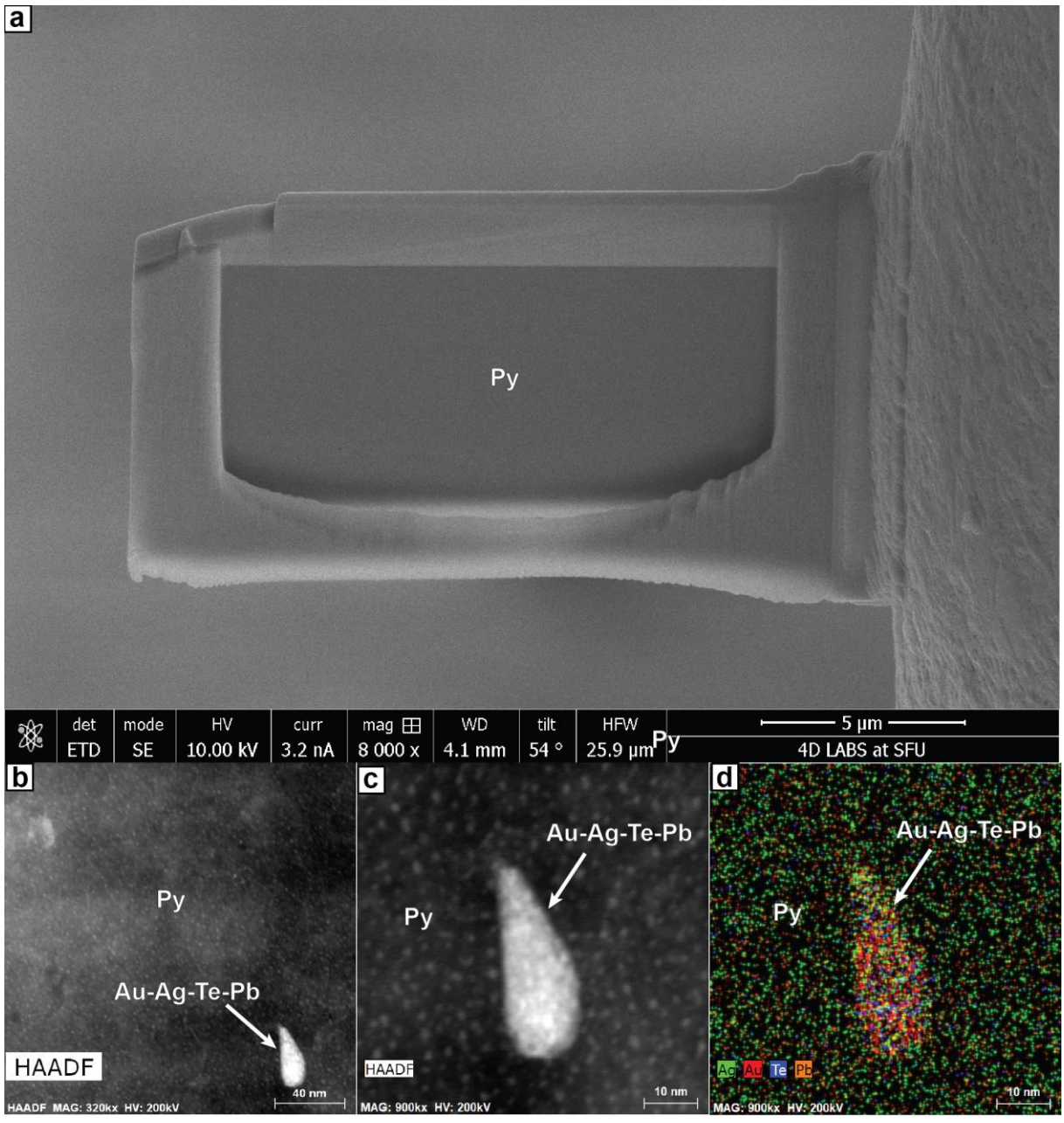

Supplementary Figure 4.1. Pyrite FIB section with nano-scale Au-Ag-Te-Pb domains. a, SEM-BSE image of the pyrite FIB section from the location shown in Fig. 4.3d. b-c, STEM images of nano-scale Au-Ag-Te-Pb domains in pyrite. d, STEM-EDS elemental map of nano-scale Au-Ag-

Te-Pb domains in pyrite. Au is in red, Ag in green, Te in blue and Pb in orange. Abbreviations: Au, gold; Ag, silver; Pb, lead; Py, pyrite; Te, tellurium.

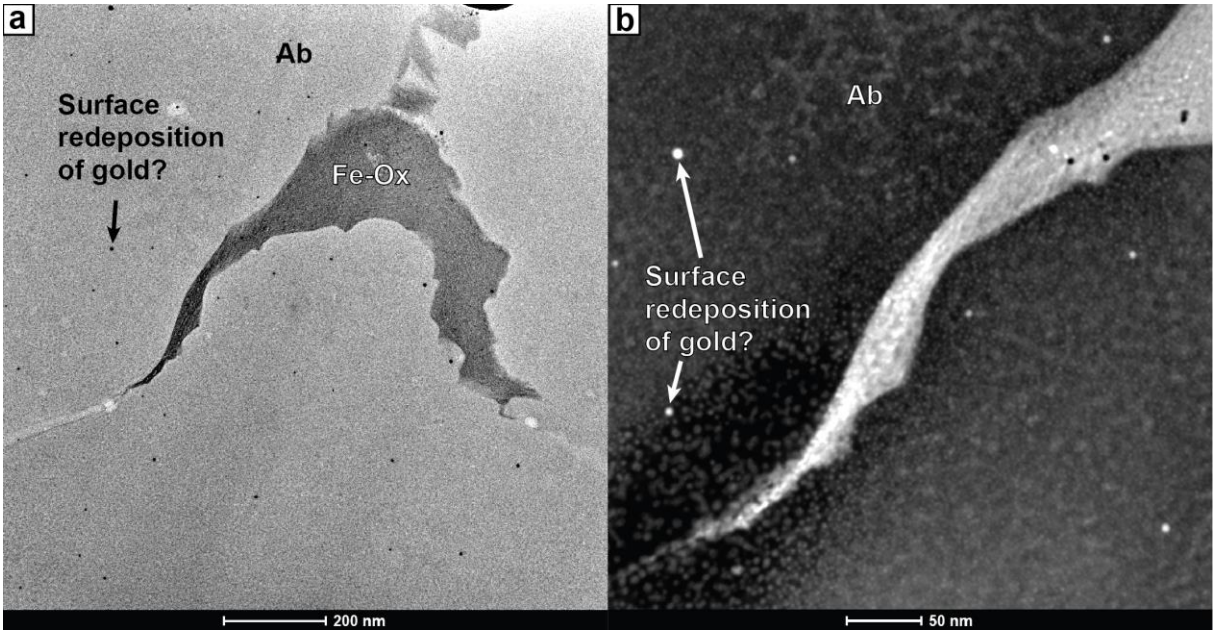

Supplementary Figure 4.2. TEM/STEM images showing possible Au redeposition. a, TEM image of Fe-oxide surrounded by albite with possible Au redeposition shown by black surface dots. b, Higher magnification STEM image of Fe-oxide surrounded by albite with possible Au redeposition shown by white surface dots. Abbreviations: Ab, albite; Fe, iron; Ox, oxide.

Chapter 5

5 General Conclusions

This thesis addressed the discrimination of Au deposits and the origins of coarse gold using a comprehensive approach that combined detailed field mapping, microscopy, bulk and in-situ geochemical methods and geochronology. A summary of more specific findings and advances to understanding ore-forming processes is presented below.

Chapter 2 has shown that field mapping combined with microscopy, geochemistry and geochronology can be used to discriminate between intrusion-related and orogenic Au deposits. More specifically, our data suggests that sanukitoid-related gold deposits form a distinct group of intrusion-related deposits. They formed in the late Archean (<2690 Ma), predate shear zone development, and are characterized by high fO_2 and low $\delta^{34}S$ values (≤-5‰). Other important findings include: (1) the greater resolution of in-situ geochemical methods over bulk methods without which the interpretation of Au-forming processes is greatly compromised; (2) new baselines for the interpretation and comparison of in-situ stable isotope, trace metal, and native gold geochemical data; and (3) the common association across Archean gold deposit types of Au with Ag, Te and Hg.

Chapters 3 and 4 reported on the importance of coupled dissolution-reprecipitation of Au-bearing sulfides in the remobilization and deposition of coarse native gold. Chapter 3 carefully describes the steps involved in the remobilization of gold and shows that fluid-mediated polymetallic melts can efficiently transport and concentrate gold. Other findings include: (1) the change in Au/Ag ratios from 1 in early pyrite to 9 in late, coarse visible gold, which is commonly observed in Archean Au deposits and which offers a tool for determining if Au is trapped in

sulfide phases or exists as free gold; (2) the presence of both As-Au oscillatory and sector zoning in primary pyrite, which argues against a fluid pulse model for chemical zoning in pyrite; and (3) the presence of LMCE (e.g., Te, Bi, Sb, Hg) in many large Au deposits (>20) across the Superior craton, which indicates that polymetallic melts may be more common than previously thought and play an important role in forming high-grade ore zones.

Chapter 4 reports for the first time on the presence of gold nanoparticles in an Archean orogenic deposit and presents evidence for gold coarsening by Ostwald ripening. Au-bearing polymetallic melts and gold nanoparticle transport could operate alone or together and provide a new interpretation on the origin of coarse gold in world-class Au deposits.

5.1 Suggestions for Future Work

Recent technological advances in analytical methods (e.g., LA-ICP-MS, atom probe tomography) now makes the direct analysis of gold more feasible along with imaging of gold atoms and micro-inclusions (Tetland et al., 2018; Hastie et al., 2020; Liu et al., 2021). This may be helpful in further understanding the origin of coarse native gold, deposit type discrimination, Au-forming processes and regional metallogenic trends that are important to exploration and metallurgy.

As Au deposit research evolves to finer scales, careful thought must go into the interpretation of such data due to quantum effects. This has been briefly discussed in Chapter 3 and Chapter 4, but is rarely discussed much further in geology. Even the behaviour of native metals is governed by quantum mechanics, due to the very nature of metallic bonding (Pauling, 1960). These points emphasize the need for new cross-disciplinary studies between geology, physics, and metallurgy because although we can predict and interpret the behaviour of metallic

minerals on a larger scale, the underlying mechanisms for many mineral processes exist in the quantum world.

5.2 References

Hastie, E.C.G., Petrus, J.A., Gibson, H.L., and Tait, K.T., 2020, Gold Fingerprinting: Using major and trace elements associated with native gold to work toward a global gold database; *in* Summary of Field Work, 2020: Ontario Geological Survey, Open File Report 6370, p. 10-1 to 10-10.

Liu, H., Beaudoin, G., Makvandi, S., Jackson, S.E., and Huang, X., 2021, Multivariate statistical analysis of trace element compositions of native gold from orogenic gold deposits: Implication for mineral exploration: Ore Geology Reviews, v. 131, 104061.

Tetland, M., Greenough, J., Fryer, B., Hinds, M., and Shaheen, M.E., 2017, Suitability of AuRM2 as a reference material for trace element microanalysis of native gold: Geostandards and Geoanalytical Research, v. 41, p. 689-700.

Pauling, L., 1960, The nature of the chemical bond, 3rd ed.: Cornell University Press, 644 p.